Final Report for

Coulomb Thrusting Application Study

Dr. Hanspeter Schaub
Aerospace and Ocean Engineering Department
Virginia Tech, Blacksburg, VA 24091-0203

Dr. Gordon G. Parker and Dr. Lyon B. King
Aerophysics, Inc.
Houghton, MI, 87185

Sponsored by
Defense Advanced Research Projects Agency
SPO
Program: Next Generation Space Technologies & Systems
DARPA ORDER No. U122/01, Program Code: 5P30
Issued by DARPA/CMO under Contract No. HR0011-05-C-0026

Report Documentation Page

Form Approved
OMB No. 0704-0188

1. REPORT DATE	2. REPORT TYPE	3. DATES COVERED
20 JAN 2006	**N/A**	**-**

4. TITLE AND SUBTITLE	5a. CONTRACT NUMBER
Coulomb Thrusting Application Study	5b. GRANT NUMBER
	5c. PROGRAM ELEMENT NUMBER
6. AUTHOR(S)	5d. PROJECT NUMBER
	5e. TASK NUMBER
	5f. WORK UNIT NUMBER
7. PERFORMING ORGANIZATION NAME(S) AND ADDRESS(ES) **DARPA/CMO 3701 N. Fairfax Street Arlington, VA 22203-1714**	8. PERFORMING ORGANIZATION REPORT NUMBER
9. SPONSORING/MONITORING AGENCY NAME(S) AND ADDRESS(ES)	10. SPONSOR/MONITOR'S ACRONYM(S)
	11. SPONSOR/MONITOR'S REPORT NUMBER(S)

12. DISTRIBUTION/AVAILABILITY STATEMENT
Approved for public release, distribution unlimited

13. SUPPLEMENTARY NOTES

14. ABSTRACT

15. SUBJECT TERMS

16. SECURITY CLASSIFICATION OF:			17. LIMITATION OF ABSTRACT	18. NUMBER OF PAGES	19a. NAME OF RESPONSIBLE PERSON
a. REPORT	b. ABSTRACT	c. THIS PAGE			
unclassified	**unclassified**	**unclassified**	**UU**	**119**	

Standard Form 298 (Rev. 8-98)
Prescribed by ANSI Std Z39-18

Summary

This report discusses the results of an 8-month inter-disciplinary research project between Virginia Polytechnic Institute and State University and Aerophysics Inc. The research task objectives are to study how Coulomb propulsion can be used to create reconfigurable distributed spacecraft formation concepts. Both formation maintenance and deployment charge and voltage levels are of interest, as well as the required reconfiguration times to change the formation size. A further task is to study the space plasma environment at low to high Earth orbit altitudes. Associated to this task is the study of the expected differential disturbance levels that Coulomb spacecraft will experience at a range of orbit altitudes. Using the results of the plasma environment study, expected spacecraft voltages are to be computed to compensate for conservative orbital perturbation estimates. Another objective is to study mechanisms to both measure the local plasma charge level, and control the spacecraft charge relative to this plasma charge level. The final task is to perform a comparison study of the Coulomb propulsion concept to other high-efficiency propulsion concepts.

The technical problems associated with Coulomb formation flying is determining the required charge level to achieve missions tasks such as deployment, orbit maintenance, formation reconfiguration, or docking maneuvers. Previously flown missions in the 70s have demonstrated that kilovolt level of charges are feasible. In this study we are assuming that this charge level can be safely increased to multiple hundreds of kilovolts using modern materials and manufacturing methods. A very challenging aspect of Coulomb thrusting based control is that these forces only act along the line of sight vector between spacecraft. As a result, the relative motion dynamics are very nonlinear and coupled, and can yield surprising, unexpected results. The current CLUSTERS mission uses Langmuir probes up to 25 meters in length to measure the local space plasma potential level very accurately. Their goal is to precisely zero the spacecraft potential relative to this plasma. With the Coulomb spacecraft control concept the craft are flying 10–100 meters apart, making such large boom impractical. Instead, the technical challenge is to find other methods to sense and servo the spacecraft charge. The Coulomb thrusting concept has distinctly different requirements than the currently flying charge control method. Thus, sensing methods must be investigated which achieve the required spacecraft charge control without adding impractical components.

The general methodology is to conduct literature reviews of the space plasma environment and charge feedback control technology, create open-loop numerical simulation studies to estimate required charge levels, write custom numerical simulations to investigate particular mission scenarios, as well as perform analytical research to investigate the closed-loop reconfiguration control of a 2-craft formation in high Earth orbit. No laboratory experiments are conducted during this study.

The important findings of the plasma environment study are that the plasma Debye length is on the order of 0.01–0.03 meters at low Earth orbit. This strong electric field masking parameter makes the Coulomb thrusting concept infeasible at this low altitude with a cold, dense space plasma. At higher altitudes the Van Allen radiation belts are of concern. The data here shows that the Debye length is still only 0.03–0.26 meters, too small for practical use with Coulomb thrusting. Beyond 5-6 Earth radii outward to geostationary altitudes the Debye length is found to vary between 100–1000 meters. The rest of the research focused on mission flying in high Earth orbits outside of the Van Allen radiation belts. At these altitude the dominant differential orbital perturbation is differential solar radiation pressure. This is true for spacecraft separation distances outward to 1000 meters. Conservative estimates show that flying spacecraft about 20 meters apart at GEO would require multiple kilovolts to compensate, assuming a 50kg craft with 0.5 meter radius. Further, considering the Earth magnetic field, for the induced Lorentz force to be comparable to differential solar radiation pressure, the craft would have to charge up to multiple mega-volt levels. The

expected open-loop maintenance charge level studies are conducted for a classical formation of spacecraft, as well as a gluon-deputy formation concept. Here the gluon craft size is enlarged to be able to carry a higher charge level. Flying 20–30 meters apart, these voltages are around 10's of kilovolt.

A study is performed to investigate voltage requirements to perform static Coulomb structures. Here the electrostatic force cancel the relative orbital acceleration to yield an invariant formation shape as seen by the rotating center of mass frame. An important finding is that it is possible to construct virtual structures where sensor craft are in a desired geometry (e.g. distributed radar interferometry), while other charged craft in this virtual structure are in a support role to help maintain the shape.

The important findings of the deployment study include numerical simulations of deputy craft being released from a mother craft using rest-to-rest or rest-to-motion scenarios. The simulations use closed-loop charge control to achieve the final position and/or velocities. Using essentially no fuel, this study shows that deputy craft can be relocated dozens of meters using 10's of kilovolt levels of charge. Maneuver times are typically several hours.

Another study investigated the required maximum charge level to change the separation distance of two inertially floating spacecraft within a specified amount of time. An important result of this research was finding a robust numerical optimization method to find such solutions. The inverse square drop off of the electrostatic field strength causes strong sensitivity issues with larger separation distance. Homotopy methods were employed to sweep through a range of separation distance, travel times, and plasma Debye lengths. To reconfigure 2 craft from 2 to 25 meters in a few hours requires 1–10's of kilovolts.

A related study investigates a closed-loop charge control of a 2-craft nadir pointing formation at GEO. Here the gravity gradient torque acting on the system is exploited to stabilize the formation attitude while changing the length. Important findings include analytical predictions of fast the craft can increase or decrease their separation distance while still guaranteeing linear stability of the non-autonomous system. Maneuver times are typically around 1–2 days to allow the weak local gravity gradient to stabilize the in-orbit-plane formation attitude.

The charge control study found a promising method servo the spacecraft voltage level. An array of small differential voltage probes are added to the vehicle which can measure the electric potential. Having a model of the vehicle geometry and materials, it is then possible to estimate the total vehicle potential. Further, to achieve this potential, a simple ion or electron gun is used. An important conclusion is that this process is insensitive to plasma potential variations. The local variations of space plasma between spacecraft is minimal due to the small separation distances. Thus, it is only necessary to control the spacecraft charge relative to the plasma. This is a substantial simplification to the charge control process on the CLUSTERS mission.

Finally, the mass and power comparison study shows that the Coulomb thrusting concept is orders of magnitudes more efficient than ion-engine technologies, and often requires as little as 1 Watt of power or less. In fact, the total electrical power requirement for Coulomb thrusting are determined not by the propulsion method needs itself, but rather by the power requirements of the supporting electronics and thermal control.

The implications for further research are that several exciting new mission concepts are determined. The virtual structure concept can be used to deploy a series of small probe satellites about a non-collaborative satellite to monitor its activities. Sensor probes could places near the target craft without interfering with it. The probe location can be actively controlled using the other charged spacecraft. The mother craft is assumed to have its own station keeping capability. Further, the Coulomb thrusting concept can be used to ploy swarms of pico-satellites. Compared to mechanical release mechanisms, the electrostatic force can control and correct the release trajectory up to

several meters away.

A very promising use of Coulomb thrusting is docking and proximity flying operations. Docking in particular is a very challenging operation that requires significant fuel amounts to perform the many small orbit corrections. Further, exhaust plume impingement is a major concern. Using a Coulomb force to control the relative motion avoids the plume impingement issue, while the required fuel requirements would be near zero. Using a nadir-pointing docking approach, the gravity gradient could be exploited. Here the Coulomb force stabilizes both the separation distance and the in-plane attitude angle. Out-of-plane motion would be compensated with conventional thrusters. This scenario would provide an elegant docking approach solution which uses minimal amounts of fuel and avoids the plume impingement issues.

Table of Contents

Chapter 1

Introduction

This report discusses the results of an 8-month inter-disciplinary research project between Virginia Polytechnic Institute and State University and Aerophysics Inc. The project goal is to investigate using Coulomb propulsion to control the relative motion of spacecraft in a variety of mission scenarios. The novel Coulomb thrusting concept exploits spacecraft charging and the associated inter-craft Coulomb forces. By controlling the electrostatic charge of the spacecraft, small forces are created cause the craft to attract or repel each other. Reference 1 shows that such forces can be generated in an essentially propellantless manner using often as little as 1 Watt of electric power. Further, this mode of propulsion is very clean compared to ion-engines. Preliminary analysis shows that Coulomb propulsion is up to 10^{10} times more fuel efficient than state-of-the-art relative motion propulsion methods, and thus warrants investigation as a possible alternative or supplement to conventional propulsion technologies. Coulomb thrusting avoids the typical plume impingement problems of ion engines for tight relative motion control on the order of dozens of meters.

This technology is significant because it will facilitate novel mission concepts which are not possible with conventional technologies. For example, high-precision, distributed aperture formation flying missions with applications to Earth imaging and surveillance are envisioned. Or, the Coulomb thrusting could be used during the deployment phase of a formation or a swarm of pico-satellites, as well as during formation maintenance periods. Having an extremely fuel-efficient method to correct the relative motion prolongs the mission durations, and allows for the interferometry aperture radius to be varied on demand. Other formation concepts investigated include along-track and nadir-pointing docking concepts, static Coulomb structures, as well as gluon satellite concepts. With the latter concept a larger spacecraft is dedicated to produce a large charge, and thus reduce the voltage requirements of the smaller deputy craft.

Spacecraft flying in Earth orbits are not operating in a pure vacuum, but rather in a space plasma environment. Here the craft is exposed to positively charged ions and negatively charged electrons. These charges will group around a charged object, and thus mask the spacecraft charge from other neighboring spacecraft. As a result the presence of a cold, dense space plasma limits the applicability of the Coulomb thrusting concept. This study investigates the expected space plasma environment from low to high Earth orbits, and determines in what regions that Coulomb thrusting appears feasible.

The expected orbit differential perturbations levels are explored orbit altitudes ranging from low to high Earth orbits. Conservative worst-case voltage requirements are computed to compensate for these formation perturbations. This study provides approximate spacecraft charge or voltage requirements. To standardize the results, a common typical deputy craft shape, size and mass is chosen across all these studies. Required open-loop maintenance voltage level are determined for classical spacecraft formations

of N craft, and for the gluon-deputy concept.

For wide-field-of-view applications, or during formation deployment, the relative spacecraft distances can be less than 100 meters. The primary goal of the virtual structure concept studies is to quantify charging requirements as a function of virtual structure formation and size scaling. For example, to achieve near-hemisphere Earth coverage at GEO requires spacecraft separation distances of 20-30 meters. Traditional formation flying concepts require numerous orbit corrections to maintain such a tight formation, resulting in a relatively short spacecraft lifetime. While some type of ion thruster is usually baselined for such formation-keeping missions, ion propulsion exhaust plumes are caustic to other spacecraft sensors and components, and thus ion-propulsion is ill suited for tight formation flying missions. The propellantless nature of Coulomb propulsion avoids these problems.

The deployment study of small Coulomb craft investigates how the electrostatic force field can be used to deploy craft, or generally control their relative motion between vehicles. Both rest-to-rest and rest-to-speed maneuvers are considered. In this study the mother craft is assumed to have its own station keeping capability, as well as its own attitude control. By using multiple controlled charge surfaces on the mother craft, general three-dimensional electrostatic fields are produced to control the relative motion of the deputy craft. Because these maneuvers involve having the spacecraft fly within multiple-spacecraft diameters from each other, a study is performed to evaluate the validity of the point-charge model of a sphere in a vacuum. The actual Coulomb force computed of a three-dimensional sphere in a plasma environment and compared to the point-charge model. The results indicate up to what separation distance the point-charge modeling assumption is valid.

Next, the results of a reconfiguration time study are presented. Here estimates of the required charge level are sought to change the nominal separation distance over a set amount of time. First the craft are assumed to be floating in inertial space. For a given final separation distance and transfer time, the required maximum voltages and charge switching times are computed. An exciting ability of the Coulomb formations is their ability to be able to change the size and shape over time. This simplified study provides a sense of required voltages to achieve a family of separation distance changes. The second section discusses in detail how a 2-craft nadir-pointing formation can vary the nominal separation distance over time. Here the relative orbital dynamics are exploited to have the gravity gradient torque acting on the formation cause the in-plane formation attitude to be stabilized. Linearizing the time-varying system, the study illustrate limits on how fast the craft separation distance can be varied while still guaranteeing stability.

The next chapter focuses on issues related to measuring the spacecraft charge or voltage level. Currently flying spacecraft with charge control require precise voltage balancing with the space plasma environment. This involves adding 25 meter Langmuir probes to the craft to sense the plasma potential level. These long probes are very impractical for the Coulomb spacecraft concept, and the small nominal separation distances. Instead, alternate methods are investigate to obtain approximate methods to level and servo the spacecraft charge level.

The final study compares the Coulomb thrusting concept to other conventional thrusting technologies. In particular, the total mass and power required to add this thrusting technologies are investigated. Also, effective fuel efficiency values are obtained to control the relative motion of the craft.

Chapter 2

Compatibility of Coulomb Thrusting with Earth Orbital Environment

2.1 Physical Principles

2.1.1 Space Plasma Nomenclature

A plasma is a gaseous mixture of particles having both positive and negative electrical charges. The Earth orbital environment is permeated by plasma to some extent at all altitudes and latitudes. Generally, space plasmas consist of electrons and hydrogen ions (protons), however at lower altitudes the presence of other atomic ions becomes more prevalent. Plasmas are characterized by their density (electrons/ions per-unit-volume) and the energy or range of energies of the constituent particles. Since plasmas are gaseous, the tools of statistical mechanics are used to specify characteristic average quantities. In particular, if a plasma environment is in equilibrium it will obey Maxwellian statistics having a single temperature that provides a representation of the magnitude and statistical spread in particle energies. Furthermore, in an equilibrium plasma the density of positive particles will equal the density of negative particles in a condition known as quasineutrality. Thus, in a quasineutral plasma, it is sufficient to specify a single plasma density n, where $n = n_e = n_i$, and $n_{e/I}$ is the electron/ion density. An equilibrium plasma is then completely described by the value of density, n, and temperature, T, with all other macroscopic properties being derived from n and T. Not surprisingly, space plasmas are rarely in equilibrium. For instance, in the inner radiation belts the plasma environment consists of low energy (cold) dense plasma produced by particles evaporating from the upper ionosphere in addition to extremely high-energy (hot) particles captured from the solar wind. In such a plasma, it is not possible to define a single density and temperature that statistically characterizes the macroscopic properties. It is common to approximate the statistics of complicated non- equilibrium plasmas using a multi-fluid model. In a multi-fluid model, the plasma is assumed to consist of a number of interpenetrating equilibrium fluids which, individually, are described by Maxwellian statistics. The most common model is the two-temperature model. In this case, quasineutrality is assumed (equal density of ions and electrons), however each species is permitted to have a different temperature. The temperatures are then denoted by T_e for the electron temperature and T_i for the ion temperature. In a straightforward extension, complicated plasmas can be described by multiple values of electron and ion density and temperature, denoted by n_{e1}, T_{e1}, n_{e2}, T_{e2}, n_{i1}, T_{i1}, etc.

2.1.2 Debye Shielding

The concept of Debye shielding is fundamental to plasma physics. Qualitatively, Debye shielding can be viewed as a screening process whereby the mobile charges in a plasma screen out, or spatially neutralize an immersed test charge. For instance, consider placing a positive

point charge within a plasma. The plasma particles, which exist in a gaseous state, are mobile and will respond to the presence of the charge: the positive test charge will attract a neighboring cloud of negative charges while creating a local void of positive charges in its vicinity. When averaged over some region in space centered on the test charge, the net charge within the specified volume will be zero. As a result, another test charge placed a long way from this volume will see a cloud with zero net charge and will thus experience very little electrostatic force from the test charge.

The Debye length is calculated from plasma parameters according to

$$\lambda_d = \sqrt{\frac{\epsilon_0 KT}{ne^2}} \tag{2.1}$$

where e is the elementary charge and k is Boltzmanns constant. In a multi-fluid model, a total Debye length for the plasma can be calculated from each species. For instance, in a two-fluid (electrons and ions) model the total Debye length is[2]

$$\lambda_d^{-2} = \lambda_{d,e}^{-2} + \lambda_{d,i}^{-2} \tag{2.2}$$

where $\lambda_{d,e/i}$ is the electron/ion Debye length defined by n_e,T_e and n_i,T_i. More complicated multi-fluid models can be treated in a straightforward extension of this summation. Because of Debye shielding, the Coulomb electrostatic interaction between charged objects is modified in plasma as compared to the interaction in vacuum. Defining $F_0(d)$ as the well known Coulomb interaction force given by

$$F_0(d) = \frac{1}{4\pi\epsilon_0}\frac{q_1 q_2}{d^2} \tag{2.3}$$

the electrostatic interaction within a plasma can be expressed as $F(d) = F_0(d)e^{-d/\lambda_d}$.

It is apparent that very little electrostatic force can be exerted over a distance more than a few Debye length. A graphical depiction of Debye shielding is shown in Figure 2.1.

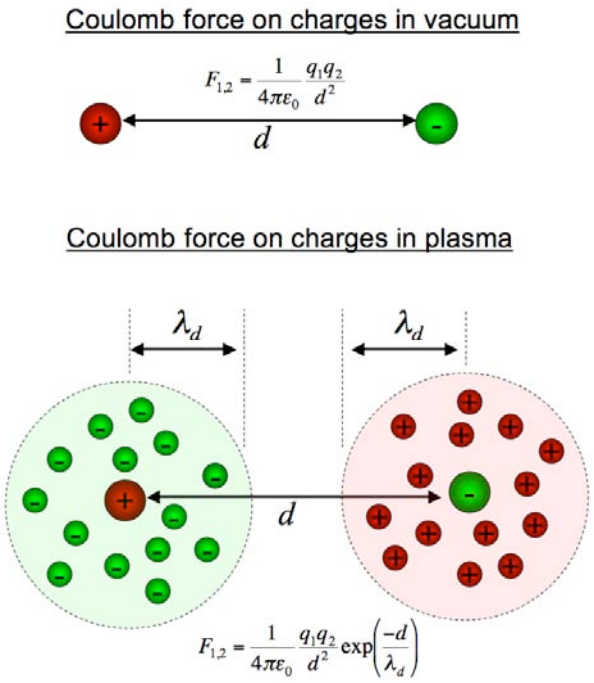

Figure 2.1: Depiction of Debye shielding in plasma.

2.1.3 Coulomb Thrusting Maneuvers in Plasma

The concept explored in this research is strongly governed by the prevailing Debye length in the vicinity of the spacecraft swarm or formation. Since the craft exert electrostatic forces on other charged vehicles, it is necessary that the inter-spacecraft spacing be less than a few Debye lengths to avoid the need for excessive and unrealistic charge magnitudes to affect Coulomb interaction.

It is convenient to define three fundamental length scales to categorize Coulomb thrusting operations. These length scales are the inter-spacecraft separation, d, the ambient plasma Debye length, λ_d, and the characteristic spacecraft size defined by D_{SC}. Using these length scales, Coulomb maneuvers can be loosely organized into three regimes defined by the length scale ordering: Proximity Operations (Prox-Ops), Formation Flight, and Swarm Flight.

2.1.3.1 ProxOps

In the operational envelope defined as ProxOps, the inter-spacecraft separation is less than both the Debye length and the spacecraft size, or $d < \lambda_d < D_{SC}$. Examples of such maneuvers are docking or deployment, where Coulomb interactions are used to control spacecraft motion at very close distance of approach. A schematic of ProxOps length scaling is shown in Figure 2.2.

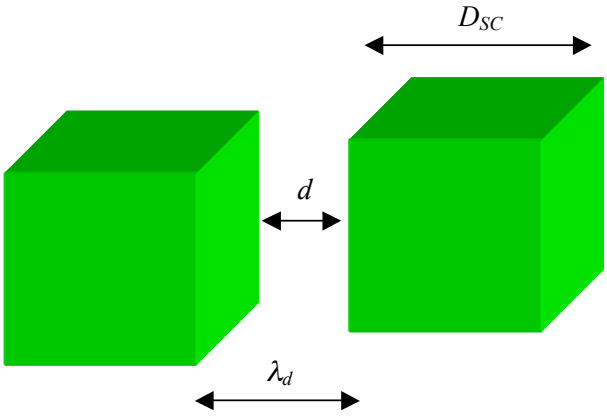

Figure 2.2: Illustration of ProxOps maneuvers in which $d < \lambda_d < D_{SC}$. Spacecraft interact only at very close separation.

2.1.3.2 Formation Flight

Formation flight represents relatively widely dispersed spacecraft in a hot, low- density plasma having large Debye length. The length scaling for formation flight is $D_{SC} < d \ll \lambda_d$. In formation flight, the electrostatic interaction between vehicles approaches that of point charges in vacuum. Furthermore, each vehicle in a formation interacts electrostatically with all or most of the other vehicles in the formation simultaneously. Formation flight dynamics are thus highly coupled. Formation flight is shown figuratively in Figure 2.3.

2.1.3.3 Swarm Flight

Swarm flight occupies an operational regime somewhat between that of Formation and ProxOps. Length scaling for Swarm flight is $D_{SC} <$

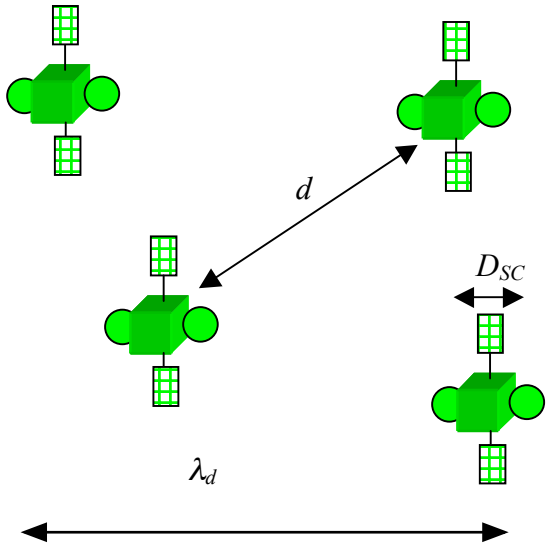

Figure 2.3: Illustration of Formation Flight dynamics. Since $D_{SC} < d \ll \lambda_d$ each vehicle is electrostatically coupled to all (or most) other vehicles in the group.

$d \approx \lambda_d$. Qualitatively, Swarm flight can be envisioned as a nearest neighbor interaction where each vehicle in the group is electrostatically coupled only to the vehicles in the immediate vicinity. In this fashion, a vehicle can electrostatically communicate with any other vehicle in the swarm by wave-like propagation through adjacent craft. A swarm schematic is shown in Figure 2.4.

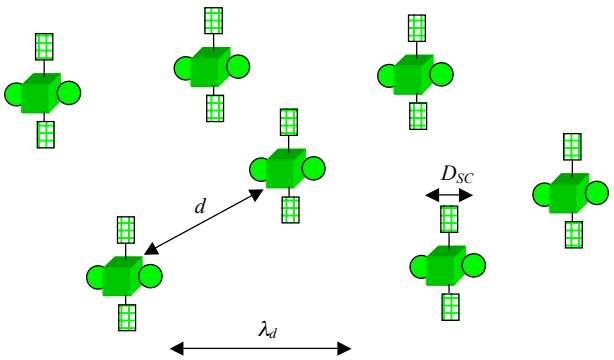

Figure 2.4: Illustration of Swarm Flight. Vehicles interact only with nearest neighbors and long-distance coupling occurs through intermediaries.

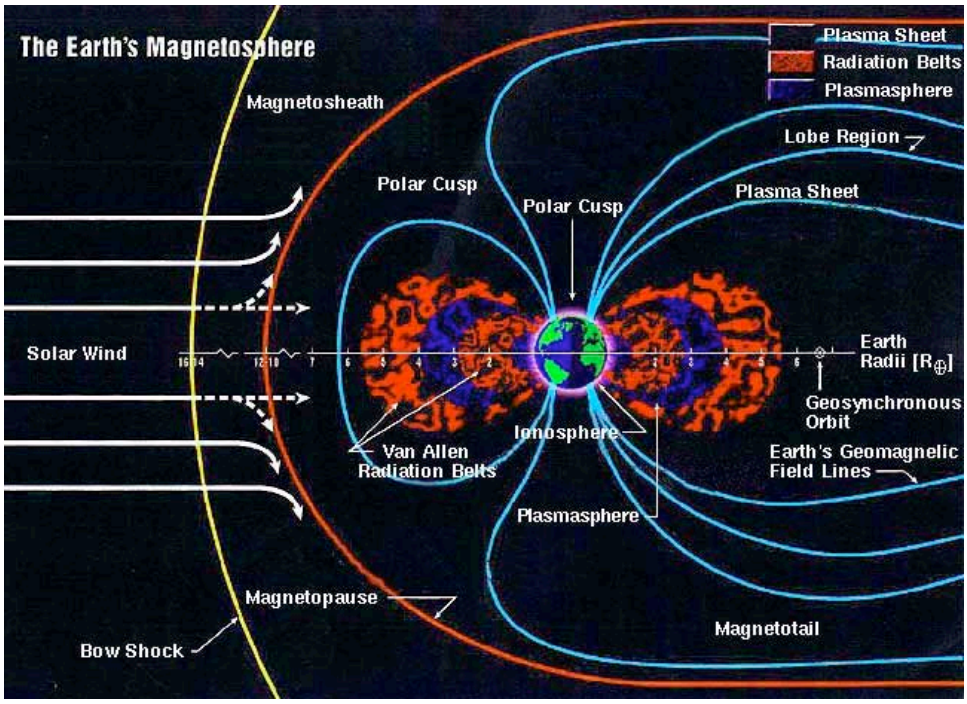

Figure 2.5: Graphical depiction of regions within the Earths magnetosphere.

2.2 Plasma Parameters in Earth Orbit

2.2.1 Overview of Earths Magnetosphere

The magnetosphere is the local plasma environment created through an interaction of the Earths magnetic field with the solar wind. An image of the magnetosphere is shown in Figure 2.5. Starting from Earth, the nearest region of the magnetosphere is known as the ionosphere. The ionosphere is created as upper atmospheric gasses are ionized through ultraviolet radiation and cosmic rays. The ionosphere plasma is relatively dense and cool and encompasses the orbital regime of Low-Earth Orbit (LEO). Extending away from the ionosphere is the plasmasphere. The plasmasphere is populated by evaporation and escape of the ionosphere plasma constituents into deep space. The lower Van Allan radiation belt exists within the plasmasphere; this belt contains a population of high-energy trapped solar wind particles superimposed on the cool plasmasphere. The plasma density in the plasmasphere smoothly decays with altitude, while the plasma temperature slowly increases. This smooth transition abruptly terminates at the plasmapause at an altitude of 4-5 Earth Radii (R_E). The plasmapause is a sharp shock-like boundary that separates the cool, dense plasmasphere from the hot, low-density plasma of the outer magnetosphere and the outer Van Allen belt. Geostationary Earth Orbit (GEO) is located beyond the Van Allen belts in the outer magnetosphere with an orbit radius of 6.6 R_E. The outer magnetosphere plasma and GEO environment is comprised of hot, low-density protons and electrons from the solar wind penetrating through the bow-shock.

Voyaging further from the Earth on the sunward side one encounters the outer edge of the magnetosphere known as the magnetopause, which separates the local Earth plasma environment from the interplanetary solar wind. Extending out from the Earth on the anti-sunward side is a long streaming tail known as the plasma sheet. The plasma sheet extends some 100 R_E and is greatly affected by solar

Table 2.1: Numerical Simulation Parameters

Region	**Altitude**	**Density** (m^{-3})	**Temperature** (eV)	**Debye Length** (m)
Ionosphere	1 R_e	10^{11}–10^{12}	0.02–0.2	0.01–0.03
Plasmasphere[3]	1–5 R_e	10^{9}–10^{10}	0.2–1.2	0.03–0.26
GEO/Outer Magneto-sphere[4]	5–10 R_e	$5 \cdot 10^{5}$–10^{7}	1,000–3,000	75–575
Plasmasheet Magnetotail[3]	10–15 R_e sunward 10–100's R_e anti-sunward	$5 \cdot 10^{5}$–$8 \cdot 10^{5}$	1,700–25,000	340–1,600
Solar Wind[5]	Outside magnetosphere	$3 \cdot 10^{6}$–$9 \cdot 10^{6}$	10–100	8–43

weather. In the high-latitude regions, the polar cusps represent open-field-line paths for the solar wind plasma to penetrate to the Earths surface. Within these cusps high-energy solar wind particles precipitate into the polar regions. The region between the polar cusp and the plasma sheet on the anti-sunward side is a magnetically protected region known as the lobe that is nearly devoid of plasma.

2.2.2 Compatible Orbits for Coulomb Thrusting

In order to perform Coulomb thrusting between spacecraft it is necessary that the plasma Debye length be greater than (or at least on the order of) the inter-spacecraft separation. This precludes the use of Coulomb control in cold, high-density plasmas such as that found in the ionosphere environment of LEO orbits. A qualitative depiction of the magnetosphere plasma environment is shown in Figure 2.6, where the diagonal lines represent constant values of Debye length with plasma density and temperature indicated on the axes. For approximate values, the Heidelberg Dust Research group has compiled a convenient set of representative plasma parameters* that are repeated in Table 2.1.

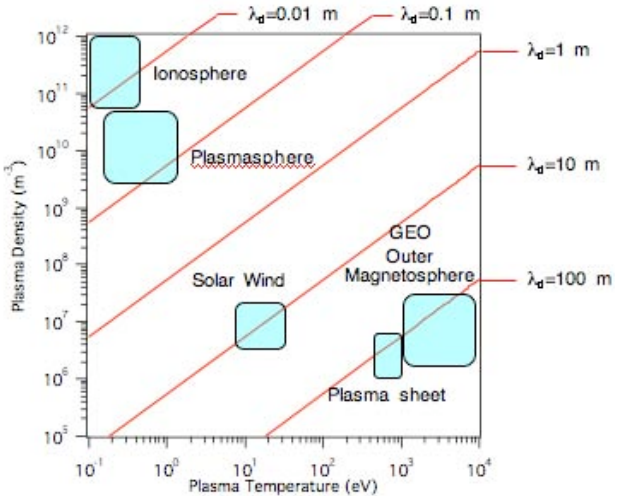

Figure 2.6: Plasma regimes of the Earths magnetosphere. Red diagonal lines indicate constant values of Debye length.

It is apparent from Figure 2.6 and Table 2.1 that the only feasible regime for inter- spacecraft Coulomb thrusting with contemporary-sized vehicles is the outer magnetosphere/GEO orbital environment. The centimeter-scale Debye lengths inside the plasmasphere render electrostatic interaction between vehicles negligible at all but the very closest separation distances.

Fortunately, detailed studies of the GEO plasma are readily available. Due to the high-value of assets placed in GEO coupled with

*http://www.mpi-hd.mpg.de/dustgroup/~graps/earth/magnetosphere.html

Table 2.2: Average GEO Environment[6]

Parameter	**Electrons**	**Ions**
Number density n_1, (1^{st} Maxwellian fit) m^{-3}	$0.78 \pm 0.7 \cdot 10^6$	$0.19 \pm 0.16 \cdot 10^6$
Temperature kT_1/e, (1^{st} Maxwellian fit) eV	$0.55 \pm 0.32 \cdot 10^3$	$0.8 \pm 1.0 \cdot 10^3$
Number density n_2, (2^{nd} Maxwellian fit) m^{-3}	$0.31 \pm 0.37 \cdot 10^6$	$0.39 \pm 0.26 \cdot 10^6$
Temperature kT_2/e, (2^{nd} Maxwellian fit) eV	$8.68 \pm 4.0 \cdot 10^3$	$15.8 \pm 5.0 \cdot 10^3$

Table 2.3: Worst-Case GEO Environment[6]

Parameter	**Electrons**	**Ions**
Number density n_1, (1^{st} Maxwellian fit) m^{-3}	$1.0 \cdot 10^6$	$1.1 \cdot 10^6$
Temperature kT_1/e, (1^{st} Maxwellian fit) eV	600	400
Number density n_2, (2^{nd} Maxwellian fit) m^{-3}	$1.4 \cdot 10^6$	$1.7 \cdot 10^6$
Temperature kT_2/e, (2^{nd} Maxwellian fit) eV	$2.51 \cdot 10^4$	$2.47 \cdot 10^4$

the propensity for potentially damaging spacecraft charging in the outer magnetosphere, the GEO plasma has been extensively characterized by early missions such as SCATHA,[7] ATS-5, and ATS-6.[8,9] The particle detectors on the ATS[4,10,11] and SCATHA[6] spacecraft have measured plasma variations for 50 complete days at 1 to 10 minute resolution from 1969 through 1980, bracketing one solar cycle.

Garrett and DeForest[4] fitted an analytical multi-fluid model to data collected over 10 different days from ATS-5 spacecraft between 1969 and 1972. These data were selected in such a way to show a wide range of geomagnetic activity including plasma injection events (i.e. sudden appearance of dense, relatively high energy plasma at GEO occurring at local midnight). The model gives reasonable and consistent representation of the variations following a substorm injection event at GEO. The parameters for this model during average GEO conditions are shown in Table 2.2 with Worst-case GEO conditions given in Table 2.3.

Based on the detailed multi-fluid GEO plasma model, work reported here will assume these values represent accurate properties of the outer magnetosphere plasma from the plasmapause out to the magnetosheath. Using the definition of Debye length for a multi-fluid model, the data from Table 2.2 and Table 2.3 imply an ambient Debye length between 110 and 180 m in the outer magnetosphere. Armed with these data, it is possible to consider the families of orbits that may be compatible with the Coulomb thrusting concept considered in this study.

Clearly, GEO orbits are well suited to the Coulomb concept, with inter-spacecraft separations of 100-300 m possible within the large Debye lengths present in this regime. Medium-Earth Orbits (MEOs) are also candidates at altitudes greater than the plasmapause at approximately 4.5 R_E. While LEO orbits are not candidates, it may be possible to exploit Highly Elliptical Orbits (HEOs), wherein Coulomb thrusting occurs at or near apogee and provides a periodic corrective ability to a low-perigee orbit. A schematic of orbit families and their relation to the plasmasphere is shown in Figure 2.7.

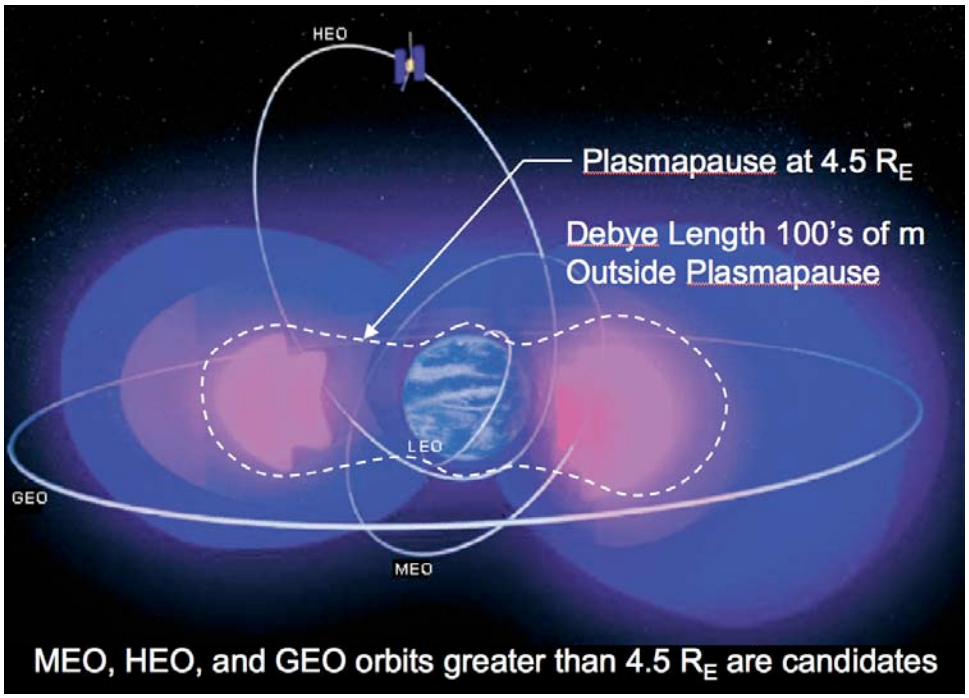

Figure 2.7: Orbital families and their relation to the Earths plasmasphere. LEO and MEO orbits with radii less than about 4.5 RE experience too much Debye shielding for electrostatic interaction. High MEO and GEO orbits are excellent candidates, with inter-spacecraft separation of 100s of meters possible. There may also be the potential to exploit HEO orbits, where Coulomb thrusting is performed at a high apogee.

2.2.3 Temporal Variation of Plasma Parameters

Plasma parameters in the magnetosphere are strongly affected by solar weather and can change on the timescale of minutes. This can affect Coulomb-interacting spacecraft in two ways: 1) a sudden increase/decrease in the ambient Debye length can cause a perturbation that must be corrected using active charge control, 2) inflation of the plasmapause can immerse a MEO-orbiting group of spacecraft within the cold, dense plasmasphere producing orders-of-magnitude decrease in the Debye length such that inter-spacecraft thrusting is no longer possible.

Variation in Debye length for outer magnetosphere/GEO regimes was captured by the Gorizont satellites. The Gorizont satellites, which are telecommunications platforms, also carried instruments to monitor the space environment. Tabulated values of plasma parameters as measured from Gorizont are available through ESAs Space Environment Effects and Education System (SPENVIS).[†] A collection of three orbital days were chosen, somewhat at random, from the list of available data to investigate the variation in local plasma conditions. Plots of Debye length at GEO are shown in Figure 2.8 as measured by Gorizont. As expected from the ATS-5 and 6 data sets, the ambient Debye length is on the order of 100 meters. Because of solar activity, the Debye length is seen to vary by as much as 400% over one orbital day.

Movement of the plasmapause can affect MEO formations whose orbit radii are near the transition to the outer magnetosphere. Since this boundary is dynamic, sudden inflation of the plasmasphere due to solar activity could envelop a low-MEO formation in cold, dense plasma rendering Coulomb interaction impossible. Data reported by the Heidelberg Dust Group presents an engineering model of the magnetospheric plasma as a function of altitude

[†] `http://www.spenvis.oma.be/spenvis/`

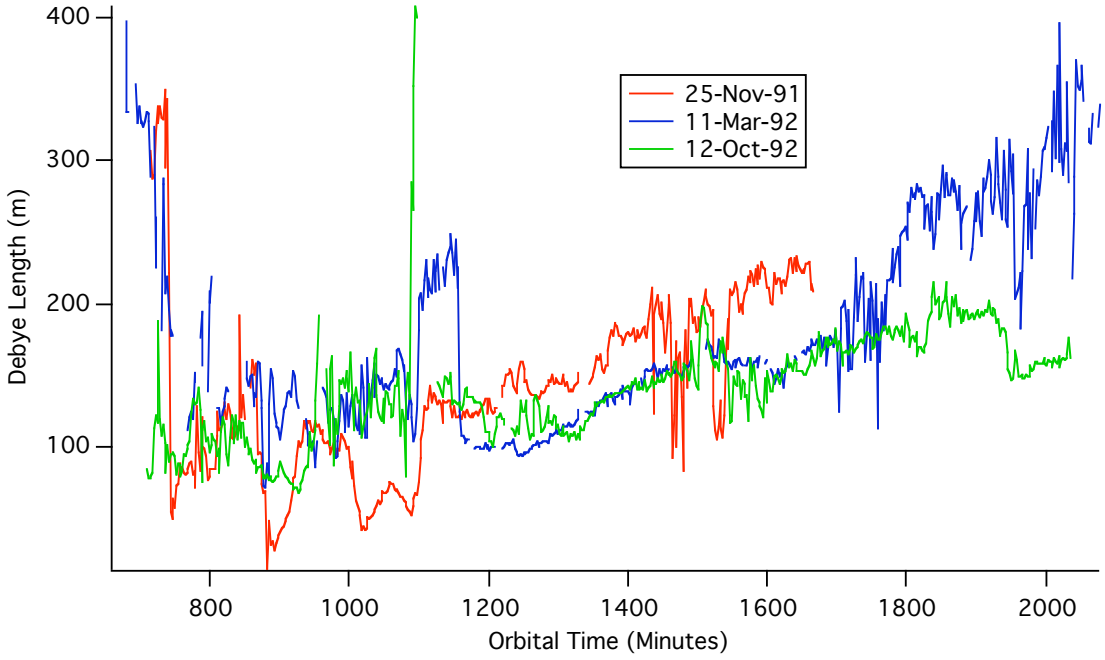

Figure 2.8: Variation in plasma Debye length at GEO as measured by Gorizont spacecraft.

and time. The model presents separate results for quiet Earth plasma conditions as well as disturbed conditions representative of high solar activity. Plots of the cold electron fluid density are shown in Figure 2.9 and Figure 2.10.[‡]

The plasmapause is apparent in Figure 2.9 and Figure 2.10 as the abrupt decrease in density that occurs between about 3 R_E and 6 R_E. During quiet conditions the plasmapause is seen to be somewhat stable and located near 5 R_E, with the exception of orbital times between 18 and 24 hours, where the cold plasma can reach 10 RE. During disturbed conditions, the overall plasma density in the region just outside of the plasmapause increases over the quiet case, although the boundary is somewhat more stationary. Thus, while it may be possible for Coulomb interaction in orbits below GEO down to about 4 R_E, any mission in this orbital regime must be robust against sudden expansion of the plasmasphere and interruption of the Coulomb thrust mechanism.

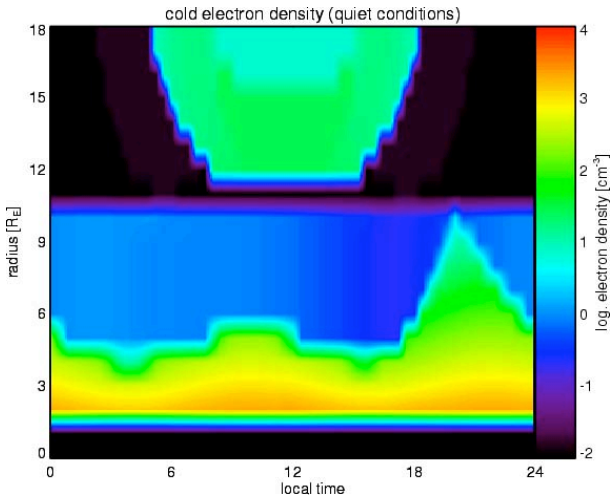

Figure 2.9: Model of cold electron magnetospheric density during quiet solar conditions

[‡]http://www.mpi-hd.mpg.de/dustgroup/~graps/earth/magnetosphere.html

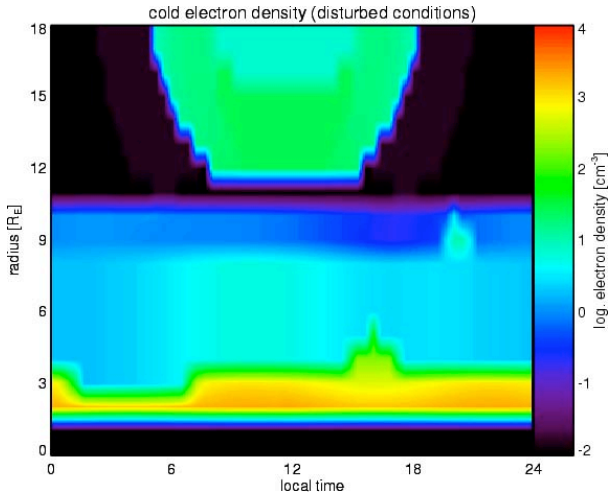

Figure 2.10: Model of cold electron magnetospheric density during active solar conditions

Chapter 3

Orbital Disturbance Study for Coulomb Spacecraft Clusters

This chapter discusses the expected disturbance levels that a cluster of spacecraft will experience. The orbit altitudes will range from Low Earth Orbit (LEO) to Geostationary Earth Orbits (GEO), while the spacecraft separation distances vary between 10 and 1000 meters. In particular, the *worst case* accelerations relative to the spacecraft cluster/formation center of mass are of interest. This information will then be used to determine minimum required maintenance charge/voltage levels to be able to compensate for these disturbances.

There are three types of disturbances that are modelled. First are the differential J_2 through J_6 gravitational zonal harmonics. Second, the atmospheric drag force due to flying in low Earth orbit is be modelled. Third, the solar radiation pressure due to the sun is also modelled. Finally, a study shows how large the magnetic Lorentz force magnitudes can grow if a charged craft is flying through Earth's weak magnetic environment.

3.1 Relative Acceleration Magnitudes

To study the relative motion of spacecraft in nearly circular orbits, the Clohessy-Wiltshire-Hill equations are commonly used.[12–14] These equations linearize the relative motion dynamics with respect to a *constantly* rotating reference orbit. They have a well-known analytical solution to the unperturbed motion which decouples the in-plane and out of orbit plane motions. The CW equations are very convenient to develop rendezvous and near-circular formation flying control laws.[15,16] With traditional spacecraft formation flying concepts, each craft contains its own inertial propulsion system, typically a high efficiency ion engine. As relative motion errors are detected, the thruster is used to correct the motion with respect to the rotating Hill frame.

However, the Coulomb thrusting concepts acts very differently. Here the spacecraft push and pull off each other to control the relative motion. The inertial orbit of the cluster is of secondary importance compared to the formation shape and is not compensated for with Coulomb thrusting. Thus, to determine the necessary relative orbit maintenance charge/voltage levels to compensate for differential perturbations, it is essential that the drift of the formation center of mass (Hill frame origin) is taken into account.

In order to avoid the linearization and constant orbit rate issues of the CW equations, we have chosen to use a full non-linear simulation of the spacecraft with the perturbations included as inertial acceleration vectors. Figure 3.1 describes the set-up of the relative motion problem and the notation to be used in the rest of this report. Let there be N charged spacecraft present. The inertial position vectors

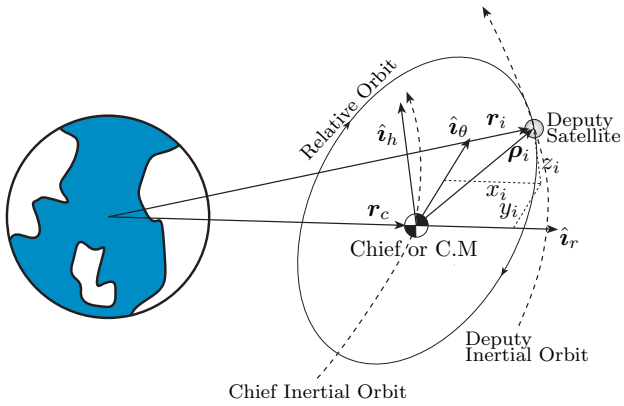

Figure 3.1: Diagram of the Relative Motion Problem

of the satellites is given by $\boldsymbol{r}_i$, while

$$\boldsymbol{r_c} = \frac{1}{M}\sum_{i=1}^{N} m_i \boldsymbol{r}_i \tag{3.1}$$

is the formation inertial center of mass vector. Here M is the total system mass and m_i is the mass of the i_{th} spacecraft. The velocity of the center of mass can be computed by differentiating the center of mass condition once to yield the following.

$$\dot{\boldsymbol{r}}_{\boldsymbol{c}} = \frac{1}{M}\sum_{i=1}^{N} m_i \dot{\boldsymbol{r}}_i \tag{3.2}$$

The Hill frame unit direction vectors $\mathcal{H}$: $\{\hat{\imath}_r, \hat{\imath}_\theta, \hat{\imath}_h\}$ are defined through:

$$\hat{\imath}_r = \frac{\boldsymbol{r}_c}{r_c} \tag{3.3}$$

$$\hat{\imath}_\theta = \hat{\imath}_h \times \hat{\imath}_r \tag{3.4}$$

$$\hat{\imath}_h = \frac{\boldsymbol{r}_c \times \dot{\boldsymbol{r}}_c}{|\boldsymbol{r}_c \times \dot{\boldsymbol{r}}_c|} \tag{3.5}$$

In the CW equations, this frame is treated as having a constant rotation rate. However, in this differential disturbance study the actual $\dot{\boldsymbol{r}}_c$ is taken into account. The rotation matrix $[HN]$, which will rotate vector components taken with respect to the inertial frame to vector components taken with respect to the the Hill frame, is defined as

$$[HN] = \begin{bmatrix} \hat{\imath}_r^T \\ \hat{\imath}_\theta^T \\ \hat{\imath}_h^T \end{bmatrix} \tag{3.6}$$

Defining the relative position vector as

$$\boldsymbol{\rho}_i = \boldsymbol{r}_i - \boldsymbol{r}_c \tag{3.7}$$

this vector can be mapped between inertial and Hill frame vector components using

$${}^{\mathcal{H}}\boldsymbol{\rho}_i = [HN]\,{}^{\mathcal{N}}\boldsymbol{\rho}_i \tag{3.8}$$

The inertial equations of motion of a satellite are given by

$$\ddot{\boldsymbol{r}}_i = -\frac{\mu}{{r_i}^3}\boldsymbol{r}_i + \boldsymbol{a}_{d_i} \tag{3.9}$$

where $\boldsymbol{a}_{d_i}$ is the disturbance acceleration acting on the i^{th} satellite. Of interest is how this disturbance acceleration will influence the motion of the satellite relative to the formation/cluster center of mass $\boldsymbol{r}_c$. In particular, we take into account here that $\boldsymbol{r}_c$ itself will also be influence by the disturbance. For example, if both satellites are experiencing the same atmospheric drag, then the differential disturbance would be zero because the center of mass is being disturbed by the same amount as the satellites. Similarly, if one satellite has twice the disturbance drag acceleration compared to the 2nd craft, then each craft would only have to compensate for half of this drag (assuming equal masses).

Equation (3.9) is used to perform any numerical simulations. Any Hill-frame specific initial conditions are first mapped into the inertial frame to start the simulation. The inertial acceleration is written as

$$\ddot{\boldsymbol{r}}_i = \ddot{\boldsymbol{r}}_c + \ddot{\boldsymbol{\rho}}_i \tag{3.10}$$

Next, let $\ddot{\hat{\boldsymbol{\rho}}}_i$ be the inertial relative acceleration if the no disturbance accelerations are present (Keplerian motion case).

$$\ddot{\hat{\boldsymbol{\rho}}}_i = \ddot{\hat{\boldsymbol{r}}}_i - \ddot{\hat{\boldsymbol{r}}}_c \tag{3.11}$$

Here $\ddot{\hat{\boldsymbol{r}}}_i$ and $\ddot{\hat{\boldsymbol{r}}}_c$ are defined as follows:

$$\ddot{\hat{\boldsymbol{r}}}_i = -\frac{\mu}{{r_i}^3}\boldsymbol{r}_i \tag{3.12}$$

$$\ddot{\hat{\boldsymbol{r}}}_c = \frac{1}{M}\sum_{i=1}^{N} m_i \ddot{\hat{\boldsymbol{r}}}_i \tag{3.13}$$

Thus the $\hat{}$ quantities are the unperturbed accelerations of the Keplerian relative motion case. Using Eq. (3.9) to integrate the satellite inertial position vectors, at any instant of time the $\boldsymbol{r}_i(t)$ will be available during post-processing, and these local "unperturbed" states can be computed.

Next, the relative inertial acceleration, $\ddot{\boldsymbol{\rho}}_i$, can be written as

$$\ddot{\boldsymbol{\rho}}_i = \ddot{\hat{\boldsymbol{\rho}}}_i + \delta\ddot{\boldsymbol{\rho}}_i \tag{3.14}$$

where we separate the naturally occurring relative acceleration from the relative acceleration due to the perturbation forces. Solving for the differential disturbance acceleration vector $\delta\ddot{\boldsymbol{\rho}}_i$ we find

$$\delta\ddot{\boldsymbol{\rho}}_i = \ddot{\boldsymbol{r}}_i - \ddot{\boldsymbol{r}}_c - \ddot{\hat{\boldsymbol{\rho}}}_i \tag{3.15}$$

To be able to maintain a cluster or formation of charged spacecraft, the spacecraft charging capabilities must be large enough to be able to compensate for the worst case differential disturbance acceleration $\delta\ddot{\boldsymbol{\rho}}_i$ which will be encountered for a particular orbit altitude and formation size. With each orbital disturbance type the differential disturbance acceleration is computed. These worst case disturbance acceleration values are then used in the next chapter to compute required minimum spacecraft charge/voltage levels to compensate for this disturbance.

Unless noted otherwise, all spacecraft are assumed to be spherical in shape and have a mass of $m_i = 50$ kg. Their radius is 0.5 meters.

3.2 Differential Gravitational Zonal Harmonics

The J_2 through J_6 perturbations arise from the fact that the Earth is not a perfect sphere, but rather ellipsoidal in shape. These effects have been estimated by observing the motion of spacecraft orbiting the Earth and are expressed in the form of zonal and tesseral spherical harmonic expansion coefficients. Of these gravitational disturbances, the 2nd order zonal harmonic called the J_2 term is about three orders of magnitude larger than the remain harmonics. It provides the dominant formation flying perturbation for spacecraft of equal type and build.[17] These formation flying spacecraft are typically envisioned to be flying about 1 km apart, or further.[18] However, for the Coulomb thrusting concept study, much smaller separation distances are considered. With these smaller separation distances the differential J_2 influence will become ever smaller. Of interest is how these differential accelerations compare to other orbital perturbations such as differential atmospheric drag and differential solar radiation pressure.

The inertial disturbance acceleration vector due to J_2 through J_6 can be modelled as direct functions of inertial position and the first six zonal harmonics. However, only the first zonal harmonic has a significant contribution for this study and is expressed as:.[14]

$$\boldsymbol{a}_{J_2} = \frac{-3}{2}J_2\left(\frac{\mu}{r^2}\right)\left(\frac{r_{\text{eq}}}{r}\right)^2\begin{pmatrix}\left(1-5\left(\frac{Z}{r}\right)^2\right)\frac{X}{r}\\ \left(1-5\left(\frac{Z}{r}\right)^2\right)\frac{Y}{r}\\ \left(3-5\left(\frac{Z}{r}\right)^2\right)\frac{Z}{r}\end{pmatrix} \tag{3.16}$$

Here r_{eq} is the equatorial radius of the Earth and μ is the gravitational constant of the Earth. The variables X, Y, and Z are the position coordinates with respect to the ECI (Earth Centered Inertial) frame and the orbit radius r takes on the form of:

$$r = \sqrt{X^2 + Y^2 + Z^2} \tag{3.17}$$

The magnitude of the J_2 induced relative motion disturbance depends on how the relative orbit is formed (is out-of-plane motion achieve through inclination or ascending node differences), and on the location (anomaly angle)

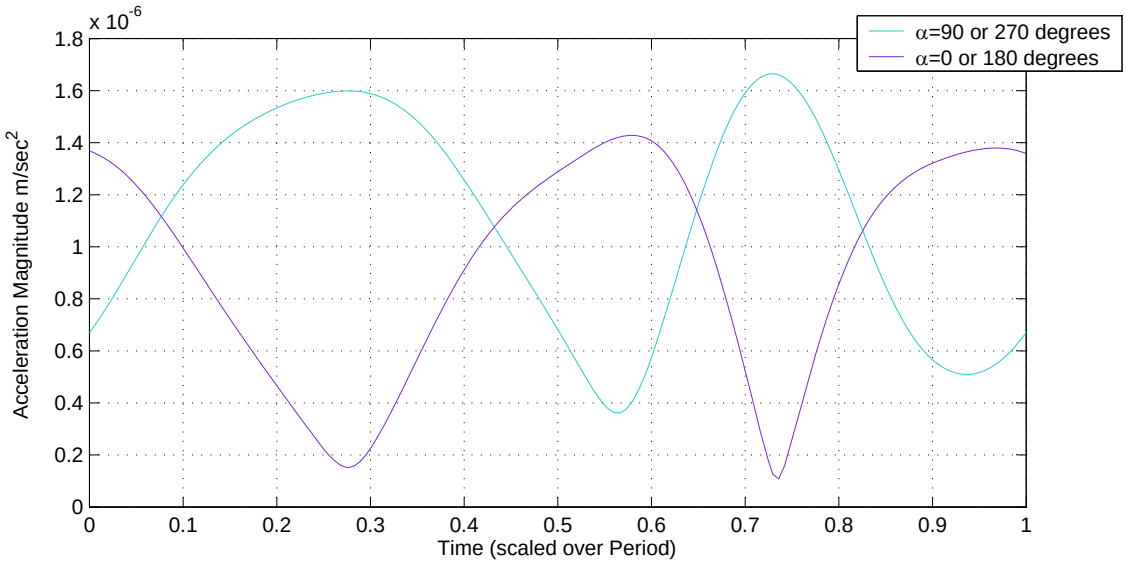

Figure 3.2: Plot of J_2 induced relative acceleration magnitude over one orbit period

within the orbit.[14,19,20] This study is based on investigating worst case scenarios to determine minimum spacecraft charge sizing requirements. The radar interferometry problem was of particular interest to this project. Here the desired relative orbits have circular projections relative to the local horizontal plane ($\hat{\boldsymbol{\imath}}_\theta$–$\hat{\boldsymbol{\imath}}_h$ plane). Let a relative position vector be written using Hill frame vector components as

$$\boldsymbol{\rho} = x\hat{\boldsymbol{\imath}}_r + y\hat{\boldsymbol{\imath}}_\theta + z\hat{\boldsymbol{\imath}}_h \tag{3.18}$$

The analytical solution to the linear CW equations shows that all bounded relative orbits with a circular chief must satisfy:[13,14]

$$x(t) = A_0 \cos(nt + \alpha) \tag{3.19}$$
$$y(t) = -2A_0 \sin(nt + \alpha) \tag{3.20}$$
$$z(t) = B_0 \cos(nt + \beta) \tag{3.21}$$

where A_0 and B_0 are relative orbit amplitudes, while α and β are phase angles of the relative motion. The parameter $n = \sqrt{\mu/r_c}^3$ is the chief's mean orbit rate. To achieve the circular projection of the relative motion in the local horizontal plane, the initial orbit must be setup such that $B_0 = 2A_0$, and either $\alpha = \beta$ or $\alpha = \beta + \pi$.[14] To determine the worst case differential J_2 accelerations, a quick study is preformed where the phase α is swept across all possible values. All orbits are initialized as they cross the equator.

The following plots in Figure 3.2 show the time histories of acceleration magnitude for J_2 perturbations, with four different initial condition α sets. From the figure we can see that when α is initially either 90 or 270 degrees produces a slightly larger acceleration magnitude over an orbit period. Because of symmetry, both satellites in those positions have the same relative acceleration magnitude over time. Since our overall goal is to size the accelerations for the worst possible case we will choose that as our initial condition for all the cases. Thus, to determine the worst case differential J_2 disturbance acceleration, these initial conditions are used to setup two satellites and then integrate the inertial equations of motion for one orbit. The worst differential acceleration is then recorded for the particular orbit altitude and relative orbit size.

Figure 3.3 and 3.4 illustrate the maximum differential J_2 accelerations in units of $\log_{10}(\mathrm{m/s^2})$. The altitude (horizontal axis) is

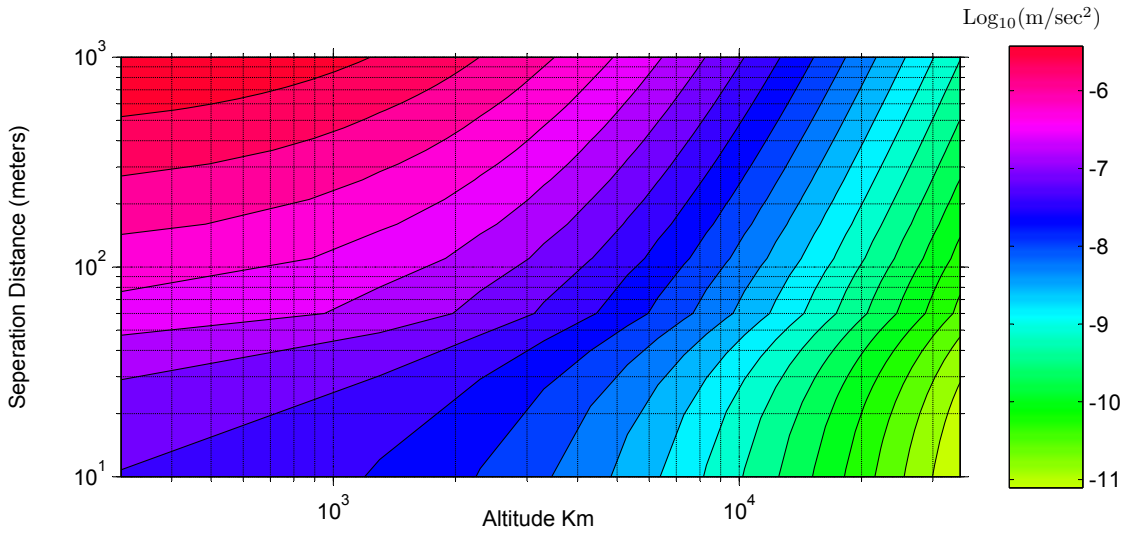

(a) Log of Max Acceleration due to J_2 trough J_6 with i=0°

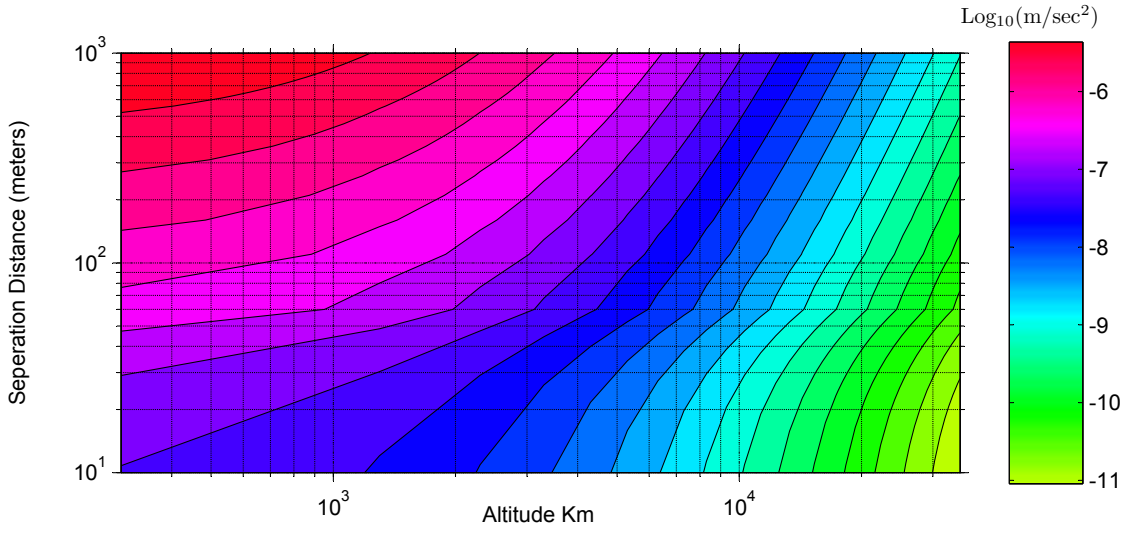

(b) Log of Max Acceleration due to J_2 trough J_6 with i=30°

Figure 3.3: Contour Plots of Acceleration in $\log_{10}(\mathrm{m/s^2})$ vs. Separation Distance and Altitude for J_2 through J_6 Perturbations

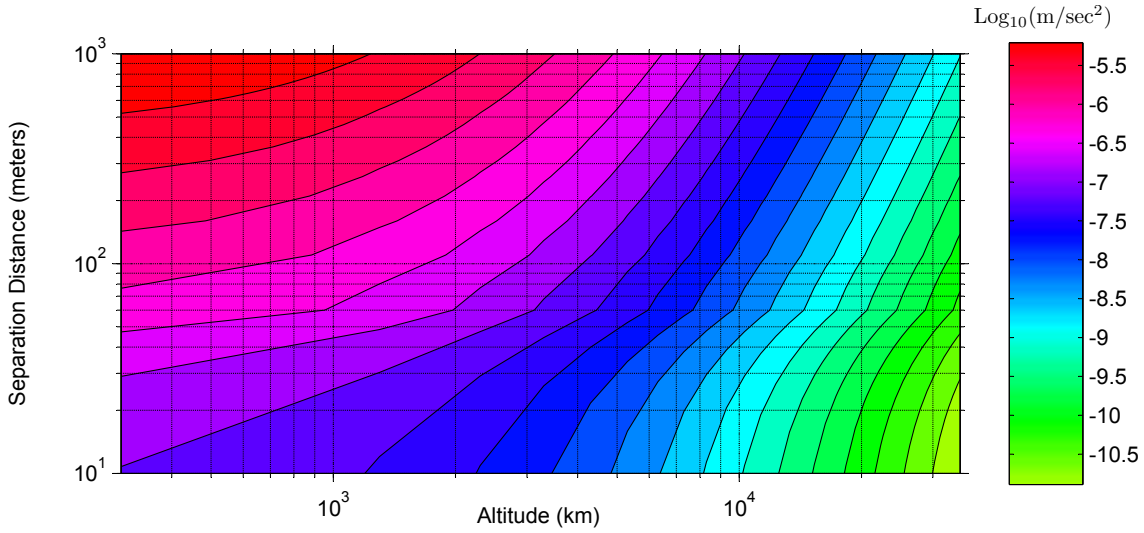

(a) Log of Max Acceleration due to J_2 trough J_6 with i=60°

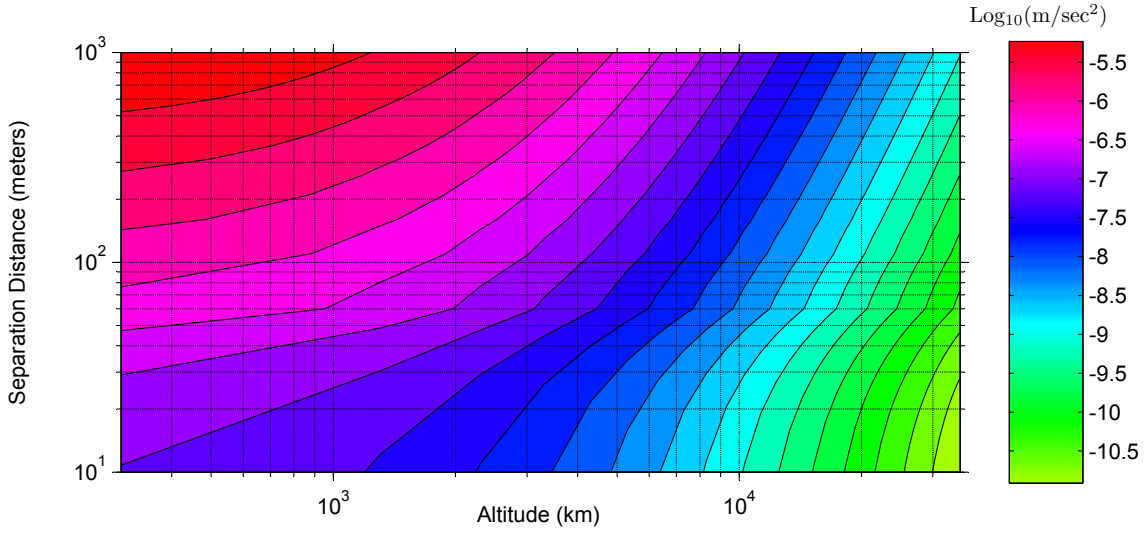

(b) Log of Max Acceleration due to J_2 trough J_6 with i=90°

Figure 3.4: Contour Plots of Acceleration in $\log_{10}(\mathrm{m/s^2})$ vs. Separation Distance and Altitude for J_2 through J_6 Perturbations

swept form LEO 300 km heights to GEO 35,000 km heights. The separation distances (the A_0 parameter in Eq. (3.19)) is swept from 10 – 1000 meters. The chief orbit is set to be a circle in each case. The contour plots illustrates the resulting maximum differential J_2 induced accelerations that were encountered. For cases are illustrated for chief inclination angles of 0, 30, 60 and 90 degrees.

As expected, the differential J_2 perturbations increase with increasing formation size and with decreasing orbit altitude. As the orbit inclinations are increased, the resulting worst cases differential accelerations increase slightly, but not substantially.

3.3 Differential Atmospheric Perturbations

The next perturbation to examine is the drag force due to the atmosphere. This effect will be dominant in the low earth orbit altitudes and become negligible at higher altitudes. The magnitude of acceleration due to atmospheric drag is modeled in the following equation.[14]

$$a_D = -\frac{1}{2}\rho(C_d A/m)V^2 \qquad (3.22)$$

Here ρ is the atmospheric density, C_D is the coefficient of drag, A is the satellite's cross-sectional area of the satellite, and V is the current inertial velocity of the spacecraft. We know that the drag force acts in the opposite direction of velocity so the vector form of the acceleration can be written as follows:[14]

$$\boldsymbol{a}_{d_i} = a_{d_i}\hat{\boldsymbol{i}}_v = a_{d_i}\frac{\dot{\boldsymbol{r}}_{\boldsymbol{i}}}{|\dot{\boldsymbol{r}}_i|} \qquad (3.23)$$

Equation 3.22 shows that the atmospheric disturbance magnitude is a function of atmospheric density, which in itself is a function of altitude. Therefore, in order to model drag force at varying altitudes we must have a reasonably accurate atmospheric density model.

The atmospheric density model used is the United States Standard Atmosphere Model from 1976. Most newer atmospheric models are functions of the time of year and solar flux, but this model contains accurate density data that is only a function of altitude. The actual model contains density data for altitudes ranging from 86 to 1000 km. Above this range it is assumed that density becomes very close to zero and the drag force is non-existent.[21]

In examining the data, the density follows an almost exponential decrease versus the increase in altitude. For this reason, a 6th order polynomial curve fit is done on the log of density versus altitude. The resulting non-exponential atmospheric curve fit versus actual data from Reference 21 is plotted in Figure 3.5.

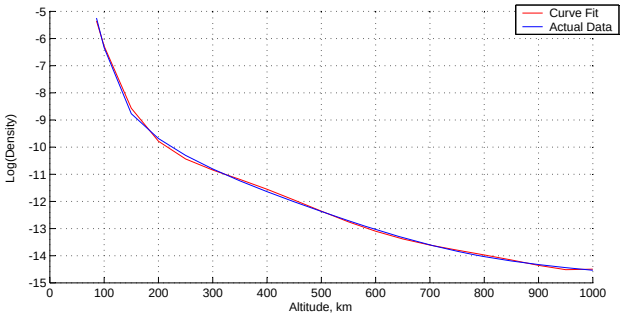

Figure 3.5: 6th Order polynomial Fit for Atmospheric Model.

From the figure we can see that the curve fit matches quite well. However, after 1000 km there is no data on atmospheric density since it is considered to be essentially zero. But, for the purpose of creating a smooth model that will apply for all altitudes, it will be assumed that the density will have a smooth exponential drop off up to GEO.

The next two variables to model in Eq. 3.22 are the coefficient of drag C_d and the cross-sectional area A. For the purpose of sizing the value of C_d, a general cylindrical shape is considered for our spacecraft rather than the previous spherical model. If spherical spacecraft of equal mass are considered, then the differential atmospheric draft would be trivially zero. Rather, in the cylindrical spacecraft case the attitude of the spacecraft will have an influence on the C_d value. This aspect allows us to study differential drag for two or more satellites in a formation. For a spacecraft with a cylindri-

cal shape without solar cells, the average value for C_d used is about 2.2.[22] However, this will vary with the attitude, and for purposes of this study we will just consider the worst and best case scenarios for C_d. Figure 3.6 shows the the orientation of a cylindrical craft with respect to the velocity vector for these two cases.

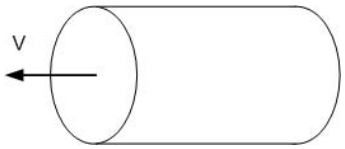

(a) Best-Case Scenario

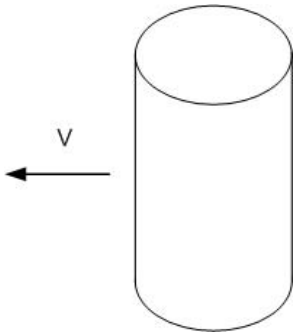

(b) Worst-Case Scenario

Figure 3.6: Diagram of Cylindrical Spacecraft

From this figure we can see that the two different cases will greatly depend on shape of the cylinder and not only its orientation. For example, if you have a cylinder with a height much smaller than its radius it would have a different C_d then a case where the height is much greater than the radius of the cylinder. This can yield a complicated relationship; so for our study, we can assume that most spacecraft will have a height and diameter ($2r$) that are close to equal, so that this kind of effect can be ignored.

The next step is to estimate the value for C_d for worst and best case scenarios based on existing data on an actual spacecraft. In Reference 22 there is one specific craft, Intercosmos-16, which is a scientific spacecraft with a cylindrical shape and no solar panels. The data table on its drag properties has a C_d for maximum cross-sectional area of 2.67 and for minimum cross-sectional area that value drops to 2.1. This data gives us a sufficient range of C_d values to use in our study of differential drag on a formation of satellites.

For a cylindrical shaped spacecraft it is fairly easy to compute the cross-sectional area for the maximum and minimum cases. For the maximum cross-sectional area, the craft will be oriented as in Figure 3.6(b). Therefore the area as seen by the velocity vector is rectangle with the equation:

$$A_{\max} = 2rh \tag{3.24}$$

For the minimum cross-sectional area, the craft would be oriented as in Figure 3.6(a). Therefore, the area as seen by the velocity vector would be a circle with the equation:

$$A_{\min} = \pi r^2 \tag{3.25}$$

Also note that the previous assumption on the shape of the spacecraft must hold for these equations to represent the maximum and minimum cross-sectional area. The assumption stated that the height is close to that of the diameter, thus assuming that our spacecraft is not a long cylinder shaped boom or a flat disc. And for our study, this will generally be the case for our spacecraft.

For our differential atmospheric drag simulations we chose the typical craft configurations with a mass of 50 kg craft, while the radius is 0.5 meters and a height equal to three times the radius. This provides our numerical simulation with a worst case scenario for differential drag forces on relative motion.

Figure 3.7 illustrates the computed differential atmospheric drag accelerations for LEO to GEO orbit, with the separation distances ranging from 10–1000 meters. Because all satellites are essentially in circular orbits (as seen by inertial frame), the inertial velocity is essentially constant here. Thus, the differential atmospheric disturbance will not depend on the spacecraft separation distant. Rather, it only depends on the orbit altitude. Note that the Standard atmosphere model used only provided data up to a height of 1000 meters. Beyond that

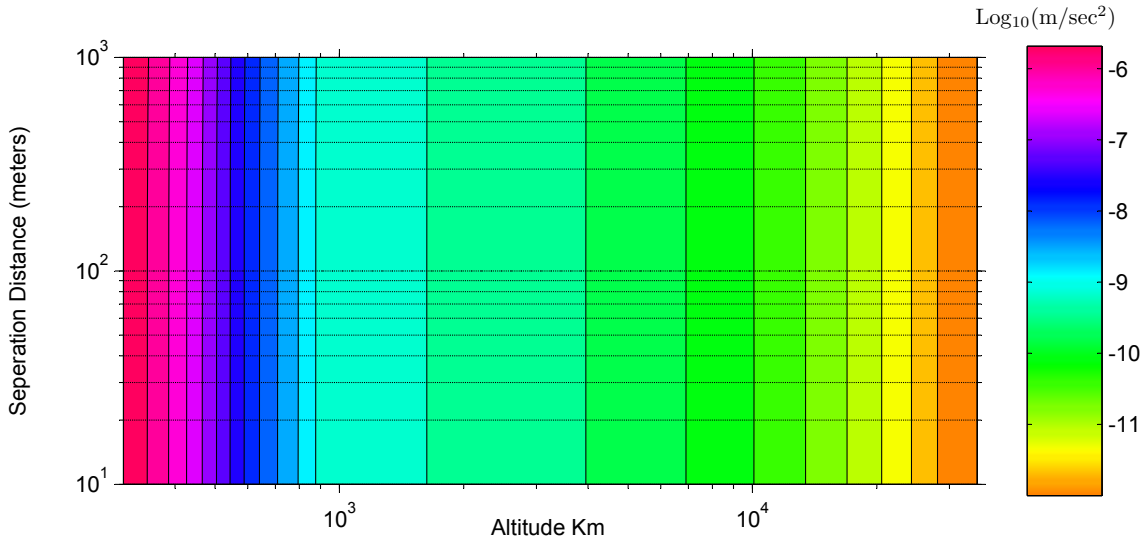

Figure 3.7: Contour Plots of Differential Atmospheric Drag Acceleration in $\log_{10}(\mathrm{m/s^2})$ vs. Separation Distance and Altitude

the atmosphere is modeled to simply decay to zero exponentially.

3.4 Differential Solar Radiation Pressure

Solar radiation drag is created by having the sun's light reflect of the spacecraft. Through momentum conservation, a small force is exerted onto the craft. The magnitude of this force depends on the apparent size and reflectivity of the spacecraft. To model the solar radiation pressure we will use a spherical spacecraft model. The equation for this model is shown below:[23]

$$\boldsymbol{a}_R = -C_R \frac{A\Phi \boldsymbol{R}}{mcR^3} \tag{3.26}$$

Where A is the cross-sectional area facing the sun, and Φ is the solar constant. Also, m is the spacecraft mass, c is the speed of light, and C_R is the pressure radiation coefficient. Lastly, the vector $\boldsymbol{R}$ is the inertial vector pointing from the sun to the planet you are orbiting in AU, while R is simply its magnitude. In this part of the equation, it is assumed that there is a quadratic drop in radiation pressure as you increase your distance past 1 AU, which is the distance from the Earth to the Sun. Without loss of generality, for our simulation we will choose a vector in vernal equinox direction. The motion of all satellites considered is insignificant here compared to the size of the Earth/Sun inertial position vector.

The other variables in the equation are simply constants. For cross-sectional area A and mass m, the same values are used as for the drag force calculation. The pressure radiation coefficient is taken to be $C_R = 1.3$ from the average value based on recent data.[23] The solar constant Φ is 1372.5398 $\mathrm{W/m^2}$ and the speed of light is c =2.997 m/s.

Figure 3.8 illustrates the resulting differential solar radiation acceleration values. Because the solar radiation drag does not depend on the satellite position about the Earth (ignoring the Earth shadowing effect), this value does not change with varying orbit altitudes or separation distances.

3.5 Overview of Dominant Perturbations Zones

The previous three sections discussed the dif-

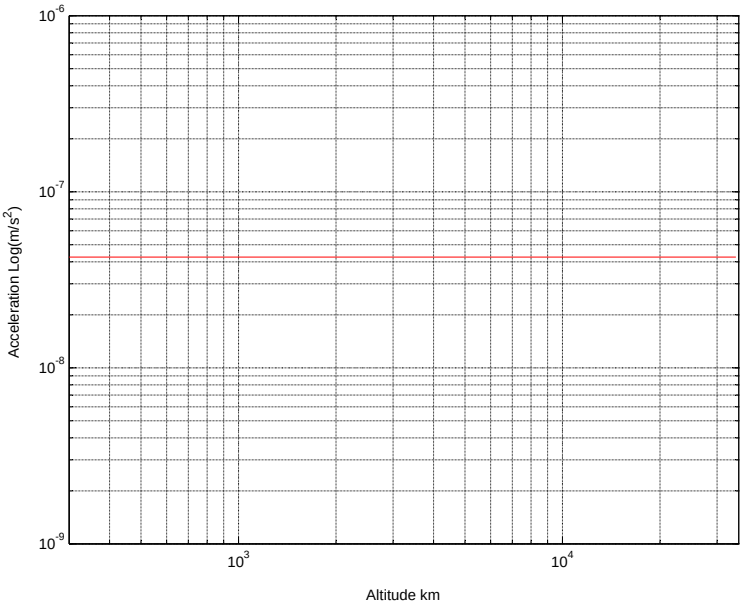

(a) Log of Max Acceleration vs. Altitude

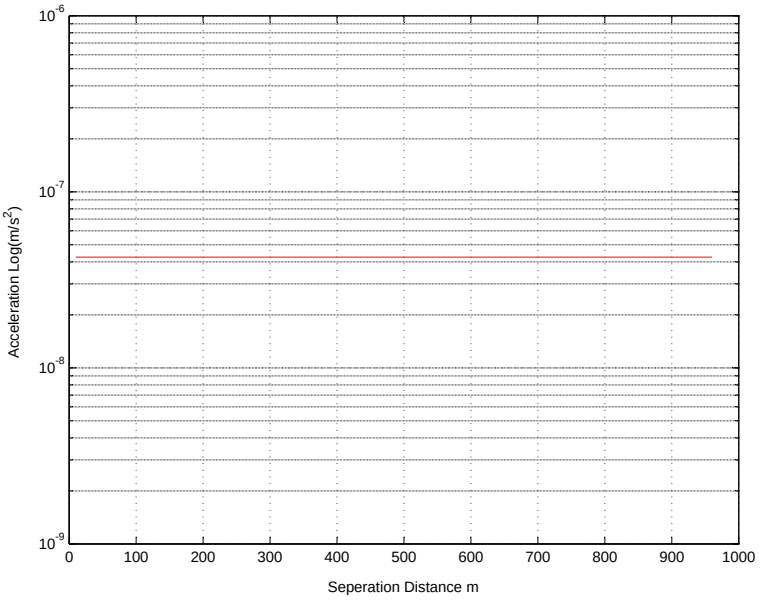

(b) Log of Max Acceleration vs. Separation distance

Figure 3.8: Contour Plots of Differential Solar Radiation Acceleration in $\log_{10}(\mathrm{m}/s^2)$ vs. Separation Distance and Altitude

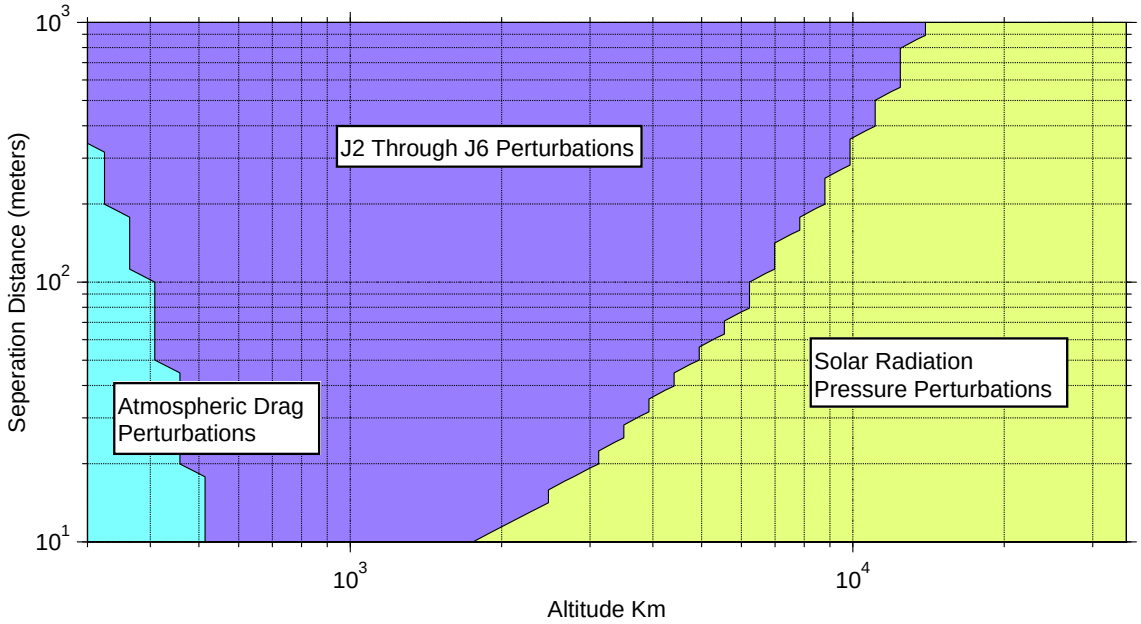

Figure 3.9: Dominant Differential Perturbation Zones Illustration.

ferential perturbations due to J_2 perturbations, atmospheric drag, as well as solar radiation drag. In all cases the craft are assumed to have a mass of $m = 50$ kg, and a nominal radius of 0.5 meter.

Figure 3.9 provides an overview of altitude and separation distance zones showing which perturbation is the most significant for a particular zone. Traditional formation flying applications treat the J_2 perturbation as the dominant disturbance of the formation geometry.[24–26] Here the craft are assumed to be of equal type and build. However, even if all craft have the same shape, different orientations can cause significant differential atmospheric drag in LEO regimes. Figure 3.9 shows that for conditions used in this study orbits the differential atmospheric drag will dominates at LEO up to separation distances of 350 meters. As the orbit altitude is increased to about 500 km, the differential atmospheric drag dominant zones vanish. For large separation distances at LEO the differential J_2 perturbation becomes dominant, even if differential spacecraft attitudes are considered. This tendency is expected because the differential J_2 perturbation increases with separation distance, while the differential atmospheric drag does not.

As the considered orbit altitudes is increased to Medium Earth Orbits (MEO) and geostationary orbits (GEO), the differential J_2 perturbation is decreased. The further away from Earth the spacecraft is, the more the Earth's gravitational potential begins to resemble that of a point-mass. This study uses a worst case differential solar radiation perturbation which does not change with orbit altitude. At high Earth orbit regions, which will typically be considered in this study for charged spacecraft missions, the differential solar radiation pressure is the largest perturbations even out to 1000 meter separation distances.

3.6 Earth Magnetic Lorentz Force

Lastly we want to explore the effects of Earth's magnetic field on our spacecraft. Because we will be generating a significant amount of charge or voltage to compensate for these orbital disturbances, that charge will in turn create an acceleration due to Earth's magnetic

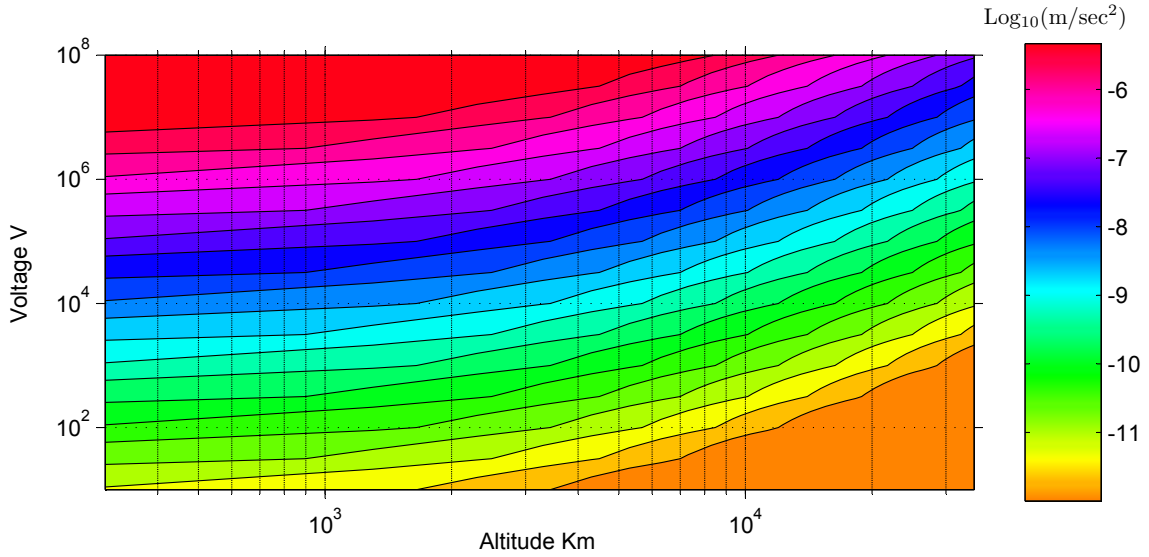

Figure 3.10: Contour Plots of Acceleration in $\log_{10}(\mathrm{m/s^2})$ vs. Voltage and Altitude over the 10° N and 100° E Location.

field. This acceleration or force is known as the Lorentz Force and is written in equation 3.27 from basic physics.

$$\boldsymbol{F} = q\ \dot{\boldsymbol{r}} \times \boldsymbol{B} \tag{3.27}$$

In this equation q is the charge generated by the craft in Coulombs, $\dot{\boldsymbol{r}}$ is the inertial velocity vector of the spacecraft in m/s, and $\boldsymbol{B}$ is the inertial magnetic field vector of the Earth in units of Tesla, T.

The Earths magnetic field generally resembles the field around a magnetized sphere, or a tilted dipole seen in Figure 3.11. As of 1999, the dipole axis was tilted approximately 11.5° from the spin axis, and drifting approximately 0.2°/yr. Its strength at the Earths surface varies from approximately 30000nT near the equator to 60000nT near the poles. Further, there exists a low magnetic intensity field at approximately 25° S and 45° W known as the Brazilian Anomaly. A high exists at 10° N and 100° E, and the two of these together suggest that not only is the dipole axis tilted, but it does not quite pass through the center of the Earth.[27]

The accepted model for Earths magnetic field is the International Geomagnetic Reference

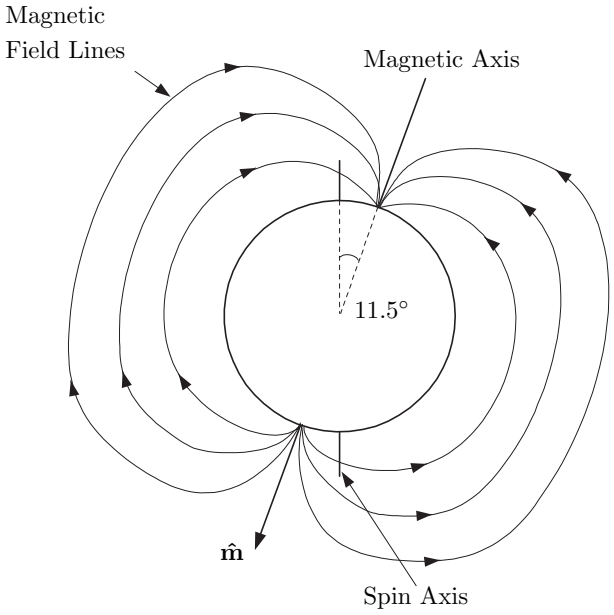

Figure 3.11: Earth Magnetic Field Model.

Field, put forth by the International Association of Geomagnetism and Aeronomy (IAGA). An overview of this model can be found on the website of the IAGAs Working Group V-MOD.*

The IGRF is essentially a set of Gaussian co-

*http://www.ngdc.noaa.gov/IAGA/vmod/igrf.html

efficients, gmn and hmn , that are put forth every 5 years by IAGA for use in a spherical harmonic model. At each of these epoch years, the group considers several proposals and typically adopts a compromise that best fits the data available. The coefficients for a given epoch year are referred to by IGRF and then the year, as in IGRF2000. The model includes both the coefficients for the epoch year and secular variation variables, which track the change of these coefficients in nano-Tessla per year. These secular variation coefficients are used to extrapolate the Gaussian coefficients to the date in question. Once data becomes available about the actual magnetic field for a given epoch year, the model is adjusted and becomes the Definitive Geomagnetic Reference Field, or DGRF. Typically the IGRF consists of 120 coefficients for each epoch year, with 80 secular variation coefficients. However, due to unprecedented geomagnetic data available, the IAGA released a new set of values for IGRF2000 in July 2003 in the 9th-generation IGRF. This new model expanded to increase the precision of the coefficients to one-tenth of a nano-Tessla (up from one nano-Tessla), and increased the number of coefficients to degree 13 (rather than 10).

For a reference case, we pick a longitude of about -100 degrees and a latitude of 10 degrees south, the Brazilian Anomaly. As the orbit altitude as swept, the magnetic field strength is computing for altitudes over this location to determine worst case conditions. For the days variable, we will pick mid-year 2005 which is about $5.5 * 365$ days. This will output the current magnetic field vector for a given radial distance. The velocity vector $\dot{\boldsymbol{r}}$ is to be taken as the circular velocity at the given altitude. Lastly, the voltage of the spacecraft and the orbit altitude are swept. The altitude range will be the same as for the previous disturbance acceleration cases. The voltage will be swept from 10^1 to 10^8 volts in order to supply force data for a broad range of voltages. The Lorentz acceleration for a 50 kg craft is then plotted on a contour plot in Figure 3.10. Also note that the contour plot is using the same contour color scale as in the previous disturbance acceleration study cases.

From the figure we can see that for reasonable voltages on the order of kilovolts to hundreds of kilovolts, the spacecraft will experience accelerations about two orders of magnitude below the expected disturbance accelerations due to the perturbations. This suggests that even though this force is small, it is still there and must be considered in higher fidelity simulations. Also notice that the accelerations become relatively high when the voltage increases to 10^8 volts, even higher than the disturbance accelerations. This can become a factor if your craft are relatively far apart and a much higher voltage is needed to compensate for a disturbance.

Chapter 4

Charged Spacecraft Mission Concepts

This chapter discusses in detail 3 different charged spacecraft mission concepts and evaluates the necessary charge levels to be able to compensate for the differential orbital perturbations. When possible, the applications of these concepts is the space-based radar interferometry problem. Here the sensor satellites are ideally placed in configurations with circular projections in the local horizontal plane. The last section discusses further Coulomb spacecraft mission concepts which were developed after evaluating the expected plasma Debye lengths for different orbit altitude regions.

4.1 Spacecraft Voltage Computation

The charges q_i are the physical quantities which determine the Coulomb force magnitude Eq. (2.3). However, when implementing such spacecraft charges, the technical concern will be the charge density (voltage) across the craft. The higher the voltage, the more challenging it will be to implement any charge control law. Thus, this study evaluates what the necessary spacecraft voltages/charge levels are to compensate for differential orbital perturbations. Note that the Coulomb forces are not sized here to compensate for the total orbital perturbation. In fact, it is impossible to change the inertial momentum of the charged satellite cluster using internal Coulomb forces. Rather, the Coulomb forces are sized such that they will be able to compensate for the differential perturbations which would cause the formation to to change shape, size or orientation.

Unless noted otherwise, the typical spacecraft is assumed to be spherical in shape, have a radius of $r = 0.5$ meters, and a mass of $m = 50$ kg. The differential perturbation levels are taken from the conservative worst case results discussed in Chapter 3. Once a required spacecraft charge q_i is computed, then the equivalent spacecraft voltage is evaluated using

$$V_i = k_c \frac{q_i}{r} \tag{4.1}$$

where k_c is the Coulomb constant. This formula assumes the charge is homogeneously distributed across a sphere of radius r. How to compute the required spacecraft charge q_i levels depends on the mission scenario being considered. This computation is outlined in detail in each of the following sections.

4.2 Free-Flying Formation Concept

4.2.1 Formation Description

Let us first consider a mission scenario where all charged spacecraft are flying within each others electrostatic spheres of influences. The spacecraft formation is designed such that the nominal geometry are control-free solutions of the relative equations of motion. Any formation flying errors relative to the formation center of mass will then be controlled using the electrostatic (Coulomb) forces. For example, consider the typical formation flying configuration where all the satellites are flying in bounded elliptical relative orbits with circular projections in the

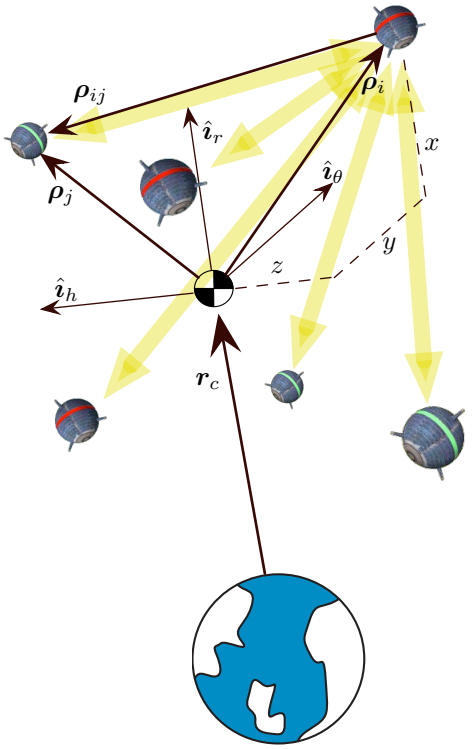

Figure 4.1: Coulomb Spacecraft Formation Illustration

local horizontal plane. If the relative orbit dimension is reduced to dozens to hundreds of meters, then the electrostatic field of one satellite will influence the motion of all other craft within this formation. This concept is illustrated in Figure 4.1. In this scenario a single craft is able to interact with all other formation craft to produce the required Coulomb force. This provides a very complex dynamical system. Let $n = \sqrt{\mu/a^3}$ be the mean orbital rate of the circular chief motion, then the CW equations are given by:[12–14]

$$\ddot{x} - 2n\dot{y} - 3n^2 x = \alpha_x \tag{4.2a}$$

$$\ddot{y} + 2n\dot{x} = \alpha_y \tag{4.2b}$$

$$\ddot{z} + n^2 z = \alpha_z \tag{4.2c}$$

If only Coulomb forces are perturbing the Keplerian orbital motion, then the disturbance acceleration vector $\boldsymbol{\alpha}$ is given by

$$\boldsymbol{\alpha} = \overset{\mathcal{H}}{\begin{pmatrix} \alpha_x \\ \alpha_y \\ \alpha_z \end{pmatrix}} = -\frac{k_c}{m_i} \sum_{j=1, j\neq i}^{N} \frac{q_i q_j}{\rho_{ij}^3} \boldsymbol{\rho}_{ij} e^{-\frac{\rho_{ij}}{\lambda_d}} \tag{4.3}$$

where $\boldsymbol{\rho}_{ij} = \boldsymbol{\rho}_j - \boldsymbol{\rho}_i$. The relative equations of motion in Eq. (4.2) are strongly coupled and highly nonlinear. This makes finding feedback stabilizing control laws a very challenging task. Some early Coulomb craft feedback control law strategies are discussed in References 28–30 which attempt to stabilize the motion of a single charged craft relative to other charged craft within the formation.

The purpose of this study is to investigate necessary spacecraft charge levels to compensate for differential orbital perturbations. The nominal formation geometry is assumed to be a control free solution. Analytical solutions to the CW equations are well known and have been applied to the formation flying problem.[15,31–33] Control free solutions of relative orbits exploiting the mean J_2 perturbations are discussed in References 24, 28, 34. To size the minimum spacecraft charge level to *maintain* a formation shape, the magnitude of the local differential orbital perturbations must be considered. Note that any final feedback strategy would require charge levels higher than those discussed in this chapter.

4.2.2 Minimum Maintenance Voltage Computation

To compute the worst case spacecraft voltage to compensate for differential orbital perturbations, we study the disturbance accelerations acting on a single spacecraft within this formation over one orbit period. Assume the formation contains N spacecraft of essentially equal type and build. Let us define the $L = N - 1$ dimensional vector charge product vector $\boldsymbol{Q}$ as

$$\boldsymbol{Q} = \begin{pmatrix} Q_{i1} & Q_{i2} & \cdots & Q_{ij} & \cdots & Q_{iN} \end{pmatrix}^T \tag{4.4}$$

with $i \neq j$ and where

$$Q_{ij} = q_i q_j \tag{4.5}$$

The parameters q_i and q_j are the charge levels of the i$^{\text{th}}$ and j$^{\text{th}}$ spacecraft respectively. Further, let us define the $3 \times L$ matrix $[A(t)]$ as

$$[A(t)] = \left[\frac{\boldsymbol{\rho}_{i1}}{\rho_{i1}^3} e^{-\frac{\rho_{i1}}{\lambda_d}} \cdots \frac{\boldsymbol{\rho}_{ij}}{\rho_{ij}^3} e^{-\frac{\rho_{ij}}{\lambda_d}} \cdots \frac{\boldsymbol{\rho}_{iN}}{\rho_{iN}^3} e^{-\frac{\rho_{iN}}{\lambda_d}} \right] \tag{4.6}$$

with $i \neq j$. Note that the space plasma influence of the electrostatic field generation has been included in this $[A(t)]$ definition. The actual control acceleration $\boldsymbol{\alpha}_i$ experienced by the i^{th} spacecraft is

$$\boldsymbol{\alpha}_i = -\frac{k_c}{m_i}[A(t)]\boldsymbol{Q} \tag{4.7}$$

Thus, to compensate for the a disturbance acceleration $\boldsymbol{a}_d$, we set it equal to the control acceleration and solve for the charge product vector $\boldsymbol{Q}$.

$$\boldsymbol{Q} = -\frac{m_i}{k_c}[A(t)]^{\dagger}\boldsymbol{a}_d \tag{4.8}$$

Note that this disturbance acceleration is computed relative to the *drifting* formation center of mass as outlined in Chapter 3. Using the pseudo-inverse of the rectangular matrix $[A(t)]$ provides the minimum norm solution of the charge product vector. The charge of the i^{th} spacecraft whose relative motion is being control is computed using

$$q_i = \sqrt{\max(|Q_{ij}|)} \tag{4.9}$$

4.2.3 Numerical Sweeps of Maintenance Voltage

To parameterize a family of Coulomb formation, the following scenario is used. Keeping space-based radar interferometry missions in mind, the analytical solution to the CW equations in Eq. (3.19) are used to setup a Coulomb formation of N craft. In particular, the circular projection condition $B_0 = 2A_0$ and $\alpha = \beta$ is enforced to yield circular formations as seen by an Earth observer. The N craft are spaced equally along the relative orbit as illustrated by Figure 4.2. The constant separation angle is $\varphi = 2\pi/N$.

To determine the disturbance acceleration $\boldsymbol{a}_d$ on the i^{th} craft, this craft is allowed to perform a complete orbit about the Earth. The $N-1$ remaining satellites are held in equivalent relative orbit positions compared to this i^{th} craft to maintain the constant separation angles φ. Thus, at any instance in this simulation,

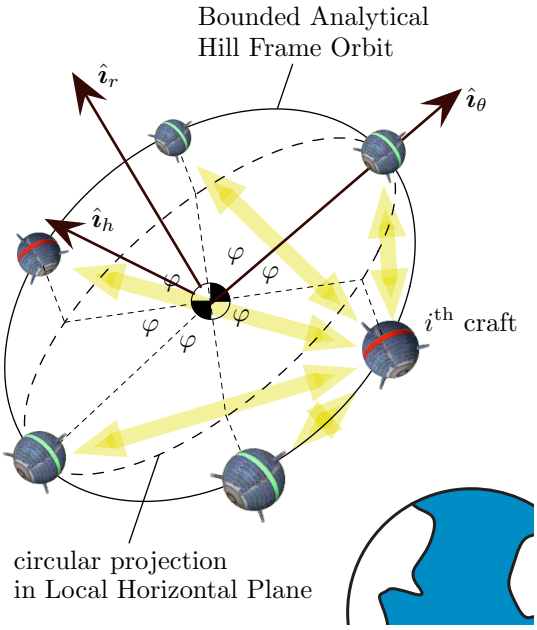

Figure 4.2: Relative Orbit Geometry Setup Illustration with a 6 Craft Formation.

the formation geometry satisfies the linearized bounded motion conditions. As the craft of interest completes its orbit, the true inertial position vectors $\boldsymbol{r}_i$ computed for all craft to determine the differential perturbation accelerations relative to the drifting formation center of mass. For a given orbit size (determined through A_0) and orbit altitude), the corresponding maximum required voltage is recorded.

Chapter 2 discusses the expected mean Debye lengths at different orbit altitudes. The only regions which are found to be feasible for Coulomb spacecraft formation flying were orbit radii greater than about 6 R_e up to GEO altitudes. Inside this radius the Van Allen radiation belts, as well as the dense, cold plasma environments of LEO altitudes yielded extremely small Debye lengths of millimeters to centimeters. Outside the Van Allen radiation belts the Debye length were found to vary from 100 meters up to 500–1000 meters, depending on the solar activities.

To perform numerical sweeps of required spacecraft voltage levels to compensate for differential orbital perturbations, all simulations use a GEO altitude. At lower HEO altitudes the Debye lengths are found to be very similar

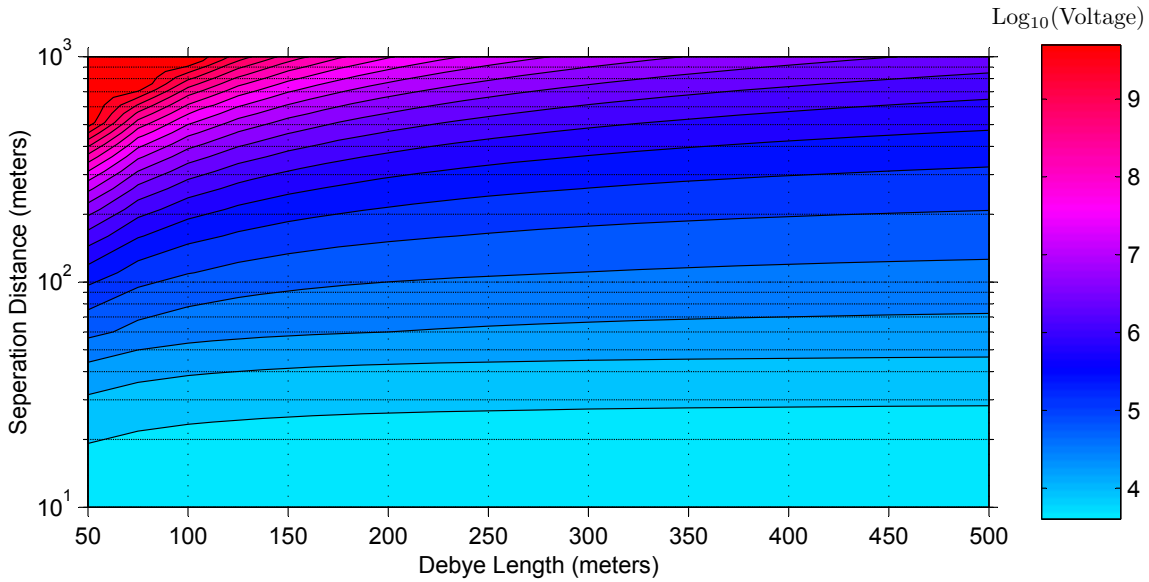

(a) $\log_{10}$ of Voltage for 2 Spacecraft

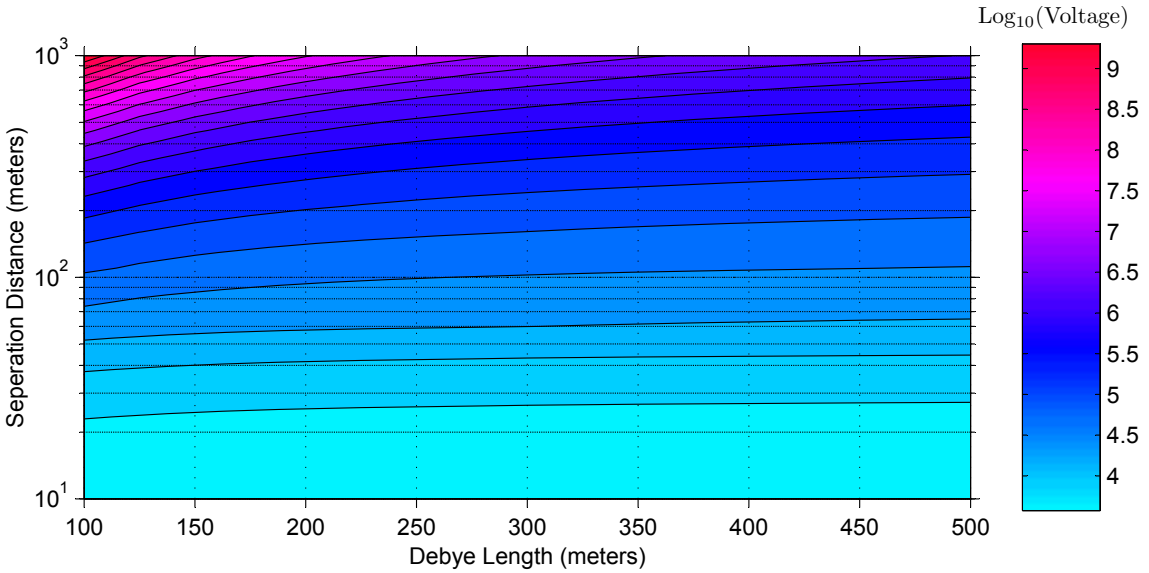

(b) $\log_{10}$ of Voltage for 3 Spacecraft

Figure 4.3: Contour Plots of Voltage in $\log_{10}(V)$ vs. Formation Size (A_0) and Debye Length for All Differential Perturbations. The Formation Consists of 2 and 3 Craft at GEO.

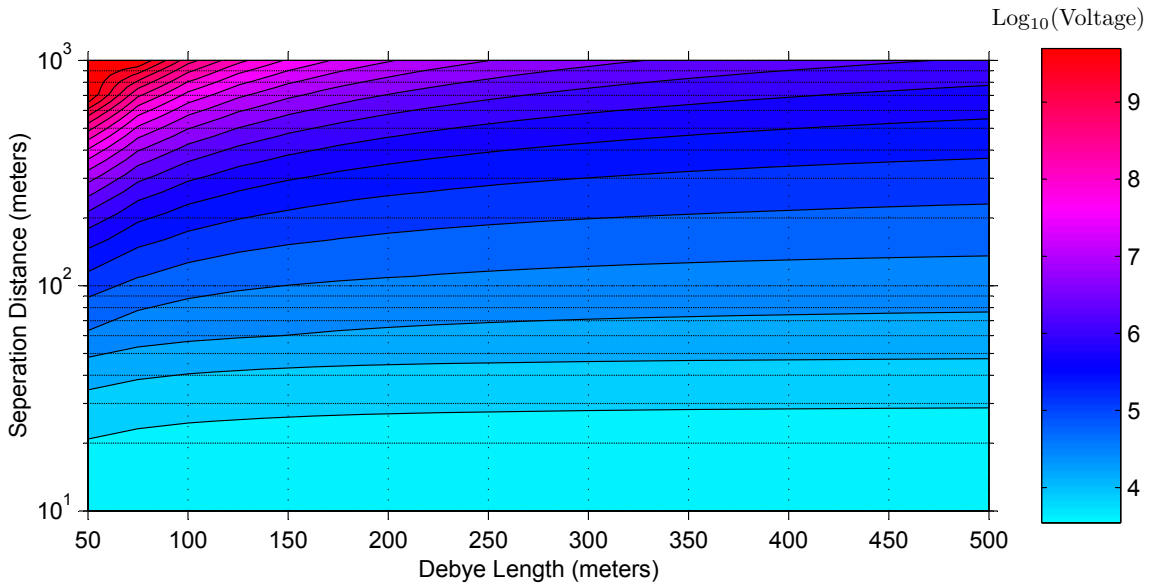

(a) $\log_{10}$ of Voltage for 4 Spacecraft

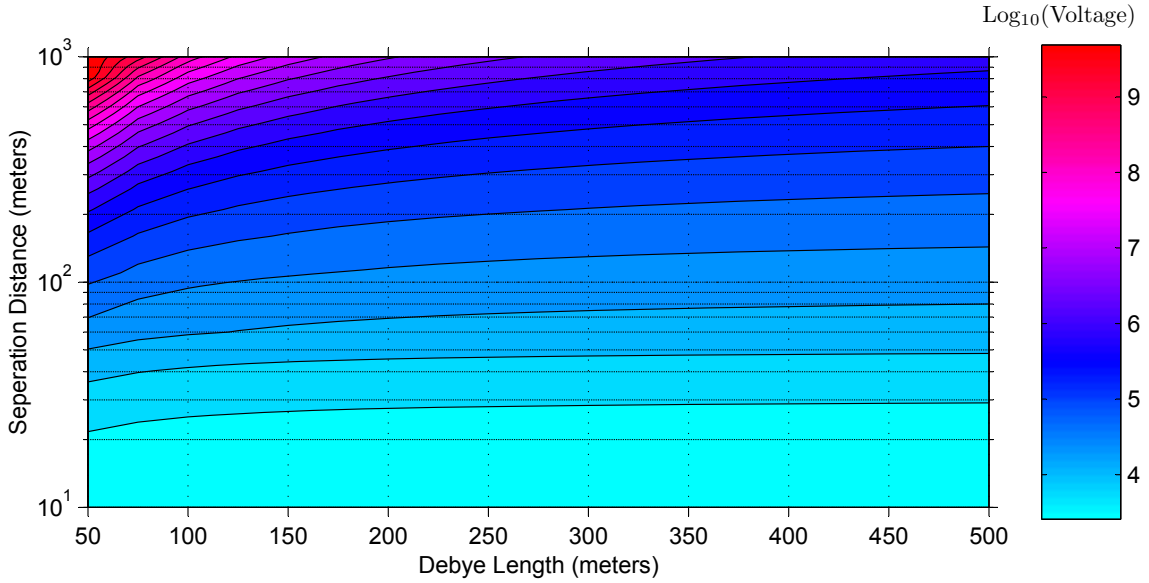

(b) $\log_{10}$ of Voltage for 5 Spacecraft

Figure 4.4: Contour Plots of Voltage in $\log_{10}(V)$ vs. Formation Size (A_0) and Debye Length for All Differential Perturbations. The Formation Consists of 4 and 5 Craft at GEO.

to the GEO altitude Debye lengths. Thus, numerical sweeps are performed where the Debye length is varied, as well as the formation size. At HEO altitudes the differential atmospheric disturbance are negligible. While the differential solar radiation pressure is the largest, the differential J_2 perturbations were included in these sweeps as well. Figures 4.3 and 4.4 illustrate contour plots of the resulting required spacecraft voltages. The results show that for separation distance of dozens of meters, the required voltages for the 0.5 meter radius craft is in the 10's of kilovolt level. To compensate for the separation distances of 100's of meters, the required voltage quickly increase into 100's of kilovolt levels.

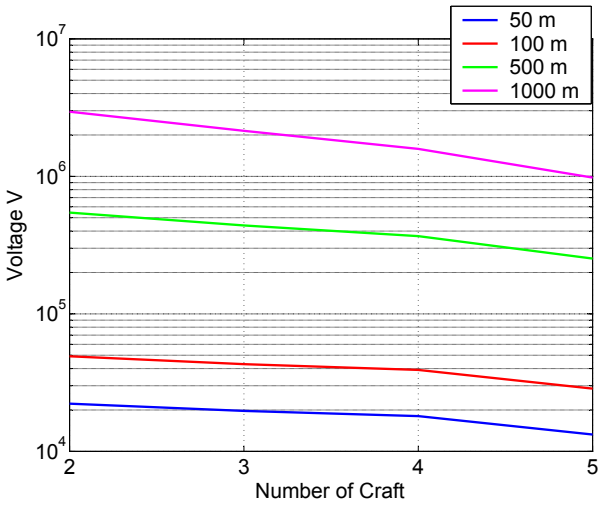

Figure 4.5: Voltage vs. Number of Craft at GEO.

Four different formation scenarios are studied where N is either 2, 3, 4 or 5. The results also show that the required voltage is decreased are more craft are present. To illustrate this effect, Figure 4.5 illustrates the required voltage level for all spacecraft craft number cases and a Debye length of 500 meters. Increasing the formation craft number does from 2 to 5 craft have reduce the required voltage by 2 to 3 fold. However, this reduction is no sufficient to be able to compensate for very small Debye lengths.

4.3 Gluon Spacecraft Concept

Next we discuss a satellite formation in which there is a massive satellite in the center, called Gluon. The deputy satellites are assumed to be in a bounded relative orbit around the Gluon or chief satellite. The main idea behind this type of formation is to have a dedicated gluon which can charge up to very high values. As a result, the deputy satellites can achieve a given inter-satellite control force using a much smaller charge level. The gluon is also much heavier and larger in size than the deputy. Because the deputy charge levels is relatively small, their mutual interactions can be neglected for 1^{st} order control studies. This contrasts with the very coupled and complex dynamics of the previously discussed Coulomb formations.

In order to accommodate high charge and still stay with in a acceptable level of voltage, the gluon will have a large surface area. Due to the significant difference in mass and surface area between the gluon and deputy satellite, the solar drag, J_2 effect and atmospheric drag experienced by them will be different. In this section we study the effect of this differential drag and differential J_2 effect, and find the approximate magnitude of Coulomb force needed to compensate for this drag.

4.3.1 Gluon Spacecraft Layout

For this study, we consider only one deputy satellite and gluon as shown in Figure 4.6. The gluon has a constant core mass and a large shell, supported by 8 thin cylindrical columns. The large shell helps in distributing the charge, thus reducing the voltage. The shell and its support structure are assumed to be made of Aluminum (or any light metal). The deputy satellite is assumed to be spherical with a fixed radius r_1 and mass m_1. Note, the size of the shell in the gluon is varied as part of the study. Hence, the mass of the gluon is not fixed and depends on the radius of the craft

$$m_2 = m_c + \left(8[2\pi r_h(r_2 - r_c)\Delta_h] + 4\pi r_2^2\Delta_s\right)\rho_{al} \tag{4.10}$$

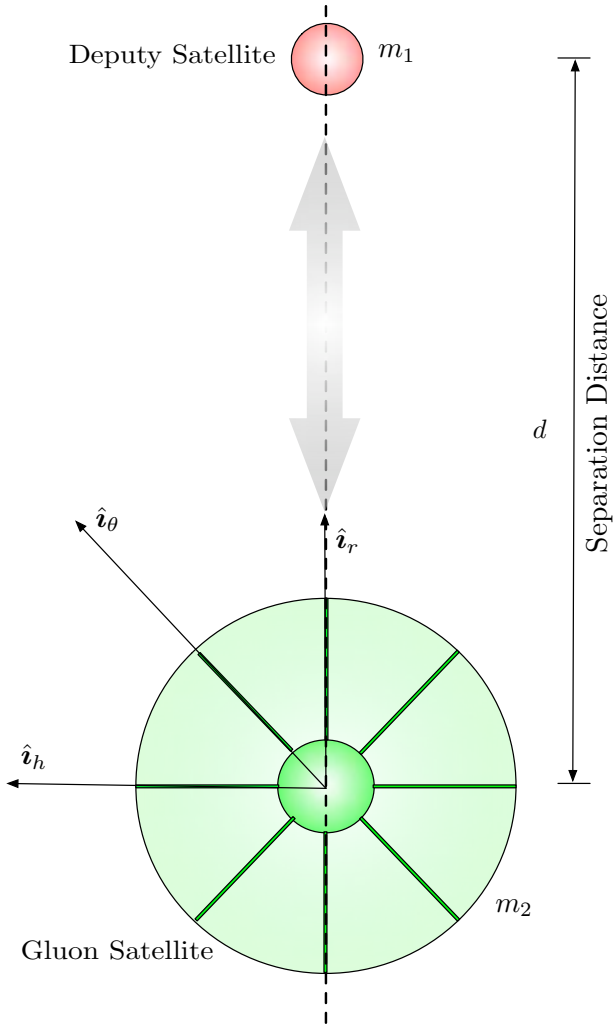

Figure 4.6: A simple gluon and deputy satellite illustration.

Here r_2, r_c and r_h are the radii of the shell, core mass and thin cylindrical columns, respectively. Δ_s and Δ_h denote the thickness of the shell and cylindrical column, and ρ_{al} is the density of Aluminum.

Initially, we investigate the various sizes (radii) of gluon and deputy that will satisfy the charge requirements while staying with in the permissible voltage levels. The relationship between voltage V and charge q of a spherical body of radius r is given by

$$V = k_c \frac{q}{r} \tag{4.11}$$

where k_c is the Coulomb constant. Figure 4.7 illustrates the voltage-charge relationship in Eq. (4.11) for spherical bodies of different radii. The voltage limit for the deputy satellite is fixed as 10 kV and the corresponding charge carried by the deputy is studied for different deputy radii from the graph in Figure 4.7. A deputy of radius 0.5m can carry about 0.5561μC of charge and this is fixed as the size of the deputy. The gluon is dedicated for carrying higher charge and does not carry any other critical equipment or component. Hence, we can assume that it can charge up to a high voltage, say 10 times the maximum voltage of the deputy (100 kV). Fixing the radius of the gluon is not as straight forward as that of the deputy. We will have to consider certain trade offs. The larger the size of the gluon, higher is the amount of charge it can carry and still stay with in the maximum allowable voltage. But, large gluon sizes might result in higher differential perturbations between the gluon and deputy which has to be compensated using Coulomb forces. Therefore, we do not fix the size of the gluon at present. The relationship between the gluon radius and differential perturbation will be studied in the following sections.

4.3.2 Voltage Requirements

In this section, we find an expression for the amount of Coulomb force which will keep the formation from drifting due to the differential perturbation. The voltages on the gluon and deputy can be calculated from the magnitude of the Coulomb force required. Consider the Figure 4.8, let $\boldsymbol{F}_1$ and $\boldsymbol{F}_2$ be the external disturbance force acting on the deputy and gluon, respectively, and $\boldsymbol{F}_Q$ be the Coulomb force. The equation of motion of the two satellites are given as

$$\boldsymbol{F}_Q + \boldsymbol{F}_1 = m_1 \ddot{\boldsymbol{r}}_1 = m_1(\ddot{\boldsymbol{r}}_c + \ddot{\boldsymbol{\rho}}_1) \tag{4.12a}$$
$$-\boldsymbol{F}_Q + \boldsymbol{F}_2 = m_2 \ddot{\boldsymbol{r}}_2 = m_2(\ddot{\boldsymbol{r}}_c + \ddot{\boldsymbol{\rho}}_2) \tag{4.12b}$$

where $\boldsymbol{r}_c$ is the inertial position vector of the center of mass, and, $\boldsymbol{\rho}_1$ and $\boldsymbol{\rho}_2$ are the position vectors of the deputy and gluon with respect to the center of mass, respectively.

The net effect of the Coulomb forces on the center of mass is zero and its equation of motion

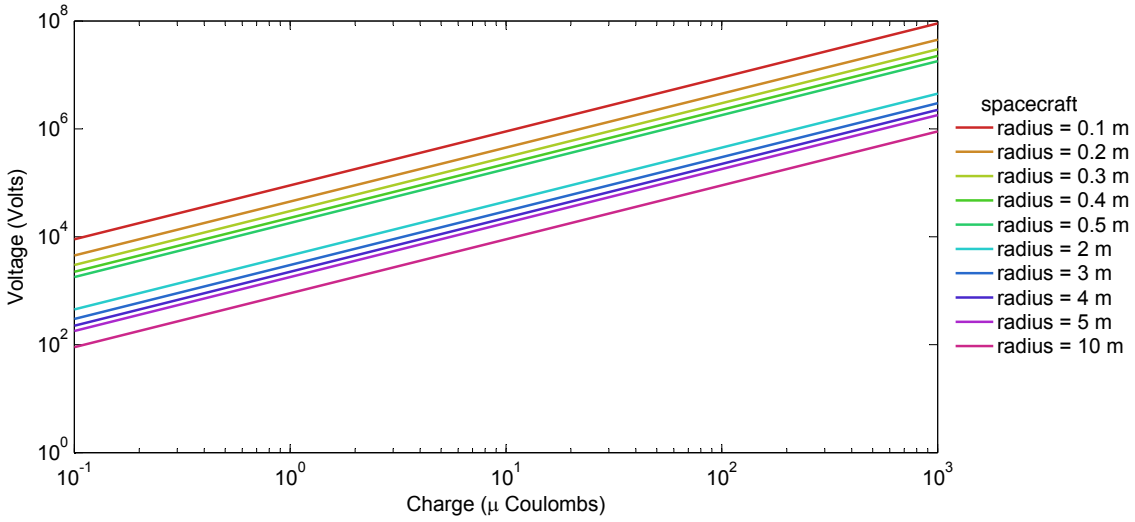

Figure 4.7: Graph illustrating the voltage-charge relationship in a spherical satellite for different radii

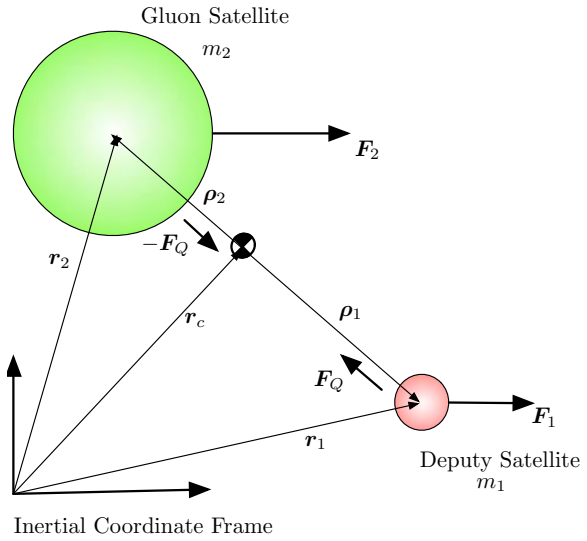

Figure 4.8: A simple gluon and deputy satellite illustration.

is given by

$$(m_1 + m_2)\ddot{\boldsymbol{r}}_c = \boldsymbol{F}_1 + \boldsymbol{F}_2 \tag{4.13}$$

In order to keep the formation from drifting, we should generate a Coulomb force $\boldsymbol{F}_Q$, which will make $\ddot{\boldsymbol{\rho}}_1$ and $\ddot{\boldsymbol{\rho}}_2$ go to zero. By setting $\ddot{\boldsymbol{\rho}}_1$ as zero in Eq. (4.12a) and solving for $\boldsymbol{F}_Q$, we get

$$\boldsymbol{F}_Q = -\boldsymbol{F}_1 + m_1\ddot{\boldsymbol{r}}_1 \tag{4.14}$$

In Eq. (4.14), Substituting for $\boldsymbol{F}_1$ from the center of mass equation in Eq. (4.13), we get

$$\boldsymbol{F}_Q = -\frac{m_2}{m_1 + m_2}\boldsymbol{F}_1 + \frac{m_1}{m_1 + m_2}\boldsymbol{F}_2 \tag{4.15}$$

The external forces, $\boldsymbol{F}_1$ and $\boldsymbol{F}_2$, in Eq. (4.15) can be rewritten in terms of acceleration as

$$\boldsymbol{F}_Q = \frac{m_1 m_2}{m_1 + m_2}(\boldsymbol{a}_2 - \boldsymbol{a}_1) \tag{4.16}$$

where, $\boldsymbol{a}_2$ and $\boldsymbol{a}_2$ are the inertial accelerations due to the external disturbance force. By writing out the full expression for the Coulomb force in Eq. (4.16) and equating the magnitudes of the force, we get

$$k_c \frac{q_1 q_2 e^{\left(\frac{-d}{\lambda_d}\right)}}{d^2} = \frac{m_1 m_2}{m_1 + m_2} a_d \tag{4.17}$$

where a_d is the differential acceleration, λ_d is the Debye length, d is the separation distance between the satellites and, q_1 and q_2 are the charges of deputy and gluon respectively. By using the voltage-charge relationship in Eq. 4.11, we rewrite Eq. 4.17 as

$$\frac{r_1 r_2 V_1 V_2 e^{\left(\frac{-d}{\lambda_d}\right)}}{k_c d^2} = \frac{m_1 m_2}{m_1 + m_2} a_d \tag{4.18}$$

In general, the voltage on the gluon will be fixed and the voltage on the deputy will be varied to compensate for the differential drag. But, in this paper we have fixed the voltage of the deputy as 10 kV (maximum permissible) and varied the gluon voltage to see if it is below the available voltage. This is because the gluon size has not been fixed and we are interested in studying the gluon voltage-size and differential perturbation-size relationships. Solving Eq. 4.18 for V_2, we get

$$V_2 = \frac{m_1 m_2}{m_1 + m_2} \frac{k_c d^2 a_d}{r_1 r_2 V_1 e^{\left(\frac{-d}{\lambda_d}\right)}} \tag{4.19}$$

4.3.3 Differential Perturbations for Variable Gluon Radius

Both the deputy satellite and gluon experience perturbations due to solar drag, atmospheric drag and J_2 effect. But, these perturbations are not equal in magnitude and cause a net force which may result in the drifting of the satellite formation. This differential perturbation depends on the mass, surface area and separation distance between the gluon and deputy. In an effort to study this dependence, we vary the gluon radius and separation distance and study the resulting differential perturbation. The satellites are assumed to at GEO (fixed altitude of 35000 m), where it has been estimated that the Debye length varies from 100 m to 500 m. We are not varying the Debye length at present and taking it to be a fixed value of 500 m.

Figure 4.9(a) shows the contours of the differential acceleration due to differential solar drag between the gluon and the deputy at GEO for different gluon radius and separation distance. The gluon radius has been varied from 2 m to 10 m, and the separation distance from 10 m to 1000 m. It can be observed from the figure that the differential acceleration does not depend on the separation distance, but gradually increases as the gluon radius is increased. Contours of required gluon voltage V_2 to compensate for the differential solar radiation drag, assuming a fixed deputy voltage V_1 (10 kV), is shown in Figure 4.9(b). Even though the differential solar radiation drag is less for smaller gluon radii, the voltage needed will increase because the smaller radii causes a higher charge density. After reaching a low around the 5 meter radius, there is a gentle increase in required voltage needed due to the increasing differential solar radiation perturbation.

Figure 4.10(a) shows the contours of the differential acceleration due to differential J_2 effect between the gluon and the deputy at GEO for different gluon radius and separation distance. It can be seen from the figure that the differential acceleration depends only on the separation distance and not on the gluon radius. The J_2 effect also depends on the orientation of the formation and the differential acceleration shown in the contour plot is the maximum possible value for a given separation distance considering all possible orientations. Contours of required gluon voltage V_2 needed to compensate for the differential J_2 effect, assuming a fixed deputy voltage V_1 (10 kV), is shown in Figure 4.10(b). The voltage needed increases with separation distance and gently decreases with increasing gluon radii.

The effect of gluon radius on the differential atmospheric drag has not been studied as it is practically negligible at GEO. From the solar drag study, we conclude that the voltage needed at higher radius to compensate differential solar drag is only marginally high and from the contour plot studying the J_2 effect, it is clear that the larger gluon radii result in smaller voltages that needed for compensating the differential J_2 effect. Therefore, it is beneficial to have large gluon radii and we will fix its value as 10 m.

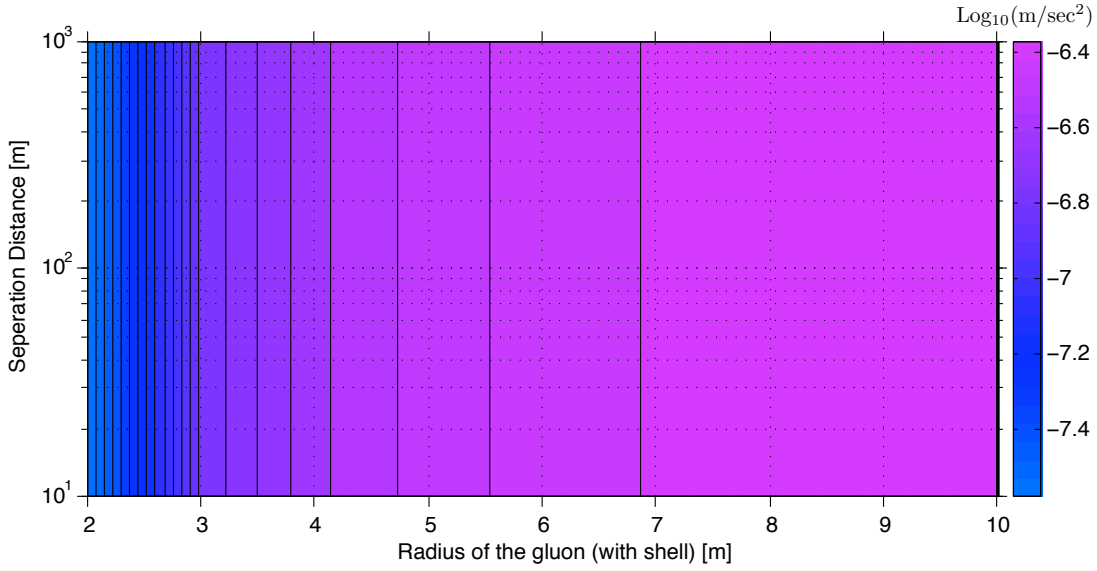

(a) Contours of the differential acceleration due to differential solar drag between the gluon and the deputy at GEO for different gluon radius. The differential acceleration shown in the contours are in log scale.

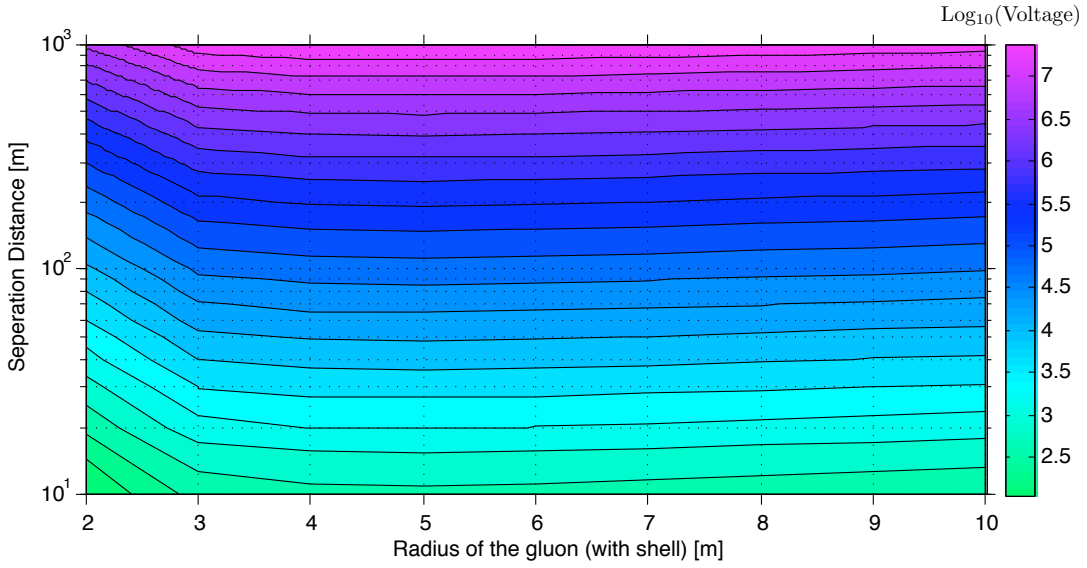

(b) Contours of voltage V_2 needed on gluon to compensate for the differential solar drag, assuming a fixed voltage V_1 (10 kV) on the deputy. The voltage shown in the contours are in log scale.

Figure 4.9: Differential Solar Drag at GEO (fixed altitude of 35000 km)

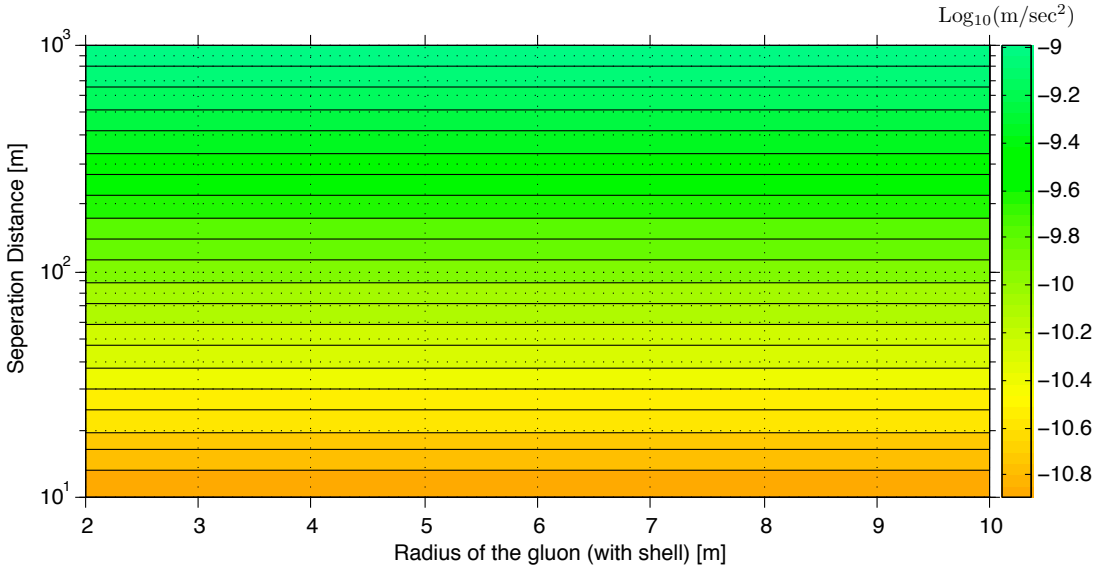

(a) Contours of the differential acceleration due to the differential J_2 effect between the gluon and the deputy at GEO for different gluon radius. The differential acceleration shown in the contours are in log scale.

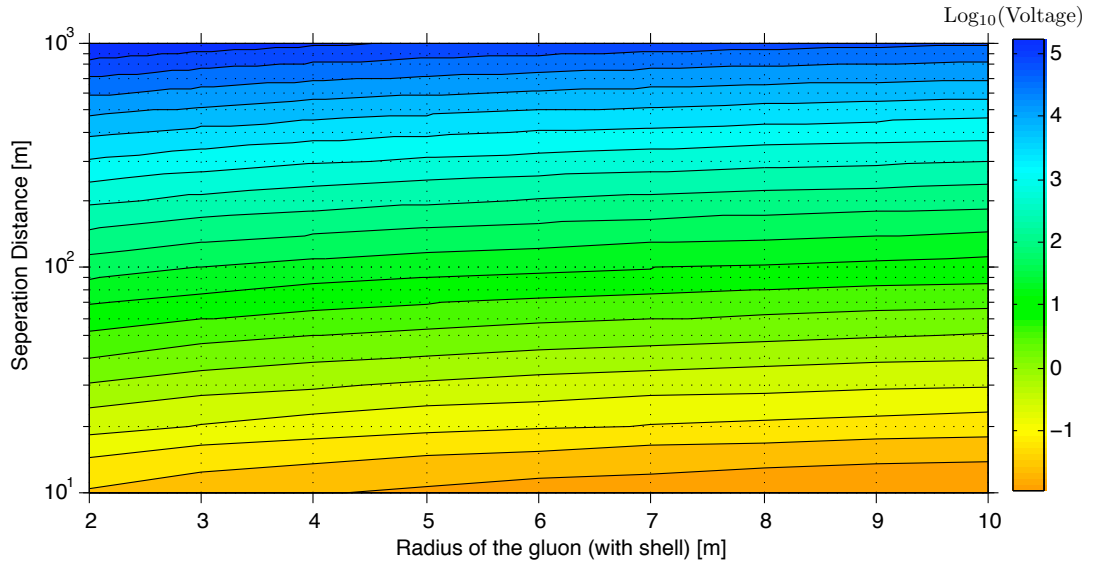

(b) Contours of voltage V_2 needed on gluon to compensate for the differential J_2 effect, assuming a fixed voltage V_1 (10 kV) on the deputy. The voltage shown in the contours are in log scale.

Figure 4.10: Differential J_2 Effect at GEO (fixed altitude of 35000 km)

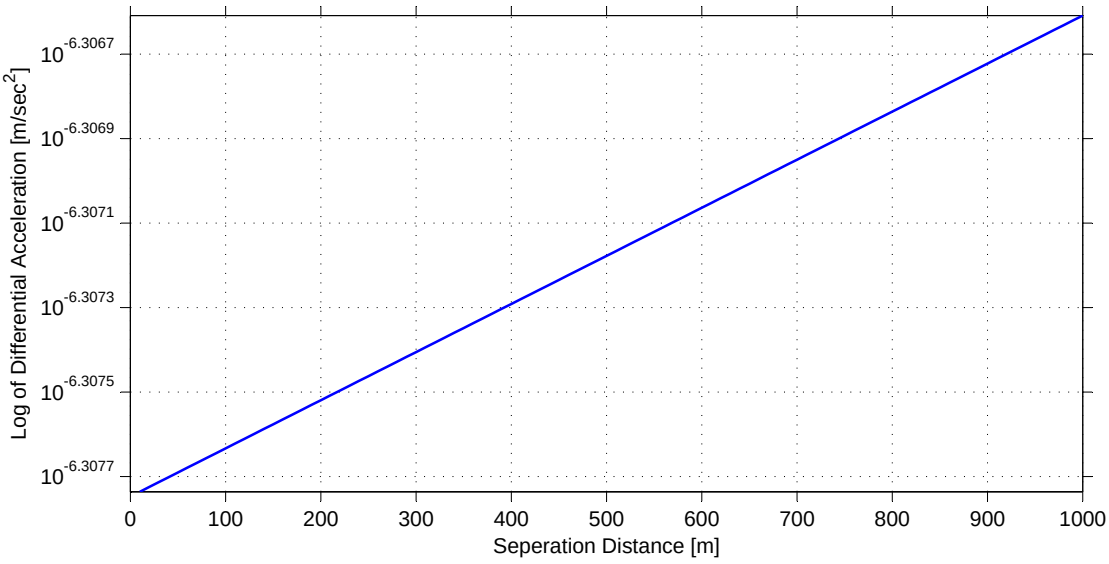

(a) The differential perturbation (includes solar drag, atmospheric drag and J_2 effect) between the gluon of radius $10\,m$ and the deputy at GEO.

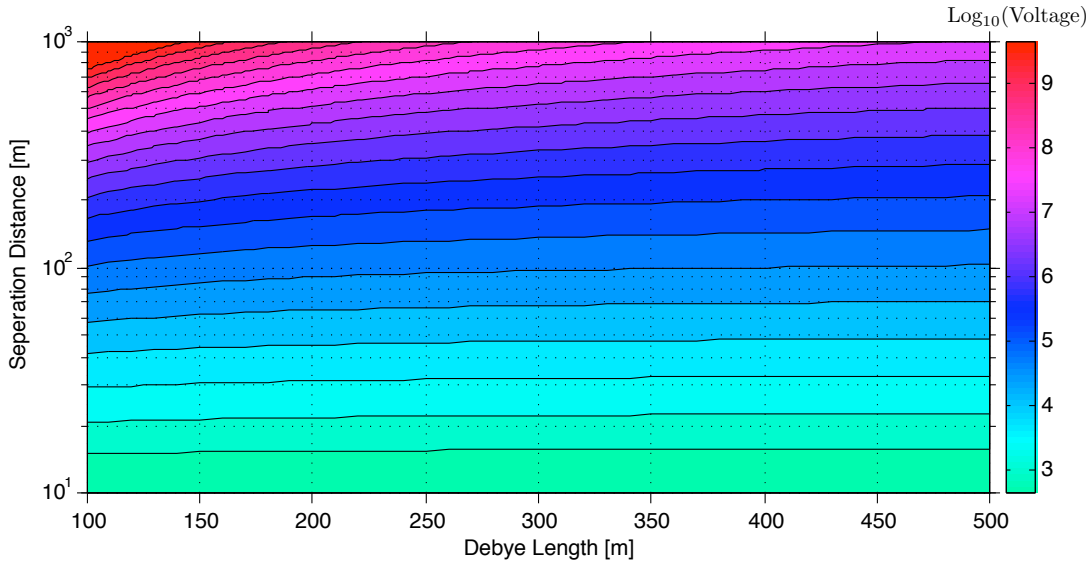

(b) Contours of voltage V_2 needed on gluon to compensate for the differential perturbation, assuming a fixed voltage V_1 (10 kV) on the deputy. The voltage shown in the contours are in log scale.

Figure 4.11: Differential Perturbation and Corresponding Voltage Requirements at GEO (fixed altitude of 35000 km)

4.3.4 Sweeps of Required Voltages at GEO

At GEO (fixed altitude of 35000 m), the Debye length varies from 100 m to 500 m. Hence, the voltage V_2 needed on the gluon to compensate for the differential acceleration at this altitude is studied for Debye lengths varying from 100m to 500m, and various separation distances between the gluon and deputy. The results from this study has been illustrated in Figure 4.11. The contour plot in Figure 4.11(a) gives the differential acceleration between the deputy and gluon due to solar drag, atmospheric drag and J_2 effect. The voltage V_2 needed on the gluon to compensate for this differential acceleration, assuming a fixed voltage V_1 (10kV) on the deputy is shown in the contour plot in Figure 4.11(b). For craft flying up to 30 meters apart, the voltages rise up to kV levels. As the Debye lengths are reduced, the voltage increase even further.

4.4 Static Coulomb Structure Concept

4.4.1 Formation Description

The focus of this section is the generation of high Earth orbit (HEO) Coulomb force structures. Coulomb force structures are a relatively new concept consisting of several electrostatically chargeable nodes with no interconnecting struts. Instead, the node charges are carefully controlled so that the net structure is held together solely by the Coulomb forces generated between all the nodes. This 'virtual structure' can also be considered as a free-flying, constant-shape formation of several spacecraft. Advantages of Coulomb force virtual structures include low mass, low propellant usage, reconfigurability, and self-assembly. Large virtual structures on the order or 20–100 meters are envisioned where controlled electrostatic force fields are used to bond the individual craft into a single structure. By changing control laws, it will be possible to increase or decrease the stiffness or flexibility of sub-components, or even change the size and shape of the overall structure. This will allow for highly reconfigurable structures which can adapt to changing mission needs.

The uniqueness of the work in this section is the examination of how to form *specified* shape structures using a subset of all available nodes. In addition, the plasma shielding effect is considered explicitly. An equilateral triangle structure example is given to illustrate the approach where 5 nodes are used in the structure, 3 of which used to satisfy the equilateral triangle shape goal.

4.4.2 Normalized Hill's Equations

Consider N spacecraft in a circular orbit about the Earth. At their center of mass is the origin of a Hill coordinate frame $\mathcal{H} : \{\hat{\boldsymbol{\imath}}_r, \hat{\boldsymbol{\imath}}_\theta, \hat{\boldsymbol{\imath}}_h\}$ such that the $\hat{\boldsymbol{\imath}}_r$ axis points radially out from the Earth, the $\hat{\boldsymbol{\imath}}_\theta$ axis points along the velocity vector of the center of mass, and the $\hat{\boldsymbol{\imath}}_h$ axis completes a right hand frame. Each of the equal mass, spherical spacecraft can have a charge, denoted q_i, and a position vector from the origin of the Hill frame, denoted $\boldsymbol{\rho}_i$. Setting the speed and acceleration terms in Hill's equations to zero yields the static Coulomb structure equilibrium equations[1, 28, 35–37]

$$\begin{aligned} -3n^2 x_i &= \frac{k_c}{m}\sum_{j=1}^{N} \frac{x_i - x_j}{|\boldsymbol{\rho}_i - \boldsymbol{\rho}_j|^3} q_i q_j e^{-|\boldsymbol{\rho}_i - \boldsymbol{\rho}_j|/\lambda_d} \\ 0 &= \frac{k_c}{m}\sum_{j=1}^{N} \frac{y_i - y_j}{|\boldsymbol{\rho}_i - \boldsymbol{\rho}_j|^3} q_i q_j e^{-|\boldsymbol{\rho}_i - \boldsymbol{\rho}_j|/\lambda_d} \\ n^2 z_i &= \frac{k_c}{m}\sum_{j=1}^{N} \frac{z_i - z_j}{|\boldsymbol{\rho}_i - \boldsymbol{\rho}_j|^3} q_i q_j e^{-|\boldsymbol{\rho}_i - \boldsymbol{\rho}_j|/\lambda_d} \end{aligned} \tag{4.20}$$

where $i \neq j$, n is the Hill frame angular velocity, k_c is Coulomb's constant ($8.99 \times 10^9 \frac{Nm^2}{C^2}$), λ_d is the Debye length, and m is the mass of the spacecraft. The quantities x_i, y_i, and z_i are the components of the i^{th} spacecraft Hill frame relative position vector, $\boldsymbol{\rho}_i$.

To start the nondimensionalization process, divide both sides of Eq. 4.20 by n^2 and rear-

$$
\begin{aligned}
-3x_i &= \sum_{j=1}^{N} \frac{x_i - x_j}{|\boldsymbol{\rho}_i - \boldsymbol{\rho}_j|^3} \left(\frac{r_{s/c}}{n\sqrt{mk_c}} V_i\right) \left(\frac{r_{s/c}}{n\sqrt{mk_c}} V_j\right) e^{-|\boldsymbol{\rho}_i - \boldsymbol{\rho}_j|/\lambda_d} \\
0 &= \sum_{j=1}^{N} \frac{y_i - y_j}{|\boldsymbol{\rho}_i - \boldsymbol{\rho}_j|^3} \left(\frac{r_{s/c}}{n\sqrt{mk_c}} V_i\right) \left(\frac{r_{s/c}}{n\sqrt{mk_c}} V_j\right) e^{-|\boldsymbol{\rho}_i - \boldsymbol{\rho}_j|/\lambda_d} \\
z_i &= \sum_{j=1}^{N} \frac{z_i - z_j}{|\boldsymbol{\rho}_i - \boldsymbol{\rho}_j|^3} \left(\frac{r_{s/c}}{n\sqrt{mk_c}} V_i\right) \left(\frac{r_{s/c}}{n\sqrt{mk_c}} V_j\right) e^{-|\boldsymbol{\rho}_i - \boldsymbol{\rho}_j|/\lambda_d}
\end{aligned} \tag{4.21}
$$

range to obtain Eq. (4.21). Note that the spacecraft voltage V_i is related to charge by

$$
V_i = \frac{q_i k_c}{r_{s/c}} \tag{4.22}
$$

where $r_{s/c}$ is the spherical spacecraft radius.

Next, define nondimensional position coordinates as

$$
\begin{aligned}
\tilde{x}_i &= \frac{x_i}{M\lambda_d} \\
\tilde{y}_i &= \frac{y_i}{M\lambda_d} \\
\tilde{z}_i &= \frac{z_i}{M\lambda_d}
\end{aligned} \tag{4.23}
$$

where M is the number of Debye lengths, and specifies the rather arbitrarily chosen characteristic length used for nondimensionalization. For example, to nondimensionalize using 3 Debye lengths, let $M = 3$. Applying this to Eq. 4.21 yields the final set of nondimensional, static equilibrium, Coulomb formation equations.

$$
\begin{aligned}
-3\tilde{x}_i &= \sum_{j=1}^{N} \frac{\tilde{x}_i - \tilde{x}_j}{|\tilde{\boldsymbol{\rho}}_i - \tilde{\boldsymbol{\rho}}_j|^3} \tilde{V}_i \tilde{V}_j e^{-M|\tilde{\boldsymbol{\rho}}_i - \tilde{\boldsymbol{\rho}}_j|} \\
0 &= \sum_{j=1}^{N} \frac{\tilde{y}_i - \tilde{y}_j}{|\tilde{\boldsymbol{\rho}}_i - \tilde{\boldsymbol{\rho}}_j|^3} \tilde{V}_i \tilde{V}_j e^{-M|\tilde{\boldsymbol{\rho}}_i - \tilde{\boldsymbol{\rho}}_j|} \\
\tilde{z}_i &= \sum_{j=1}^{N} \frac{\tilde{z}_i - \tilde{z}_j}{|\tilde{\boldsymbol{\rho}}_i - \tilde{\boldsymbol{\rho}}_j|^3} \tilde{V}_i \tilde{V}_j e^{-M|\tilde{\boldsymbol{\rho}}_i - \tilde{\boldsymbol{\rho}}_j|}
\end{aligned} \tag{4.24}
$$

where

$$
\tilde{V}_i = \frac{r_{s/c}}{n\sqrt{m\left(M\lambda_d\right)^3 k_c}} V_i \tag{4.25}
$$

Finding a charge/position set (i.e. $\tilde{\boldsymbol{\rho}}_i$, $\tilde{V}_i$ for $i = 1 \ldots N$) that satisfies Eq. 4.24 for a specified Debye length fraction (M) yields a family of equilibrium formations for any altitude (n), spacecraft radius ($r_{s/c}$), spacecraft mass (m) and Debye length (λ_d). The Hill frame angular velocity can be found by

$$
n = \sqrt{\frac{\mu}{r^3}} \tag{4.26}
$$

where μ is the standard gravitational parameter for Earth ($\mu = 3.986 \times 10^{14} \frac{\mathrm{m}^3}{\mathrm{s}^2}$) and r is the circular orbit radius. Table 4.1 shows these values for various r.

4.4.3 Application of Nondimensional Equations to Static Formation Solution Generation

Eq. 4.24, in conjunction with a gradient-based optimization code, is used to determine the relationship between spacecraft voltage, separation distance, and Debye length for a charged spacecraft formation with application to Earth imaging. The formation consisted of 5 spacecraft ($N = 5$), and thus contains 17 free parameters - 20 parameters for spacecraft charge and position ($\tilde{\boldsymbol{\rho}}_i, \tilde{V}_i, \quad i = 1 \ldots 5$) less 3 position parameters to satisfy the constraint that the center of mass is at the Hill frame origin. From Eq. 4.24 it is clear that there are 15 nonlinear equations to be solved.

Formally, the problem has two additional sets of constraints

1. 3 of the craft must form an equilateral triangle as viewed from Earth

Table 4.1: Speed information as a function of circular orbit altitude.

Altitude (km)	**Radius** (m)	**Period** (hr)	**Speed** (m/s)	**Mean Orbit rate** (rad/s)
300	6.68×10^6	1.51	7720	116×10^{-5}
500	6.88×10^6	1.58	7610	111×10^{-5}
2000	8.38×10^6	2.12	6900	82.3×10^{-5}
10000	16.4×10^6	5.81	4930	30.1×10^{-5}
35800	42.2×10^6	24.0	3070	7.28×10^{-5}

2. The Hill frame must be the principal axes of the static formation.[38]

These constraints are implemented during the optimization process using a penalty function. The cost function, with penalty terms, is shown in Eq. 4.27.

$$\begin{aligned} J = & \left(\frac{\max \left| \tilde{V}_i \right|}{\min \left| \tilde{V}_i \right|} \right) \sum_{i=1}^{5} |\tilde{\boldsymbol{r}}_i| \\ & + w_1 \Big\{ \left| \text{Proj}_{\hat{y},\hat{z}} \left(\tilde{\boldsymbol{\rho}}_2 - \tilde{\boldsymbol{\rho}}_1 \right) - L_0 \right| \\ & \quad + \left| \text{Proj}_{\hat{y},\hat{z}} \left(\tilde{\boldsymbol{\rho}}_2 - \tilde{\boldsymbol{\rho}}_3 \right) - L_0 \right| \\ & \quad + \left| \text{Proj}_{\hat{y},\hat{z}} \left(\tilde{\boldsymbol{\rho}}_3 - \tilde{\boldsymbol{\rho}}_1 \right) - L_0 \right| \Big\} \\ & + w_2 \Big\{ \left| I_{xy} \right| + \left| I_{xz} \right| + \left| I_{yz} \right| \Big\} \end{aligned} \tag{4.27}$$

where $\tilde{\boldsymbol{r}}_i$ is

$$\tilde{\boldsymbol{r}}_i = \left\{ \begin{array}{c} 3\tilde{x}_i + \sum_{j=1}^{N} \dfrac{\tilde{x}_i - \tilde{x}_j}{\left| \tilde{\boldsymbol{\rho}}_i - \tilde{\boldsymbol{\rho}}_j \right|^3} \tilde{V}_i \tilde{V}_j e^{-M \left| \tilde{\boldsymbol{\rho}}_i - \tilde{\boldsymbol{\rho}}_j \right|} \\ \sum_{j=1}^{N} \dfrac{\tilde{y}_i - \tilde{y}_j}{\left| \tilde{\boldsymbol{\rho}}_i - \tilde{\boldsymbol{\rho}}_j \right|^3} \tilde{V}_i \tilde{V}_j e^{-M \left| \tilde{\boldsymbol{\rho}}_i - \tilde{\boldsymbol{\rho}}_j \right|} \\ -\tilde{z}_i + \sum_{j=1}^{N} \dfrac{\tilde{z}_i - \tilde{z}_j}{\left| \tilde{\boldsymbol{\rho}}_i - \tilde{\boldsymbol{\rho}}_j \right|^3} \tilde{V}_i \tilde{V}_j e^{-M \left| \tilde{\boldsymbol{\rho}}_i - \tilde{\boldsymbol{\rho}}_j \right|} \end{array} \right\} \tag{4.28}$$

The first term of J ensures that Hill's equations are satisfied (Eq. 4.24) while keeping the nondimensional spacecraft charges near each other. The second term favors an equilateral triangle projection onto the $\hat{\boldsymbol{\imath}}_\theta$–$\hat{\boldsymbol{\imath}}_h$ plane with a nondimensional separation distance of L_0. The third term forces the principal axis requirement. The penalty function weights, w_1 and w_2 were both chosen as 10.0.

The solution for $M = 1$ and $L_0 = 0.5$ is used to illustrate a typical solved formation shape. The nondimensional spacecraft charges are shown in Table 4.2.

Table 4.2: Nondimensional spacecraft voltages for a 5 craft formation, with $M = 1$ and the nondimensional, equilateral triangle separation distance of $L_0 = 0.5$.

Spacecraft No.	**Voltage** $\tilde{V}_i$
1	1.2840
2	-0.7583
3	-0.7583
4	0.8841
5	1.6398

A view from Earth and a perspective view are given in Figures 4.12 and 4.13. The color bar is the nondimensional voltage magnitude as a percent of the maximum (1.6398).

Because the nondimensional separation distance was constrained to 0.5 and $M = 1$, the actual equilateral triangle separation distance (between craft 1,2,3) in meters is

$$L_\Delta = .5 L_\lambda \tag{4.29}$$

4.4.4 Numerical Results

Solutions were obtained for several values of M. Table 4.3 shows the results of converting nondimensional, maximum spacecraft voltages

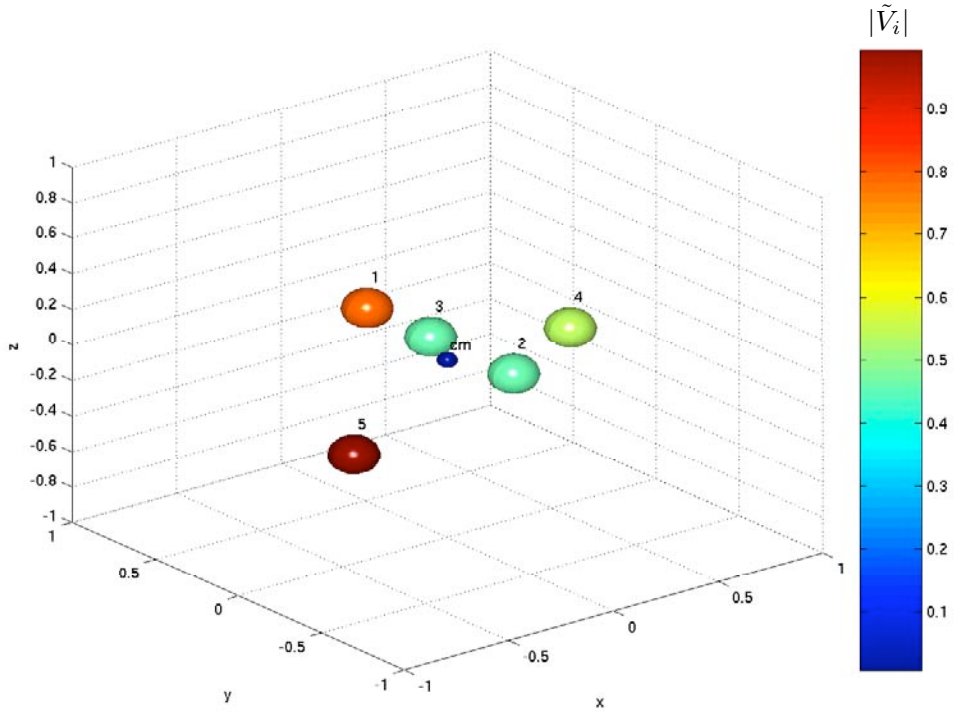

Figure 4.12: 5 spacecraft static formation - perspective view. The formation center of mass is shown as a small blue sphere, but of course, has no voltage associated with it.

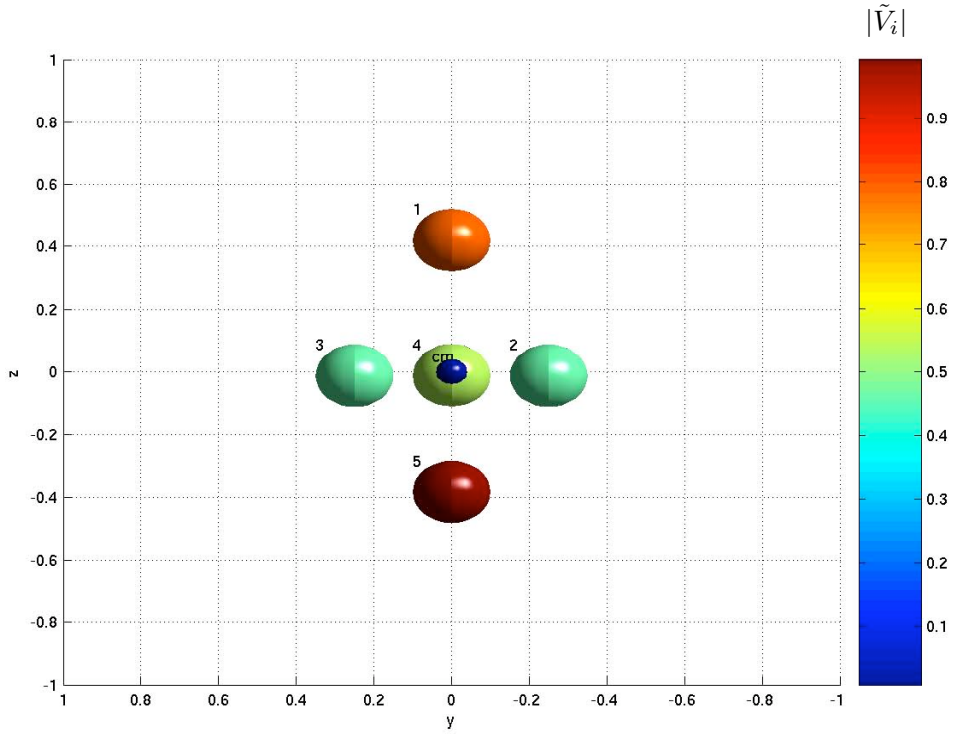

Figure 4.13: 5 spacecraft static formation - view from Earth. The formation center of mass is shown as a small blue sphere, but of course, has no voltage associated with it.

back to true voltages for a variety of altitudes, Debye lengths, and equilateral triangle separation distances. This illustrates that to obtain 'reasonable' equilateral spacecraft separation distances, the formation should exploit the large Debye lengths at GEO. If spacecraft voltages must stay in the 10,000 volt range, then equilateral separation distances of about 10 meters are feasible.

Table 4.3: True spacecraft voltages for a variety of altitudes, Debye lengths, and equilateral triangle separation distances.

Altitude (km)	λ_d (m)	L_Δ (m)	$V_{\max}$
300	.01	.005	2.50
		.01	10.5
		.02	60.9
10000	.05	.025	7.30
		.05	30.5
		.1	177
35800	20	10	14,100
		20	59,000
		40	343,000
	50	12	16,100
		25	55,700
		50	233,000
		100	1,360,000
	100	12	16,100
		25	48,600
		50	158,000
		100	660,000
		200	3,830,000

Figure 4.14 Shows the maximum true spacecraft voltage as a function of both Debye length and the L_Δ/L_λ ratio. The absolute voltage levels can be extracted from the log scale color bar at the right of the plot. For example, for a $L_\lambda = 50$ meters, and an $L_\Delta = 50$ meters, the maximum voltage is approximately $V_{\max} = 10^{5.4} = 250,000$ volts.

4.5 Other Mission Concepts

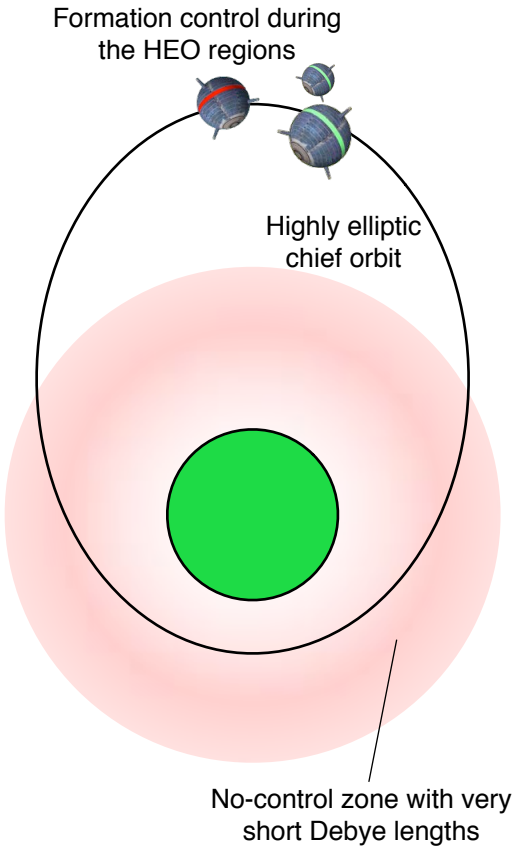

Figure 4.15: Illustration of Coulomb Formation Control on Highly Eccentric Orbit.

4.5.1 Elliptic Chief Orbits

The cold, dense plasma environment results in centimeter-level Debye length in LEO. This makes using Coulomb thrusting impractical at low orbit altitudes. Any electrostatic fields around a craft are quickly masked by the plasma ions and electrons shielding this charge from other craft. The Debye lengths increase slowly with altitude due to decreasing plasma density. The Van-Allen radiation belts have a higher concentration of ions, but their kinetic energy (temperature) levels are much higher as well. This regime is also not practical for charged spacecraft control applications. The plasma environment study concludes that for orbits at 5-6 Earth radii or higher (outside the

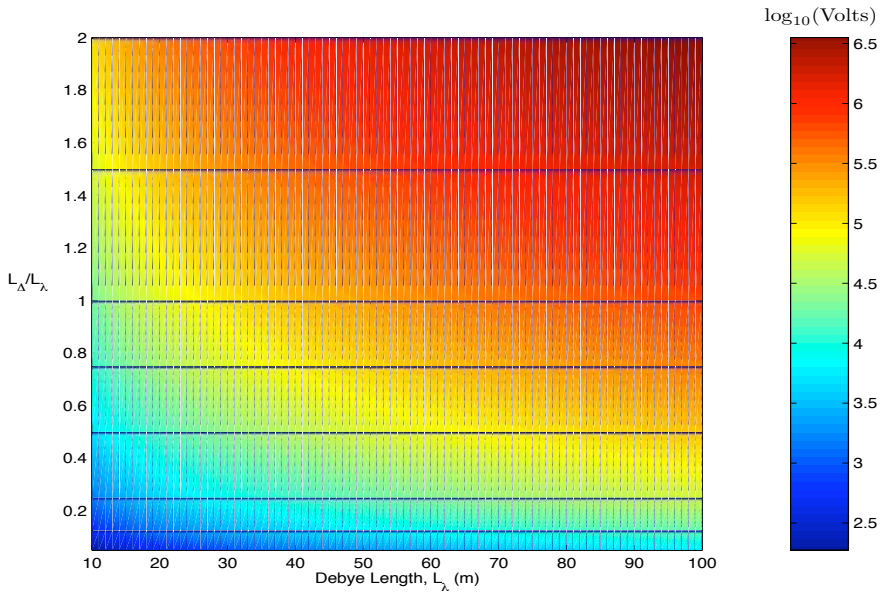

Figure 4.14: Maximum spacecraft voltages needed to maintain craft 1,2,3 in an equilateral triangle. The color bar is on a $\log_{10}$ scale, therefore 2.5 corresponds to $10^{2.5}$ volts and 6.5 corresponds to $10^{6.5}$ volts.

radiation belts) the Debye length can vary between 50-500 meters, and be even higher at GEO.

So far all the coulomb formation flying missions considered had circular chief orbit with a constant orbit radius. Here the orbit altitude is or is not acceptable for Coulomb control. A new mission concept envisions using highly elliptical orbits as illustrated in Figure 4.15. On these orbits the spacecraft relative motion is only controlled near the apoapses region which is sufficiently outside the radiation belts. After the relative orbit errors are canceled using Coulomb thrusting, the formation dives closer to the planet to have smaller Earth sensing distances. No formation control is possible for the LEO regions. The orbit must be designed such that sufficient time is spent in the HEO region to be able to compensate for any differential perturbations the craft encountered during their previous near-Earth passage.

This type of formation scenario can allow for short Earth sensing distances, but can also provide long dwell time over higher latitude Earth regions. The Russian Molniya satellites have highly eccentric satellites to provide communication coverage to the high latitude regions of their country. Having clusters of satellites on eccentric orbits could provide similar long dwell times over polar regions.

When designing such eccentric formations, care must be taken about the formation size contraction during the chief periapses passages. For example, consider the simple leader-follower formation where one satellite leads another satellite through the mean anomaly difference δM. All other orbit elements of these satellites are identical. Small differences in mean anomaly map to small differences in true anomaly angles using

$$\delta f = \frac{a\sqrt{1-e^2}}{r^2}\delta M \tag{4.30}$$

where a is the chief semi-major axis and e is the chief eccentricity. Note that while the true anomaly differences δf will vary over an orbit period, the mean anomaly differences δM remain constant, even on highly eccentric orbits. This allows to investigate by how much a formation size will be contracted during periapses passage. The chief orbit is designed to have an apoapses radius of r_a, and a periapses radius

of r_p. Let $\delta y(t)$ be the along track separation distance between the two craft. This state is at apoapses

$$\delta y(t_a) = r_a \delta f(t_a) \tag{4.31}$$

and at periapses

$$\delta y(t_p) = r_p \delta f(t_p) \tag{4.32}$$

Using the relationship in Eq. (4.30), as well as the fact that $\delta M(t_a) = \delta M(t_p)$, the along track separation distance will contract/expand according to:

$$\frac{\delta y(t_p)}{\delta y(t_a)} = \frac{r_a}{r_p} \tag{4.33}$$

Thus, if the sensor requirements state a separation distance of 25 meters at periapses, and the ratio r_a/r_p is 7 (outside of radiation belt), then the apoapses separation distances will be on the order of 175 meters. Such separation distances will be challenging to implement if the Debye length is of the order of 50-500 meters. During typical conditions where λ_d is 80-150 meters, the required spacecraft charge to achieve the necessary orbit corrections will be very large. Thus, it will be challenging to design such highly eccentric orbits where the periapses separation distances are safe to fly uncontrolled, while the apoapses separation distances are small enough to employ Coulomb thrusting.

4.5.2 Rendezvous and Docking Scenarios

Flying spacecraft with small separation distances on the order of a few dozen meters is very challenging. Using ion-engines or conventional thrusters, there is a very large exhaust plume impingement problem which must be addressed. In particular, if a spacecraft is approaching another for docking, and it is closing in too fast, care must be taken when firing thrusters to slow down the craft to avoid hitting the target craft. Further, the large number of small orbit corrections required to align the docking mechanisms make these docking operations fuel-expensive.

Because essentially no mass is emitted with the Coulomb thrusting concept it does not pose any plume impingement issues. It is a very clean method to control close proximity operations. Further, the Coulomb thrusting is the most effective for small separation distances which are a multiple of the spacecraft dimensions. The extremely low power and fuel requirement, the absence of plume impingement issues, as well as the high control bandwidth at which the spacecraft charge can be controlled make this technology a very strong candidate for rendezvous and docking operations. The following subsections outline two charged docking approach scenarios, as well as a potential soft-docking application.

4.5.2.1 General-Docking Concept

The first docking concept has the target craft equipped with several charge surfaces as illustrated in Figure 4.16. Each device is assumed to be electrically isolated to avoid charge bleeding through the craft. These charge devices are arranged such that they can produce general 3D electrostatic fields in the near vicinity. The docking craft is also controlled to have a non-zero electrostatic potential. Interacting with the 3D field of the target craft will allow a general force vector to be produced on the docking craft.

A sample docking scenario is as follows. The docking craft positions itself ahead of the docking mechanism of the primary craft using conventional propulsion systems. It is not necessary to match the target craft's velocity perfectly. Instead, once the docking craft is position within a parking tolerance box, the charge control is engaged. The docking craft maintains a constant charge level from here on relative to the space plasma environment. The target craft is equipped with telemetry sensors which are able to track the docking craft motion relative to the docking port. After computing a control solution to carefully pull the docking craft in, the target craft charging mechanisms are engaged. The required three-dimensional control force vector is now implemented by generating the required three-dimensional electrostatic field around the docking craft. By measuring

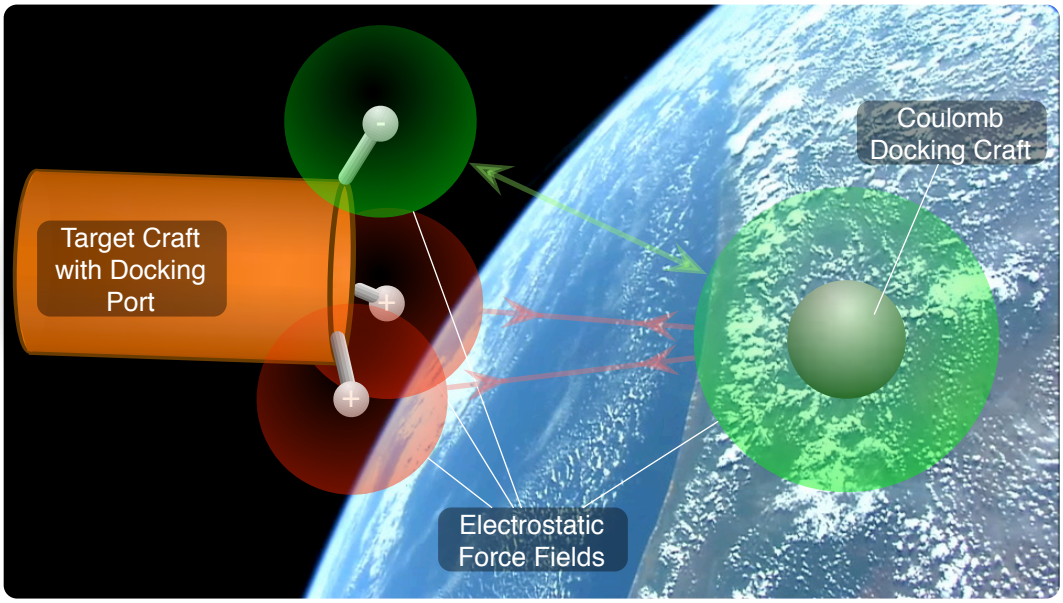

Figure 4.16: Illustration of a Coulomb docking vehicle being guiding into the docking mechanism of a target craft using Coulomb forces.

the actual relative trajectory off the docking craft, the control solution is updated using feedback control laws.

As the target craft is being pulled in, an equal and opposite force vector is produced onto the target craft. This will required the target craft to have its own attitude control to maintain a particular heading. If the target craft is much more massive than the docking craft, then the target craft motion is expected to be very small.

Compared to conventional thrusting, no plume impingement issues are presented. The final relative motion between the craft is controlled using only the efficient electrostatic forces in a clean manner. Further, if the docking craft has a differential charging across its surface, then the 3D force fields could also be used to control the docking craft attitude. The high control bandwidth will allow for very precise alignment of either craft.

4.5.2.2 Nadir-Pointing Docking Concept

If two charged craft are present, then the Coulomb control force will only act along the relative position vectors. Because the Coulomb force is a formation internal force, Coulomb forces cannot change the total inertial angular momentum. Thus, it is difficult to control the formation attitude using two electrostatic charges. However, in an orbit a rigid spacecraft experiences differential gravitational forces across its body due to the different distances to the Earth's center. The resulting torque onto the rigid body is referred to as the gravity gradient torque.[14] The nadir-pointing charged docking scenario seeks to exploit this external torque acting on the two-craft formation, and and use it to stabilize the in-plane motion of the craft.

In Reference 36 the nadir pointing two-craft Coulomb formation is identified as an equilibrium solution. Given two spacecraft of mass m_1 and m_2 with charges q_1 and q_2, the charge product must satisfy

$$Q_{12}^* = q_1 q_2 = -3\frac{n^2 L^3}{k_c}\left(\frac{m_1 m_2}{m_1 + m_2}\right) \qquad (4.34)$$

where L is the spacecraft center-to-center separation distance. If two craft are placed distance L apart with the charges satisfying Eq. (4.34) and no velocity relative to the rotating center of mass orbit frame, then the Coulomb forces will

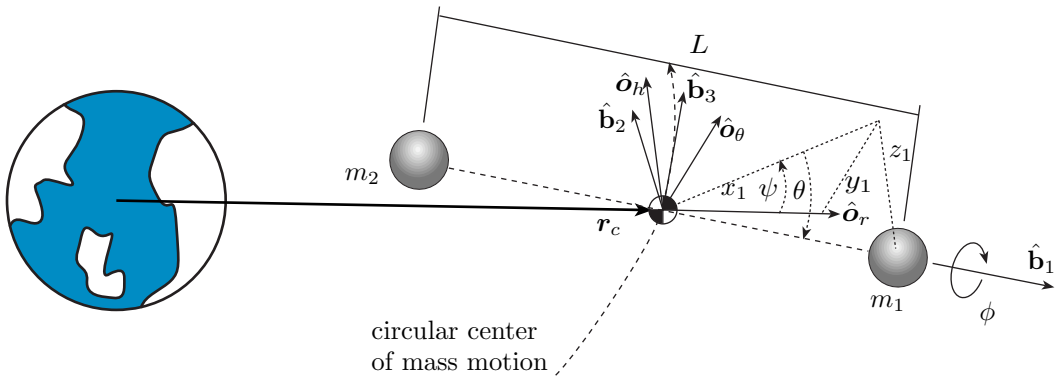

Figure 4.17: Euler Angles Representing the Attitude of Coulomb Tether with Respect to the Orbit Frame

cancel any relative accelerations and yield a relative equilibrium solution. In this configuration the gravity gradient torque, given by[14]

$$\boldsymbol{\tau}_g = 3n^2\hat{\boldsymbol{o}}_r \times ([I]\hat{\boldsymbol{o}}_r) \tag{4.35}$$

is zero because the formation principal axis is aligned with the orbit radial unit direction vector $\hat{\boldsymbol{o}}_r$.

However, this is only an open-loop result. With any perturbations or state errors present this static Coulomb structure will loose its shape and fly apart. Using a charge feedback law, Reference 30 illustrates how the separation distance L can be stabilized about a constant reference length L_r. To develop a feedback law to stabilize the separation distance using the Coulomb forces, the small charge product variation δQ is treated as a small control variable relative to the constant open-loop charge product Q_{12}^*. The actual charge product is given by

$$Q_{12} = Q_{12}^* + \delta Q \tag{4.36}$$

Because the charge of each craft causes a force along the relative position vector, the Coulomb charges can be used to control the spacecraft separation distance. The charge feedback control law is defined as

$$\delta Q = \frac{m_1 m_2 L_{\text{ref}}^2}{(m_1+m_2)\,k_c}(-C_1\delta L - C_2\delta\dot{L}) \tag{4.37}$$

where δL is the separation distance error and C_1 and C_2 are positive feedback gains. Let ψ be the in-plane rotation angle between the two craft as illustrated in Figure 4.17, while θ is the out of plane angle. The resulting linearized closed-loop equations of motion are

$$\ddot{\theta} + 4\Omega^2\theta = 0$$
$$\ddot{\psi} + \frac{2\Omega}{L_{\text{ref}}}\delta\dot{L} + 3\Omega^2\psi = 0$$
$$\delta\ddot{L} + C_2\delta\dot{L} - (2\Omega L_{\text{ref}})\dot{\psi} + (C_1 - 9\Omega^2)\delta L = 0$$

As is the case with rigid bodies, the out-of-plane θ equations of motion decouple from the separation distance δL and in-plane ψ equations of motion. As a result, the charge feedback control will not be able to compensate for out-of-plane motion. However, if the feedback gains satisfy

$$C_1 > 9n^2 \qquad C_2 > 0 \tag{4.38}$$

then Reference 30 shows that the both the resulting δL and ψ states are asymptotically stabilized by the charge feedback control in Eq. (4.37). This is achieved by only measuring the separation distance L. The relative orbital dynamics and the gravity gradient torque are exploited to achieve asymptotic convergence.

With the nadir-docking concept the craft is positioned essentially above or below the target craft as shown in Figure 4.18. The in-plane errors don't have to be canceled perfectly. After

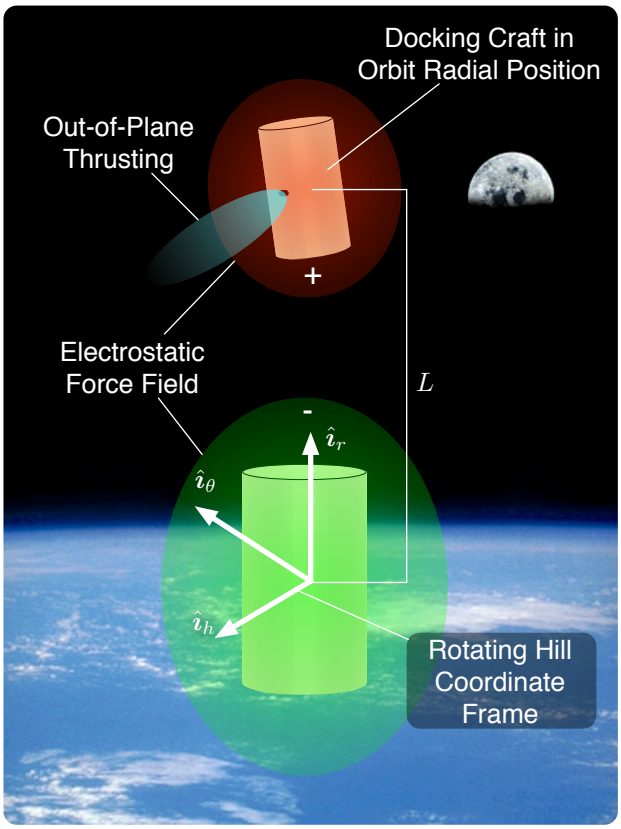

Figure 4.18: Illustration the inter-spacecraft electrostatic force being used to dock 2 spacecraft in a nadir pointing formation.

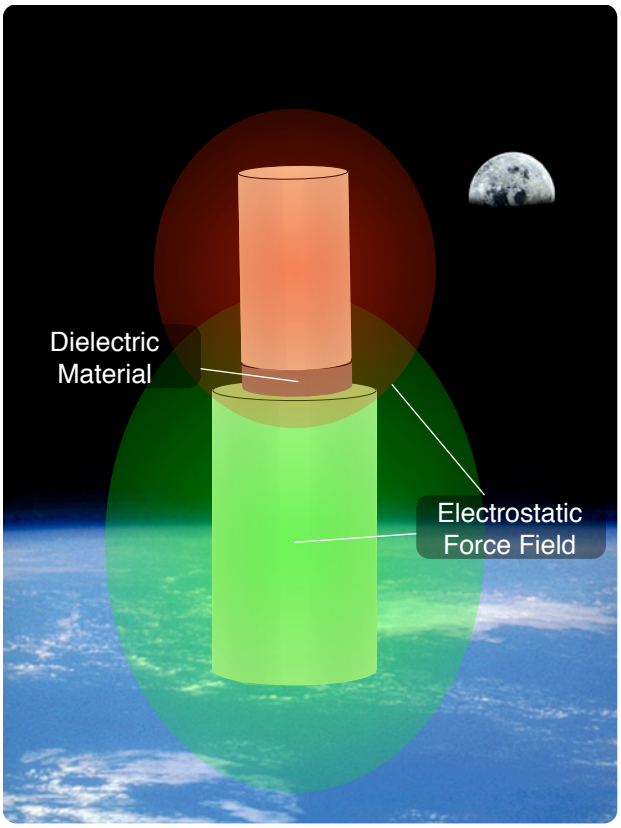

Figure 4.19: Illustration of a two craft using electrostatic forces to perform a soft-dock.

engaging the Coulomb force fields, the two craft are tied together through this virtual Coulomb tether. Any residual in-plane motion between the craft is then negated by controlling the separation distance and exploiting the local gravity gradient. By developing a new charge feedback control law to track a time varying separation distance, it is possible to both keep the craft in-plane alignment, as well as to carefully reduce the separation distance. Because the Coulomb thrusting concept does not cause plume impingement issues, the approach speed can be precisely controlled through the electric fields. Any out-of-plane relative ψ motion between the craft will be compensated for with conventional thrusters as illustrated in Figure 4.18. However, because these thrusters don't aim at the target craft, no plume impingement issues will arise. Thus, the nadir-docking scenario envisions a hybrid control actuation scheme where Coulomb forces are used to stabilize both the approach speed as well as the in-plane relative motion, while conventional thrusters are used to control any out-of-plane motion.

The attitude of each craft is assumed to be controlled internally using momentum exchange devices. Compared to the general Coulomb docking concepts, this approach does not allow for prescribed three-dimensional electric fields to be formed.

4.5.2.3 Soft-Dock with Coulomb Force

A very challenging component of docking operations is the soft docking process, which very precisely moves the two craft into position for final mechanical hard docking. During soft-dock the two craft make physical contact, but don't have all the final interlocks in place. Due to Newton's second law, if the two craft just bump into each other without grabbing hold, then the satellites

will begin to drift apart again. Mechanisms employed in this process are necessarily complex in order to provide general 6 dof motion. Typically mechanical receptor mechanisms are used to establish initial contact, though the use of electromagnets has also been considered. Another option is to use Coulomb forces to apply a small force between the two craft to keep them together until the final interlocks are established as illustrated in Figure 4.19. The contact surface must consist of a dielectric material which has sufficient insulator properties while still allowing electrical fields to penetrate. The electrostatic fields take less power to create, and are more far-reaching than magnetic fields. Further, with this approach complex mechanism systems and associated launch mass are avoided.

Chapter 5

Deployment Study of Small Coulomb Craft

Deployment will be defined as moving a spacecraft along a desired path, or imparting onto it a final state by the use of Coulomb forces. Three cases are examined in this section. First, a tutorial two-craft operation is considered. The chief vehicle is assumed to have its own station-keeping propulsion system, while the single deputy is free-flying. The deployment objective is to create a rest-to-rest maneuver of the deputy. The purpose of this study is to illustrate typical voltage levels required, providing some insight into the practicality of repositioning spacecraft using Coulomb forces. Second, a multiple charge chief spacecraft is used to reposition deputies in a near simultaneous maneuver. A charge cycling approach, one of the novel outcomes of this research, is exploited to permit force-decoupled control design of the formation. Third, the multiple charge chief is used to impart a desired final speed onto a deputy spacecraft without regard for the path taken.

5.1 Rest-to-Rest Motion

Consider a chief in a fixed circular orbit about the Earth and a deputy located initially close to the chief. The objective of the maneuver is to reposition the deputy to a specified distance in the Hill frame z direction as shown in Figure 5.1. The dynamic equation of motion in the z direction is

$$m\left(\ddot{z} + n^2 z\right) = k_c \frac{1}{z^2} V_0 V_1 e^{-\frac{z}{\lambda_d}} \qquad (5.1)$$

where m is the deputy's mass, n is the angular velocity of the Hill frame, k_c is Coulomb's constant, d is the distance between the chief and the deputy, λ_d is the Debye length, and V_0 and V_1 are the voltages of the chief and deputy respectively.

A bang-bang time history charge profile is postulated and shown in Figure 5.2. The initial positive product of $V_0 V_1$ causes the deputy to move in the positive z direction. During the second phase of the maneuver, when the charge product is negative, the chief is attempting to arrest the deputy motion. One interpretation of the initial positive charge product is that of an impulse.

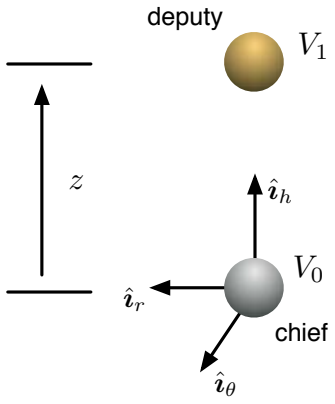

Figure 5.1: Rest-to-rest deployment of a free-flying deputy using a fixed orbit chief.

An optimization process was used to select the voltage product amplitude and switch time such that the deputy craft achieved a desired

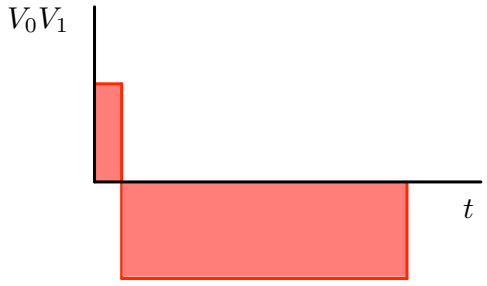

Figure 5.2: Postulated time history of the product of the deputy and chief voltages.

position with zero final speed. The deputy was assumed to be 50kg with a radius of 0.5 meters. It started from rest with its center 1.5 meters from the center of the chief. Without loss of generality, the magnitudes of V_0 and V_1 were assumed equal with their signs the same during the first phase of the maneuver and opposite during the second phase. The charge amplitude, or "Equal Sphere Voltage" is plotted in Figure 5.3 as a function of inverse Debye length for three different final position values and a range of total maneuver times. Although this choice of abscissa seems odd, it yields a linear relationship permitting easy extrapolation for Debye lengths less than 2.5 meters. For easy reference, voltages are given on the right side of the plot corresponding to the log values that were actually graphed. As expected, the voltage increases with maneuver length and decreases with increasing maneuver time. Some interesting observations from this data are

1. There is a nearly linear relationship between the log of the spacecraft voltage and the inverse of Debye length

2. The difference in $\log(V)$ between a fast maneuver (6 hours) and a slow maneuver (24 hours) is nearly invariant with respect to Debye length and total maneuver distance.

3. The rate of voltage increase with Debye length increases with increasing total maneuver distance

4. For the specific example considered, 10kV charging is adequate for up to 30 meter maneuvers.

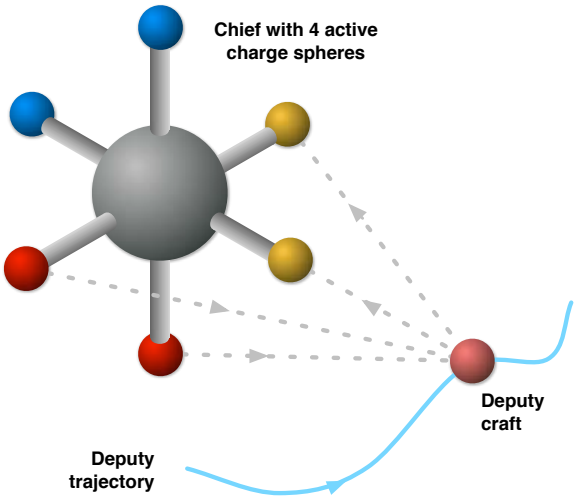

Figure 5.4: Steerable Coulomb force deployment scenario. The chief shown has 6 charge spheres, 4 of which are active.

It should be noted that the data of Figure 5.3 is easily extended to any deputy mass and spacecraft radius. The process requires that the voltages first be normalized to "remove" the mass and radius values used in the example. Next, the new mass and radius must be applied. This is illustrated in Eq. 5.2 where m_{new} and $r_{\text{sc,new}}$ are the deputy radius and mass of interest. A sample calculation is shown in Eq. 5.3 where the new radius is 0.6 meters, the new mass is 20 kilograms and the maneuver of interest is a 10 meter repositioning in 24 hours with a Debye length of 2.5 meters. The possible scenario is a large, inflatable charged spacecraft.

$$V_{1,\text{new}} = \left(V_1 \frac{r_{sc}}{\sqrt{m}}\right) \frac{\sqrt{m_{\text{new}}}}{r_{sc,\text{new}}} \tag{5.2}$$

$$V_{1,\text{new}} = \left(10000 \frac{.5}{\sqrt{50}}\right) \frac{\sqrt{10}}{.6} = 2795.1\text{V} \tag{5.3}$$

5.2 Rest-to-Rest Steered Deployment

The focus of this study is high Earth orbit (HEO) deployment of relatively small deputy

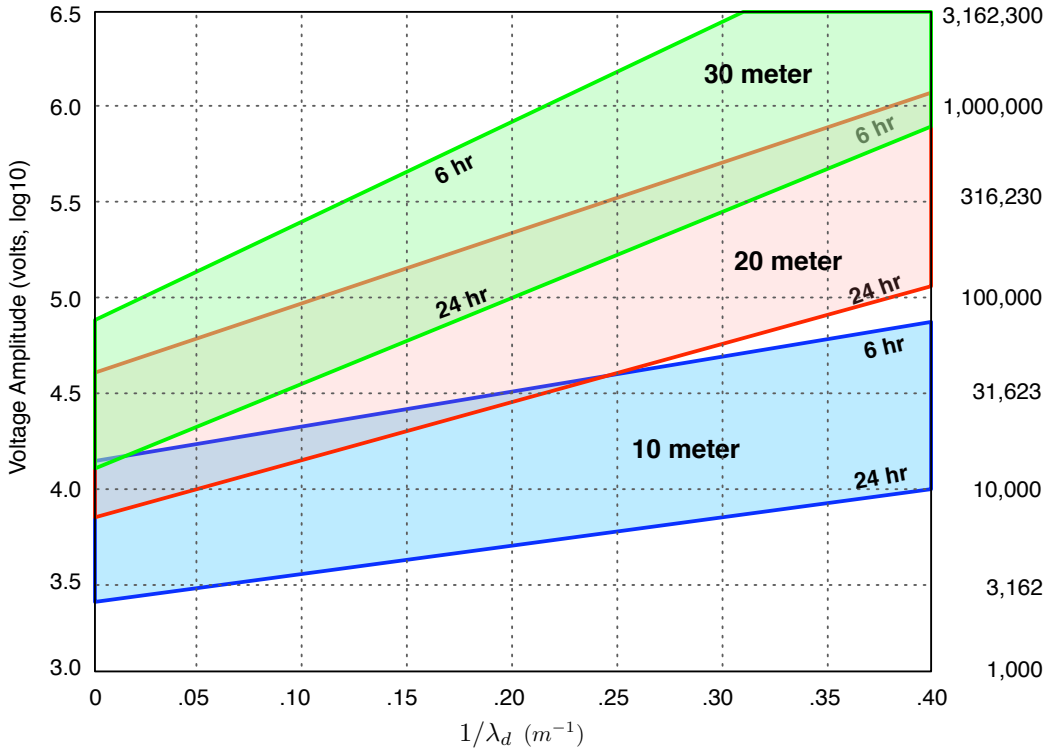

Figure 5.3: Chief and deputy voltage amplitude as a function of Debye length for rest-to-rest maneuvers.

spacecraft using Coulomb forces generated between a chief satellite and the deputies, and is depicted in Figure 5.4. It is assumed that the chief craft has its own conventional propulsion system, and is in a circular orbit about Earth. Furthermore, the chief has several controllable spherical charge surfaces. The deputy craft are assumed to be spherical, with their own controllable charge capability. Deployment consists of simultaneously repositioning the deputies from an initial configuration near the chief to a specified end-shape, typically multiple chief radii's away. During deployment, the deputies react against the chief, exploiting the chief's station keeping capability to generate accurate motions.

5.2.1 Dynamic Model

Consider a system consisting of N_d deputy craft, and a chief containing N_c charge points. The specific case of 3 deputies and 1 charge sphere is shown in Fig. 5.5. The position vectors of the N_d+N_c bodies are ordered such that $\boldsymbol{p}_1$ through $\boldsymbol{p}_{N_d}$ are the deputy vectors and $\boldsymbol{p}_{N_d+1}$ through $\boldsymbol{p}_{N_d+N_c}$ are the charge sphere vectors, all relative to the center of the chief satellite. Each position vector has elements x_i, y_i and z_i. Referring to the example of Fig. 5.5, the 3 deputy craft position vectors are denoted $\boldsymbol{p}_1$ through $\boldsymbol{p}_3$ and the chief's charge sphere position vector is denoted $\boldsymbol{p}_4$. The chief is assumed to be in a circular orbit about the Earth with a Hill coordinate frame at its center as shown in Fig. 5.5. The $\hat{\boldsymbol{\imath}}_r$ unit vector is pointing radially outward from the center of the Earth and the $\hat{\boldsymbol{\imath}}_\theta$ axis is in the direction of the chief's velocity vector. Each of the $N_d + N_c$ bodies is assumed to be have charge q_i.

Applying the Coulomb forces to the right side of Hills Equations, yields the system dynamic equations for small motions about the

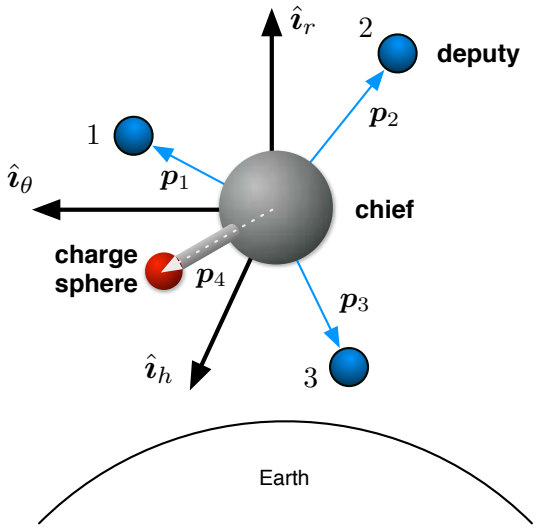

Figure 5.5: Three virtual structure nodes orbiting the Earth illustrating the notation used in the model development.

chief satellite and are shown in (5.4)

$$\ddot{x}_i - 2n\dot{y}_i - 3n^2 x_i = \frac{k_c}{m} \sum_{j=1}^{N_d+N_c} \frac{x_i - x_j}{d_{ij}^3} q_i q_j e^{-\frac{d_{ij}}{\lambda_d}} \tag{5.4a}$$

$$\ddot{y}_i + 2n\dot{x}_i = \frac{k_c}{m} \sum_{j=1}^{N_d+N_c} \frac{y_i - y_j}{d_{ij}^3} q_i q_j e^{-\frac{d_{ij}}{\lambda_d}} \tag{5.4b}$$

$$\ddot{z}_i + n^2 z_i = \frac{k_c}{m} \sum_{j=1}^{N_d+N_c} \frac{z_i - z_j}{d_{ij}^3} q_i q_j e^{-\frac{d_{ij}}{\lambda_d}} \tag{5.4c}$$

for $i = 1 \ldots N_d$, $j \neq i$ during the summation and $d_{ij} = \|\boldsymbol{p}_i - \boldsymbol{p}_j\|$. The Hill frame angular velocity is denoted as n and the mass of each deputy is m. Equation (5.4) is nonlinear and results in a challenging control problem if the goal is to simultaneously move the deputies from initial positions near the chief to final states away from the chief. When all the deputies are charged, the $q_i q_j$ terms limit the ability to create arbitrary force vector directions. Furthermore, as the craft move away from each other and the chief, the Debye length effect exponentially reduces the force capability. It should be noted that the Debye length λ_d can be as little as 10 cm at low altitudes. Therefore, the ability to generate Coulomb forces between craft at large distances is impractical. However, imparting large initial velocities is still quite feasible. At high altitudes, such as geostationary orbit (35,800 km, $n = 7.28 \times 10^{-5}$rad/sec), λ_d varies from 75 m to 575 m. Thus, long-distance positioning capability is possible.

5.2.2 Control Strategy

The movement of one deputy is considered first, followed by the extension to multiple deputies. For the single deputy case, $N_d = 1$, (5.4) becomes

$$\ddot{x}_1 - 2n\dot{y}_1 - 3n^2 x_1 = \frac{k_c}{m} \sum_{j=2}^{1+N_c} \frac{x_1 - x_j}{d_{1j}^3} q_1 q_j e^{-\frac{d_{1j}}{\lambda_d}} \tag{5.5a}$$

$$\ddot{y}_1 + 2n\dot{x}_1 = \frac{k_c}{m} \sum_{j=2}^{1+N_c} \frac{y_1 - y_j}{d_{1j}^3} q_1 q_j e^{-\frac{d_{1j}}{\lambda_d}} \tag{5.5b}$$

$$\ddot{z}_1 + n^2 z_1 = \frac{k_c}{m} \sum_{j=2}^{1+N_c} \frac{z_1 - z_j}{d_{1j}^3} q_1 q_j e^{-\frac{d_{1j}}{\lambda_d}} \tag{5.5c}$$

where $d_{1j} = \|\boldsymbol{p}_1 - \boldsymbol{p}_j\|$. Assume that the charge of the deputy, q_1, is held to some nonzero, constant value and that $N_d = 3$. Next, denote the right sides of each equation in (5.5), specifiable forces, using the variables $f_{d,x}$, $f_{d,y}$, and $f_{d,z}$, or in vector form, $\boldsymbol{f}_d$. As long as the rank of the matrix

$$\boldsymbol{P} = \begin{bmatrix} (\boldsymbol{p}_1 - \boldsymbol{p}_2) & (\boldsymbol{p}_1 - \boldsymbol{p}_3) & \cdots & (\boldsymbol{p}_1 - \boldsymbol{p}_{1+N_d}) \end{bmatrix} \tag{5.6}$$

is 3, then any desired force, $\boldsymbol{f}_d$, can be applied to the deputy. Because it is possible to generate any force vector, it is clear that a suitable control law can now be applied depending on the application (e.g. tracking, regulation, etc.). For example, a simple proportional controller with rate feedback and orbital dynamics cancellation is suitable for moving the deputy from

some initial point to a final point with zero final speed

$$\boldsymbol{f}_d = \begin{bmatrix} -2n\dot{y}_1 - 3n^2 x_1 \\ 2n\dot{x}_1 \\ n^2 z_1 \end{bmatrix} + \boldsymbol{K_p}\left(\boldsymbol{p}_{1d} - \boldsymbol{p}_1\right) - \boldsymbol{K_d}\boldsymbol{v}_1 \tag{5.7}$$

where $\boldsymbol{K_p}$ and $\boldsymbol{K_d}$ are 3×3 diagonal gain matrices, $\boldsymbol{p}_{1d}$ is the desired final position of the deputy, and $\boldsymbol{v}_1$ is the velocity of the deputy.

At this point, it is convenient to rewrite the right side of (5.5) as $\boldsymbol{f}_d = \boldsymbol{B}\boldsymbol{q}$ where the j^{th} column of the $3 \times N_c$ matrix $\boldsymbol{B}$ is

$$\boldsymbol{B}_j = k_c\left(\boldsymbol{p}_1 - \boldsymbol{p}_j\right) \cdot \left(\frac{e^{-\frac{d_{1j}}{\lambda_d}}}{d_{1j}^3} \right) q_1 \tag{5.8}$$

and the $N_d \times 1$ vector of inputs, $\boldsymbol{q}$, is

$$\boldsymbol{q} = \begin{Bmatrix} q_2 \\ q_3 \\ \vdots \\ q_{(1+N_d)} \end{Bmatrix}. \tag{5.9}$$

Some comments on the number of chief charge spheres is in order. If $N_c = 3$, the charge spheres form a plane and defines a singular region where forces orthogonal to the plane cannot be achieved. Thus, a minimum of 4 charge spheres is needed to guarantee complete maneuverability of the deputy. This introduces redundancy in the control law solution. This could be handled by switching between sets of 3 charge spheres, or by utilizing all the charge sphere assets according to some optimization criteria. In this work, a weighted least squares solution is used. Specifically, given the desired force vector to be applied to the deputy, $\boldsymbol{f}_d$, the charge sphere charge values are computed according to

$$\boldsymbol{q} = \boldsymbol{W}^{-1}\boldsymbol{B}^T\left(\boldsymbol{B}\boldsymbol{W}^{-1}\boldsymbol{B}^T\right)^{-1}\boldsymbol{f}_d \tag{5.10}$$

where $\boldsymbol{W}$ is an $N_c \times N_c$ matrix of constants used to focus control authority onto specific charge spheres. The identity matrix is used in the example below.

Extending this method to multiple deputies can be accomplished in several ways. One approach is to move each deputy to its final state sequentially. In some applications, this may be appropriate. However, if the goal is to have all the deputies be at their goal points at the same time, this would not be suitable. The orbital dynamics quickly result in a loss of positioning accuracy once the Coulomb force is removed and the deputies move according to their own Keplerian motion. The method used in this work is to focus control sequentially between the participating deputies. For example, the formation control period, denoted ΔT, would be divided into N_d equal pieces as $\delta T = \Delta T / N_d$. During each δT only 1 deputy is charged, and the solution to (5.10) is formed with a $\boldsymbol{B}$ matrix where the $\boldsymbol{p_1}$ of (5.8) is replaced with i for the i^{th} deputy. It should be noted that from a practical perspective, this assumes that: (1) the deputy charges can be cycled from zero to the maximum value at least 10 times faster than δT, (2) the chief and deputies have a communication protocol that allows the chief to designate which deputy is under control, (3) the chief can measure the deputy position vectors.

5.2.3 Example

Three deputies are considered, $N_d = 3$, and 6 charge spheres, $N_c = 6$. The goal is to move the deputies from their initial locations, near the chief, to a final zero speed state such that they lie on a circle, as viewed from Earth, with a radius of 30 meters. The deputies and charge sphere radii are all 0.5 meters, each with a mass of 50 kg. The initial and final coordinates of the deputies are given in Table 5.1 along with the coordinates of the charge spheres where $L_i = 3/\sqrt{2}$, $L_f = 30$, and $L_c = 2$. The Debye length is assumed to be 100 meters, and the altitude of the chief is 35,800 km (the orbital period is 24 hours). The time that each deputy is being controlled by the chief's charge spheres is $\delta T =$ 5 minutes and the piece-wise constant charge of the deputies is 20,000 volts.

Fig. 5.6 shows the trajectories of all three deputies - blue for $\boldsymbol{p}_1$, green for $\boldsymbol{p}_2$ and red for $\boldsymbol{p}_3$. The hollow circles indicate the initial positions and the filled circles the end points. The charge spheres are not shown. The only care

Table 5.1: Initial and final coordinates of the deputy craft, and the coordinates of the charge spheres.

Position Vector	x (m)	y (m)	z (m)
Initial $\boldsymbol{p}_1$	0	L_i	L_i
Initial $\boldsymbol{p}_2$	0	$-L_i$	$-L_i$
Initial $\boldsymbol{p}_3$	0	$-L_i$	L_i
Final $\boldsymbol{p}_1$	0	$\frac{1}{2}L_f$	$\frac{1}{2\sqrt{3}}L_f$
Final $\boldsymbol{p}_2$	0	0	$-\frac{1}{\sqrt{3}}L_f$
Final $\boldsymbol{p}_3$	0	$-\frac{1}{2}L_f$	$\frac{1}{2\sqrt{3}}L_f$
$\boldsymbol{p}_4$	L_c	0	0
$\boldsymbol{p}_5$	$-L_c$	0	0
$\boldsymbol{p}_6$	0	L_c	0
$\boldsymbol{p}_7$	0	$-L_c$	0
$\boldsymbol{p}_8$	0	0	L_c
$\boldsymbol{p}_9$	0	0	$-L_c$

taken in selecting the initial and end points was to inhibit significant x-axis motion. This was done merely to create an example that could be viewed easily on a two-dimensional plot. As seen in Fig. 5.6 the motion in the x direction is small compared to the y and z motion.

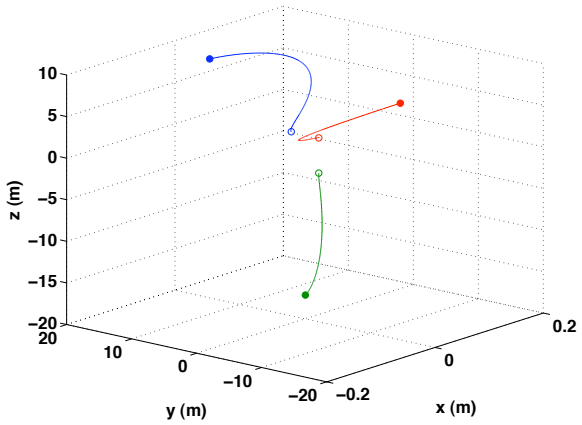

Figure 5.6: Trajectories of all three deputies. The hollow circles are the initial configuration, and the filled circles the final positions.

Fig. 5.7 shows the charge spheres, black circles, and the trajectories of the deputy spacecraft. Again, blue denotes $\boldsymbol{p}_1$, green denotes $\boldsymbol{p}_2$, and red denotes $\boldsymbol{p}_3$. The hollow black sphere at the origin indicates the location of the $\boldsymbol{p}_4$ and $\boldsymbol{p}_5$ charge spheres and are outside the $y-z$ plane. As expected from the control strategy, the motion of the deputies is in a straight line to their respective goals since the desired force vector, $\boldsymbol{f}_d$ is always pointed from the deputy toward its goal. This feature may be useful in the future for path planning.

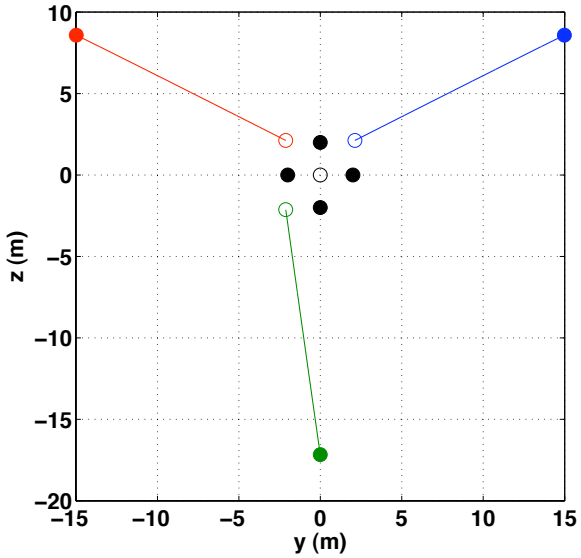

Figure 5.7: Trajectories of all three deputies projected onto the $y-z$ plane. Hollow circles are the initial positions, and the filled circles the final positions.

Fig. 5.8 shows the x, y, and z coordinates for each deputy. The x motion is a dotted line, the y motion a solid line, and the z motion a dashed line in all cases. From this view it is clear that the deputies achieve their final end points in approximately 2 orbits (2 days).

Voltage time histories are shown in Fig. 5.9 and Fig. 5.10. It's clear that the maximum voltage required is approximately 20,000 volts. It should be noted that since the current requirements are extremely small, this requires very little power compared to conventional thrusters. The oscillatory nature of these time histories is due to the switching, every 5 minutes, of the control objective to a different deputy. This is seen more clearly in the "zoomed view" of the $\boldsymbol{p}_4$ charge sphere shown in Fig. 5.11. It should

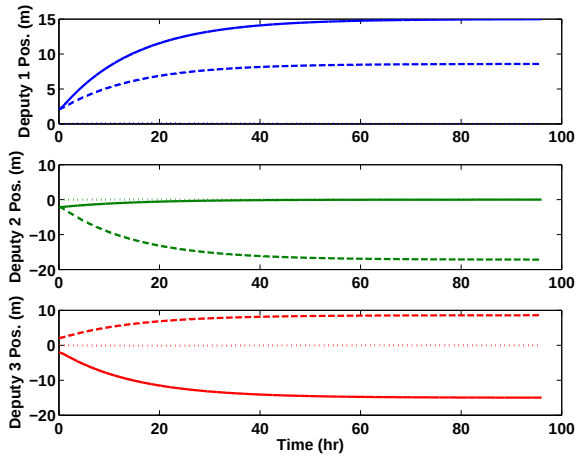

Figure 5.8: Time histories of all three deputies where in each plot the dotted line is the x coordinate, the solid line is the y coordinate, and the dashed line is the z coordinate.

be noted that the steady-state part of Fig. 5.9 and Fig. 5.10, after about 50 hours, is keeping the deputies at the desired fixed positions, constantly working to overcome the orbital forces.

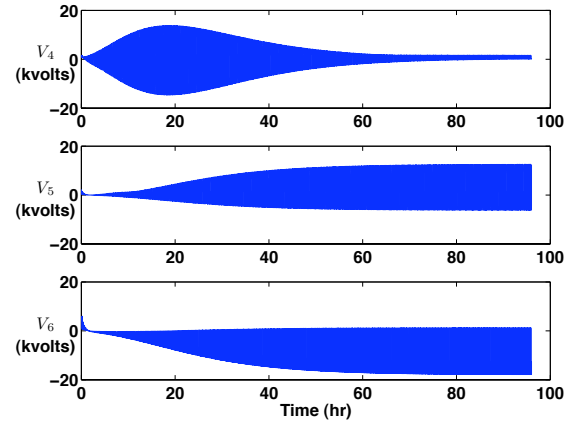

Figure 5.9: Charge sphere voltage time histories for spheres 4,5, and 6.

5.2.4 Rest-to-Rest Deployment Summary

A method was developed for Coulomb control positioning of deputy spacecraft using charged spheres attached to a chief satellite. By focusing on one deputy at a time, a linear control solution was applied to a single deputy. This was extended to simultaneous movement of all the deputies by cycling the charge between deputies. The requirement for the existence of a control solution was given in (5.6). In practice one should plan the trajectories such that the deputies do not need to cross through the volume bounded by the charge spheres. This is not a very restrictive constraint, and means that the deputies should be moving outward from the chief.

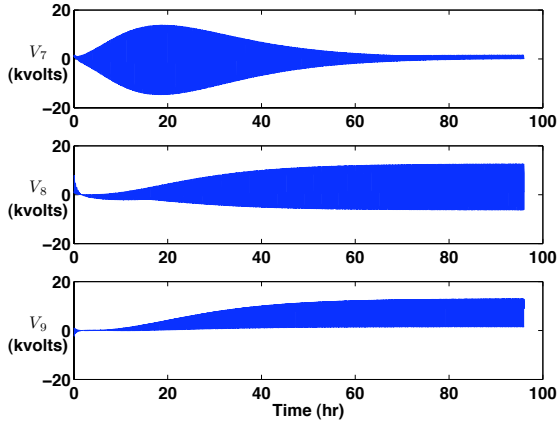

Figure 5.10: Charge sphere voltage time histories for spheres 7,8, and 9.

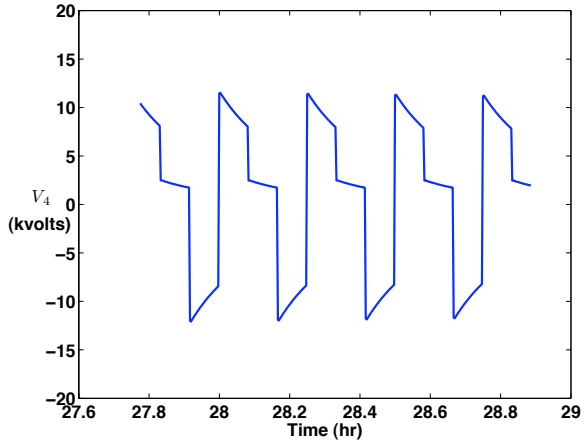

Figure 5.11: Zoomed view of charge sphere 4 showing the control authority switching.

5.3 Final Speed Deployment

The previous section focused on placing deputy craft in arbitrary rest positions using a multiple charge chief. This section is an extension of that concept where the deputy is given a specified speed. The control approach is similar to Eq. 5.7 through Eq. 5.10, with a resulting speed time history having a first order response. A range of possible scenarios could be exploited including moving the deputy to the rear of the chief, then applying the desired final speed command. A simpler case will be illustrated here where the goal it to generate a deputy final velocity having components in all three Hill frame coordinates as shown in Eq. 5.11, at a specified final time, t_f. For $t > t_f$ the charges are set to zero and thus the deputies motion is governed strictly by its Keplerian orbit. The most interesting result of this work is the illustration of the trade-off between the deputy acceleration and final time at which the final speed should be attained.

$$\boldsymbol{v}_{1d} = \frac{v_{1d}}{\sqrt{3}} \begin{Bmatrix} 1 \\ 1 \\ 1 \end{Bmatrix} \tag{5.11}$$

The control law for applying a desired final velocity, $\boldsymbol{v}_{1d}$, is given in Eq. 5.12. In conjunction with the minimum norm solution of Eq. 5.10 for computing charges

$$\boldsymbol{f}_d = \begin{bmatrix} -2n\dot{y}_1 - 3n^2 x_1 \\ 2n\dot{x}_1 \\ n^2 z_1 \end{bmatrix} + \boldsymbol{K_d}\left(\boldsymbol{v}_{1d} - \boldsymbol{v}_1\right) \tag{5.12}$$

Table 5.2 shows the maximum charge, including the deputy and the 6 multiple charge chief, during the $0 < t < t_f$ maneuver for several final speeds and final times. In each case, there exists a minimum value of "Max. Voltage" for each "Final Speed" condition. As the final time is decreased from 1 orbit, the maximum voltage decreases until the minimum (t_f, V_{max}) pair is reached. Increasing the final time beyond this point causes the maximum voltage to increase again. This effect is easily described by shifting dominance between orbital and Coulomb forces as the deputy moves away from the chief. For example, when v_{1d} is 1.0 and t_f is 1.0, the chief must apply large voltages (792V) when $t \approx t_f$ since the deputy has moved far from the chief. Increasing t_f beyond the minimum value of $t_f = 0.5$ again requires large $V_{\max}$ due to the large accelerations required to achieve v_{1d} in a short amount of time.

Table 5.2: Maximum charge as a function of final speed and final time.

Final Speed v_{1d} (m/orbit)	**Final Time** t_f (orbits)	**Max. Voltage** $V_{\max}$ (Volts)
1	1.0	792
1	0.5	621
1	0.25	1,225
1	0.1	1,928
10	1.0	9,644
10	0.5	4,308
10	0.25	3,873
10	0.1	6,099
100	1.0	848,530
100	0.5	232,380
100	0.25	115,760
100	0.1	22,361

This phenomenon can also be interpreted as establishing a limit for deputy final speed as a function of the maximum voltage capability of the crafts. Consider the case where the maximum voltage of either the deputy or the chief's charge spheres is 50kV. In addition, assume that the desired velocity is given by Eq. 5.11, the deputy mass is 50kg, with a radius of 0.5 meters, and is initially 3 meters from the center of the chief. The maximum final speed is then 300 meters/orbit ($\approx$ 3.5 mm/sec), and occurs at roughly 1 hour into the maneuver. Holding that speed longer requires ever increasing voltages due to the dominance of orbital dynam-

ics over Coulomb forces. Likewise, requiring this same speed earlier in the operation requires more voltage due to the increased accelerations needed.

Figure 5.12 shows the first order, closed-loop response of the deputy due to the control law of Eq. 5.12. The shortest time constant possible when limiting the maximum voltage to 50kV was approximately 13 minutes. The 6 chief sphere voltages are shown in Figure 5.13. The transition from Coulomb dominating forces to orbital dynamic forces is clear at approximately 0.6 hours and occurs at a distance of about 10 meters from the chief's charge spheres.

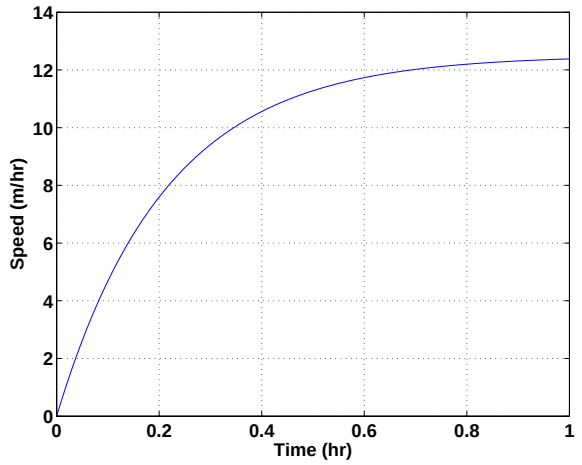

Figure 5.12: Speed time-history where the final speed of 12.5 m/hour (300 m/orbit) is achieved at $t_f = 1$ hour.

In conclusion, final speeds can be readily imparted to the deputy from a multiple charge chief spacecraft. The voltages required are heavily dependent on both the plasma characteristics, and the desired velocity vector. The voltage levels become large if long periods of closed-loop speed control is desired in conjunction with large speed magnitudes that take the deputy far from the Coulomb influence of the chief. These charge levels can be reduced by increasing the number of charge spheres on the chief, at the expense of increased chief complexity, but not an increase in control law complexity.

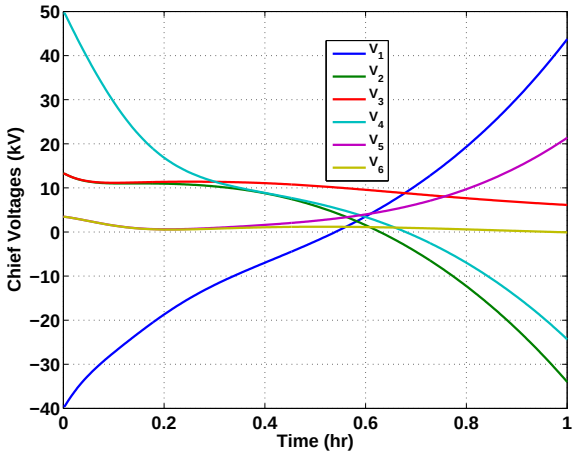

Figure 5.13: Voltages of the chief's charge spheres when applying a final speed to the deputy of 12.5 m/hour at $t_f = 1$ hour.

5.4 3D Spherical Charge Study in Plasma Environment

5.4.1 Motivation

Gauss's law[39,40] states that the net electric flux coming out of a closed surface in a vacuum is directly proportional to the net charge enclosed by the surface. Using this law it can be shown that the electric field at any point outside a uniformly charged conducting sphere (solid or shell) is same as if the net charge were concentrated at the center of the sphere (like a point charge). This concept can be extended while calculating the force between two charged spheres. They can be modeled as point charges at the center of each sphere provided the separation distance between the sphere centers is larger than the sum of the sphere radii. At very small separation distances the surface charge distribution will not be even due to the induced charge effects and the point charge model will not hold.

The behavior of the charge particle is significantly different in a plasma environment compared to vacuum. If a test point charge (positive) is placed in a uniform plasma environment, it will attract electrons and repel the positive

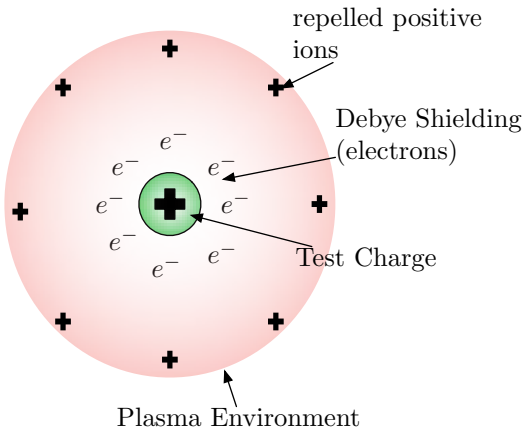

Figure 5.14: Figure illustrates the Debye Shielding.

ions in the plasma. This results in the the electrons gathering around the positive test charge, which will create a shielding cloud that cancels the effect of the test charge. Thus the electric field strength decays much faster in plasma environment than in vacuum. This phenomenon is called Debye shielding[41,42] and is illustrated in Figure 5.14. In Reference 41 and 42, an expression for the electric field E of a point charge in a plasma is given and a new parameter called the length Debye length λ_d is introduced.

$$E = k_c \frac{q}{d^2} e^{-d/\lambda_d} \tag{5.13}$$

At separation distances d that are greater than the Debye length λ_d the electric field or potential decays exponentially and at separation distances d that are much smaller than the Debye length the electric field is very close to the point charge field in vacuum.

In MEO (Medium Earth orbit) and LEO (Low Earth orbit), the Debye lengths are very small (on the order of a few millimeters to centimeters) and one possible application of Coulomb force is the docking of two satellites. Here the surface-to-surface separation distances can become very small, while the center-to-center separation distances remain relatively large. The point charge model of 3D spheres is only an approximation if the craft are in a plasma environment with Debye shielding present. This section will study how large the electrostatic force magnitude model errors are if the point charge model is used instead of the three-dimensional charge distribution. As the separation distances are increased, it is anticipated that the point charge models will become increasingly accurate. However, what if tow 0.5 meter radius spherical spacecraft are only 0.2 meters apart, and the Debye length is 0.1 meters? Will the point charge model over- or under-estimate the resulting electrostatic force magnitude?

The craft are modeled as two spheres. We study the Coulomb force between these two spheres in close quarters in a plasma environment. The spheres are hollow shells with a large charge surface area (similar to the Gluon craft concept) and are porous such that the plasma can seep into it. Thus, the environment inside and outside the spheres is the same. However, the charged surface section which are the closest to each other might have a greater interaction than the charged surface sections which are on the opposite sides of the spheres. This is due to the fact that the effectiveness of the charge on the surfaces that are further away will be reduced because of Debye shielding. Hence, point charge modeling of spheres based on Gauss's law will not give the accurate Coulomb force acting between the spheres that are in plasma environment. It should be noted that this problem is not very acute when the Debye lengths are very large or when the separation distance between the spheres is large.

5.4.2 3D Spacecraft Modeling

In this study we have discretized the surface of the spheres into small elemental areas and the elemental charges in these areas are considered to be point charges. The resultant Coulomb force between the two spheres are found by adding, vectorially, the forces due each elemental charge that make up the spheres. While calculating the forces due to the elemental charges the effect of Debye shielding is taken into account. The net force obtained from the dis-

cretized model is compared with that of the the point charge model and situations in which point charge model will fail are identified. Two spheres in close quarters might introduce induced charge separation within the sphere surface. For instance, a positively charged sphere will attract more electrons in the other sphere to move to the surface facing the positively charged sphere as shown in Figure 5.15. This induced charging results in a nonuniform surface charge distribution and coupled with the Debye shielding effects can drastically change the net effective Coulomb force. But, for the scope of this study, we are neglecting this induced charge effect and assume the spheres to have a uniform surface charge density. This allows us to quantify the effect of the Debye shielding on three-dimensional spheres and determine how valid the point charge models are for small separation distances.

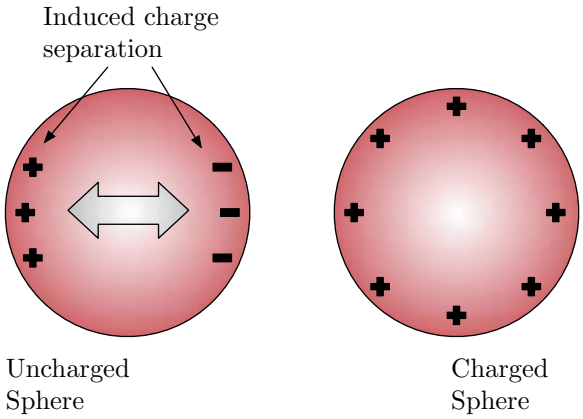

Figure 5.15: Figure illustrates the induced charge in a neutral sphere in the vicinity of a charged sphere.

To model the homogeneously charged surface, the sphere is discretized into a finite number of polygons. Consider a small elemental area as shown in Figure 5.16 on the surface of a sphere of radius r. The polar coordinates of the elemental area are given by the radius r and angles ψ and θ. The expression for the area of this element is given by

$$\mathrm{d}A = r\cos(\psi)\mathrm{d}\theta\mathrm{d}\psi \tag{5.14}$$

Let the charge density on the surface of the sphere be σ, then the elemental charge $\mathrm{d}q$ on the elemental surface area $\mathrm{d}A$ can be written as

$$\mathrm{d}q = \sigma\mathrm{d}A = \sigma r\cos(\psi)\mathrm{d}\theta\mathrm{d}\psi \tag{5.15}$$

Rewriting Eq. (5.15) in terms of the total charge q carried by the sphere, we get

$$\mathrm{d}q = \frac{q}{4\pi r^2} r\cos(\psi)\mathrm{d}\theta\mathrm{d}\psi \tag{5.16}$$

This elemental charge dq can be considered as a point charge and its position in terms of the cartesian coordinates (with origin at the center of the sphere) can be written as

$$\boldsymbol{\rho} = \begin{pmatrix} x \\ y \\ z \end{pmatrix} = \begin{pmatrix} r\cos(\psi)\cos(\theta) \\ r\cos(\psi)\sin(\theta) \\ r\sin(\psi) \end{pmatrix} \tag{5.17}$$

Similarly, by varying the polar angles ψ and θ from -90^{o}–90^{o} and 0^{o}–360^{o}, respectively, all the discretized elemental charges and their position can be identified.

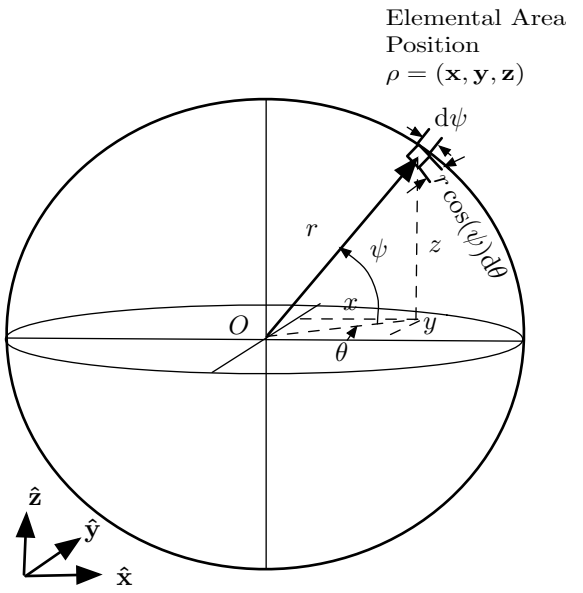

Figure 5.16: A simple spherical surface with the illustration of an elemental surface.

Now, let us consider two such discretized spheres with n elemental areas in each. The net Coulomb force acting between the spheres

is the vector sum of the interaction of each individual elemental charge. The Coulomb force using the discretized model can be written as

$$\boldsymbol{F} = \sum_{i=1}^{n}\sum_{j=1}^{n} k_c \frac{\mathrm{d}q_i \mathrm{d}q_j}{|\boldsymbol{\rho}_j - \boldsymbol{\rho}_i|^3}(\boldsymbol{\rho}_j - \boldsymbol{\rho}_i) \qquad (5.18)$$

where k_c is the Coulomb constant, $\mathrm{d}q_i$ and $\boldsymbol{\rho}_i$ are the i^{th} elemental charge and its cartesian position vector on sphere one, and similarly, $\mathrm{d}q_j$ and $\boldsymbol{\rho}_j$ are the j^{th} elemental charge and its cartesian position vector on sphere two.

The force between two spheres based on the point charge model is given by

$$\boldsymbol{F} = k_c \frac{q_1 q_2}{d^2} \qquad (5.19)$$

where q_1 and q_2 are the respective total charges on sphere 1 and 2, and d is the center to center separation distance.

In order to establish acceptable mesh size (i.e. $\mathrm{d}\psi$ and $\mathrm{d}\theta$ values), the Coulomb force between two test spheres based on the discretized model is calculated for various $\mathrm{d}\psi$ and $\mathrm{d}\theta$ values. Recall that when operating in a vacuum (i.e. neglecting plasma effect) and when the induced charge redistribution effects are neglected, the point charge model of the sphere holds perfectly. Hence, the force calculated from the discretized model is compared with the point charge model and the percentage error is plotted for various $\mathrm{d}\psi$ and $\mathrm{d}\theta$ values as shown in Figure 5.17. A $\mathrm{d}\psi$ and $\mathrm{d}\theta$ value that resulted in a percentage error of less than 1% is an acceptable discretization level. Studying Figure 5.17 the $\mathrm{d}\psi$ and $\mathrm{d}\theta$ values are chosen as 10^{o} or 0.17 radians which results in a percentage discretization error of 0.46% (well with in 1%).

5.4.3 Discretized Model in Plasma Environment

The Coulomb force experienced by a test charge $\mathrm{d}q$ which is at a distance d from a point charge q in a plasma environment is given by

$$\boldsymbol{F} = k_c \frac{q\ \mathrm{d}q}{d^2} e^{\frac{-d}{\lambda_d}} \qquad (5.20)$$

where λ_d is the Debye length. It can be inferred from Eq. (5.20) that as the separation distance d increases the Coulomb force exponentially decays, and the decay is more severe when d is greater than the Debye Length λ_d.

A charged sphere in a plasma environment modeled as an equivalent point charge at the center of the sphere might not give accurate results depending on the spacecraft radii, separation distances, and the Debye length value. At small Debye lengths, the charge on the surface sections that are facing each other might have separation distances smaller than the Debye length. This yields a greater interaction than the charge on the opposite surface sections of the spheres because their attraction/repulsion might be masked due the Debye shielding level. In this study we have modeled the spheres as porous shells and assumed that the plasma can seep through. This assumption might lead us to believe that the point charge approximations will be well with in acceptable limits. This is not the case for all situations. When the separation distances are comparable to the radius of the spheres and at Debye lengths that are less than the separation distances, then the Coulomb force computed by replacing the spheres with equivalent point charges at the center would have acutely decayed. But, in reality the charges on the surface of the sphere that are closest to each other might be well with in the Debye length and their interaction might result in a net Coulomb force that is significantly higher than the force calculated using the point charge model. Thus, our main aim of this study is to identify those regions of separation distance and Debye lengths where the point charge model fails and discretized surface model should be used instead.

The Coulomb force between two spheres in plasma environment is given using the discretized model as

$$\boldsymbol{F}_d = \sum_{i=1}^{n}\sum_{j=1}^{n} k_c \frac{\mathrm{d}q_i \mathrm{d}q_j}{|\boldsymbol{\rho}_j - \boldsymbol{\rho}_i|^3}(\boldsymbol{\rho}_j - \boldsymbol{\rho}_i) e^{\frac{-|\boldsymbol{\rho}_j - \boldsymbol{\rho}_i|}{\lambda_d}} \qquad (5.21)$$

where the definition of $\mathrm{d}q_i$, $\boldsymbol{\rho}_i$, $\mathrm{d}q_j$ and $\boldsymbol{\rho}_j$ are

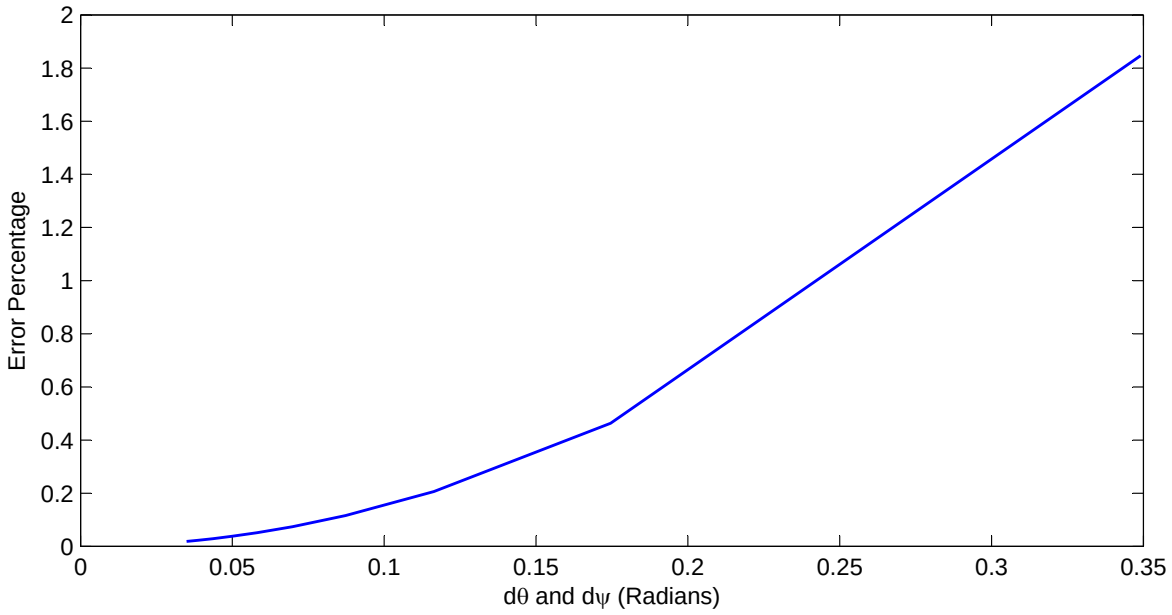

Figure 5.17: Graph showing the percentage error in the Coulomb force calculated using the point charge model and the discretized surface model for two spheres for different discretization mesh size.

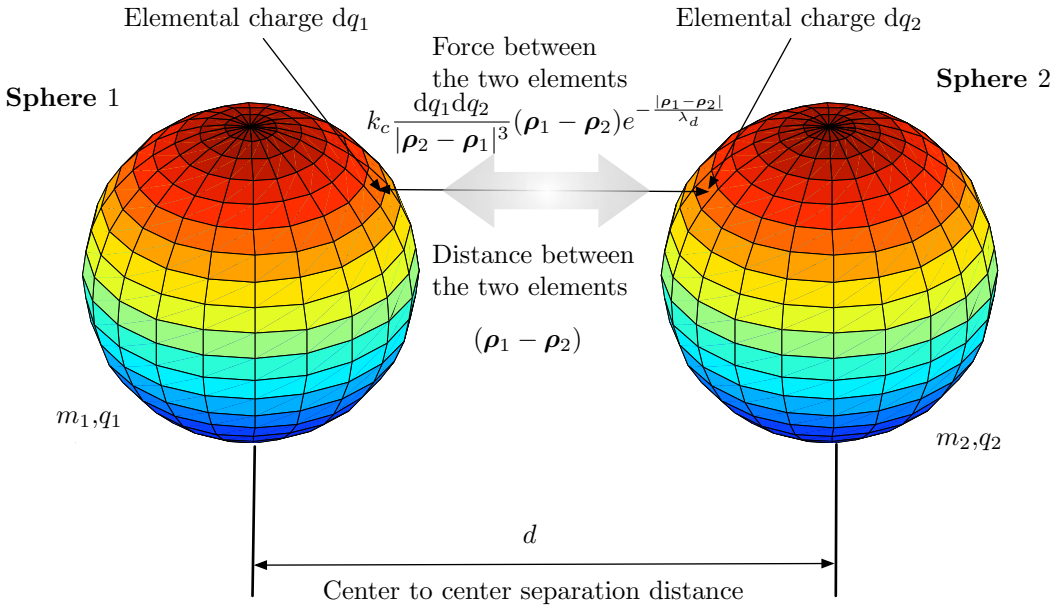

Figure 5.18: Figure illustrates two spheres with discretized surfaces resulting in discretized surface charges and their interaction.

the same as in Eq. (5.18). This process is illustrated in Figure 5.18. The force between two spheres in a plasma environment is based on the point charge model is given by

$$\boldsymbol{F}_p = k_c \frac{q_1 q_2}{d^2} e^{\frac{-d}{\lambda_d}} \tag{5.22}$$

where q_1 and q_2 are the respective total charges on sphere 1 and 2, and d is the center to center separation distance. The percentage error between the two methods is calculated as

$$\text{Error} = \frac{|\boldsymbol{F}_p - \boldsymbol{F}_d|}{|\boldsymbol{F}_p|} 100\% \tag{5.23}$$

The Coulomb force computed using the point charge model and the discretized model are calculated for various combinations of radii-separation distances ratios and separation distance to Debye length ratios. For each case the percentage error is calculated. Figure 5.19 shows the contour plots for the percentage error in the Coulomb force calculated using the point charge model and the discretized surface model for two spheres under plasma screening.

In Figure 5.19(a), the separation distance-Debye length ratio ($\frac{d}{\lambda_d}$) is varied from 0.1 to 1. It can be observed from this plot that at high separation distance-radius ratio ($\frac{d}{r}$), the difference between the point charge model and discretized model is insignificant even when the Debye lengths are comparable to the separation distance (i.e. at high $\frac{d}{\lambda_d}$ ratios). There is considerable difference when separation distance-Debye length ratio ($\frac{d}{\lambda_d}$) is low and the Debye lengths are comparable to the separation distance, and in this region the Coulomb force due to the discretized model is higher than the point charge model. This phenomenon is further illustrated in Figure 5.19(b) in which the separation distance-Debye length ratio ($\frac{d}{\lambda_d}$) varies from 0.1 to 5. At separation distances which are much greater than the Debye lengths and at low separation distance-radius ratios ($\frac{d}{r}$) the difference between the models is more than 100%.

From this study it can be concluded that for two sphere that are in plasma the environment the difference between the force calculated using the point charge model and discretized model is negligible, provided the separation distances are large compared to the radius of the sphere and the Debye length is very large compared to the separation distance. The point charge model only fails at separation distances that are close to the radius of the sphere and when the Debye lengths are comparable to or greater than the separation distance. In these situations the point charge model *severely overestimates the influence of the plasma shielding.* Using our old example of 2 craft with 0.5 meter radii, assume the surfaces are only 0.1 meters apart and that the Debye length is 0.2 meters. The point charge model assumes that the equivalent point charges have a separation distance of 1.1 meters, which is over 5 times the Debye length distance. Thus, the point charge model predicts that there would be essentially no electrostatic force between the two spheres. However, because small surface sections are only 0.1 meters apart, which is half the Debye length, the 3D spheres would actually experience a much larger force than predicted by the point charge model.

Note that this 3D effect of the charged surface drops off quickly with the separation distance. It is encouraging that the actual forces are larger than originally anticipated. Future work will need to investigate the induced charging effect. The induced redistribution of charge can be calculated by solving the Maxwell's equation with appropriate boundary conditions. This new surface charge distribution can be used to find a more accurate Coulomb force between two spheres.

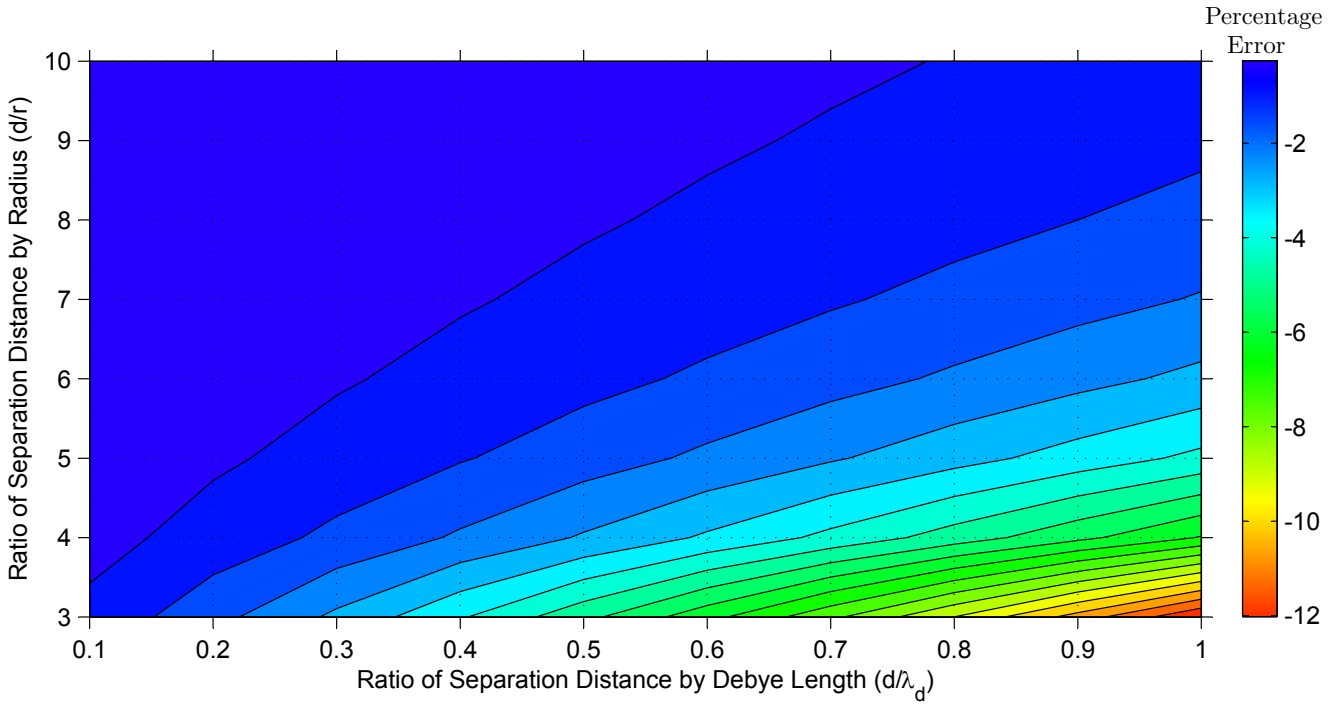

(a) Separation distance by Debye length ratio varies from 0.1 to 1

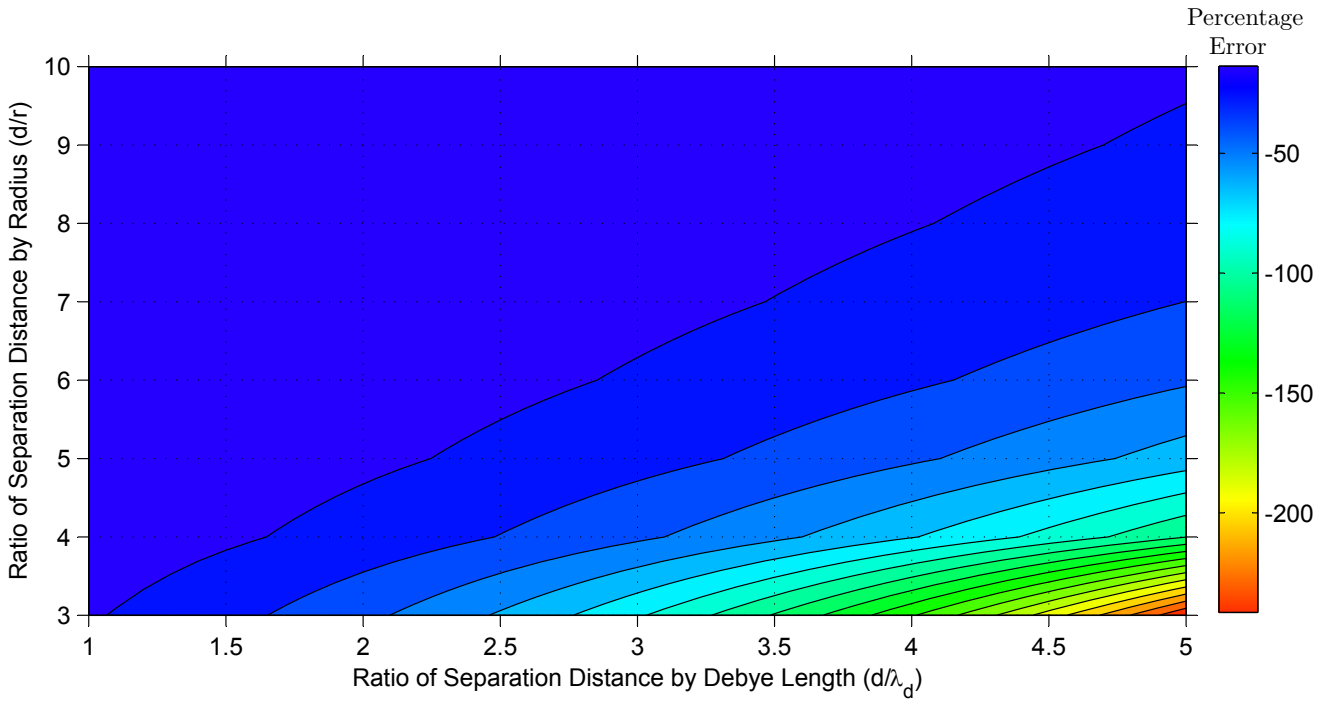

(b) Separation distance by Debye length ratio varies from 1 to 5

Figure 5.19: Contour plots showing the percentage error in the Coulomb force calculated using the point charge model and the discretized surface model for two spheres under plasma screening.

Chapter 6

Reconfiguration Time Study of Coulomb Craft

The study of electrostatic charging data of the SCATHA spacecraft[6] verified that spacecraft can charge to very high voltages in low plasma environments such as GEO. The associated electric power requirement is typically less than 1 Watt. The charged spacecraft can produce electrostatic Coulomb forces which can be used to increase or decrease the relative distance between the two craft. Henceforth, this kind of reconfiguration using Coulomb forces is referred to as Coulomb reconfiguration. This novel propellantless reconfiguration concept has many advantages over conventional thrusters like ion engines. Coulomb propulsion effectively uses no consumables and is also a very clean method of propulsion compared to ion engines, thereby avoiding the thruster plume contamination issue with neighboring crafts.

However, this Coulomb reconfiguration also has its own set of limitations. The Coulomb electrostatic force magnitude is inversely proportional to the square of the separation distance. Additionally, the Coulomb force effectiveness is diminished in a space plasma environment due to the presence of charged plasma particles. The electric field strength drops off exponentially with increasing separation distance. The severity of this drop off is characterized with the Debye length.[41,42] For low earth orbits (LEO), the Debye length is of the order of millimeters to centimeters, making the Coulomb reconfiguration concept impractical at these low orbit altitudes. At geostationary orbit (GEO) altitudes or higher, which has a hotter and less dense plasma environment, the Debye length can vary between 100-1000 meters depending on the solar activity cycles. The Coulomb reconfiguration concept appears to be feasible at this altitude.

6.1 Inertial Space Reconfiguration Study

In this section, we study the feasibility and the charge requirements for Coulomb reconfiguration. The craft are assumed to be in free-space (inertial-space) and the orbital mechanics effects are neglected. Assume first that the craft are reconfigured using a conventional thrusters, and that the craft have a maximum acceleration that they can experience. The classical fuel-optimality solution dictates that a bang-bang control strategy be used. Here the craft is accelerated for half the maneuver time with a positive constant acceleration, and decelerated with the negative constant maximum acceleration.

A similar bang-bang-type of control is proposed for the charged reconfiguration. We still assume the craft are at rest to begin with, and require them to be at rest at the end of the maneuver. Initially, the crafts are given a fixed charge of same polarity. This causes them to accelerate away from each other. After a fixed time the polarity of one craft is reversed. The resulting attraction between the craft decelerates their motion and brings them to a com-

plete stop at the required separation distance. Assume a craft can only be charged up to a maximum charge level $q_{\max}$. Then, to reach a new separation distance d as quickly as possible, we need to accelerate and decelerate the craft as quickly as possible. However, compared to the classical bang-bang solution with reverses the direction of the constant thrust half-way through the maneuver, the constant charge control will cause a time varying acceleration to act on the craft. The further apart the craft become, the smaller the resulting breaking force will be. This causes the switching time to not be at the maneuver half way point, but earlier.

The goal of the study is study a series of rest-to-test charged spacecraft maneuvers. The desired final separation distances, and the maneuver times, are swept over a finite range. For each setup we determine the constant charge magnitude and the switch time at which the polarity has to be reversed. Two scenarios, one with 2 craft of equal masses and the other with a Gluon-Deputy arrangement are studied. The effects of Debye lengths are included as well .

6.1.1 Free-Space Reconfiguration Dynamics

Consider a two satellite arrangement as shown in Figure 6.1. Let the origin be located at the center of mass. The distance of craft 1 and craft 2 from the origin are x_1 and x_2, respectively. The separation distance between the two craft is d, given by

$$d = x_1 - x_2 \tag{6.1}$$

Since the origin is located at the center of mass, the center of mass condition dictates that

$$m_1 x_1 + m_2 x_2 = 0 \tag{6.2}$$

Therefore, once we know the motion of one craft, the motion of the other craft can be determined using the above condition. From Eq. (6.1) and Eq. (6.2), the position of the craft 1 can be written as

$$x_1 = d\left(1 + \frac{m_1}{m_2}\right)^{-1} \tag{6.3}$$

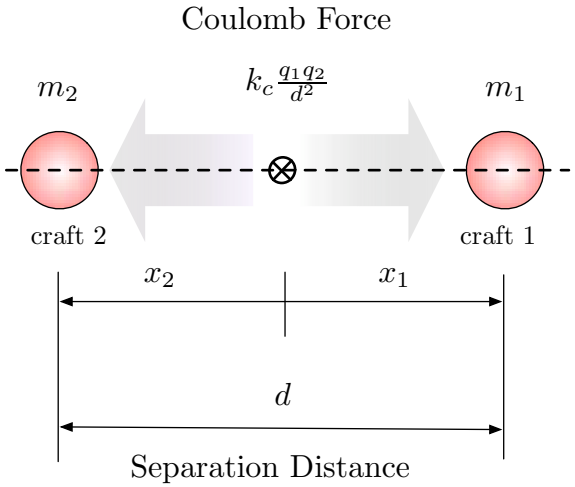

Figure 6.1: Figure illustrating the 2 craft arrangement.

The two craft are assumed to be in free space and no other external force is acting on the formation. The initial internal forces acting on the deputy are the gravitational force and Coulomb force. The former is given by the formula

$$F_g = G\frac{m_1 m_2}{d^2} \tag{6.4}$$

where G is the universal gravity constant and, m_1 and m_2 are the mass of craft 1 and craft 2, respectively. The Coulomb force is given by

$$F_c = k_c \frac{q_1 q_2}{d^2} \tag{6.5}$$

where k_c is the Coulomb constant and, q_1 and q_2 are the charges of craft 1 and craft 2, respectively. The force expression in Eq. (6.5) can be rewritten using the voltages produced due to the charges as

$$F_c = \frac{r_1 r_2}{k_c}\frac{V_1 V_2}{d^2} e^{\left(\frac{-d}{\lambda_d}\right)} \tag{6.6}$$

where V_1 and r_1 are the voltage and radius of craft 1 and, V_2 and r_2 denote the same for craft 2. The exponential decay term is due to the Debye shielding where λ_d is the Debye Length.

Using Newton's second law, the equation of motion of craft 1 (m_1) is written as

$$m_1 \ddot{x}_1 = -G\frac{m_1 m_2}{d^2} + \frac{r_1 r_2}{k_c}\frac{V_1 V_2}{d^2} e^{\left(\frac{-d}{\lambda_d}\right)} \tag{6.7}$$

Using Eq. (6.3), separation distance d in Eq. (6.7) can be substituted with an expression in terms of x_1. The Gravitational force acting on the satellites is very small compared to the Coulomb forces (with kV voltages and higher), such that the equation of motion of craft 1 (m_1) is simplified to

$$m_1\ddot{x}_1 = \frac{r_1 r_2}{k_c}\frac{V_1 V_2}{x_1^2\left(1+\frac{m_1}{m_2}\right)^2}e^{\left(\frac{-x_1\left(1+\frac{m_1}{m_2}\right)}{\lambda_d}\right)} \quad (6.8)$$

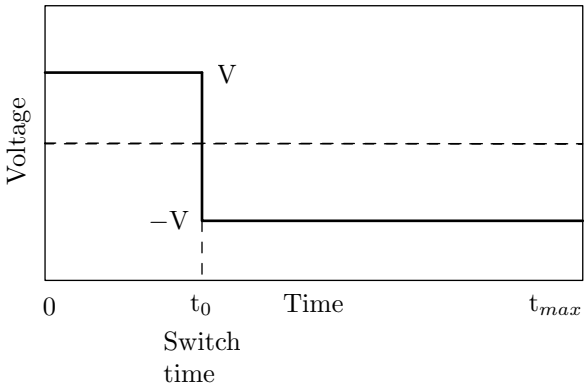

Figure 6.2: Schematic representation of the bang-bang charging.

6.1.2 Bang-Bang Charging

The main idea behind bang-bang charging is to use a fixed common voltage for accelerating the craft and reversing the polarity of one craft after some time to decelerate both craft. Figure 6.2 shows a schematic representation of this kind of charging. Here the voltage is maintained at a constant value V until it reaches the switching time t_0, and after that the voltage polarity is reversed.

$$\text{Voltage} = \begin{cases} V & 0 < t \leq t_0 \\ -V & t_0 < t < t_{\max} \end{cases} \quad (6.9)$$

For a given final separation distance $\bar{d}$ and time ($t_{\max}$) for achieving this distance, a unique voltage V and switch time t_0 can be determined. Given this maximum craft voltage V the distance $\bar{d}$ is the largest separation that can be achieved given the maneuver time $t_{\max}$.

Our aim is to generate contour plots of the voltages required to carry out these bang-bang maneuvers for different final separation distances and maneuver times. Figure 6.3 gives the schematic representation of the homotopies used in generating the contour plots. Initially, for small change in separation distance and a small maneuver time, we use an initial guess along with the shooting method to find the optimal switch time and the constant voltage magnitude. Using this result, the first set of homotopies are carried across the maneuver time, while keeping the separation distance constant. It should be noted that the homotopy just means using the converged results in the previous case as the initial guess for the current problem, while a shooting method is then used to converge to the new optimal answer. The other homotopies are performed across the final separation distance using the results of the first set of homotopies as initial conditions.

The numerical two-point boundary value problem solution is started with an initial guess, and then uses a shooting method to converge to a unique solution. For small changes in separation distances the $1/d^2$ drop off in the force magnitude is not that significant. This allows us to approximate the switching time with the constant acceleration special where where

$$t_0 = \frac{t_{\max}}{2} \quad (6.10)$$

Let $\bar{d}$ be the final desired separation and $\bar{x}_1$ correspond to the position of mass m_1 at this separation distance. Then the initial guess for the product of voltages is given by

$$V_1 V_2 = 2(\bar{x}_1 - x_1)t_{\max}^2 \frac{k_c \bar{d}^2}{r_1 r_2 e^{\left(\frac{-\bar{d}}{\lambda_d}\right)}} \quad (6.11)$$

This voltage product is computed assuming that the corresponding craft accelerations are constant. The actual accelerations will naturally decay with the inverse square of the separation distance. However, this approximation works well small small initial separation distances.

From Eq. (6.8), it is clear that we have a $1/d^2$ type of decay for the force acting between the

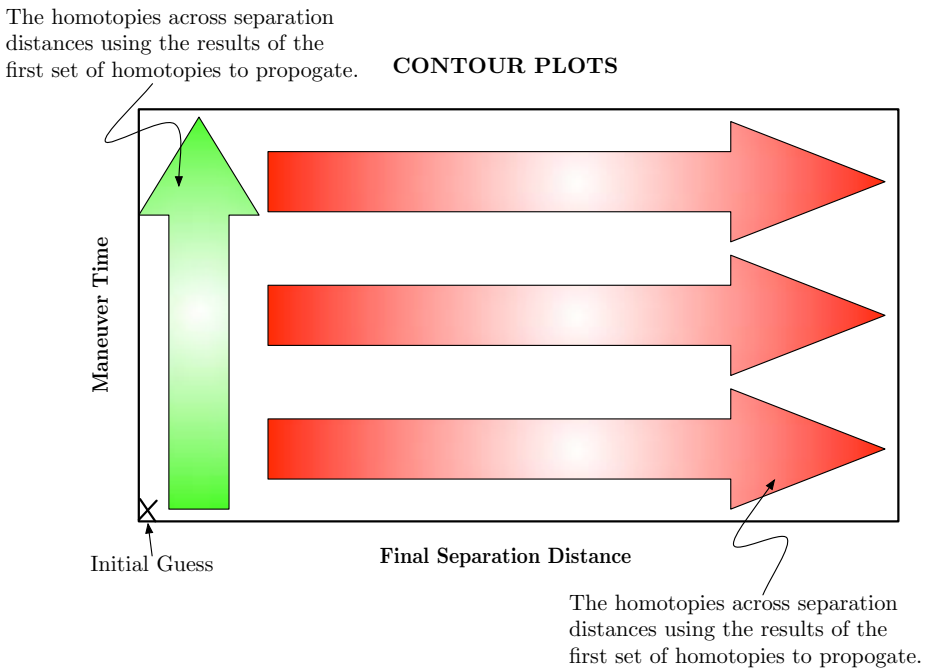

Figure 6.3: Schematic representation of the homotopies used in generating the contour plots.

craft as the separation distance increases. In addition to this, there is also an exponential decay term due to the Debye shielding effect. Due to these reasons, the initial conditions in Eq. (6.10) and Eq. (6.11) will not work well for maneuvers with large transfer distances. In order to overcome this difficulty the method of homotopy is used. In this method the distances are increased in small incremental steps and the converged solution (using shooting method) for the previous step is used as the current initial guess. By choosing small enough changes in $\bar{d}$ or $t_{\max}$, the previous solution is still a good guess for the next numerical search. The otherwise very sensitive and difficult to converge two-point boundary value problem is thus sufficiently desensitized.

Figure 6.4 illustrates the bang-bang charging process for sample maneuvers where the separation distance between two craft of equal masses is increased from 2 m to 3 m. Figures 6.4(a), 6.4(b) and 6.4(c), illustrate the voltage, coulomb force experienced and the position time histories of mass m_1. It can be seen from theses figures that as the total maneuver time is increased from 0.1 day to 1 day, the voltage required falls rapidly and the switch time increases. In all cases the craft perform a rest-to-rest maneuver ending with $x_1 = 1.5$ m, and $\dot{x}_1 = 0$ m/s. Further, note the nonlinear Coulomb force time histories in Figure 6.4(b). As the separation distance d increases, the force applied to craft 1 diminishes.

6.1.3 Simulation Results

The simulations are carried out for two different scenarios. In the first one, the two craft are of equal mass and size. In the second scenario the gluon-deputy arrangement is used. Here the gluon is much heavier and larger in size than the deputy craft. Due to its huge mass the distance moved by the gluon will be very small and we can consider it to be stationary. In this case, the total separation distance will be roughly equal to the distance moved by deputy. Where as in the equal mass case the two crafts will move equal distance and the total separation distance

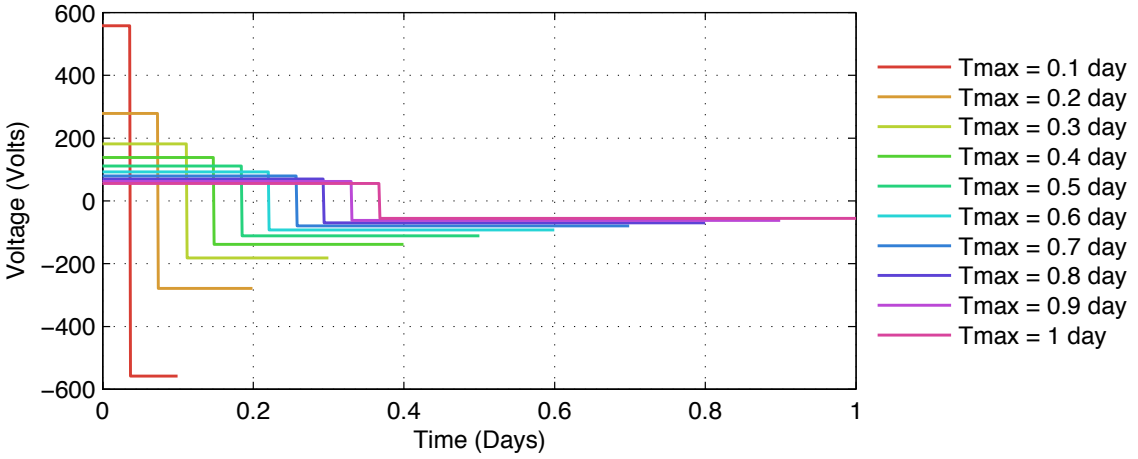

(a) Voltage time histories

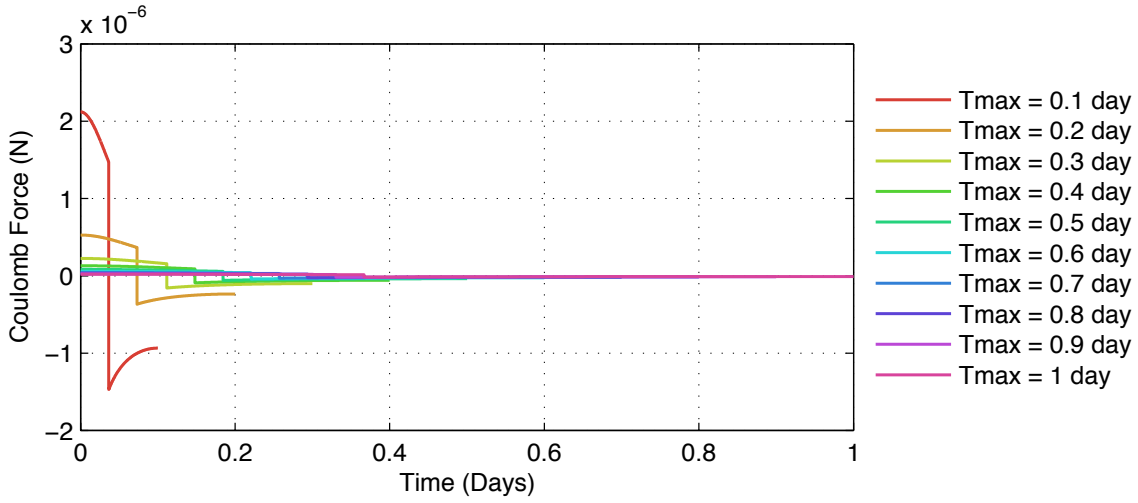

(b) Coulomb force time histories

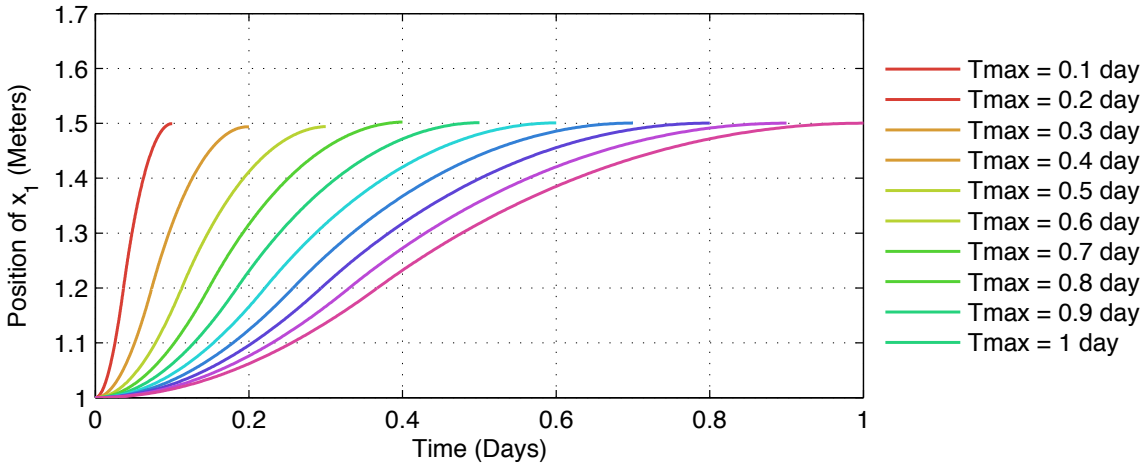

(c) Time histories of the position of mass m_1

Figure 6.4: Graphs illustrate the bang-bang charging process. Increasing the separation between two satellites of equal masses from 2 m to 3 m in different maneuver time.

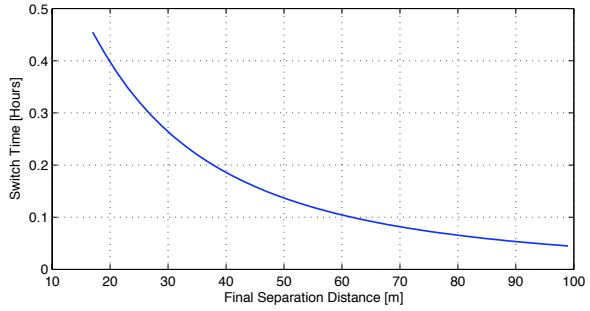

(a) Switch Time Vs Separation Distance

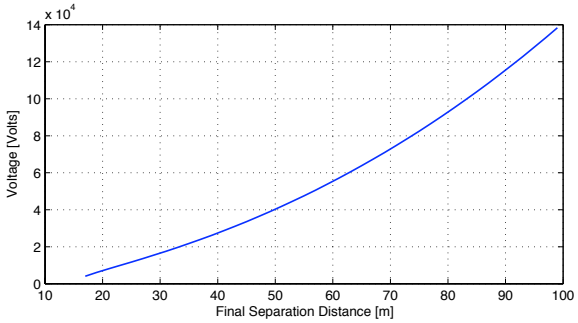

(b) Voltage Vs Separation Distance

Figure 6.5: Graphs illustrates how the switch time and voltage required varies as the separation distance is increased from 15 m to various amounts. These voltages and switch time correspond to the gluon-deputy arrangement with a constant maneuver time of 1.0 hour.

will be twice the distance moved by any one on the craft. The various input parameters are given in Table 6.1.

In order to get a feel for how the voltage and switch time vary across the separation distance for a fixed maneuver time, let us study the numerical simulation results illustrated in the Figure 6.5. For a fixed maneuver time of 1 hour the Figures 6.5(a) and 6.5(b) give the switch time t_0 and voltage V, respectively, for the gluon-deputy arrangement to increase their separation distance from 15 m to various amounts. Observe that the increase in voltage with increase in separation distance is essentially quadratic, whereas the switch time t_0 decreases exponentially with increasing separation distances. This exponential decrease is due to the $1/r^2$ term in the Coulomb force and without this term the switch time would have been exactly half the

Table 6.1: Input Parameters Used in Simulation

Parameter	Equal Mass Crafts	Gluon-Deputy Crafts
Craft 2 Mass, m_1	50 kg	50 kg
Craft 2 Mass, m_2	50 kg	1000 kg
Craft 1 Radius, r_1	0.5 m	0.5 m
Craft 2 Radius, r_2	0.5 m	10 m
Initial Separation distance, d	2 m	15 m

total maneuver time. We can also observe in Figures 6.5(a) that for very small separation distances the switch time approaches 0.5 hours which is half of the 1.0 hour maneuver time. As the final separation distance increases the switch time approaches zero (i.e. the initial voltage becomes a pulse).

Figure 6.6 shows the contour plots of the voltage required to increase the separation distance between two craft to several meters with different maneuver times. The craft have equal mass and the initial separation distance is always 2 m. The contour plots have been evaluated for two different Debye lengths of 100 m and 50 m. The white patches in the contour plots represent regions where we are unable to find a converged solution. In the shooting method, we use the MATLAB function `ode45` with an absolute and relative tolerance of $e-12$. As the final separation distance increases, even though we use homotopy, for large enough separation distances the integration tolerance exceeds the allowed limit. This is the reason why we are not able to find converged solutions at these points at the present time. Further investigation needs to be carried out to find these solutions. However, the contour plots gives the general trend in the voltage requirements. For example, in Figure 6.6(a) the voltage required to increase the separation distance in 4 hours from 2 m to 5 m is roughly $10^{2.75}$ volts, and to increase 10 m it is $10^{3.5}$ volts.

One reason for this very sensitive nature of this two-point boundary value problem can be seen in the switching time plot in Figure 6.5(a). Here the maneuver time is held constant, while the maximum separation distance value is swept from 15–100 meters. The switching time t_0 curve is visibly flatting out. As a result, for large separation distances, the switching time computation is becoming increasingly critical. A small change in the switching time corresponds to a very large change in the separation distances. With the current simulation setup using the variable time-step Matlab Runge-Kutta integrator, the numerical integration accuracy control begins to break down after certain separation distances.

The second set of simulations are for the gluon-deputy arrangement. The specifications of the gluon and deputy are given in table 6.1. The initial center to center separation distance between the gluon and the deputy is 15 m. Figure 6.7 gives the simulation result for this arrangement. The voltages appear similar to the previous case. But, it should be noted that the gluon, due to its large radius, is carrying a greater charge for the same voltage levels.

The final simulation is carried out using the same gluon deputy arrangement as above. But the initial separation distance is varied and the separation distance is increased by a fixed distance of 10 m. Figure 6.8 gives the contour plots of the voltage needed for this maneuver. Again, the simulation is carried out for two different Debye lengths (100 m and 50 m).

6.2 Closed-Loop Reconfiguration of 2-Craft Coulomb Tether in GEO

Next a Coulomb structure reconfiguration is performed in a circularly restricted GEO orbit. A closed-loop charge feedback control law is developed to stabilize the time varying separation distance. The orbital dynamics are exploited to stabilize the in-plane attitude motion with the gravity gradient torque.

A 2-satellite formation is considered as shown in the Figure 6.9. The center of mass is assumed to maintain a circular Keplerian orbit and the two satellites are nominally aligned along the orbit radial direction. In essence, these two charged spacecraft will behave like a conventional 2-craft tether system, with the exception that this electrostatic tether is capable both of attractive and repulsive forces. Reference 30 shows that the relative distance between the two satellites can be controlled using electrostatic Coulomb forces. A charge feedback law is used to maintain the relative distance at a constant value. As a result, the two satellites behave like a long slender nearly rigid body and the differential gravitational attraction is used to stabilize the attitude of this formation about the orbit radial direction. From this point onwards, this will be referred to as the Coulomb tether regulation problem. These concepts are extended for the time varying Coulomb tether length tracking problem. The main aim in the tracking (reconfiguration) problem is to increase or decrease the relative distance between the satellites by forcing them to move relative to

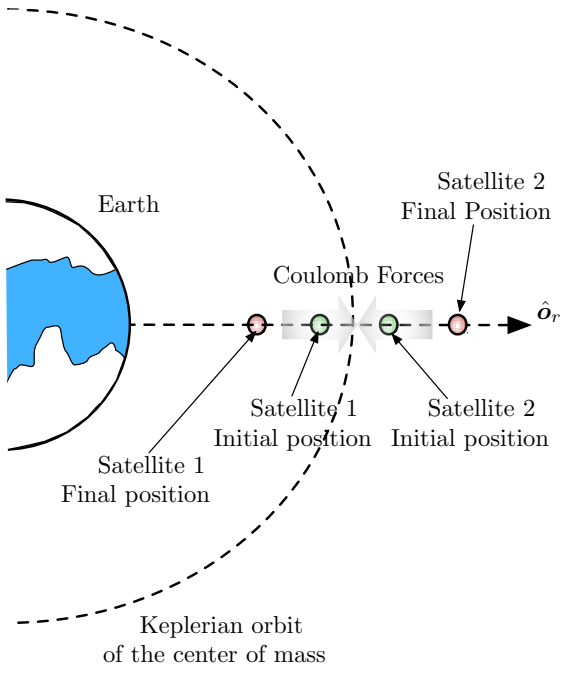

Figure 6.9: A simple Coulomb tracking illustration.

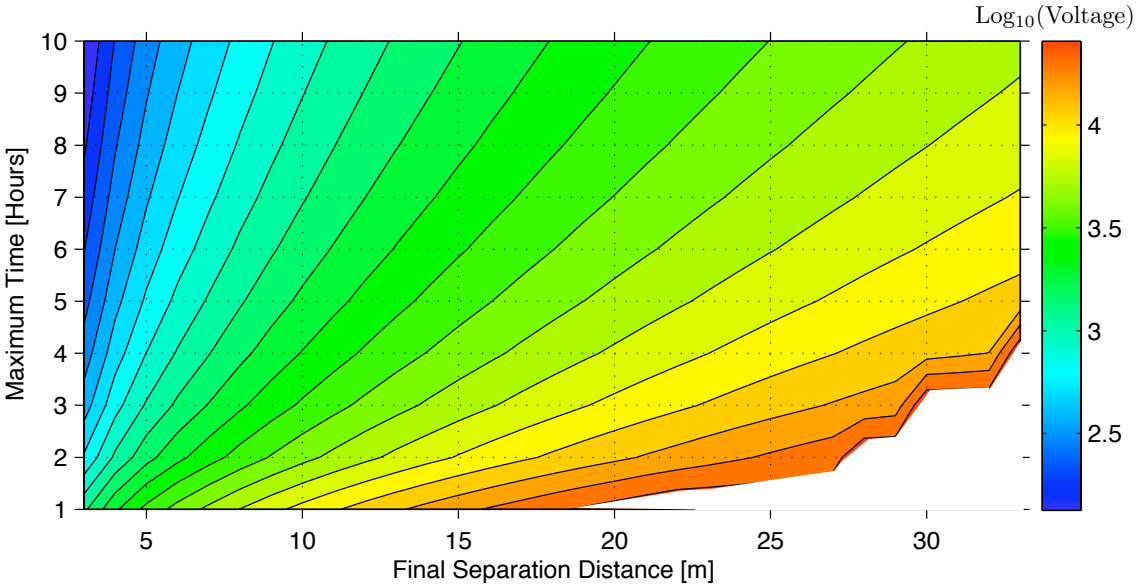

(a) Debye length of 100 m

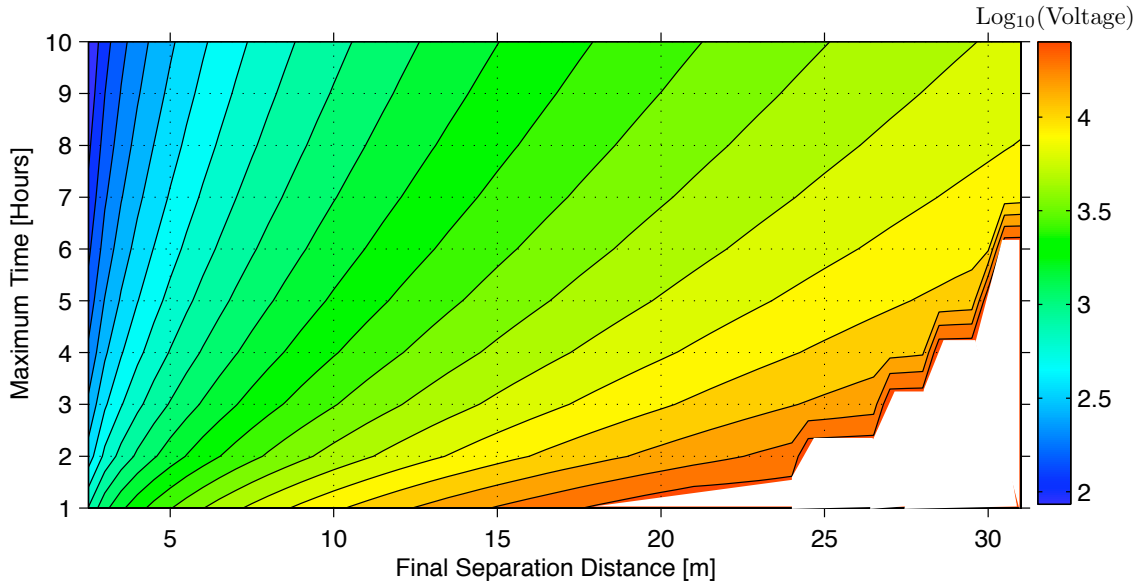

(b) Debye length of 50 m

Figure 6.6: Graphs illustrates the contour plot of the voltage (log) needed on two craft of equal mass to increase the separation distance from 2 m to several meters in different maneuver time, using bang-bang charging.

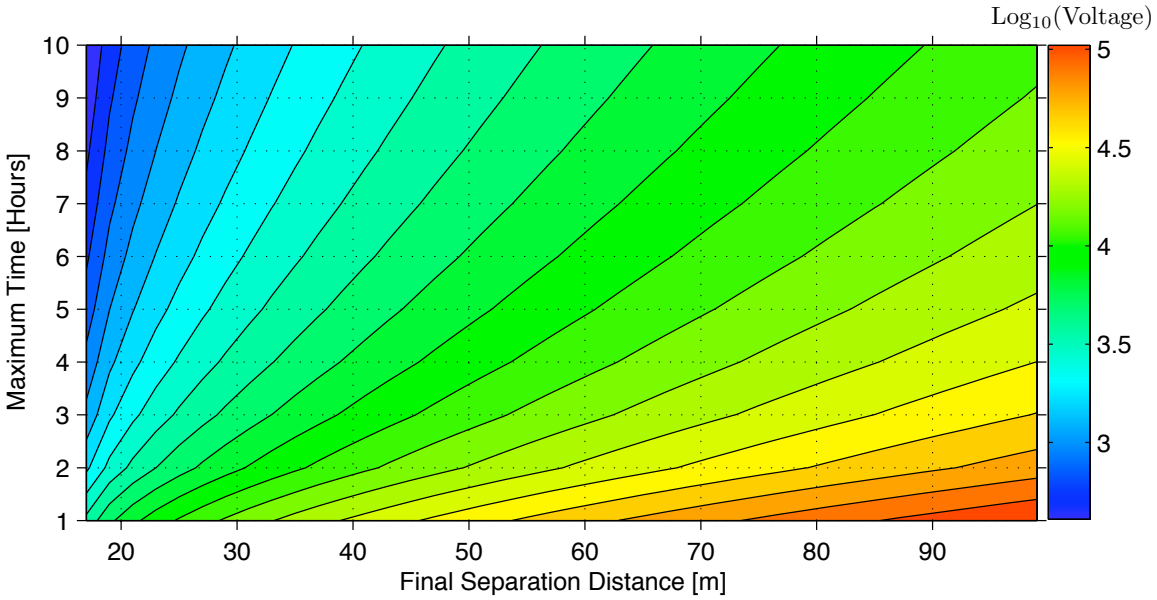

(a) Debye length of 100 m

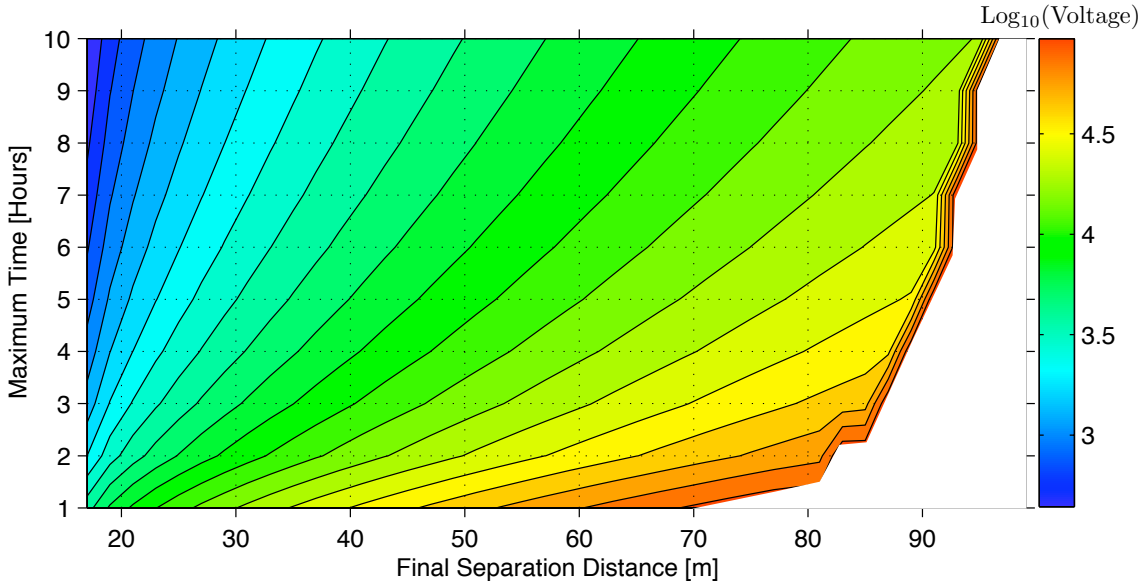

(b) Debye length of 50 m

Figure 6.7: Graphs illustrates the contour plot of the voltage (log) needed for a gluon-deputy satellite arrangement to increase the separation distance from 15 m to several meters in different maneuver time, using bang-bang charging.

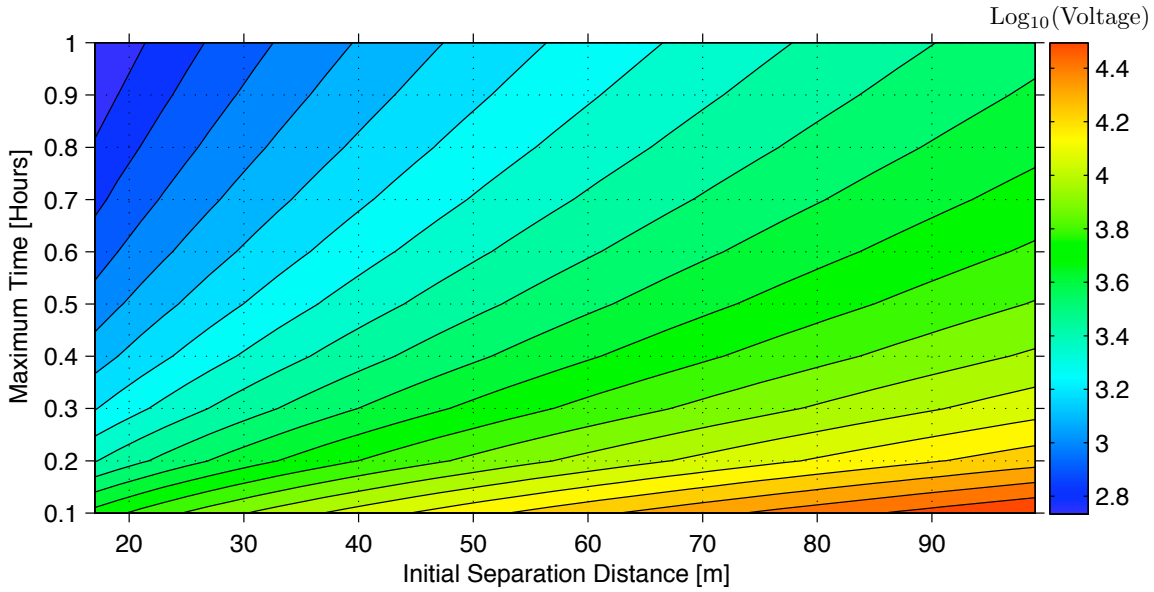

(a) Debye length of 100 m

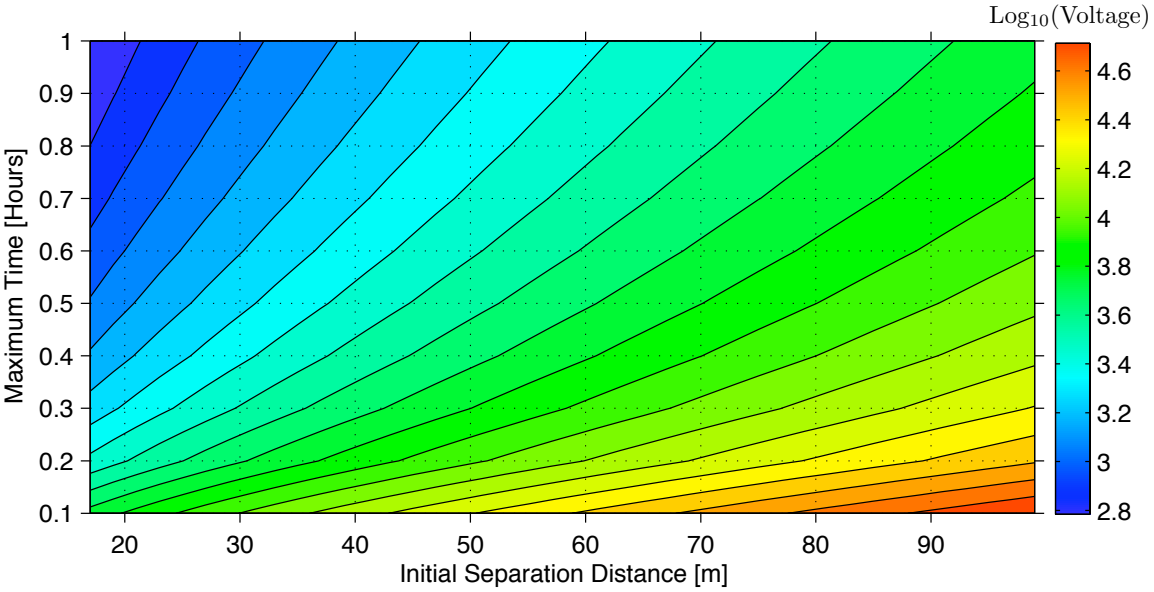

(b) Debye length of 50 m

Figure 6.8: Graphs illustrates the contour plot of the voltage (log) needed for a gluon-deputy satellite arrangement to increase the separation distance by 10 m for various initial separation distances in different maneuver time, using bang-bang charging.

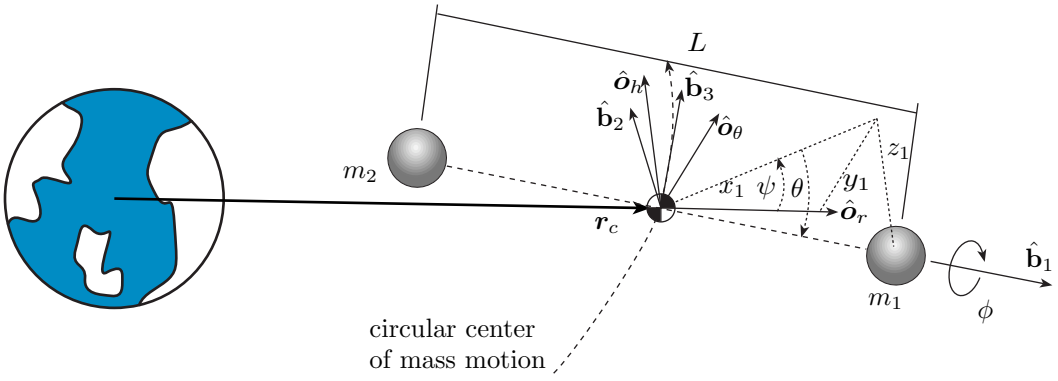

Figure 6.10: Coulomb Tethered Two Satellite Formation with the Satellites Aligned Along the Orbit Nadir Direction

each other along a prescribed path. This static Coulomb structure reconfiguration is to be accomplished without loosing altitude stability.

6.2.1 Dynamic Modeling

The Clohessy-Wiltshire-Hill's equations[12–14] for one of the spacecraft in the 2-craft Coulomb tether formation is given by

$$\ddot{x}_1 - 2n\dot{y}_1 - 3n^2 x_1 = \frac{k_c}{m_1}\frac{(x_1 - x_2)}{L^3} q_1 q_2$$
$$\ddot{y}_1 + 2n\dot{x}_1 = \frac{k_c}{m_1}\frac{(y_1 - y_2)}{L^3} q_1 q_2$$
$$\ddot{z}_1 + n^2 z_1 = \frac{k_c}{m_1}\frac{(z_1 - z_2)}{L^3} q_1 q_2$$

where $\boldsymbol{\rho}_i = (x_i, y_i, z_i)^T$ is the position vector of the i^{th} satellite in Hill frame components, m_1 and q_1 are the mass and charge of satellite 1, and L is the distance between the satellites 1 and 2. The constant chief orbital rate is given by $n = \sqrt{\mu/r_c^3}$, where μ is the gravitational coefficient and $\boldsymbol{r}_c$ is center of mass position vector. The parameter $k_c = 8.99 \cdot 10^9$ Nm^2/C^2 is the Coulomb constant. As the Hill frame origin is set to be identical to the formation center of mass, the motion of the 2^{nd} craft can be found by noting that the center of mass vector is constant due to conservation of linear momentum. This yields[43,44]

$$m_1\boldsymbol{\rho}_1 + m_2\boldsymbol{\rho}_2 = 0 \tag{6.12}$$

The differential equation of the separation distance L, between the two satellites is given by[30]

$$\ddot{L} = (2n\dot{\psi} + 3n^2)L + \frac{k_c}{m_1} Q \frac{1}{L^2}\frac{m_1 + m_2}{m_2} \tag{6.13}$$

For the Coulomb tether regulation problem, L is taken as a sum of a constant reference length L_{ref} and a small varying length δL. Similarly, let Q be the sum of Q_{ref}, which is the ideal constant charge needed to maintain the satellites in a rigid formation of length L_{ref}, and a small charge variation δQ.

$$L(t) = L_{\text{ref}} + \delta L(t) \tag{6.14a}$$
$$Q(t) = Q_{\text{ref}} + \delta Q(t) \tag{6.14b}$$

The reference charge Q_{ref} is a function of L_{ref} and is computed analytically from the linearized Hill frame equations. The analytical expression for Q_{ref} is written as[30,36]

$$Q_{\text{ref}} = -3n^2 \frac{L^3}{k_c}\frac{m_1 m_2}{m_1 + m_2} \tag{6.15}$$

It should be noted that in the Coulomb tether regulation problem L_{ref} is constant and the differential equation given in Eq. (6.13) is linearized by assuming a small δL separation distance error. This can be slightly modified to accommodate the Coulomb tracking problem. The reference Coulomb structure length $L_{\text{ref}}(t)$

us made time varying, but the separation distance errors $\delta L(t)$ are still assumed to be small.

$$L(t) = L_{\text{ref}}(t) + \delta L(t) \tag{6.16a}$$
$$Q(t) = Q_{\text{ref}}(t) + \delta Q(t) \tag{6.16b}$$

Here $L_{\text{ref}}(t)$ is the time varying reference separation distance and $Q_{\text{ref}}(t)$ is the corresponding reference charge which can be calculated using Eq. (6.15). Substituting the assumptions in Eq. (6.16) into Eq. (6.13) and linearizing assuming small δL, we get

$$\delta\ddot{L} = -\ddot{L}_{\text{ref}} + 2nL_{\text{ref}}\dot{\psi} + 9n^2\delta L + \frac{k_c}{m_1}\delta Q\frac{1}{L_{\text{ref}}^2}\frac{m_1+m_2}{m_2} \tag{6.17}$$

This equation establishes the relation between the additional charge δQ required and the change in relative separation of the satellites. We observe that this relation is coupled to the angular in-plane perturbation rate $\dot{\psi}$. In order to obtain an expression for this, we resort to a stability analysis using the gravity gradient. The derivation of the expression for angular perturbation closely follows the derivation given in Reference 30 for the Coulomb regulation problem. The linearized attitude dynamics of the Coulomb tether body frame $\mathcal{B}$ are written along with the separation distance equation as:

$$\ddot{\theta} + \frac{2\dot{L}_{\text{ref}}}{L_{\text{ref}}}\dot{\theta} + 4n^2\theta = 0 \tag{6.18a}$$

$$\ddot{\psi} + \frac{2\dot{L}_{\text{ref}}}{L_{\text{ref}}}\dot{\psi} + \frac{2n}{L_{\text{ref}}}\delta\dot{L} - \frac{2\dot{L}_{\text{ref}}}{L_{\text{ref}}^2}n\delta L + \frac{2\dot{L}_{\text{ref}}}{L_{\text{ref}}}n + 3n^2\psi = 0 \tag{6.18b}$$

$$\delta\ddot{L} + \ddot{L}_{\text{ref}} - 2nL_{\text{ref}}\dot{\psi} - 9n^2\delta L - \frac{k_c}{m_1}\delta Q\frac{1}{L_{\text{ref}}^2}\frac{m_1+m_2}{m_2} = 0 \tag{6.18c}$$

Thus, Eqs. (6.18a) – (6.18c) are the linearized equations of motion of the Coulomb tracking about the static nadir reference configuration. Only the linearized δL differential equation was obtained using the Clohessy-Wiltshire-Hill equations, while the linearized differential equations of ψ and θ were derived from the full formation angular momentum expression along with Euler's equation. Compared to the regulation problem, these differential equations are non-autonomous and depend explicitly on time through $L_{\text{ref}}(t)$. This greatly complicates the stability analysis of any feedback control law.

Let the charge product variation δQ be the control signal. The Coulomb regulation feedback control is then modified to incorporate a time-varying $L_{\text{ref}}(t)$ term.

$$\delta Q = \frac{m_1 m_2 L_{\text{ref}}^2(t)}{(m_1+m_2)\,k_c}(-C_1\delta L - C_2\delta\dot{L}) \tag{6.19}$$

The constants C_1 and C_2 are the position and velocity feedback gains. Incorporating this feedback law in to the δL differential equation in Eq. (6.18c), we get following closed-loop separation distance dynamics.

$$\delta\ddot{L} + \ddot{L}_{\text{ref}} - 2nL_{\text{ref}}\dot{\psi} + (C_1 - 9n^2)\delta L + C_2\delta\dot{L} = 0 \tag{6.20}$$

It can be observed that the linearized equations in Eq. (6.18a) – (6.18c) depend on the mean orbit rate n which has a very small value at GEO. In order to eliminate the numerical issues that might arise while integrating due to the small n value, the following normalization transformation is employed to make these equations independent of n.

$$\mathrm{d}\tau = \Omega \mathrm{d}t \tag{6.21a}$$
$$(*)' = \frac{\mathrm{d}(*)}{\mathrm{d}\tau} = \frac{1}{\Omega}\frac{\mathrm{d}(*)}{\mathrm{d}t} \tag{6.21b}$$

The orbit rate independent form of the linearized equations in Eq. (6.18a) – (6.18c) are written as

$$\theta'' + \frac{2L'_{\text{ref}}}{L_{\text{ref}}}\theta' + 4\theta = 0 \tag{6.22a}$$

$$\psi'' + \frac{2L'_{\text{ref}}}{L_{\text{ref}}}\psi' + \frac{2}{L_{\text{ref}}}\delta L' - \frac{2L'_{\text{ref}}}{L_{\text{ref}}^2}\delta L + \frac{2L'_{\text{ref}}}{L_{\text{ref}}} + 3\psi = 0 \tag{6.22b}$$

$$\delta L'' + L''_{\text{ref}} - 2L_{\text{ref}}\psi' + (\tilde{C}_1 - 9)\delta L + \tilde{C}_2\delta L' = 0 \tag{6.22c}$$

where $\tilde{C}_2 = (C_2/\Omega)$ and $\tilde{C}_1 = (C_1/\Omega^2)$ are non-dimensionalized feedback gains. These equations show that the out-of-plane motion $\theta(t)$ is decoupled from the charge product term δQ and separation distance variation $\delta L(t)$. Therefore, it is not possible to control the out-of-plane motion using charge control in this linearized analysis. However, the in-plane motion $\psi(t)$ is coupled to the $\delta L(t)$ motion in the form of a driving force and hence, requiring a coupled in-plane attitude and separation distance stability analysis.

6.2.2 Stability Analysis

With time varying $L_{\text{ref}}(t)$, the equations of motion are linear and time dependent. Rosenbrock[45] has shown that the linear time-dependent system given by $\dot{\boldsymbol{x}} = A(t)\boldsymbol{x}$ is asymptotically stable if the frozen system for each t is stable and the rate of change of $A(t)$ is very small. He also established bound for $A'(t)$ when $A(t)$ is in the control canonical form. We will analyse the stability of our system based on this method. Using the state vector $\boldsymbol{x} = (\psi, \psi', \delta L, \delta L')^T$, the coupled δL and ψ equations in Eq. (6.22b) – (6.22c) can be written in the state space form

$$\boldsymbol{x}' = A(t)\boldsymbol{x} + \boldsymbol{d}(t) \tag{6.23}$$

where

$$A(t) = \begin{bmatrix} 0 & 1 & 0 & 0 \\ -3 & -\frac{2L'_{\text{ref}}}{L_{\text{ref}}} & \frac{2L'_{\text{ref}}}{L^2_{\text{ref}}} & -\frac{2}{L_{\text{ref}}} \\ 0 & 0 & 0 & 1 \\ 0 & 2L_{\text{ref}} & 9-\tilde{C}_1 & -\tilde{C}_2 \end{bmatrix} \tag{6.24}$$

and

$$\boldsymbol{d}(t) = \begin{pmatrix} 0 \\ -\frac{2L'_{\text{ref}}}{L_{\text{ref}}} \\ 0 \\ -L''_{\text{ref}} \end{pmatrix} \tag{6.25}$$

Note that the forcing vector $\boldsymbol{d}(t)$ goes to zero at the end of the maneuvers where L_{ref} becomes constant. If the reference separation distance is varied linearly, then only the 2nd entry will be non-zero. The time dependency of the square $A(t)$ matrix is due to the terms L_{ref} and L'_{ref}. The stability of the system greatly depends on the rate at which L_{ref} is varied. The rate of change of reference length L'_{ref}, can be chosen according to the mission requirement or design. Of interest is how large L'_{ref} can be while still guaranteeing stability. From Eq. (6.23), we can observe that there is a disturbance term in the equation of motion which might lead to a steady state offset as long as L_{ref} is time varying. The analytical expression for the steady state offset is given as follows

$$\begin{aligned} \begin{pmatrix} \psi_{\text{offset}} \\ \delta L_{\text{offset}} \end{pmatrix} &= \begin{pmatrix} -\frac{2L'_{\text{ref}}}{3L_{\text{ref}}} + \frac{2L'_{\text{ref}}L''_{\text{ref}}}{3(-9+3\tilde{C}_1)L^2_{\text{ref}}} \\ +\frac{L''_{\text{ref}}}{(-9+3\tilde{C}_1)} \end{pmatrix} \\ &= \begin{pmatrix} -\frac{2\dot{L}_{\text{ref}}}{3nL_{\text{ref}}} + \frac{2\dot{L}_{\text{ref}}\ddot{L}_{\text{ref}}}{3n(-9n^2+3C_1)L^2_{\text{ref}}} \\ +\frac{\ddot{L}_{\text{ref}}}{(-9n^2+3C_1)} \end{pmatrix} \end{aligned} \tag{6.26}$$

Before fixing the limits for L'_{ref}, let us choose the values for gains so that the $A(t)$ matrix is Hurwitz at any given time t. In the regulation problem the feedback gains were expressed in terms of scaling factor c and α. Since this work is an extension of the regulation problem, the same scaling factor for the gains are chosen. They can be written as

$$\tilde{C}_1 = c \tag{6.27}$$

and

$$\tilde{C}_2 = \alpha\sqrt{c-9} \tag{6.28}$$

The characteristic equation of the $A(t)$ matrix is given by

$$\begin{aligned} &\lambda^4 + (\tilde{C}_2 + 2\frac{L'_{\text{ref}}}{L_{\text{ref}}})\lambda^3 + (\tilde{C}_1 + 2\tilde{C}_2\frac{L'_{\text{ref}}}{L_{\text{ref}}} - 2)\lambda^2 \\ &+ (3\tilde{C}_2 - 22\frac{L'_{\text{ref}}}{L_{\text{ref}}} + 2\tilde{C}_1\frac{L'_{\text{ref}}}{L_{\text{ref}}})\lambda + 3(\tilde{C}_1 - 9) = 0 \end{aligned} \tag{6.29}$$

Let $k = L'_{\text{ref}}/L_{\text{ref}}$ be a time varying coefficient which is determined through the chosen reference separation time history $L_{\text{ref}}(t)$. With

this simplification the characteristic equation of $A(t)$ becomes

$$\lambda^4 + (\tilde{C}_2 + 2k)\lambda^3 + (\tilde{C}_1 + 2\tilde{C}_2 k - 2)\lambda^2 + (3\tilde{C}_2 - 22k + 2\tilde{C}_1 k)\lambda + 3(\tilde{C}_1 - 9) = 0 \tag{6.30}$$

To ensure stability, roots of the characteristic equation should have negative real parts (Hurwitz matrix). This requirement is satisfied using the Routh-Hurwitz stability criterion. Based on this criterion it is established that $\tilde{C}_1$ should have a value greater than 9 and the range of possible values for k and α for certain fixed $\tilde{C}_1$ is shown in Figure 6.11. The shaded region illustrates the possible values of k and α which guarantee that roots of the characteristic equation (i.e. the eigenvalues of the matrix $A(t)$) have negative real parts. It can be observed from Figure 6.11 that for $\tilde{C}_1 > 10$ there is no bounds on k when we are expanding the separation distance. But, for contracting or decreasing the separation distance (i.e. $-k$) we have a tight limit on k. The α value is fixed such that we have a maximum range of k. From Figures 6.11(b) and 6.11(c), the values of α are taken as 1.4 and 0.9 for the $\tilde{C}_1$ values of 12 and 14, respectively.

By satisfying the Routh-Hurwitz criterion, the eigenvalues of $A(t)$ at any fixed time t will always be in the left half of the plane. This is not sufficient to guarantee stability of the system. The sufficient condition is that rate of change of $A(t)$ be very small. Rosenbrock[45] established bounds for this rate of change and stated it as a theorem when $A(t)$ is in the control canonical form ($A_c(t)$). For the sake of continuity the theorem is stated here, but the reader should refer to Reference 45 for the detailed derivation of the theorem. Let the matrix L be defined as

$$L = SA_c^T + A_c S - S' + \eta I < 0 \tag{6.31}$$

$$(S_{ij}) = \sum_{k=1}^{n} \lambda_k^{i-1} \bar{\lambda}_k^{j-1} \tag{6.32}$$

where S_{ij} are the elements of the S matrix, λ_k and $\bar{\lambda}_k$ are the eigenvalues and its conjugate, S' is the derivative of S and $\eta > 0$ is some arbitrary constant. When all the eigen values of A_c are distinct and in the left half of the plane at any given instant of time, and L is negative definite throughout the maneuver, the system is asymptotically stable about $\boldsymbol{x} = 0$. For our problem, this requires the time varying reference separation distance $L_{\text{ref}}(t)$ to be carefully chosen so that the L is negative definite at all times. This theorem is based on the fact that for a matrix in the control canonical form, the eigenvalues are uniquely related to the elements of the matrix and hence, the bounds on the rate of change of the matrix can be replaced by bounds on the rate of change of the eigenvalues. Some more details about the S matrix are given in the following equation.

$$S = HH^* \tag{6.33}$$

where H is the is the eigenvector matrix and H^* is the transposed complex conjugate of H. The matrix H is defined as

$$H = \begin{bmatrix} 1 & 1 & \cdots & 1 \\ \lambda_1 & \lambda_2 & \cdots & \lambda_n \\ \lambda_1^2 & \lambda_2^2 & \cdots & \lambda_n^2 \\ \vdots & \vdots & \ddots & \vdots \\ \lambda_1^{n-1} & \lambda_2^{n-1} & \cdots & \lambda_n^{n-1} \end{bmatrix} \tag{6.34}$$

Studying the characteristic equation in Eq. (6.30), note that if $L_{\text{ref}}(t)$ is chosen such that the coefficient $k = L'_{\text{ref}}/L_{\text{ref}}$ is constant, then the eigenvalues of $A_c(t)$ are also constant. For this special case the Rosenbrock stability conditions on the rate of change of $A(t)$ are trivially satisfied, and the overall stability is determined through the Routh-Hurwitz stability conditions. However, having a constant k coefficient is not a practical maneuver because it requires exponential expansion or contraction.

The $A(t)$ matrix in Eq. (6.23) is not in the control canonical form, but it can be transformed in a control canonical form using a similarity transformation $\boldsymbol{\xi} = T\boldsymbol{x}$ which yields the differential vector equation

$$\boldsymbol{\xi}' = A_c(t)\boldsymbol{\xi} \tag{6.35}$$

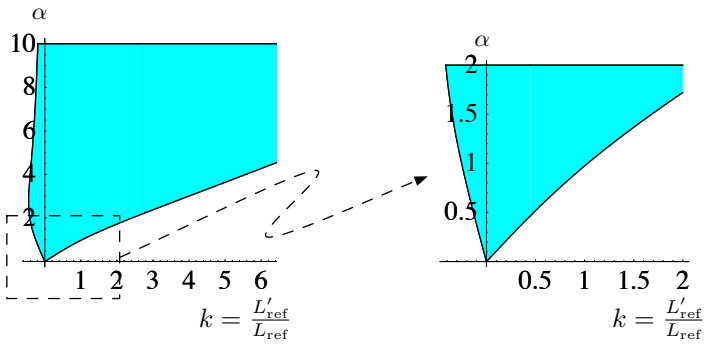

(a) Case with $\tilde{C}_1 = 10$

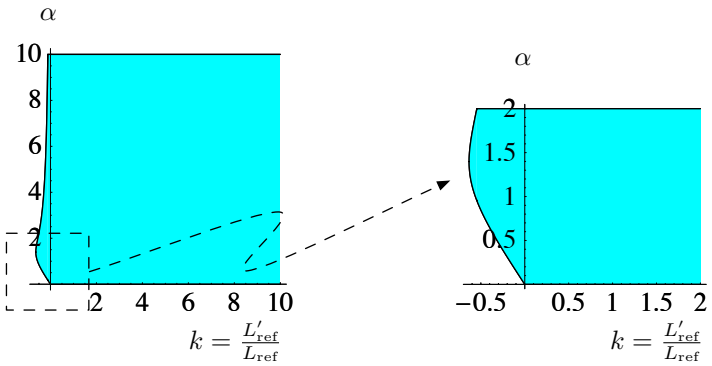

(b) Case with $\tilde{C}_1 = 12$

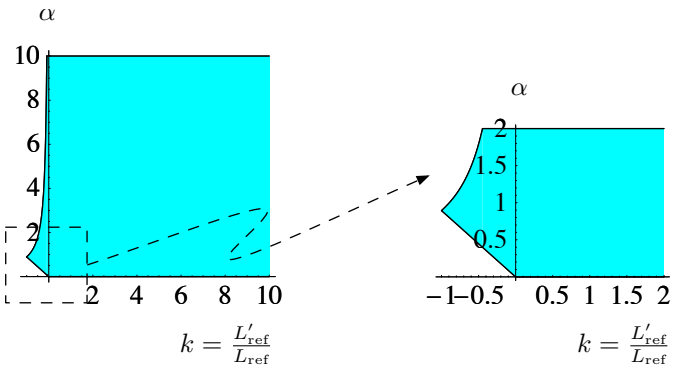

(c) Case with $\tilde{C}_1 = 14$

Figure 6.11: Plots showing the regions that satisfy the Routh Hurwitz stability criterion for an autonomous dynamical system.

It should be noted that the characteristic equation of the transformed matrix $A_c(t)$ is the same as the original matrix $A(t)$. Hence, the values of gains chosen earlier will keep the eigenvalues in the left half plane. For this transformed matrix we can establish the bounds on L_{ref} and L'_{ref} which guarantee that the matrix L remains negative definite. The transformed states $\boldsymbol{\xi}$ are linear combinations of the original states $\boldsymbol{x}$. Therefore, if the transformed states are stable then the original states are also stable. The control canonical form of the matrix $(A_c(t))$ for the given matrix $A(t)$ can be easily written by observing the characteristic equation.

$$A_c(t) = \begin{bmatrix} 0 & 1 & 0 & 0 \\ 0 & 0 & 1 & 0 \\ 0 & 0 & 0 & 1 \\ a_{41} & a_{42} & a_{43} & a_{44} \end{bmatrix} \tag{6.36}$$

where

$$a_{41} = -3(\tilde{C}_1 - 9) \tag{6.37a}$$
$$a_{42} = -(3\tilde{C}_2 - 22k + 2\tilde{C}_1 k) \tag{6.37b}$$
$$a_{43} = -\tilde{C}_1 + 2\tilde{C}_2 k - 2) \tag{6.37c}$$
$$a_{44} = -(\tilde{C}_2 + 2k) \tag{6.37d}$$

Because $A_c(t)$ is a 4×4 matrix, analytically finding the expression for eigenvalues and using them in the inequality in Eq. 6.31 is very challenging. The resulting expressions are too complex to be insightful. Instead the feasible values of L_{ref} and L'_{ref} that satisfies the inequality in Eq. 6.31 for the chosen values of $\tilde{C}_1$ and α are identified numerically. These feasible values are shown in Figure 6.12.

When designing the reconfiguration maneuver and the corresponding $L_{\text{ref}}(t)$ values, care must be taken that the L_{ref} versus L'_{ref} phase plots remain within the solid colored area. Observe that the longer the virtual Coulomb structure is, the more aggressive the reconfiguration maneuvers can be. This can be explained by treating the 2-craft formation as a single slender rigid body at any instance of time. The relative equilibria conditions of a rigid body in orbit require it to have the axis of least inertia in the orbit nadir direction $\hat{\boldsymbol{o}}_r$, while the axis of maximum inertia is about the orbit normal direction $\hat{\boldsymbol{o}}_h$.[14] As the separation distance is decreased, the formation principle axes are less well determined, resulting in a smaller regions of stability.

6.2.3 Numerical Simulation

To illustrate the performance and stability of Coulomb tether reconfiguration maneuvers, the following numerical simulations are performed. The simulation parameters that used are listed in Table 6.2. The initial attitude values are set to $\psi = 0.1$ radians and $\theta = 0.1$ rad. The separation length error (Coulomb tether length error) is $\delta L = 0.5$ meters. All initial rates are set to zero through $\dot{\psi} = \delta\dot{L} = \dot{\theta} = 0$. Two sets of maneuvers, expanding the Coulomb tether formation from 25m to 35m in 1.8 days and contracting the formation from a separation distance of 25m to 15m, are shown.

Table 6.2: Input Parameters Used in Simulation

Parameter	Value	Units
m_1	150	kg
m_2	150	kg
k_c	8.99×10^9	$\frac{\text{Nm}^2}{\text{C}^2}$
Ω	7.2915×10^{-5}	rad/sec
$\delta L(0)$	0.5	m
$\psi(0)$	0.1	rad
$\theta(0)$	0.1	rad

The Coulomb tether performance is simulated in two different manners. First the linearized spherical coordinate differential equations are integrated. This simulation illustrates the charge control performance operating on the linearized dynamical system. Second, the exact nonlinear equations of motion of the deputy satellites are solved using the same charge feedback control, and compared to the performance of the linearized dynamical system. The nonlinear deputy equations are given

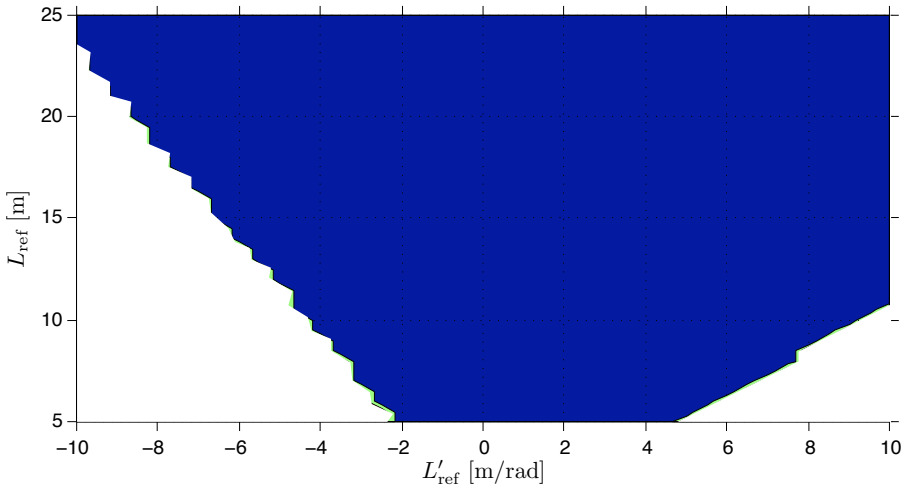

(a) For $\tilde{C}_1 = 12$ and $\alpha = 1.4$

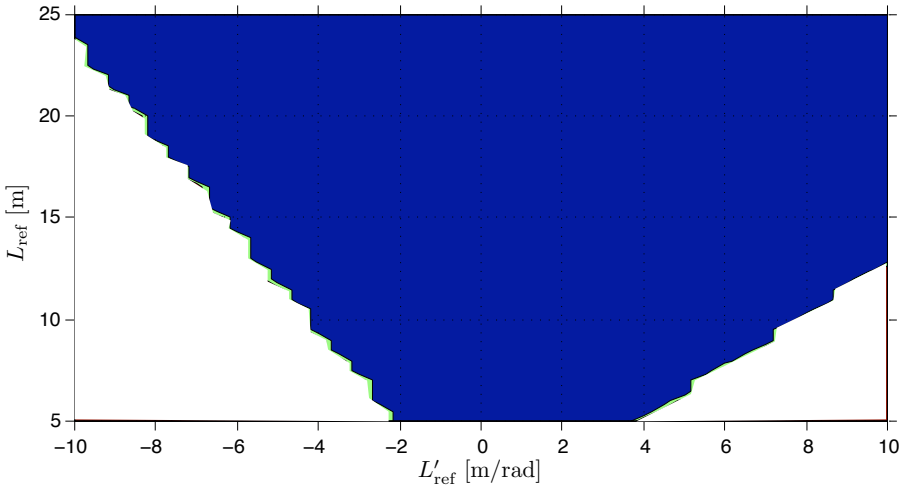

(b) For $\tilde{C}_1 = 14$ and $\alpha = 0.9$

Figure 6.12: Plots showing the regions that satisfy the Routh Hurwitz stability criterion and Rosenbrock bounds.

through Cowell's equations

$$\ddot{\boldsymbol{r}}_1 + \frac{\mu}{r_1^3}\boldsymbol{r}_1 = \frac{k_c}{m_1}\frac{Q}{L(t)^3}(\boldsymbol{r}_1 - \boldsymbol{r}_2) \tag{6.38a}$$

$$\ddot{\boldsymbol{r}}_2 + \frac{\mu}{r_2^3}\boldsymbol{r}_2 = \frac{k_c}{m_2}\frac{Q}{L(t)^3}(\boldsymbol{r}_2 - \boldsymbol{r}_1) \tag{6.38b}$$

where $\boldsymbol{r}_1 = \boldsymbol{r}_c + \boldsymbol{\rho}_1$ and $\boldsymbol{r}_2 = \boldsymbol{r}_c + \boldsymbol{\rho}_2$ are the inertial position vectors of the the masses m_1 and m_2, while $L = \sqrt{(\boldsymbol{r}_2 - \boldsymbol{r}_1)\cdot(\boldsymbol{r}_2 - \boldsymbol{r}_1)}$. The vector $\boldsymbol{r}_c$ denotes the position of the formation center of mass or chief location. The gravitational coefficient μ is defined as $\mu \approx GM_e$. After integrating the motion using inertial Cartesian coordinates, the separation distance L, as well as the in-plane and out-of-plane angles ψ and θ, are computed in post-processing using the exact kinematic transformation.

Figure 6.13(a) shows the Coulomb tether motion for increasing the separation distance from 25m to 35m in the linearized spherical coordinates $(\psi, \theta, \delta L)$, along with the full nonlinear spherical coordinates shown as continuous lines. The expansion is done in 1.8 days and this corresponds to a constant L'_{ref} of 0.88. After 1.8 days, the L'_{ref} is zero and the formation is allowed to stabilize about the final separation

distance. The feedback gains are $\tilde{C}_1 = 12$ and $\alpha = 1.4$. With the presented charge feedback law, both the yaw motion ψ and the separation distance deviation δL converge to zero. By stabilizing the δL state to zero, the in-plane rotation $\psi(t)$ also converges to zero. As expected, the pitch motion $\theta(t)$ was a stable sinusoidal motion, decoupled from the controlled in-plane orbital motion. Further, Figure 6.13(a) shows that the nonlinear simulation closely follows the linearized simulation, validating the linearizing assumption and illustrating robustness to the unmodelled dynamics. Since L'_{ref} is constant, there is no steady state offset for δL and the offset for ψ is very small (order of 10^{-2} rad) and hence, not visible in the graph.

Figure 6.13(b) shows the spacecraft control charge q_1 (on craft 1) for both the linearized and full nonlinear simulation models. Both are converging to the reference value pertaining to the static equilibrium at each instant of time. Note that the deviation from the value of reference charges is small, justifying the linearization assumptions used. The magnitude of the control charges is in the order of micro-Coulomb which is easily realizable in practice using charge emission devices. The charge on craft 2 will be equal and opposite to the charge on craft 1.

Figure 6.14(a) and Figure 6.14(b) show Coulomb tether motion and charge time histories for decreasing the separation distance from 25m to 15m. Contractions are more challenging because the angular momentum will cause to destabilize the in-plane attitude motion. The maneuvers must be performed slow enough to allow the gravity gradient to maintain stability. Again the maneuver is done in 1.8 days which means L'_{ref} is -0.88 and the gains are same as above expansion maneuver. These two sets of maneuvers are repeated for the gain values $\tilde{C}_1 = 14$ and $\alpha = 0.9$ and, Figure 6.15 and Figure 6.16 illustrate their time histories. It can be observed from these two graphs that even though the system is stable, the performance could potentially be improved by tuning the feedback gains.

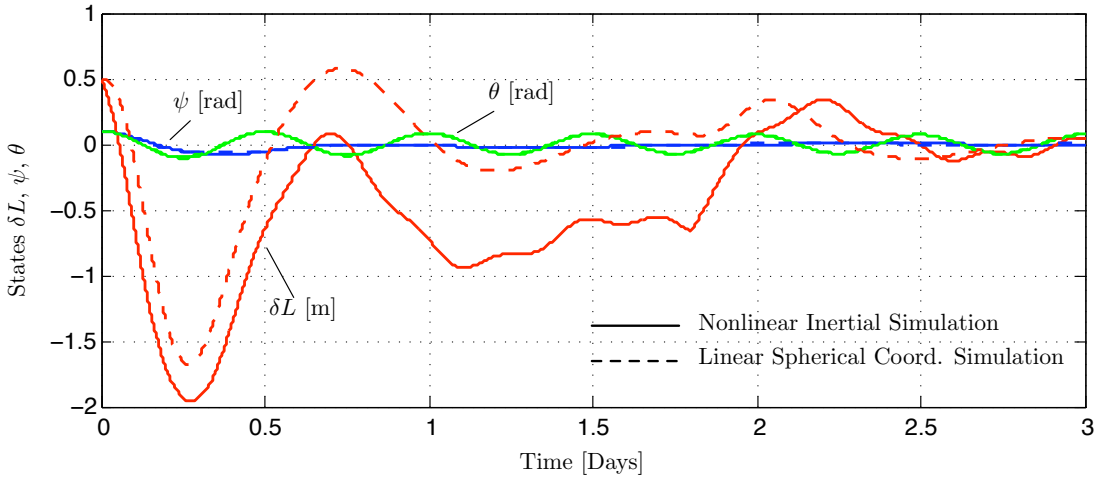

(a) Time histories of length variation δL, in-plane rotation angle ψ, and out-of-plane rotation angle θ.

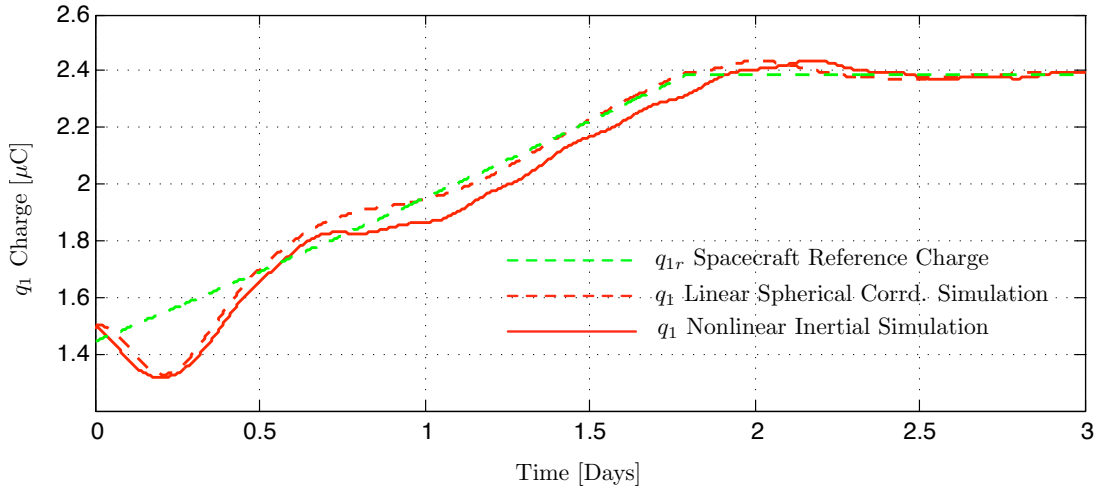

(b) Spacecraft charge time histories

Figure 6.13: Simulation results for expanding the spacecraft separation distance from 25 m to 35 m in 1.8 days. The feedback gains are $\tilde{C}_1 = 12$ and $\alpha = 1.4$.

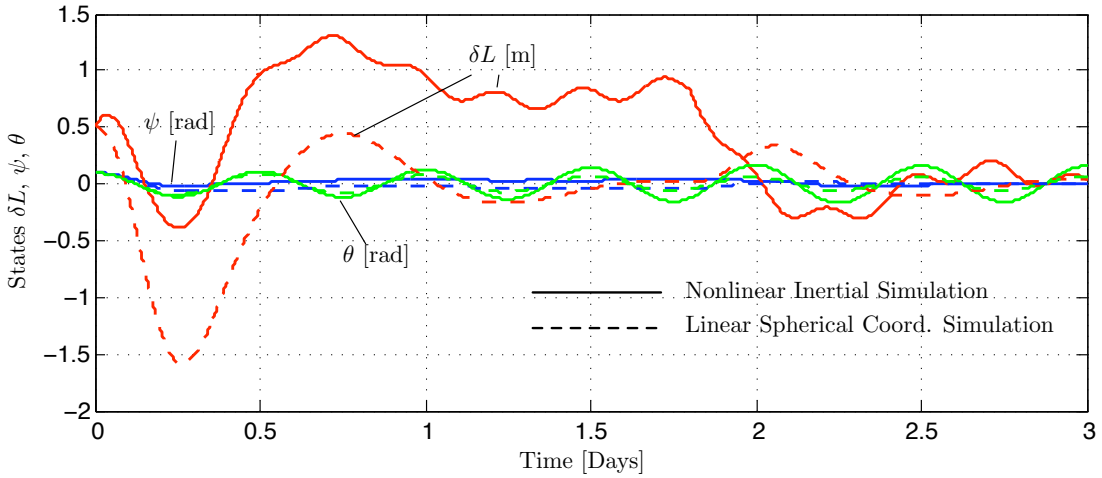

(a) Time histories of length variation δL, in-plane rotation angle ψ, and out-of-plane rotation angle θ.

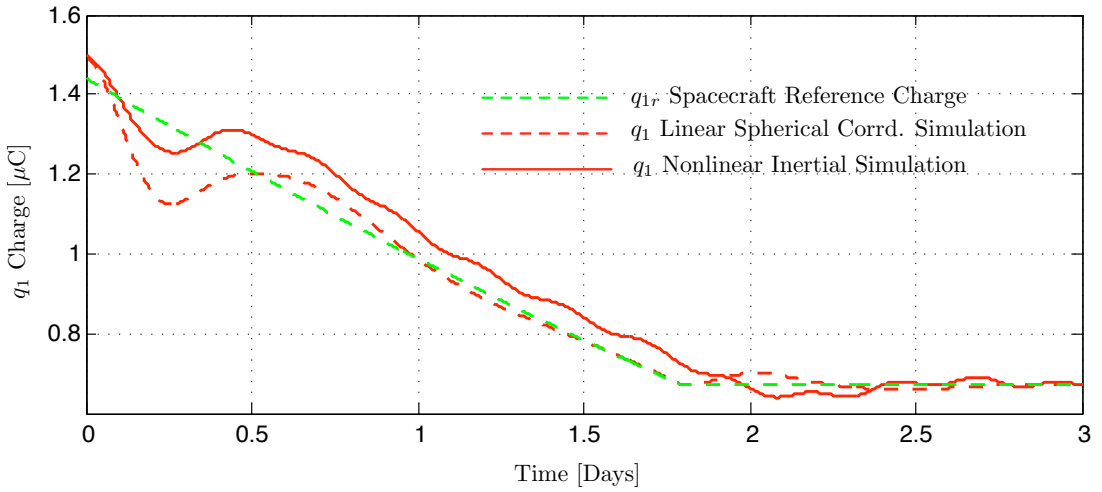

(b) Spacecraft charge time histories

Figure 6.14: Simulation results for contracting the spacecraft separation distance from $25\,m$ to $15\,m$ in 1.8 days. The feedback gains are $\tilde{C}_1 = 12$ and $\alpha = 1.4$.

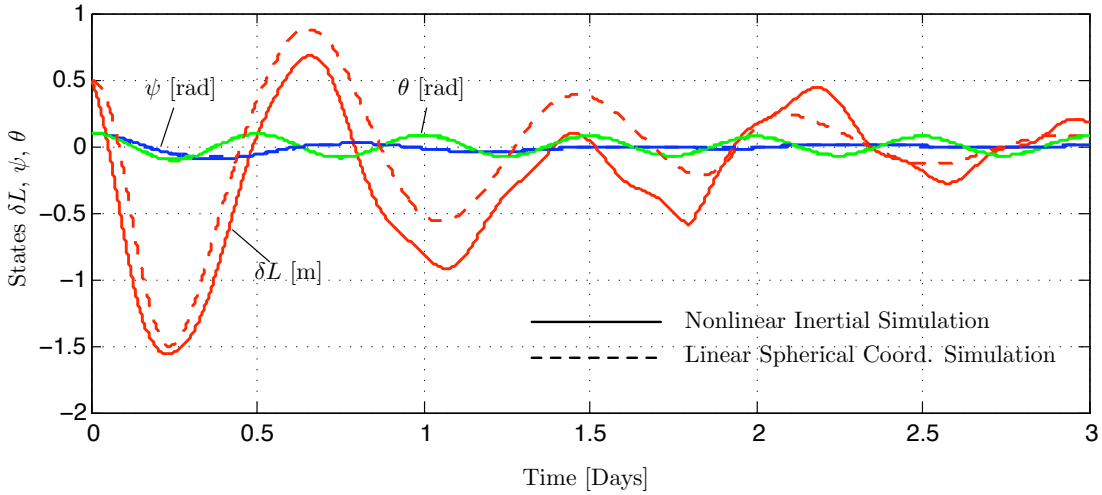

(a) Time histories of length variation δL, in-plane rotation angle ψ, and out-of-plane rotation angle θ.

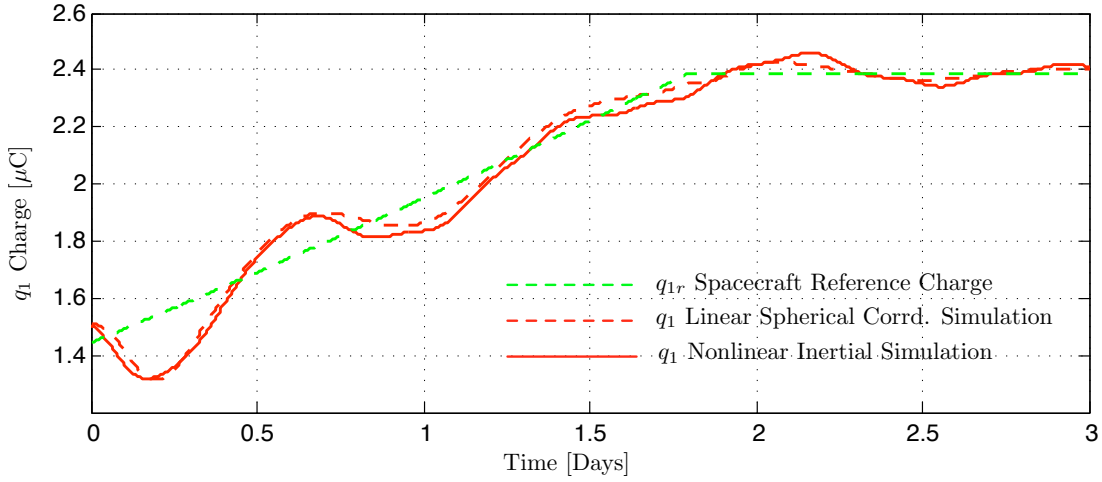

(b) Spacecraft charge time histories

Figure 6.15: Simulation results for expanding the spacecraft separation distance from 25 m to 35 m in 1.8 days. The feedback gains are $\tilde{C}_1 = 14$ and $\alpha = 0.9$.

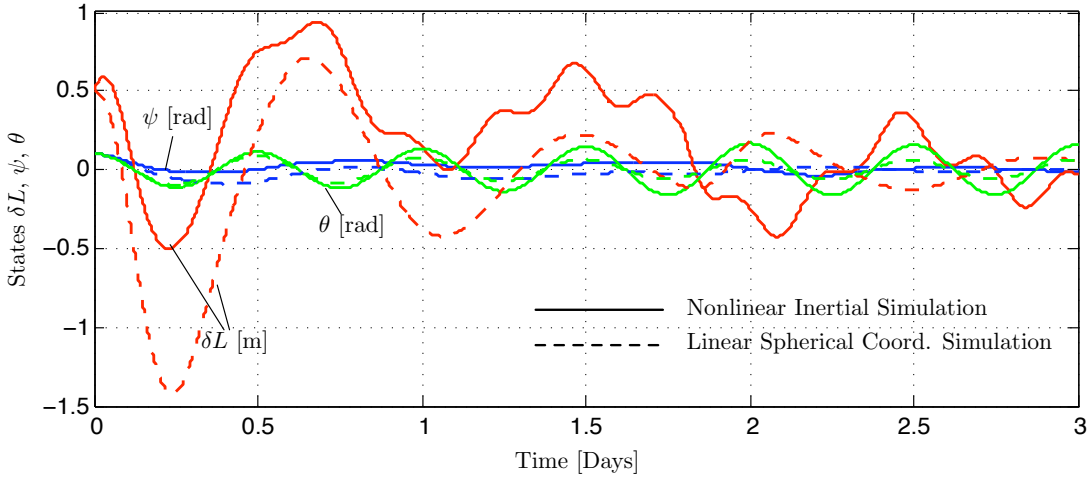

(a) Time histories of length variation δL, in-plane rotation angle ψ, and out-of-plane rotation angle θ.

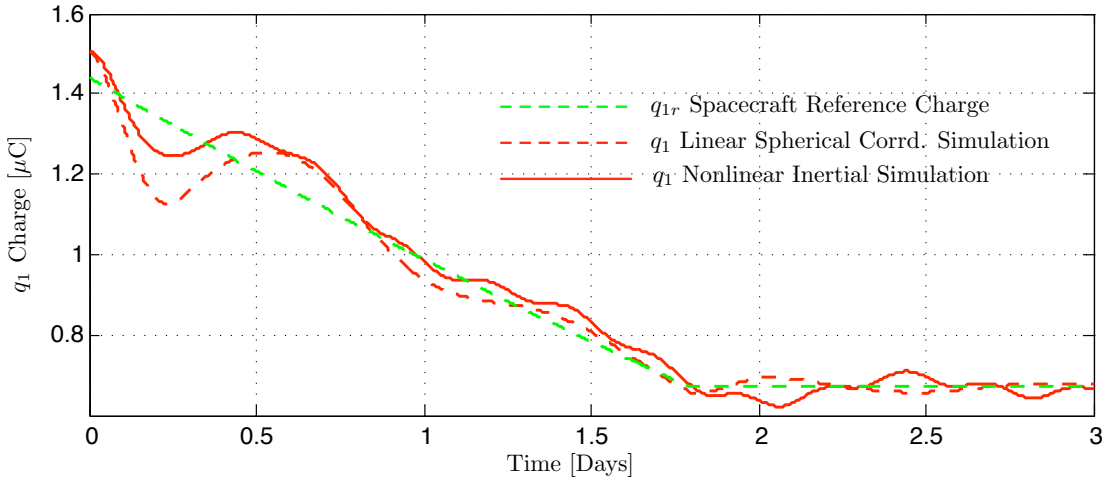

(b) Spacecraft charge time histories

Figure 6.16: Simulation results for contracting the spacecraft separation distance from $25\,m$ to $15\,m$ in 1.8 days. The feedback gains are $\tilde{C}_1 = 14$ and $\alpha = 0.9$.

Chapter 7

Spacecraft Charge Control and Sensing

7.1 Spacecraft Charging Fundamentals

7.1.1 The Phenomenon of Spacecraft Charging

Since a spacecraft has no physical ground connection to the surrounding space plasma environment, it is free to assume an electrical potential that is different from that in the plasma. Such a potential difference occurs naturally from the balance of free charge (currents) to and from the vehicle. In the most simple case, the currents involved are those due to the free electrons in the space plasma – generating a negative current to the vehicle – and the free ions in the plasma, which generate a positive current to the vehicle. The magnitudes of these plasma currents (amount of charge per-time) depend on the density of the particles and their velocity towards the spacecraft.

In an equilibrium plasma, the particle velocities are given by the thermal motion and are written as

$$v_{th} = \sqrt{\frac{kT}{2\pi m}}$$

where k is Boltzmanns constant, T is the plasma temperature, and m is the particle mass. Typical space plasmas are composed mainly of electrons and H^+ ions (protons). Thus, if both plasma species are at the same temperature and density, the electrons, being 2,000 times less massive than the ions, will have significantly higher thermal velocity. In a given time, more electrons will reach the surface of the spacecraft than ions. This would result in a larger negative current to the vehicle than positive current.

Because there is nowhere for this net negative current to "go" once it reaches the vehicle, equilibrium is obtained in the steady state by a change in spacecraft potential. The spacecraft will assume a negative value, such that the electron current is reduced through electrostatic repulsion, while the ion current is increased through attraction. The magnitude of the equilibrium negative potential will be sufficient for the electron current to be exactly equal to the ion current. Equilibrium is then defined as the potential required for zero net current to the vehicle. This concept is illustrated in Figure 7.1.

A number of real effects can change the spacecraft potential from this simple equilibrium value. For instance, in LEO conditions the plasma is relatively cool, while the spacecraft velocity through the plasma is high. In such cases the spacecraft velocity is much greater than the ion thermal velocity but less than the electron thermal velocity. In these conditions the ions can only impact the upstream, or ram, side of the vehicle, while the electrons accumulate on all surfaces resulting in an increased negative charge.

During day-side orbital conditions, the emission of photoelectrons can have a profound effect on the spacecraft potential. Ultraviolet radiation from the sun causes exposed spacecraft

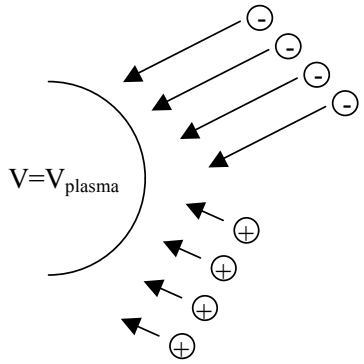

(a) Case where $V = V_{\text{plasma}}$

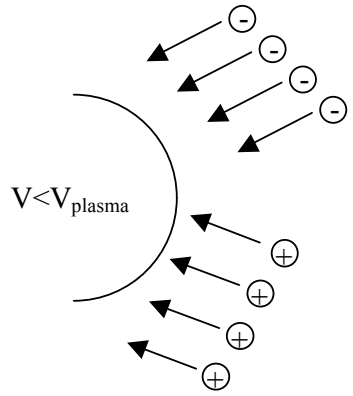

(b) Case where $V < V_{\text{plasma}}$

Figure 7.1: Illustration of spacecraft charging in equilibrium two-component plasma. When spacecraft potential is equal to or greater than space plasma potential, more electrons than ions reach the surface per-unit-time. As the spacecraft potential is reduced, the electrons are slowed by repulsion while the ions are attracted.

surfaces to emit photoelectrons, which is a positive current to the spacecraft. Depending upon surface material properties, the photoelectron current can be the dominant source of charge transfer with the plasma and can cause the spacecraft potential to actually become positive. A figure showing the balance of the plasma and photoelectric current is shown in Figure 7.2.

7.1.2 Absolute vs. Differential Charging

For 30 years spacecraft charging has been studied and an abundant history has been documented of spacecraft failures and anomalies

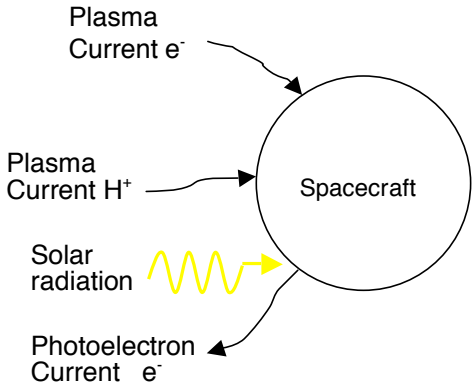

Figure 7.2: Balance of space environmental currents with a spacecraft. Plasma electron and ion current is balanced by photoelectric emission from solar-irradiated surfaces. Spacecraft equilibrium potential will obtain such that the net current is zero.

attributed to this phenomenon. Perhaps the most notorious case was the complete loss of Telsat Canadas Anik E2 satellite in January, 1994, leaving Telsat with the unpleasant loss of a $228 million asset and revenues of an estimated $3 billion.[46] Since the subject of this report is the intentional charging of spacecraft to intimidating voltages, it is important to address the difference between absolute and differential charging.

Spacecraft charging of the type discussed in Section 7.1.1 is known as absolute, or frame charging. In absolute charging the overall vehicle achieves a potential that is different from the surrounding plasma. Pure absolute charging is not, inherently, dangerous to vehicle subsystems. The term "spacecraft charging" typically refers to differential charging of the vehicle. Differential charging can arise from, for example, photoemission on the sunlit side of the vehicle or ram cloud build-up on the upstream face and results in portions of the vehicle achieving different potentials because of localized effects. Differential charging is exacerbated by the use of dielectric materials (such as Kapton and Teflon), which enable components to become electrically isolated from the spacecraft frame and each other.

Differential charging can cause sudden discharge (arcs) between vehicle components

and/or the existence of low-level currents through dielectrics and semiconductors. Arcs and small currents can be disruptive to on-board electronics, which typically utilize low-voltage and low-charge solid-state circuits. Problems can include logic failures, anomalous behavior, or complete destruction of hardware. The susceptibility of a spacecraft for damage due to differential charging depends on the grounding configuration used on the vehicle.

While absolute charging is not associated with the type of catastrophic upsets typical of differential charging, it is not completely without problems. Long-term effects arising from highly biased spacecraft can include surface damage from continuous low-level current discharge to the plasma, spacecraft contamination from re-attraction of emitted or off-gassed material, and sputter erosion from impacting high-energy ions. Such effects can alter thermal performance and/or optical properties of sensitive surfaces like photovoltaic arrays or science instruments.

7.1.3 Active Charge Control

As discussed in Section 7.1.1, an isolated spacecraft will assume an equilibrium charge state such that the net environmental current due to plasma and photoelectron emission is zero. It is possible to change the net vehicle charge by emitting current from the spacecraft. For example, if it is desired to drive the spacecraft charge more negative the emission of positive charge from the vehicle will cause a net surplus of on-board electrons and a lowering of the potential. In order to emit such a current, the charges must be ejected with sufficient kinetic energy to escape the potential well created by the vehicle in space. This is accomplished by biasing an accelerator surface to a positive potential and electrostatically repelling ions from this surface into space. If the vehicle is negatively charged at a potential $-V_{\rm SC}$ referenced to space, then ions must be repelled from a surface maintained at voltage $V_{\rm PS}$ (referenced to spacecraft frame), where $V_{\rm PS}$ must be greater than $|-V_{\rm SC}|$. This is illustrated schematically in Figure 7.3.

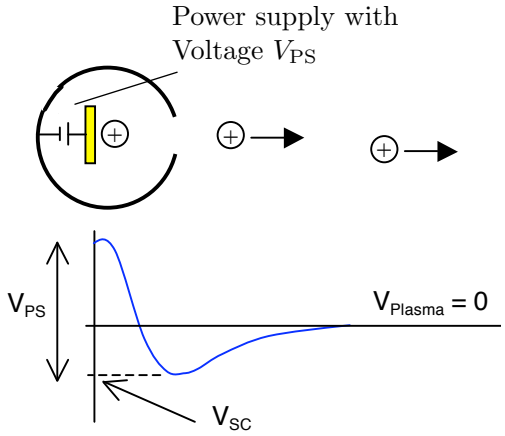

Figure 7.3: Schematic showing required voltage for current emission from spacecraft. $V_{\rm PS}$ is the voltage of the on-board power supply, referenced to spacecraft frame, used to accelerate the ions. $V_{\rm SC}$ is the spacecraft voltage referenced to the space plasma (taken to be zero).

While $V_{\rm PS}$ is greater than $|-V_{\rm SC}|$ ions are emitted with sufficient kinetic energy to be able to escape the spacecraft, the net current to the spacecraft is not zero, and the charge state (potential) of the vehicle will change. Once the spacecraft reaches a potential where $V_{\rm SC} = -V_{\rm PS}$, the emitted ions have insufficient energy to escape the spacecraft (they cant climb the potential hill) and the current is returned. In this case the net current is again zero and the spacecraft charge state will remain stable. This is demonstrated in Figure 7.4

The spacecraft potential will thus stabilize at $V_{\rm SC} = -V_{\rm PS}$. At this increased negative potential, the vehicle will attract a larger amount of ion plasma current from the environment. If the increased ion current from the plasma reaches the spacecraft, the vehicle potential will increase slightly (become more positive), allowing some of the emitted ion current to escape the vehicle and restore the potential to the more negative value. Thus the emitted ion current, I_e, must be at least as large as the environmental ion current, $I_{\rm environ}$, to maintain the vehicle at the steady state potential. If I_e were less than $I_{\rm environ}$, the vehicle power supply would be insufficient to maintain the spacecraft potential

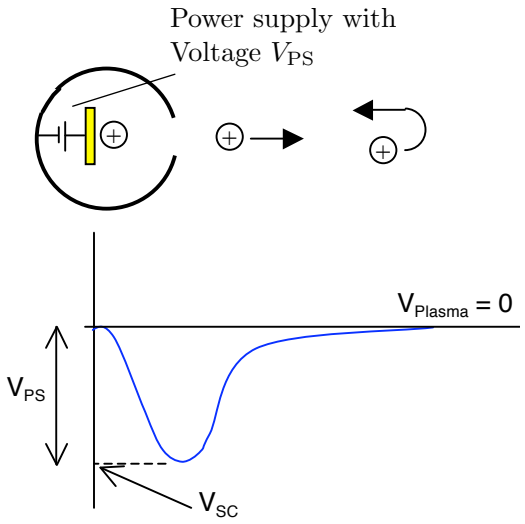

Figure 7.4: Vehicle potential will stabilize when V_{SC} reaches the value of V_{PS}. The energy of the emitted current is no longer sufficient to escape the vehicle and the net current is zero.

at $V_{SC} = -V_{PS}$. The above discussion could easily be extended to include electron emission raising the vehicle potential to some positive value.

The ideal case, presented in Figures 7.3 and 7.4, describes how to actively force a spacecraft potential to some desired value. This is accomplished by accelerating a beam of charges into space through a voltage difference equal to the desired final spacecraft potential. If the current in the beam is greater than the current reaching the spacecraft from the ambient plasma, then the vehicle potential will reach a value equal to the emission voltage and will passively stabilize at that value as long as the emission continues.

7.1.4 Spacecraft-Plasma Interaction

In order to actively charge a spacecraft, the emission control current must be greater than the current to the spacecraft from the ambient plasma. It is thus instructive to analyze the magnitude of the ambient plasma current to the vehicle. A spacecraft in ambient plasma behaves like an isolated probe (Langmuir Probe), repelling or collecting free charges depending upon the vehicle potential. The current-voltage characteristic of a spacecraft is shown in Figure 7.5. In region 1, when the spacecraft has a large negative potential, almost all the plasma electrons are repelled and the current to the vehicle is dominated by plasma ions. This ion current is termed ion saturation current. As the potential of the vehicle is increased, the ion current is reduced because of electrostatic repulsion and a greater number of electrons are able to reach the spacecraft as a result of their kinetic energy. Thus region 2 represents the regime in which both ions and electrons are partially repelled/attracted. At a certain negative potential known as the floating potential, or V_f, the partially repelled electron current will balance with the partially attracted ion current, resulting in a zero net current to the vehicle. This floating potential is the value that a spacecraft would assume in equilibrium and is given by (for $V_{SC} < 0$)

$$V_f = -\frac{kT_e}{e} \ln \left[\sqrt{\frac{T_i m_i}{T_e m_e}} \left(1 - \frac{eV_{SC}}{kT_i} \right) \right] \quad (7.1)$$

For a plasma consisting of protons and electrons at approximately the same temperatures,

$$V_f = -2.5 \frac{kT_e}{e} \quad (7.2)$$

The spacecraft floating potential is thus on the order of, and scales proportionally with, the electron temperature.

Region 3 represents the case where the vehicle potential is highly positive. In this regime, all of the plasma ions are electrostatically repelled from the vehicle and contribute no current, while all of the plasma electrons are attracted. This electron current is termed electron saturation current.

Considering a simple spherical geometry for the spacecraft, the entire J-V characteristic of the vehicle within a space plasma can be given as an expression for the plasma current density, J_p, as a function of spacecraft potential, V_{SC} in two parts. If $V_{SC} < 0$, then

$$J_p = J_{e0} e^{\frac{-e|V_{SC}|}{kT_e}} - J_{i0} \left(1 + \frac{e|V_{SC}|}{kT_i} \right)$$

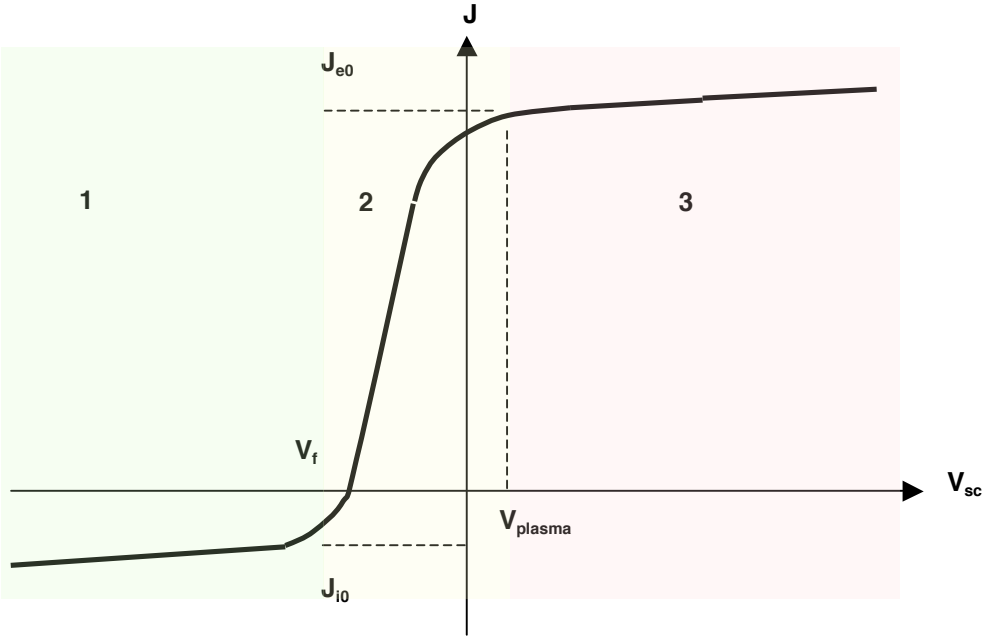

Figure 7.5: . J Vs V Graph for Spacecraft. J is current density (A/m^2) and V is spacecraft potential with respect to space plasma.

If $V_{\rm SC} > 0$, then

$$J_p = J_{e0}\left(1 + \frac{eV_{sc}}{kT_e}\right) - J_{i0}e^{\frac{-eV_{\rm SC}}{kT_i}}$$

where J_{e0} and J_{i0} are the electron and ion saturation current densities, respectively, and are given by

$$J_{e0} = en_e\sqrt{\frac{kT_e}{2\pi m_e}}$$
$$J_{i0} = -en_i\sqrt{\frac{kT_i}{2\pi m_i}}$$

where e is electron charge in C, $n_{i(e)}$ is ion (electron) density in m^{-3}, k is Boltzmann constant in J/K, $T_{i(e)}$ is ion/electron temperature and $m_{i/e}$ is the mass of an ion (electron) measured in kg. For average plasma conditions outside of the plasmapause, such as those given in Table 2.2, the electron and ion saturation currents are on the order of 10_{-6} A/m_2.

In addition to the plasma current to the vehicle, light absorption results in emission of photoelectrons during the day. The flux of electron emission is proportional to the flux of absorbed photons. For the sake of simplicity we assume that the emitted photoelectrons follow a Maxwellian velocity distribution characterized by an average temperature of T_{pe}. When the spacecraft potential is negative, all of the photoelectrons are repelled and emitted into space. When the spacecraft is positive, some of the photoelectrons will be attracted back to the vehicle and the emitted current will be reduced. The photoelectron current density is for $V_{\rm SC} < 0$

$$J_{pe} = J_{pe0} = \text{constant}$$

and for $V_{\rm SC} > 0$

$$J_{pe} = J_{pe0}e^{\frac{-eV_{\rm SC}}{kT_{pe}}}\left(1 + \frac{eV_{\rm SC}}{kT_{pe}}\right)$$

Where T_{pe} is temperature of photoelectrons. The photoelectric current constant, J_{pe0}, is dependent upon material properties and can vary widely, however typical values are on the order of the plasma electron saturation current.

The total current density to the vehicle can then be given by the sum of electron plasma current, ion plasma current and photoelectron

current as follows. If $V_{SC} \leq 0$ then

$$J_p = J_{e0} e^{\frac{-e|V_{SC}|}{kT_e}} - J_{i0}\left(1 + \frac{e|V_{SC}|}{kT_i}\right) - J_{pe0}$$

and if $V_{SC} > 0$, then

$$J_p = J_{e0}\left(1 + \frac{eV_{SC}}{kT_e}\right) - J_{i0} e^{\frac{-eV_{SC}}{kT_i}} - J_{pe0} e^{\frac{-eV_{SC}}{kT_{pe}}}\left(1 + \frac{eV_{SC}}{kT_{pe}}\right)$$

7.2 Review of Active Charging Technology

The mission most directly relevant to the concept discussed here is the SCATHA flight experiment. The SCATHA satellite was launched in January, 1979 with the goal of measuring the build-up and breakdown of charge on various spacecraft components and to characterize the natural environment at GEO altitudes.[7] The satellite potential with respect to space plasma potential was monitored on the SCATHA craft. During passive operation of the satellite, the spacecraft potential was seen to vary from near ground to many kilovolts negative. This natural charging is in agreement with the phenomena as discussed in Chapter 2. One goal of the SCATHA mission was to test the validity of actively controlling the spacecraft potential by emitting charge through an electron beam. To this end, an electron gun was used to transfer charge from SCATHA to the space plasma at various current and voltage levels up to 13 mA and 3 kV.[47]

During experiments with the electron emission system, a very important result, as reported by Gussenhoven, et al., was that, "*the electron beam can achieve large, steady-state changes in the vehicle potential and the returning ambient plasma.*"[48] In fact, Gussenhoven found that when a 3 kV electron beam was operated, "*the satellite became positively charged toa value approaching beam energy for 0.10 mA*" emission current. Similarly, Cohen, et al. report that "*spacecraft frame and surfaces on the spacecraft went positive with respect to points 50 meters from the satellite when the gun was operated. Depending upon ejected electron currents and energies, spacecraft frame-to-ambient-plasma potential differences between several volts and 3 kV were generated.*"[49] These findings support the concept of beam-induced charging as presented in Figures 7.1 and 7.2.

More recent missions employing active spacecraft potential control have focused on avoiding spacecraft charging entirely, rather than purposely charging the vehicle as in the SCATHA experiment. For instance, the international space station (ISS) is equipped with a number of so-called plasma contactors. These devices emit a continuous stream of ions and electrons into the space plasma. The stream of charged particles serves as an electrical ground between the ISS frame and the space plasma, ensuring that the station does not achieve large potential differences from the surrounding environment. This mitigates discharge issues from the 160-volt ISS electrical power system and differential charging along the very large structure.

A number of recent magnetospheric mapping missions have utilized active spacecraft charge control to avoid corrupting data obtained from on-board instruments designed to characterize the surrounding plasma. For instance, if a spacecraft is charged negative with respect to the space plasma, then free electrons reaching on-board detectors will have been decelerated from their undisturbed values, while ions will have been accelerated. It is then of great interest to maintain the spacecraft potential as close as possible to that of the surrounding plasma to obtain accurate characterization of the magnetospheric conditions. Missions showing the feasibility of active charge control include INTERBALL-2,[50] Equator-S,[51] Geotail,[52] and Cluster-II.[53,54]

7.3 Attributes of Coulomb Charge Actuators

7.3.1 Ion/Electron Emission Sources

A variety of technology options exist for

the type of high-energy ion and electron emission sources required for a Coulomb-controlled spacecraft. Each vehicle in a Coulomb formation will likely require both an ion and electron source, to enable positive and negative charging as desired. The electron source will be a relatively straightforward subsystem. The most attractive candidate is some type of field-emission source, so that active heating of a thermionic emitter is not required. The necessary beam currents of tens to hundreds of micro-Amps will not be a challenge, as multiple emitter tips can be employed in parallel to easily satisfy the emission requirement.

Although employed for a different goal, the ion emission system utilized on INTERBALL-2, Equator-S, Geotail, and Cluster-II spacecraft would likely be compatible with the concept explored in this work. In these existing systems, the ion emitter is a solid-needle type liquid-metal ion source using indium as the emission species. A solid needle made of tungsten, with a tip radius between 2 and 5 μm, is mounted in a reservoir with the indium. The reservoir is heated to melt the indium. A potential of 5 to 8 kV is applied between the needle and an extractor electrode. Since the needle is well wetted by the indium, the electrostatic stress at the needle tip pulls the liquid metal towards the extractor electrode. This stress is counteracted by the surface-tension forces of the liquid. The equilibrium configuration assumed by the liquid surface is that of a Taylor cone. The field evaporation of positively charged metal atoms in the strong apex field of the Taylor cone leads to emission of a high-brightness external ion beam. The technology is well developed on an industrial basis.[53,55]

Single tips, as used in the INTERBALL-2 instrument, can produce currents of several tens of μA. The mass efficiency is high. One gram of indium suffices for about 10,000 hours of continuous operation at 10 to 15 μA.[50] For the type of potential control examined in this study, the beam current from a single tip would not be sufficient. It would be straightforward, however, to fabricate an emission system with multiple tips to produce the required current for spacecraft charge control.

7.3.2 Required Power

Basic concepts can be used to calculate the power required to maintain the spacecraft at some steady state potential. To maintain the spacecraft at a voltage of $|V_{\rm SC}|$, current must be emitted in the amount of $|I_e| = 4\pi r^2 |J_p|$, where J_p is the current density to the vehicle from the plasma, using a power supply having voltage of at least $|V_{\rm PS}| = |V_{\rm SC}|$. Quantitatively,

$$P = |V_{\rm SC} I_e| \tag{7.3}$$

For a two-spacecraft formation with each vehicle using Power P, the total system power is just the sum of the individual power to each vehicle. Assuming spherical spacecraft and using Gauss Law to relate the surface potential to the encircled point charge, it is possible to relate the Coulomb force (thrust) on a vehicle to the emission current and the required power

$$F_c = 4\pi\epsilon_0 e^{-d/\lambda_d} \frac{r_A r_B P^2}{d^2 I_{eA} I_{eB}} \tag{7.4}$$

where $r_{A(B)}$ and $I_{eA(B)}$ are the radius and emission current of spacecraft $A(B)$, and d is the vehicle separation.

Eqn. (7.4) yields the power required to produce a steady-state thrust for a given emission current. Since the space environment will be constantly changing (and, hence the emission current to maintain steady state), it is important to calculate the required power to affect a change in potential from some initial value to a desired steady state value. In the pedagogical analysis here, the capacitance of the spherical spacecraft can be used to estimate the power required for a change in voltage (thrust). Using an equivalent circuit model where $\frac{{\rm d}V_{\rm SC}}{{\rm d}t} = \frac{I}{C}$, the rate of change of spacecraft potential can be related to the current absorbed from the plasma and the emitted control current

$$\frac{{\rm d}V_{\rm SC}}{{\rm d}t} = \frac{4\pi r^2 J_p + I_e}{4\pi\epsilon_0 r} \tag{7.5}$$

where J_p is the absorbed plasma current density. The value of J_p can easily be evaluated using traditional plasma probe theory for a sphere

and will take the form $J_p = J_p(V_{SC}, T_e, T_i)$. If V_{final} is the desired steady state spacecraft voltage, then the emission current power supply must have power $P = I_e V_{final}$. Substituting $I_e = P/V_{final}$ into Eqn. (7.5) and using an analytic form for the plasma current, an explicit equation is obtained of the form

$$\frac{dV_{SC}}{dt} = f(P, V_{SC}, T_e, T_i, r) \tag{7.6}$$

which can be numerically integrated to produce a function

$$V_{SC} = V_{SC}(T_e, T_i, r, P, t) \tag{7.7}$$

As a numerical example, Figure 7.6 shows a plot of the function obtained for Eqn. (7.7) assuming a 1-m-diameter spacecraft charging from $V_{SC} = 0$ to V_{final} =6 kV in the average GEO plasma environment. From this plot it is evident that only 200 mW of power is required to change the spacecraft potential by 6 kV within 8 msec.

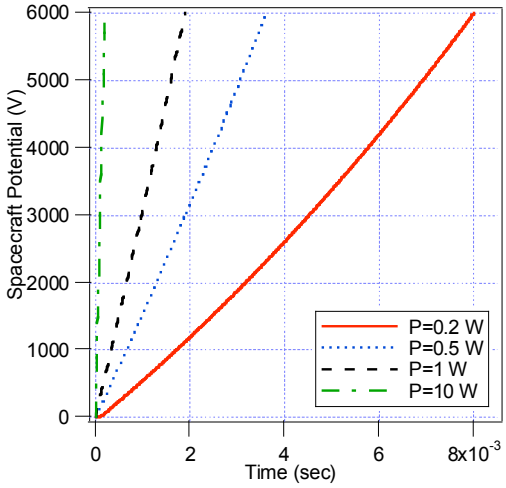

Figure 7.6: Numerical integration of the transient response of a 1-m-diameter model spacecraft in an average GEO plasma as a function of the power in the emitted control beam.

7.3.3 Mass Flow Rate and I_{sp}

Mass flow rate is defined by the rate of gaseous ions expelled per unit time to maintain potential of the vehicle. As electrons have negligible mass we can say that the mass flow rate of electrons is zero and thus driving the potential positive requires zero mass flow. If I_e is the emission current constituting ions, m_{ion} is the mass of ion, and q_{ion} is the charge, then the ion mass flow rate is given by

$$\dot{m} = \frac{I_e m_{ion}}{q_{ion}} \tag{7.8}$$

For a two spacecraft combination, propellant mass flow rate will be the sum of mass flow rates for individual spacecraft and can be related to their individual emission currents

$$\dot{m}_{total} = \frac{m_{ion}}{q_{ion}}(I_{eq} + I_{eB}) \tag{7.9}$$

A common performance parameter used for propulsion systems is specific impulse I_{sp}. This parameter compares the thrust derived from a system to the required propellant mass flow rate. Although I_{sp} is traditionally used as a parameter to evaluate momentum transfer (rocket) systems, we can use the formal definition to compare the Coulomb system. For a Coulomb control system the specific impulse I_{sp} is given by

$$I_{sp} = \frac{F}{\dot{m}_{Total} g_0} \tag{7.10}$$

Since Coulomb force calculations are meaningless for a single vehicle, we will treat the system as two separate vehicles, each subject to a force of F_c given by Eqn. (7.4), so that the sum of the forces experienced by all spacecraft in the formation is $F = 2F_c$.

$$I_{sp} = \frac{8\pi\epsilon_0 e^{-d/\lambda_d} q_{ion}}{g_o m_{ion}} \frac{r_A r_B P^2}{d^2 I_{eA} I_{eB}(I_{eA} + I_{eB})} \tag{7.11}$$

Where g_0 is the gravitational constant (9.81 m/s^2). If $r_A = r_B = r_{sc}$, and $I_e = I_{eA} = I_{eB}$, then Eqn. (7.11) becomes,

$$I_{sp} = \frac{4\pi\epsilon_0 e^{-d/\lambda_d} q_{ion} r_{sc}^2 P^2}{g_0 m_{ion} d^2 I_e^3} \tag{7.12}$$

Note that, unlike a rocket system, the definition of I_{sp} of a Coulomb system is meaningless for a single vehicle. For a formation of two spacecraft, Eqn. (7.12) indicates that the specific impulse of the formation is a function of the radii of the spacecraft, power supplied to the ion (electron) gun, the separation between the two spacecraft, the emission currents of both vehicles, and the mass of the charge carriers, m_{ion}.

Consider a two-spacecraft formation with identical 1-m-diameter vehicles in the average GEO plasma environment charged to the same negative potential. In order to reach and maintain this negative potential, the vehicles must emit an ion current. Consequently, the spacecraft will attract ion saturation current from the plasma, so I_e must be equal to the plasma ion saturation current for steady state. Calculated values of specific impulse for each vehicle in the formation is shown in Figure 7.7 for various system input power levels. The emitted species is taken to be H^+; the data can be extended to any emitted species by dividing the I_{sp} value from the figure by the desired atomic mass. For 1 mW systems with vehicle separation on the order of 20 m, I_{sp} values of 104 seconds are obtained, with values increasing to 10^{10} sec for just 1 W of power. It should be noted that for a positive vehicle potential the emitted species would be electrons and, thus, the calculated values of I_{sp} would be a factor of 2,000 greater.

7.3.4 Emission Current Jet Force

Generating net charge on a spacecraft for Coulomb force requires the emission of current. Because the charge is carried away from the vehicle by particles with non-zero mass, such mass ejection results in a momentum jet force on the vehicle as in a traditional electric propulsion thruster. In the case of electron emission, the mass of the charge carriers is insignificant and the resulting jet force is negligible. Ion emission, however, may produce a significant reaction force. It is instructive to consider how the Coulomb force between spacecraft compares with the momentum reaction on the vehicle induced by the beam of ion current.

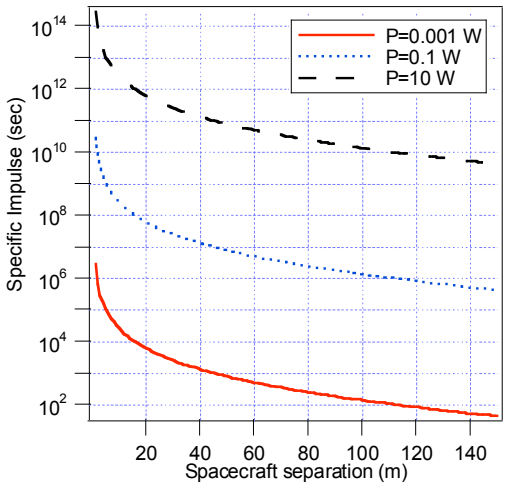

Figure 7.7: Specific impulse for a two-spacecraft Coulomb formation as a function of spacecraft separation, d, and input power, P.

The reactive thrust force of an ejected mass flow is computed as

$$F_j = \dot{m} u_e \tag{7.13}$$

where $\dot{m}$ is the ejected mass flow rate and u_e is the exhaust velocity at which the mass is emitted. Assuming steady state Coulomb force generation, the ions will be electrostatically accelerated through a spacecraft potential of V_{SC}, such that

$$u_e = \sqrt{\frac{2 q_{\text{ion}} V_{\text{SC}}}{m_{\text{ion}}}} \tag{7.14}$$

With this simplification and recognizing that the mass flow is related to the emission current, the momentum jet force of the emitted ion current is

$$F_j = I_e \sqrt{\frac{2 m_{\text{ion}} V_{\text{SC}}}{q_{\text{ion}}}} \tag{7.15}$$

The jet force can also be written in terms of the input power to the emission system as

$$F_j = \sqrt{\frac{2 m_{\text{ion}} P I_e}{q_{\text{ion}}}} \tag{7.16}$$

We can compare the magnitude of the jet reaction force with the induced Coulomb force

between two vehicles. Assume identical spacecraft charged to the same value of $V_{\rm SC}$. From Eqn. (7.4) and Eqn. (7.16) we can write the ratio of F_C/F_J (taking F_C as the total Coulomb force on both vehicles) in terms of the input power as

$$\frac{F_C}{F_j} = 4\sqrt{2}\pi\epsilon_0\sqrt{\frac{q_{\rm ion}}{m_{\rm ion}}}\frac{r_A r_B P^{3/2} e^{-d/\lambda_d}}{I_{eA} I_{eB}(I_{eA}+I_{eB})d^2} \tag{7.17}$$

If $r_A = r_B = r_{\rm sc}$, and $I_e = I_{eA} = I_{eB}$ then Eqn. (7.17) becomes,

$$\frac{F_C}{F_j} = 2\sqrt{2}\pi\epsilon_0\sqrt{\frac{q_{\rm ion}}{m_{\rm ion}}}\frac{r_{\rm sc}^2 P^{3/2} e^{-d/\lambda_d}}{I_e^3 d^2} \tag{7.18}$$

Similar to the calculations for specific impulse, if we consider a formation of two identical spacecraft in GEO having the same diameter of 1 m, charged to the same high negative voltage V_{SC} and provided with same power P, they will each draw ion saturation current from the ambient plasma. So the (ion) emission current I_e will be also the same. Figure 7.8 shows the ratio of Coulomb to jet force assuming hydrogen ion emission in average GEO plasma.

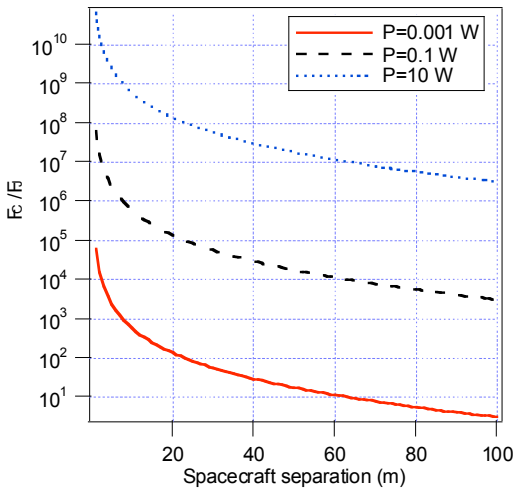

Figure 7.8: Comparison between induced Coulomb force and the momentum reaction of the emitted ion beam used to maintain the spacecraft charge for three power levels.

It can be seen from Figure 7.8 that for separations up to 100 m and system power greater than 1 mW the Coulomb force is considerably higher than the jet force. This implies two conclusions: 1) the Coulomb force is a wiser use of power than a mass-emitting ion thruster, and 2) the directional jet force will not be a significant perturbation to the Coulomb control system

7.4 Attributes of Coulomb Charge Sensors

Emission of charged particle beams can be used to change the spacecraft charge state. To implement this actuator in an active control system, a means to sense the spacecraft charge is necessary. Past missions utilized long (up to 50 m) booms extended into the surrounding space to sense the ambient plasma potential, which the vehicle potential was then measured against. The long booms were necessary to obtain a plasma potential measurement that was outside of the region in space influenced by the charged spacecraft. In these missions, the quantity of interest was the spacecraft voltage with respect to the surrounding plasma. As an example the SCATHA spacecraft is shown in Figure 7.9 and the INTERBALL-2 vehicle is shown in Figure 7.10. On these vehicles the tips of the probes are electrically isolated from the spacecraft and are, presumably, in electrical contact with the undisturbed space plasma potential. The vehicle potential is then measured referenced to the probe tip voltage.

For the work investigated here, the value of spacecraft voltage referenced to undisturbed plasma potential is not critical. Instead, what is of interest is the total net charge of the vehicle. It is the net charge that determines the Coulomb interaction with surrounding charged vehicles. It should be possible to measure this net charge without the use of long probes extending into space. The method identified in the present work to sense spacecraft net charge relies on short differential voltage probes and Gauss Law.

The familiar Gauss Law relates the electric field distribution on the perimeter of a closed surface with the net charge enclosed by the sur-

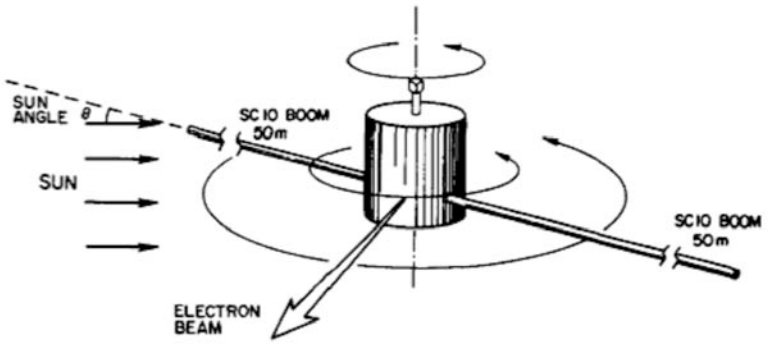

Figure 7.9: Schematic of SCATHA spacecraft. Electrically isolated probes were located at the tips of 50-m booms.[47]

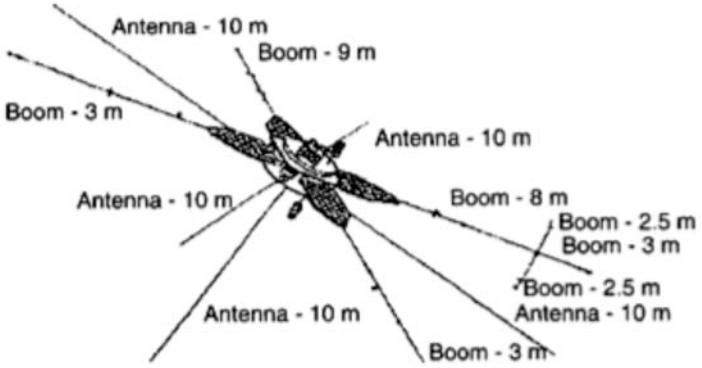

Figure 7.10: The antenna and DC electric field probe configuration of INTERBALL-2.[50]

face. In integral form, the law is expressed as

$$\oint \boldsymbol{E} \cdot \mathrm{d}A = \frac{q}{\epsilon_0}$$

where $\mathrm{d}A$ is an element of surface area and q is the total encircled electric charge. For a simple spherical spacecraft, it is possible to measure the value of the radial electric field at a single point on the spacecraft surface and use Gauss Law to determine the amount of charge contained in the spacecraft. For this geometry the integral becomes simply

$$\oint \boldsymbol{E} \cdot \mathrm{d}A = 4\pi r^2 E\Big|_r = \frac{q}{\epsilon_0}$$

and the net vehicle charge is determined by

$$q = 4\pi r^2 \epsilon_0 E\Big|_r$$

For a representative spacecraft with radius 1 m charged to kilovolt potentials, this implies a radial electric field at the spacecraft surface of 1,000 V/m.

Because of the spherical symmetry, the radial electric field for this simple case could be measured in a straightforward manner using two isolated electric probes separated by some radial distance Δr. If the impedance between each probe and spacecraft frame is large enough, the probes will float to the local value of electric potential. The radial field can be obtained by taking the voltage difference between the probes divided by the separation, Δr. Such a technique to measure DC electric fields is commonly used and has, in fact, been employed in space on-board the Fast Auroral Snapshot (FAST) spacecraft, where isolated probes were used to measure the DC electric field in the

Earths auroral region.[56] On the FAST mission, it was possible to resolve very weak ambient magnetospheric electric fields. The typical Coulomb-actuator-induced radial field of 1,000 V/m would manifest as an easily measurable voltage difference of 100 V between two probes separated by 10 cm. A schematic of this is shown in Figure 7.11. This concept assumes that the ambient plasma Debye length is large compared to the spacecraft, such that the electric field created by the charged vehicle is not shielded by the plasma until an appreciable distance from the craft.

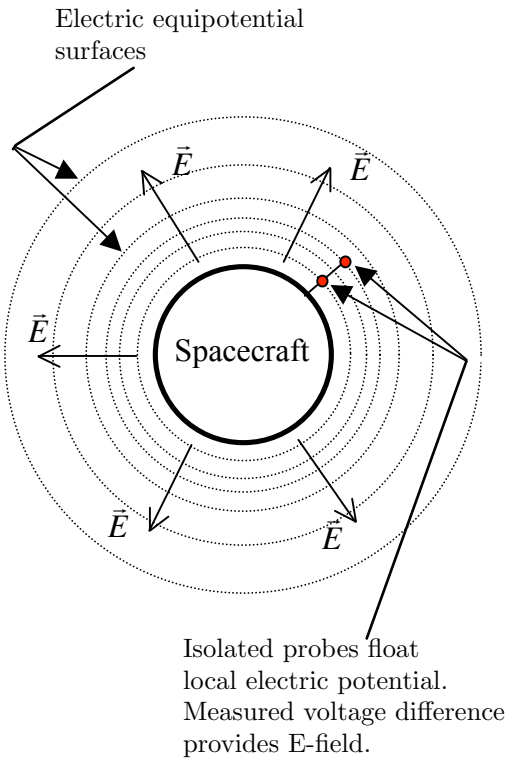

Figure 7.11: Concept of using differential voltage probes to measure the electric field surrounding a spacecraft. For this simple spherical geometry, a single differential probe can provide the information necessary to solve Gauss Law for the net spacecraft charge.

Since spacecraft are, of course, not likely to be spherical, actual implementation of the proposed technique would require real-world modifications. In principle the technique would be identical. The difference arises from the more complicated geometry of the control surface and the need to measure the electric field at a number of points around the vehicle to obtain a sufficiently accurate approximation to the surface integral in Gauss Law. It is possible that even complex vehicle geometries could be accommodated through extensive characterization and finite-element modeling of the geometry.

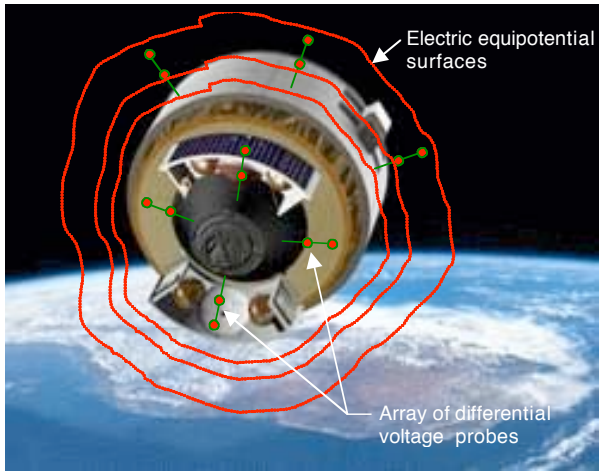

Figure 7.12: Real spacecraft would require an array of differential voltage probes and finite-element vehicle characterization to provide an adequate approximation to the surface integral in Gauss Law.

Chapter 8

Performance Comparison of Coulomb Propulsion vs. Conventional Electric Thrusters

8.1 Performance Metrics

The purpose of this section is to compare the method of Coulomb thrusting to that of more conventional propulsion systems. Since the missions under consideration in this study typically utilize micro-Newton-level forces for formation-keeping and repositioning, the conventional thrusters that are relevant are micro electric propulsion (EP) devices. The figures of merit for EP devices are specific impulse (I_{sp}), power (P), and thrust (T).

Specific impulse is a measure of "fuel efficiency" for a thruster. By definition, specific impulse is the total impulse delivered by the thruster divided by the mass of propellant required to deliver the impulse:

$$I_{\text{sp}} = \frac{T\tau}{M_{\text{prop}}g} \tag{8.1}$$

where T is the maneuver-averaged thrust and τ is the time required to perform the maneuver. The factor g (the acceleration due to gravity at Earths surface) is included as a constant of convenience – its purpose is to ensure that Isp is expressed in seconds regardless of unit system chosen. Rearranging, specific impulse can be written in its more familiar form:

$$I_{\text{sp}}\frac{T}{\dot{m}g} \tag{8.2}$$

where $\dot{m}$ is the mass-flow rate of propellant consumption. Realizing that the thrust force is $T = \dot{m}u_{\text{jet}}$, where u_{jet} is the velocity of the particles expelled from the thruster, specific impulse can be related to the jet velocity by:

$$I_{\text{sp}} = \frac{u_{\text{jet}}}{g} \tag{8.3}$$

Thus, the specific impulse is a direct measure of the effective jet exhaust velocity – its numerical value (in seconds) is roughly $1/10^{\text{th}}$ the exhaust velocity (in m/s).

For any kinetic (rocket) propulsion system, a fundamental relation exists between the figures-of-merit. The relation can be derived by realizing that the rate of momentum emission (thrust) from the jet is given by $T = \dot{m}u_{\text{jet}}$ while the rate of energy emission (power) from the jet is $P = \frac{1}{2}\dot{m}u_{\text{jet}}^2$. Dividing thrust by power and utilizing the definition of specific impulse,

$$T = \frac{2P}{gI_{\text{sp}}} \tag{8.4}$$

In EP devices, the jet power is derived from some on-board electrical source (batteries or solar arrays). There is some conversion efficiency between the electrical power supplied, P_{sup}, and the power that is deposited into kinetic energy of the jet, P_{sup}. Expressing the device efficiency as

$$\eta = \frac{P}{P_{\text{sup}}} \tag{8.5}$$

the relation between performance metrics can finally be written as

$$T = \frac{2\eta P_{\text{sup}}}{g I_{\text{sp}}} \tag{8.6}$$

It is important to realize that this relation only holds true for kinetic (rocket) propulsion systems. Because the Coulomb thrusting system analyzed here is not a kinetic system, the above relation does not apply. It is, however, possible to calculate *effective* specific impulse and power quantities for Coulomb systems to facilitate direct comparison with EP devices. These quantities are derived fully in Section 7.3.

8.2 Conventional Electric Thrusters

For the types of missions considered in this study, there are three EP systems of sufficient maturity to warrant comparison. The first of these is a micro-pulsed plasma thruster (μPPT). The μPPT is essentially an electromagnetic accelerator, which uses solid Teflon bars as propellant. It is a pulsed thruster with characteristically very short pulse width of the order of tens of microseconds. In principle, it can be throttled using pulse-width-modulation (although it is typically not operated in this mode). The minimum amount of impulse that can be imparted to a spacecraft in one pulse (the impulse bit) can be as small as 2 μNewton-seconds. μPPTs can be characterized by $I_{\text{sp}} =$ 500 sec and $\eta = 2.6\%$.[57,58] With a power range of a few to a few tens of Watts, the thrust range is 10 – 100 μN.

The second candidate EP device is the colloid thruster. A colloid thruster extracts charged droplets (and/or free ions) from an electrolytic liquid using strong electric fields in a manner not unlike that of an inkjet printer nozzle. Common examples of propellant mixtures include combinations of formamide or glycerol as solvents and sodium iodide (NaI) or lithium chloride (LiCl) as solutes. Colloid thruster performance can be characterized by $I_{\text{sp}} =$ 1,000 sec and efficiency $\eta = 65\%$.[57] By changing the number of needle-tip emitters in a single device, thrust has been demonstrated from 1 μN to several mN.

The third EP technology is the Field-emission electric propulsion (FEEP) device. Similar to the colloid thruster, the FEEP device extracts charged particles from a liquid propellant. The difference is in the propellant used and operating voltage range. Instead of electrolytic fluid, FEEP uses liquid phase metal, like cesium or indium because of their low ionization potential, high atomic weight and low melting point. Ions are directly extracted by field emission and subsequently accelerated down the electric potential. In order to overcome the ionization potential they need to be operated at higher voltages than the colloid thrusters. The FEEP technology can be characterized with performance parameters of $I_{\text{sp}} =$ 10,000 sec and efficiency $\eta =$ 65%.[57] Power ranges from 10^{-5} W for a single emitter up to a few W for clustered emitters.

Another important figure of merit for EP devices is the power-specific mass. This parameter characterizes the inert mass of the required power processing hardware to convert the onboard electrical power to the form required for the EP device. It can include voltage amplification, current regulation, and pulse-forming. The parameter is usually given by the symbol β and is expressed in units of kg/W. The three candidate EP devices are summarized in Table 8.1.

8.3 Modeling Coulomb Performance

It is possible to calculate representative propulsive figures of merit for Coulomb thrusting maneuvers such as those presented in Chapters 5 and 6. To facilitate comparison with EP devices, the goal is to calculate the mass flow and power required to perform a given thrust history using Coulomb propulsion. These parameters can then be used to derive the effective specific impulse of the Coulomb maneuver along with the power required for charge control of the participating vehicles.

Table 8.1: Typical performance statistics of EP devices capable of performing the missions analyzed in this study.

Device	Power (W)	Thrust (μN)	I_{sp} (s)	Efficiency	β (kg/W)
μPPT	1–10	10–100	500	2.6%	0.37
Colloid	10^{-3} – 10	1 – 1,000	1,000	65%	0.27
FEEP	10^{-3}	0.01 – 100	10,000	65%	0.11

The model described here uses as inputs the force vs. time and charge vs. time histories from simulations in Chapter 5 and 6. The spacecraft potential is related to the vehicle net charge according to

$$V_{\text{SC}} = \frac{q}{4\pi\epsilon_0 r} \tag{8.7}$$

where q is the spacecraft charge and r is the vehicle radius (assuming spherical spacecraft). As discussed in Chapter 7, in order to maintain a vehicle at a steady potential, V_{SC}, the Coulomb emission system must be capable of ejecting a beam of current with potential V and magnitude equal to the current arriving at the spacecraft from the ambient plasma. The ambient plasma current as a function of spacecraft voltage is shown in Figure 7.5. For the model discussed here this $I-V$ characteristic is simplified to ease calculations and provide a worst-case value of plasma current. The simplified spacecraft $I-V$ characteristic due to the plasma is given as:

$$J_p = \begin{cases} V_{\text{SC}} \leq 0 & J_p = -J_{i0}\left(1 + \frac{e|V_{\text{SC}}|}{kT_i}\right) \\ J_p = V_{\text{SC}} > 0 & J_{e0}\left(1 + \frac{e|V_{\text{SC}}|}{kT_e}\right) \end{cases} \tag{8.8}$$

Graphically, such an $I-V$ characteristic would look as shown in Figure 8.1. The assumed characteristic does two things: (1) ignores the transition region between electron and ion saturation currents and, instead, models the plasma current as either electron saturation or ion saturation current, and (2) ignores the effect of photoelectron emission. The first property has the effect of introducing a plasma current that is greater than the actual current for voltages less than the plasma electron temperature, while the second property assumes away the photoelectron current, avoiding the need to specify spacecraft material properties and sun angles.

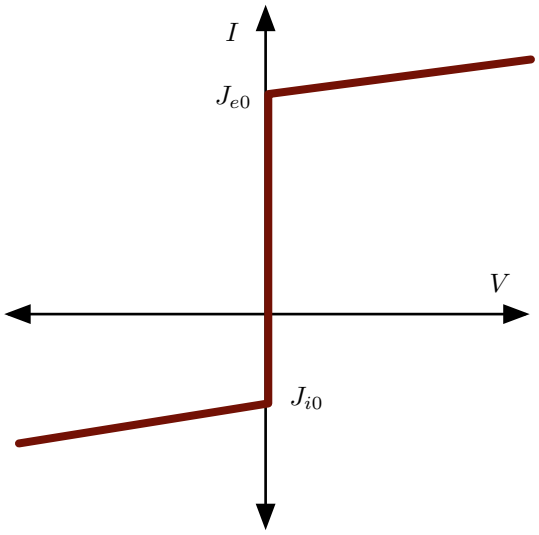

Figure 8.1: Simplified $I-V$ characteristic for space plasma current to vehicle.

To maintain a steady-state spacecraft voltage of V_{SC}, the charge emission system must then emit a beam, with energy eV_{SC} and magnitude given by

$$I_e = 4\pi r^2 J_p \tag{8.9}$$

The power required to supply this beam is

$$P = I_e|V_{\text{SC}}| \tag{8.10}$$

as discussed in Chapter 7. For the maneuvers considered in Chapters 5 and 6, the spacecraft voltage (net charge) is not steady and, instead, changes in time to affect the desired trajectory. The required beam emission current can be adjusted in a straightforward manner to account

Table 8.2: 2-vehicle repositioning maneuvers used to evaluate propulsive performance of Coulomb thrusting.

Case Name	Vehicle 1 Mass (kg)	Vehicle 2 Mass (kg)	Vehicle 1 Radius (m)	Vehicle 2 Radius (m)	Separation Goal (m)	Maneuver Time (h)
2-1-12	50	50	0.5	0.5	12	1
2-1-22	50	50	0.5	0.5	22	1
2-3-12	50	50	0.5	0.5	12	3
2-3-22	50	50	0.5	0.5	22	3
G-1-25	50	1000	0.5	10	25	1
G-1-35	50	1000	0.5	10	35	1

for the change in vehicle charge. If, at time t, the vehicle potential is $V_{\rm SC}$and the net charge is changing at a rate of $\mathrm{d}q/\mathrm{d}t$, the required beam emission current is simply

$$J_e = 4\pi r^2 J_p + \frac{\mathrm{d}q}{\mathrm{d}t} \tag{8.11}$$

The spacecraft must emit (1) enough charge to cancel the current from the ambient plasma, and (2) enough charge to cause the vehicles net charge to change according to the proscribed charge vs. time history specified for the maneuver. At time t the power is still given by $P = I_e|V_{\rm SC}|$, however the emission current now contains two terms.

The mass flow rate required to control the vehicles charge can be calculated based on the emission current. If the charge vs. time maneuver requires the emission system to eject negative charge (either maintain a positive vehicle potential or increase the instantaneous potential), then the required mass flow is zero because this can be accomplished using an electron beam. However, if the maneuver requires the emission of positive charges then atomic ions must be emitted resulting in a finite system mass flow. For a required positive charge emission current of I_e, the resulting mass flow is

$$\dot{m} = \frac{I_e m_{\rm ion}}{e} \tag{8.12}$$

where $m_{\rm ion}$ is the mass (kg) of the emitted species and we have assumed that all atoms are singly ionized.

8.4 Representative Mission Analysis

Two representative maneuvers using Coulomb thrusting were analyzed to calculate propulsive figures-of-merit. In the first maneuver, two identical spacecraft with 0.5-m radii are initially located 2 m apart. Coulomb thrusting is used to deploy the spacecraft to a new separation distance and to halt the deployment once the spacecraft reach the desired state (see Section 6.1.3). The second maneuver considered was similar, with the exception that the vehicles are not identical. In the second case, one of the vehicles had radius of 10 m (so-called gluon vehicle) while the second had radius of 0.5 m. The initial separation between spacecraft was 15 m. Both maneuver time and final separation distance were varied. The representative missions profiles are tabulated in Table 8.2.

The input to the performance models were the charge vs. time and force vs. time histories computed in Section 6.1.3 These parameters were used along with the modeling equations of Section 8.3 to calculate power history, mass flow, and specific impulse. Sample input files for maneuver 2-1-12 are shown in Figures 8.2(a) and 8.2(b).

Based on the vehicle radius and the required charge, the vehicle potential can be derived and is plotted in Figure 8.3(a). Given the spacecraft potential, the simplified $I - V$ characteristic of Section 8.3 is used to calculate the required emission current from the Coulomb

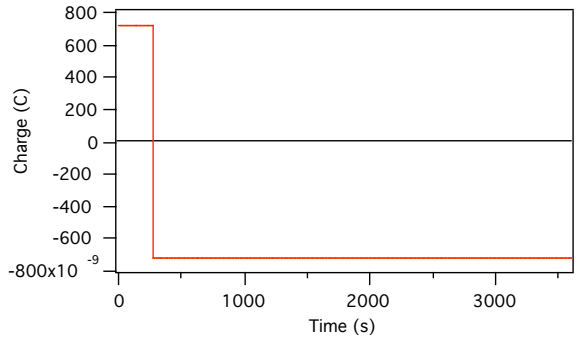

(a) Charge Time History

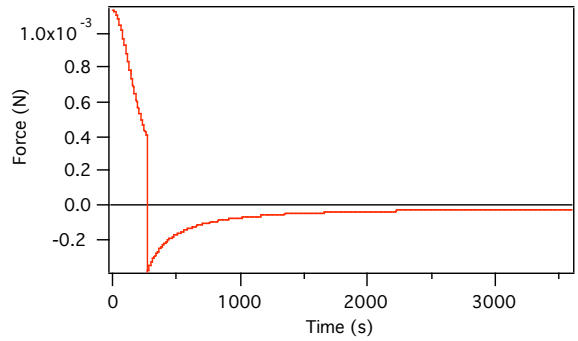

(b) Force Time History

Figure 8.2: Maneuver 2-1-12 Illustration

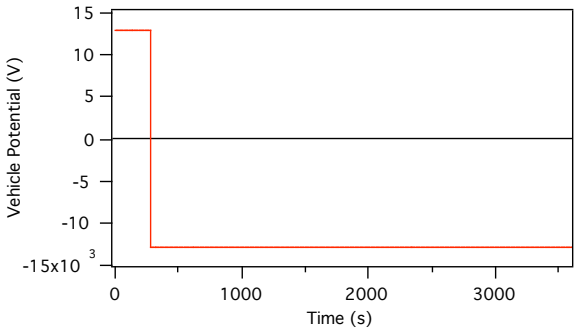

(a) Spacecraft Voltage

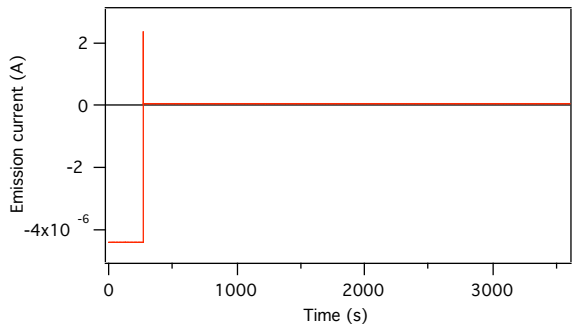

(b) Ion Emission

Figure 8.3: Voltage and Ion Emission for Case 2-1-12

charge actuator. The emission current is plotted in Figure 8.3(b) and the sign convention is taken that positive charge emission from the vehicle equates to positive emission current.

With the current and voltage requirements of the Coulomb actuator known, the time history of actuator power can be calculated according to the methods in Section 7.3; this history is shown in Figure 8.4(a). The required propellant mass is obtained from the emission current. While negative emission current (ejection of electrons) requires zero mass flow, the emission of positive current requires ion ejection. Based on the success of the charge actuator used on the Cluster mission[54] the analysis here assumes indium will be the charge-carrying species. The actuator mass-flow-rate is shown in Figure 8.4(b). The mass flow rate can be integrated in time to calculate the total mass required for the maneuver, while the force vs. time history can supply the total maneuver impulse. With these parameters known, the effective specific impulse of maneuver 2-1-12 is calculated to be $3.08 \cdot 10^8$ seconds.

Similar analyses were performed for all cases shown in Table 8.2. Since maneuver profiles were similar, the trends in current, power, and mass flow are similar for all cases. The propulsive performance metrics are summarized in Table 8.3. Here, the values of effective specific impulse and peak power (max power required during maneuver) are reported.

8.5 Concluding Remarks

In comparing Table 8.1 with Table 8.3 it is apparent that the Coulomb actuators have specific impulse at least two orders of magnitude greater than competing electric thrusters. For all maneuvers with the exception of the gluon cases, the required beam power is only a few tens of mW for Coulomb control. The largest emis-

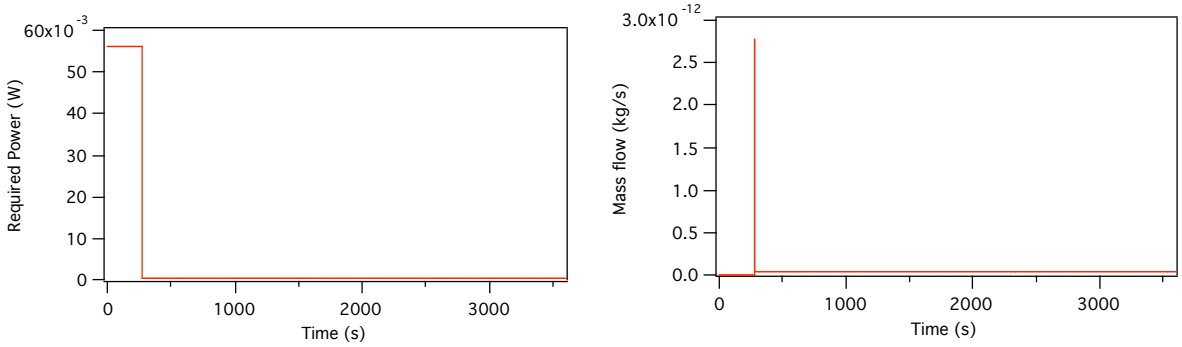

(a) Power characteristics for Coulomb actuator

(b) Actuator mass flow rate

Figure 8.4: Coulomb Thrusting Performance for Case 2-1-12

Table 8.3: Summary of propulsive figures-of-merit for representative Coulomb repositioning maneuvers.

Case Name	Vehicle 1 Peak Power(W)	Vehicle 2 Peak Power (W)	Vehicle 1 Specific Impulse (s)	Vehicle 2 Specific Impulse (s)
2-1-12	$56 \cdot 10^{-3}$	$56 \cdot 10^{-3}$	$3.08 \cdot 10^{8}$	$3.08 \cdot 10^{8}$
2-1-22	$50 \cdot 10^{-3}$	$50 \cdot 10^{-3}$	$1.4 \cdot 10^{10}$	$1.4 \cdot 10^{10}$
2-3-12	$7.4 \cdot 10^{-3}$	$7.4 \cdot 10^{-3}$	$6.5 \cdot 10^{7}$	$6.5 \cdot 10^{7}$
2-3-22	$42 \cdot 10^{-3}$	$42 \cdot 10^{-3}$	$9.8 \cdot 10^{7}$	$9.8 \cdot 10^{7}$
G-1-25	$4.7 \cdot 10^{-3}$	$17.9 \cdot 10^{-3}$	$6.02 \cdot 10^{8}$	Inf (zero mass flow)
G-1-35	$154 \cdot 10^{-3}$	$60 \cdot 10^{-3}$	$7.2 \cdot 10^{8}$	Inf (zero mass flow)

sion current and, hence, the greatest mass flow, is demanded during spacecraft polarity change when it is desired to change the net charge from positive to negative in a very short time. Compare the charge vs. time history of Figure 8.2(a) with the emission current (Figure 8.3(b)) and the corresponding mass flow (Figure 8.4(b)). The fast polarity switching requires a relatively large burst of emission current. Maneuvers that did not require sudden polarity change would thus be expected to have an even higher effective specific impulse.

The gluon cases of G-1-25 and G-1-35 show an interesting behavior involving spacecraft scaling. As the vehicle radius (r_{SC}) is increased, the vehicle potential required to obtain the desired net charge decreases by the relation

$$V_{\mathrm{SC}} = \frac{q}{4\pi\epsilon_0 r_{\mathrm{SC}}} \tag{8.13}$$

Thus, it seems intuitive that the emitted beam power (emission current multiplied by vehicle potential) would be less for larger vehicles. This is not the case, however. As the vehicle radius becomes larger and the surface area grows according to r_{SC}^2, the current from the ambient plasma, given by $4\pi r_{\mathrm{SC}}^2$, increases. While the required beam voltage decreases as $1/r_{\mathrm{SC}}$, the required beam current to overcome the ambient plasma current increases by r_{SC}^2, so the net effect is that required actuator power increases linearly with vehicle size. It is noted, however, that even the 5-m-radius gluon considered here only required an actuator power of 60 W for the most demanding maneuver.

A more difficult parameter to characterize is the total inert mass required of a Coulomb actuator system. To arrive at a meaningful value, it is necessary to know the power-specific mass

of the Coulomb actuation system. As in an EP system, this mass would include such components as amplifiers, filters, and pulse-forming devices. Some insight is possible by analyzing the Cluster active charge controller that has been successfully flown.[54] In this device, the beam emission system was, essentially, an indium FEEP electric thruster. It is reasonable to assume, then, that the power-specific mass for a Coulomb actuator would be similar to that of the FEEP technology at β=0.11 kg/W. While it would be presumptuous to calculate inert mass numbers based on such approximations, it is justified to say that the inert mass of a Coulomb actuator would be no greater than that of a competing EP thruster of the same power. Moreover, since the Coulomb system requires far less power than a kinetic EP device of the same thrust, the inert mass of a Coulomb actuator would be less than a competing EP thruster. Coupled with the greatly increased specific impulse, which results in a corresponding decrease in propellant mass, the Coulomb control system promises strong benefits over EP thrusters

Chapter 9

Bibliography of Published Work

1. C. C. Romanelli, A. Natarajan, H. Schaub, G. G. Parker, and L. B. King, "Coulomb Spacecraft Voltage Study Due to Differential Orbital Perturbations," Accepted to the AAS Space Flight Mechanics Meeting, Tampa Florida, January 22–26, 2006.

2. A. Natarajan, H. Schaub, and G. G. Parker, "Reconfiguration of a 2-Craft Coulomb Tether," Accepted to the AAS Space Flight Mechanics Meeting, Tampa Florida, January 22–26, 2006.

3. G. G. Parker, L. B. King, and H. Schaub, "Charge Determination for Specified Shape Coulomb Force Virtual Structures," Submitted to 47^{th} AIAA/ASME/ASCE/AHS/ASC Structures, Structural Dynamics, and Materials Conference, Newport, Rhode Island, May 1–4, 2006.

4. G. G. Parker, L. B. King, and H. Schaub, "Steered Spacecraft Deployment Using Interspacecraft Coulomb Forces," Submitted to American Controls Conference, Minneapolis, Minnesota, June 14–16, 2006.

Chapter 10

Concluding Remarks

10.1 Conclusion

This report discusses the results of an 8-month inter-disciplinary research project between Virginia Polytechnic Institute and State University and Aerophysics Inc. The important findings of the plasma environment study are that the plasma Debye length is on the order of 0.01–0.03 meters at low Earth orbit. This strong electric field masking parameter makes the Coulomb thrusting concept infeasible at this low altitude with a cold, dense space plasma. At higher altitudes the Van Allen radiation belts are of concern. The data here shows that the Debye length is still only 0.03–0.26 meters, too small for practical use with Coulomb thrusting. Beyond 5-6 Earth radii outward to geostationary altitudes the Debye length is found to vary between 100–1000 meters. The rest of the research focused on mission flying in high Earth orbits outside of the Van Allen radiation belts. At these altitude the dominant differential orbital perturbation is differential solar radiation pressure. This is true for spacecraft separation distances outward to 1000 meters. Conservative estimates show that flying spacecraft about 20 meters apart at GEO would require multiple kilovolts to compensate, assuming a 50kg craft with 0.5 meter radius. Further, considering the Earth magnetic field, for the induced Lorentz force to be comparable to differential solar radiation pressure, the craft would have to charge up to multiple mega-volt levels. The expected open-loop maintenance charge level studies are conducted for a classical formation of spacecraft, as well as a gluon-deputy formation concept. Here the gluon craft size is enlarged to be able to carry a higher charge level. Flying 20–30 meters apart, these voltages are around 10's of kilovolt.

A study is performed to investigate voltage requirements to perform static Coulomb structures. Here the electrostatic force cancel the relative orbital acceleration to yield an invariant formation shape as seen by the rotating center of mass frame. An important finding is that it is possible to construct virtual structures where sensor craft are in a desired geometry (e.g. distributed radar interferometry), while other charged craft in this virtual structure are in a support role to help maintain the shape.

The important findings of the deployment study include numerical simulations of deputy craft being released from a mother craft using rest-to-rest or rest-to-motion scenarios. The simulations use closed-loop charge control to achieve the final position and/or velocities. Using essentially no fuel, this study shows that deputy craft can be relocated dozens of meters using 10's of kilovolt levels of charge. Maneuver times are typically several hours.

Another study investigated the required maximum charge level to change the separation distance of two inertially floating spacecraft within a specified amount of time. An important result of this research was finding a robust numerical optimization method to find such solutions. The inverse square drop off of the electrostatic field strength causes strong sensitivity issues with larger separation distance. Homotopy methods were employed to sweep through a range of separation distance, travel times, and

plasma Debye lengths. To reconfigure 2 craft from 2 to 25 meters in a few hours requires 1–10's of kilovolts.

A related study investigates a closed-loop charge control of a 2-craft nadir pointing formation at GEO. Here the gravity gradient torque acting on the system is exploited to stabilize the formation attitude while changing the length. Important findings include analytical predictions of fast the craft can increase or decrease their separation distance while still guaranteeing linear stability of the non-autonomous system. Maneuver times are typically around 1–2 days to allow the weak local gravity gradient to stabilize the in-orbit-plane formation attitude.

The charge control study found a promising method servo the spacecraft voltage level. An array of small differential voltage probes are added to the vehicle which can measure the electric potential. Having a model of the vehicle geometry and materials, it is then possible to estimate the total vehicle potential. Further, to achieve this potential, a simple ion or electron gun is used. An important conclusion is that this process is insensitive to plasma potential variations. The local variations of space plasma between spacecraft is minimal due to the small separation distances. Thus, it is only necessary to control the spacecraft charge relative to the plasma. This is a substantial simplification to the charge control process on the CLUSTERS mission.

Finally, the mass and power comparison study shows that the Coulomb thrusting concept is orders of magnitudes more efficient than ion-engine technologies, and often requires as little as 1 Watt of power or less. In fact, the total electrical power requirement for Coulomb thrusting are determined not by the propulsion method needs itself, but rather by the power requirements of the supporting electronics and thermal control.

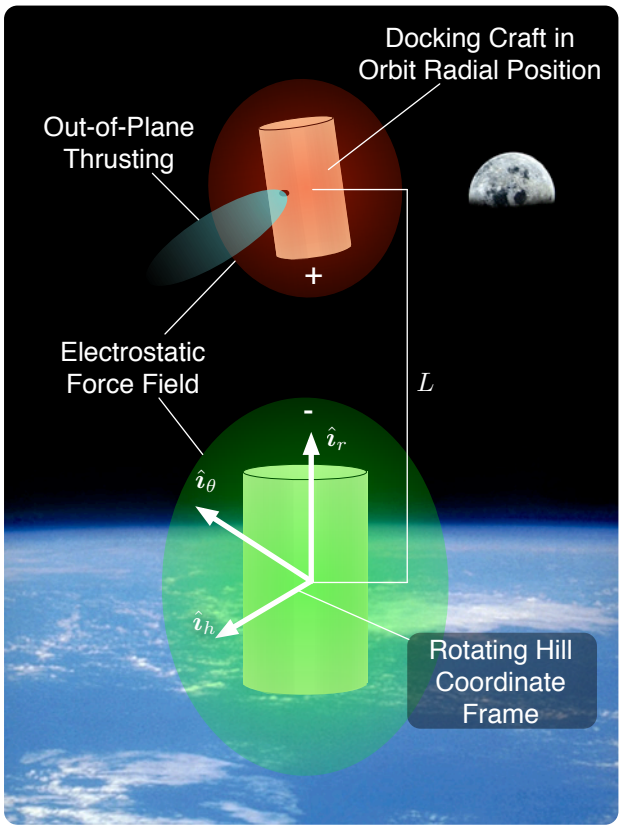

Figure 10.1: Illustration the inter-spacecraft electrostatic force being used to dock 2 spacecraft in a nadir pointing formation.

10.2 Implications for Further Research

10.2.1 Docking Operations

A very promising use of Coulomb thrusting is docking and proximity flying operations. Docking in particular is a very challenging operation that requires significant fuel amounts to perform the many small orbit corrections. Consider the scenario where one craft is approaching another. If the approach speed is too large, a thruster is conventionally used to slow the relative motion. However, for optimal fuel efficient maneuvering, the thruster would be firing the same direction as the target craft. The resulting exhaust plume could damage the other vehicle, or even push it away. Instead, the control thruster must be angled away from the target craft. Here some of the thrusting components

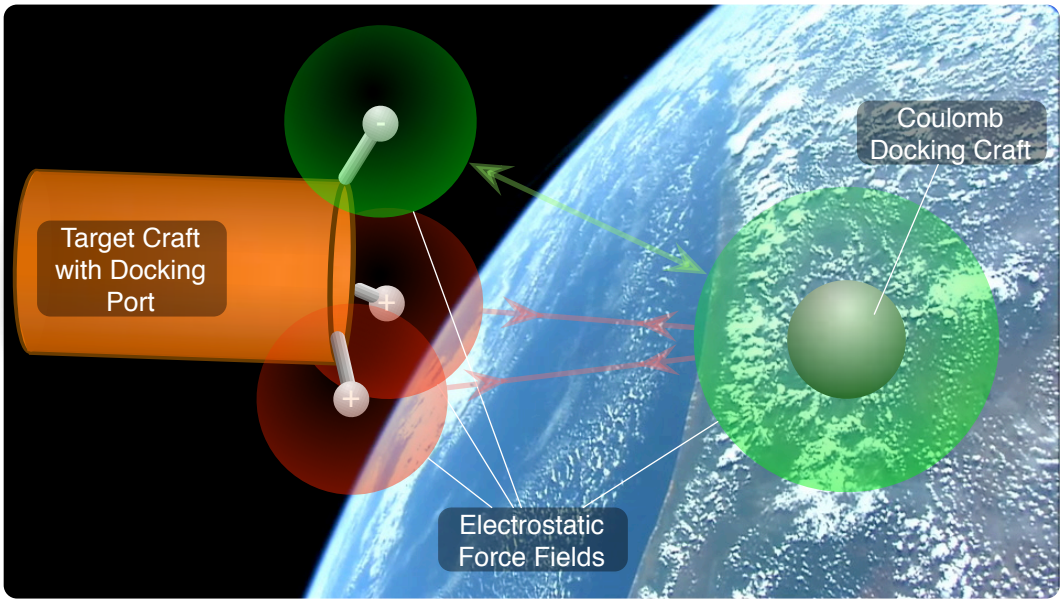

Figure 10.2: Illustration of a Coulomb docking vehicle being guiding into the docking mechanism of a target craft using Coulomb forces.

will mutually cancel each other, while only a fraction of the thrusting is used to achieve the desired slow down.

Using a Coulomb force to control the relative motion avoids the plume impingement issue, while the required fuel requirements would be near zero. One docking concept envisions using a nadir-pointing docking approach. The chaser craft maneuvers above the target craft and arrests its relative motion. Without further control, such a nadir-pointing 2-craft formation is unstable and will drift apart. However, by engaging the Coulomb thrusting mechanisms between the two craft it is possible to stabilize the in-plane relative motion. The electrostatic force is used to directly regulate the separation distance as illustrated in Figure 10.1. Note that each craft is charged to a common voltage level. No differential charging is used in this approach. By employing a nadir-pointing docking approach, the 2 craft with a regulated separation distance behave similar to a slender rigid body in orbit. The gravity gradient torque acting on the formation is exploited here to stabilize the in-plane orientation simultaneously as the separation distance is regulated. The out-of-plane motion linearly decouples from the other two degrees of freedom. To zero any such out-of-plane relative motion, this concept employs traditional thrusters firing in the orbit normal direction. Plume impingement issues are avoided because the craft formation is nadir-pointing. This scenario provides an elegant docking approach solution which uses minimal amounts of fuel and allows for well controlled separation distance control.

Another docking concept employing Coulomb forces is illustrated in Figure 10.2. The target craft is equipped with several charging surfaces which can be servoed to different voltage levels. The connecting rods are made out electrically isolating material to avoid charge leakage. This setup allows for general three-dimensional electrostatic fields to be projected ahead of the docking mechanism. By charging up the chaser craft to a fixed voltage level, a general three-dimensional force vector is created between the craft. Note that this is a conceptual difference to the nadir-align approach strategy where only a force vector along the spacecraft center of masses can be produced. The chaser craft can now be carefully pulled in towards the target craft docking mechanisms. Conventional thrusting is only employed here to estab-

lish the chaser craft within a particular parking box ahead of the chaser craft. The target craft is assumed to have its own station keeping and attitude control capability.

10.2.2 Swarm Deployment

Another are of future research is the use of Coulomb thrusting to deploy a swarm of small satellites. For example, pico-satellites only have about 200-500 grams of mass. Such small craft cannot carry very much fuel onboard, if any, to perform orbit corrections. If a mechanical deployment mechanism is used, then the ejected spacecraft velocity is determined at the time or release. Any launch errors in heading or speed cannot be corrected release. However, if the deployed craft is charged to a fixed value, and the mother craft has several charge surfaces similar to the general docking concept, then the deployed craft trajectory can be controlled and corrected for dozens of meters after release. This concept is illustrated in Figure 10.3. A cluster of small satellites could be deployed very precisely using such a system.

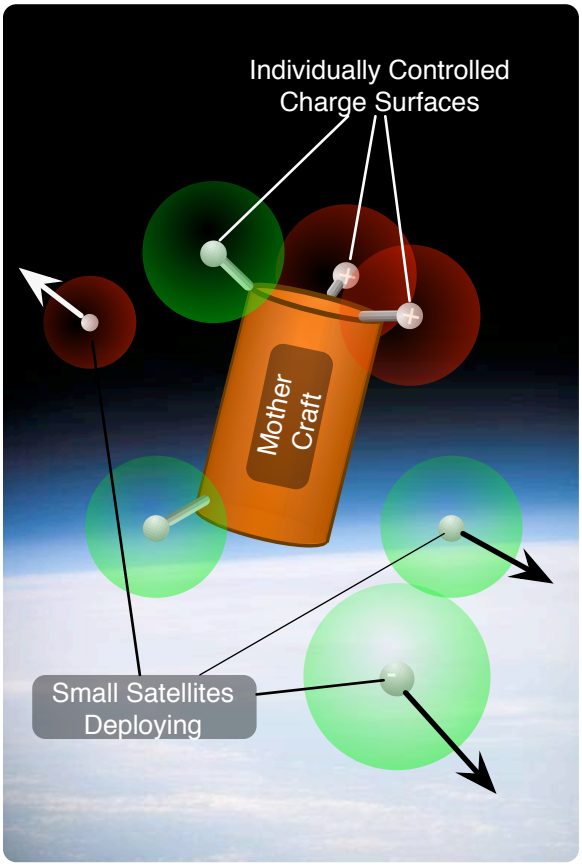

Figure 10.3: Illustration of a Swarm of Small Spacecraft Being Deployed from a Mother Craft using Coulomb Forces

10.2.3 Virtual Sensing Structure About Other Spacecraft

The virtual Coulomb structure concept employs a number of charge-controlled satellites whose control law makes them act as a single rigid structure. The original concept was born out of the discovery of relative equilibria solutions of the charged relative equations of motion. Such structures could replace solid structures and provide substantial mass savings and a very adjustable and robust formation shape.

A future research area of virtual Coulomb structures is to deploy a series of small probe satellites about another satellite to sense for damage. Flying craft in close proximity (dozens of meters) is always a very challenging undertaking because of the collision potential and the thruster plume impingement issues. However, being able to place sensor probes this close to another craft would allow for sophisticated remote diagnostic operations to be performed on another satellite without direct contact. Using the virtual Coulomb structure concept, the deployed charged craft would be parked in a natural relative equilibria constellation about the target craft. Using conventional formation or proximity flying it is impossible to keep a satellite slightly below another craft at all times without continually thrusting. The different orbit periods would cause the satellite to quickly drift apart. With the static Coulomb structure research candidate formation solutions are being identified where it is possible to have one satellite remain in a lower orbit. As a result it would be able to remotely diagnose Earth pointing sensors or the target craft. While such solutions require a continuous charge control to be available, the extremely fuel and power efficient nature of this concept the traditionally high fuel costs of such non-Keplerian formation

considerations.

Even though it might be possible to build space structures 100's of meters in size in the future, deploying such a structure about a target craft will be a nearly impossible challenge. With the modular Coulomb structure concept, the craft would be deployed about the mother craft using electrostatic forces and exploiting the naturally occurring orbital dynamics. Because the structure concept is determined through feedback control laws, it is possible to change the sensor location, or the structure size, shape and stiffness, over as as the mission requirements change.

Bibliography

[1] King, L. B., Parker, G. G., Deshmukh, S., and Chong, J.-H., "Spacecraft Formation-Flying using Inter-Vehicle Coulomb Forces," Tech. report, NASA/NIAC, January 2002, `http://www.niac.usra.edu`.

[2] Chen, F. F., *Plasma Physics and Controlled Fusion Volume 1: Plasma Physics*, Plenum Press, New York, 1984.

[3] Juhasz, A. and Horanyi, M., "Dynamics of charged space debris in the Earth's plasma environment," *Journal of Geophysical Research*, Vol. 102, No. A, April 1997, pp. 7237–7246.

[4] Garrett, H. B. and DeForest, S. E., "An Analytical Simulation of the Geosynchronous Plasma Environment," *Planetary Space Science*, Vol. 27, 1979, pp. 1101–1109.

[5] Craven, T. E., *Physics of Solar System Plasmas*, Cambridge University Press, 1997.

[6] Mullen, E. G., Gussenhoven, M. S., Hardy, D. A., A.Aggson, T., and Ledley, B. G., "SCATHA Survey of High-Voltage Spacecraft Charging in Sunlight," *Journal of the Geophysical Sciences*, Vol. 91, No. A2, 1986, pp. 1474–1490.

[7] Osgood, R. N., "Operational status of the space test program P78-2 spacecraft and payloads," *Proceedings of the 3rd Spacecraft Charging Technology Conference*, Nov. 12–14 1980, pp. 365–369, NASA Conference Publication 2182.

[8] Whipple, E. C. and Olsen, R. C., "Importance of differential charging for controlling both natural and induced vehicle potentials on ATS-5 and ATS-6," *Proceedings of the 3rd Spacecraft Charging Technology Conference*, Nov. 12–14 1980, p. 887, NASA Conference Publication 2182.

[9] Deininger, W. D., Aston, G., and Pless, L. C., "Hollow-cathode plasma source for active spacecraft charge control," *Review of Scientific Instruments*, Vol. 58, No. 6, June 1987, pp. 1053–1062.

[10] Garrett, H. B., Schwank, D. C., and DeFrost, S. E., "A Statistical Analysis of the Low Energy Geosynchronous Plasma Environment. -I Protons," *Planetary Space Science*, Vol. 29, 1981b, pp. 1045–1060.

[11] Garrett, H. B., Schwank, D. C., and DeFrost, S. E., "A Statistical Analysis of the Low Energy Geosynchronous Plasma Environment. -I Electrons," *Planetary Space Science*, Vol. 29, 1981a, pp. 1021–1044.

[12] Hill, G. W., "Researches in the Lunar Theory," *American Journal of Mathematics*, Vol. 1, No. 1, 1878, pp. 5–26.

[13] Clohessy, W. H. and Wiltshire, R. S., "Terminal Guidance System for Satellite Rendezvous," *Journal of the Aerospace Sciences*, Vol. 27, No. 9, Sept. 1960, pp. 653–658.

[14] Schaub, H. and Junkins, J. L., *Analytical Mechanics of Space Systems*, AIAA Education Series, Reston, VA, October 2003.

[15] Sedwick, R., Miller, D., and Kong, E., "Mitigation of Differential Perturbations in Clusters of Formation Flying Satellites," *AAS/AIAA Space Flight Mechanics Meeting*, February 1999, Paper No. AAS 99-124.

[16] Kapila, V., Sparks, A. G., Buffington, J. M., and Yan, Q., "Spacecraft Formation Flying: Dynamics and Control," *Proceedings of the American Control Conference*, San Diego, California, June 1999, pp. 4137–4141.

[17] Alfriend, K. T. and Schaub, H., "Dynamics and Control of Spacecraft Formations: Challenges and Some Solutions," *Journal of the Astronautical Sciences*, Vol. 48, No. 2 and 3, April–Sept. 2000, pp. 249–267.

[18] Burns, R., McLaughlin, C. A., Leitner, J., and Martin, M., "TechSat 21: formation design, control, and simulation," *IEEE Aerospace Conference Proceedings*, Vol. 7, Big Sky, MO, March 18–25 2000, pp. 19–25.

[19] Battin, R. H., *An Introduction to the Mathematics and Methods of Astrodynamics*, AIAA Education Series, New York, 1987.

[20] Roy, A. E., *Orbital Motion*, Adam Hilger Ltd, Bristol, England, 2nd ed., 1982.

[21] Office, U. G. P., "U.S. Standard Atmosphere," Washington, D.C., 1976.

[22] Wertz, J. R. and Larson, W. J., *Space Mission Analysis and Design*, Kluwer Academic Publishers, Dordrecht, The Netherlands, 1991.

[23] Toshihiro, K., "Solar radiation pressure model for the relay satellite of selene," *Earth Space and Planets*, Vol. 51, September 1999, pp. 979–986.

[24] Schaub, H. and Alfriend, K. T., "J_2 Invariant Relative Orbits for Spacecraft Formations," *Celestial Mechanics and Dynamical Astronomy*, Vol. 79, No. 2, 2001, pp. 77–95.

[25] Sengupta, P. and Vadali, S. R., "A Lyapunov-Based Controller for Satellite Formation Reconfiguration in the Presence of J_2 Perturbations," *AAS Space Flight Mechanics Meeting*, Maui, Hawaii, February 8–12 2004, Paper No. AAS-04-253.

[26] Alfriend, K. T., Schaub, H., and Gim, D.-W., "Gravitational Perturbations, Nonlinearity and Circular Orbit Assumption Effect on Formation Flying Control Strategies," *Proceedings of the Annual AAS Rocky Mountain Conference*, Breckenridge, CO, Feb. 2–6 2000, pp. 139–158.

[27] Makovec, K. L., *A Nonlinear Magnetic Controller for Three-Axis Stability of Nanosatellites*, Master's thesis, Virginia Polytechnic Institute and State University, Blacksburg, VA, July 2001.

[28] Schaub, H., Parker, G. G., and King, L. B., "Challenges and Prospect of Coulomb Formations," *Journal of the Astronautical Sciences*, Vol. 52, No. 1–2, Jan.–June 2004, pp. 169–193.

[29] Schaub, H., "Stabilization of Satellite Motion Relative to a Coulomb Spacecraft Formation," *Journal of Guidance, Control and Dynamics*, Vol. 28, No. 6, Nov.–Dec. 2005, pp. 1231–1239.

[30] Natarajan, A. and Schaub, H., "Linear Dynamics and Stability Analysis of a Coulomb Tether Formation," *AAS Space Flight Mechanics Meeting*, Copper Mountain, CO, Jan. 23–27 2005, Paper No. AAS 05–204.

[31] Kong, E. M., Miller, D. W., and Sedwick, R. J., "Optimal Trajectories and Orbit Design for Separated Spacecraft Interferometry," Tech. report, Massachusetts Institute of Technology, November 1998, SERC #13–98.

[32] Vadali, S. R., Alfriend, K. T., and Vaddi, S., "Hill's Equations, Mean Orbit Elements, and Formation Flying of Satellites," *The Richard H. Battin Astrodynamics Conference*, College Station, TX, March 2000, Paper No. AAS 00-258.

[33] Kong, E., Miller, D. W., and Sedwick, R. J., "Exploiting Orbital Dynamics for Aperture Synthesis using Distributed Satellite Systems," *Proceedings of the Space Flight Mechanics Meeting*, Breckenridge, CO, Feb. 7–10 1999, pp. 385–301, Paper AAS-99-112.

[34] Schaub, H., Vadali, S. R., and Alfriend, K. T., "Spacecraft Formation Flying Control Using Mean Orbit Elements," *Journal of the Astronautical Sciences*, Vol. 48, No. 1, 2000, pp. 69–87.

[35] King, L. B., Parker, G. G., Deshmukh, S., and Chong, J.-H., "Study of Interspacecraft Coulomb Forces and Implications for Formation Flying," *AIAA Journal of Propulsion and Power*, Vol. 19, No. 3, May–June 2003, pp. 497–505.

[36] Berryman, J. and Schaub, H., "Analytical Charge Analysis for 2- and 3-Craft Coulomb Formations," *AAS/AIAA Astrodynamics Specialists Conference*, Lake Tahoe, CA, Aug. 7–11, 2005 2005, Paper No. 05-278.

[37] Berryman, J. and Schaub, H., "Static Equilibrium Configurations in GEO Coulomb Spacecraft Formations," *AAS Spaceflight Mechanics Meeting*, Copper Mountain, CO, Jan. 23–27 2005, Paper No. AAS 05–104.

[38] Schaub, H., Hall, C., and Berryman, J., "Necessary Conditions for Circularly-Restricted Static Coulomb Formations," *AAS Malcolm D. Shuster Astronautics Symposium*, Buffalo, NY, June 12–15 2005, Paper No. AAS 05–472.

[39] Duffin, W. J., *Electricity and Magnetism*, McGraw-Hill Publishing Company, Maidenhead, UK, 1965.

[40] Halliday, D. and Resnick, R., *Fundamentals of Physics*, John Wiley and Sons, New York, 1st ed., 1970.

[41] Nicholson, D. R., *Introduction to Plasma Theory*, Krieger, Malabar, FL, 1992.

[42] Gombosi, T. I., *Physics of the Space Environment*, Cambridge University Press, New York, NY, 1998.

[43] Schaub, H. and Parker, G. G., "Constraints of Coulomb Satellite Formation Dynamics: Part I – Cartesian Coordinates," *Journal of Celestial Mechanics and Dynamical Astronomy*, 2004, submitted for publication.

[44] Schaub, H. and Kim, M., "Orbit Element Difference Constraints for Coulomb Satellite Formations," *AIAA/AAS Astrodynamics Specialist Conference*, Providence, Rhode Island, Aug. 2004, Paper No. AIAA 04-5213.

[45] Rosenbrock, H. H., "The Stability of Linear Time Dependent Control Systems," *J. of Electronics and Control*, Vol. 15, 1968, pp. 73–80.

[46] Leach, R. D. and Alexander, M. B., "Failures and anomalies attributed to spacecraft charging," Tech. Report Reference Publication 1375, NASA, August 1995.

[47] Lai, S. T., "An overview of electron and ion beam effects in charging and discharging of spacecraft," *IEEE Transactions on Nuclear Science*, Vol. 36, No. 6, Dec. 1989, pp. 2027–2032.

[48] Gussenhoven, M. S., Cohen, H. A., Hardy, D. A., Burke, W. J., and Chesley, A., "Analysis of ambient and beam particle characteristics during the ejection of an electron beam from a satellite in near-geosynchronous orbit on March 30, 1979," *3rd Spacecraft Charging Technology Conference*, No. 12–14, NASA Conference Publication 2182, 1980, pp. 642–664.

[49] Cohen, H. A. and et. al, "P78-2 Satellite and payload responses to electron beam operations on March 30, 1979," *3rd Spacecraft Charging Technology Conference*, No. 12–14, NASA Conference Publication 2182, 1980, pp. 642–644.

[50] Torkar, K. and et. al, "An experiment to study and control the Langmuir sheath around INTERBALL-2," *Annales Geophysicae*, Vol. 16, 1998, pp. 1086–1096.

[51] Torkar, K. and et. al., "Spacecraft Potential Control aboard Equator-S as a Test for Cluster-II," *Annales Geophysicae*, Vol. 17, 1999, pp. 1582–1591.

[52] Schmidt and et. al, "Results from active spacecraft potential control on the Geotail spacecraft," *Journal of Geophysical Research*, Vol. 100, No. A9, 1995, pp. 253–259.

[53] Riedler and et. al, "Active Spacecraft Potential Control," *Space Science Reviews*, Vol. 79, 1997, pp. 271–302.

[54] Torkar, K., Riedler, W., Escoubet, C. P., and et. al, "Active Spacecraft Potential Control for Cluster – Implementation and First Results," *Annales Geophysicae*, Vol. 19, No. 10/12, 2001, pp. 1289–1302.

[55] Schmidt and et. al, "A novel medium-energy ion emitter for active spacecraft potential control," *Rev. Sci. Instrum.*, Vol. 64, No. 8, August 1993, pp. 2293–2297.

[56] Ergun and et. al, "The FAST satellite fields instrument," *Space Science Reviews*, Vol. 98, No. 1–2, 2001, pp. 67–91.

[57] Rayburn, C., Campbell, R., Hoskins, W., and Cassady, R., "Development of a Micro Pulsed Plasma Thruster for the Dawgstar Nanosatellite," *36^{th} Joint Propulsion Conference & Exhibit*, Huntsville, AL, July 16–29 2000, Paper No. AIAA 2000-3256.

[58] Martinez-Sanchez, M. and Pollard, J. E., "Spacecraft Electric Propulsion – An Overview," *Journal of Propulsion and Power*, Vol. 14, No. 5, Sept.–Oct. 2003, pp. 688–699.